"DEPOSITION OF NICKEL COBALT PHOSPHATE THIN FILMS ON CONDUCTING SUBSTRATE FOR SUPERCAPACITOR APPLICATION"

A THESIS SUBMITTED

TO

D. Y. PATIL EDUCATION SOCIETY

(DEEMED TO BE UNIVERSITY), KOLHAPUR

FOR THE DEGREE OF

DOCTOR OF PHILOSOPHY

IN

PHYSICS

UNDER THE FACULTY OF

CENTRE FOR INTERDISCIPLINARY STUDIES

BY

MISS SUPRIYA JAYKUMAR MARJE

M. Sc.

UNDER THE GUIDANCE OF

Dr. UMAKANT. M. PATIL

M. Sc., Ph. D.

ASSISTANT PROFESSOR, (DST-INSPIRE FACULTY)

CENTRE FOR INTERDISCIPLINARY STUDIES,

D. Y. PATIL EDUCATION SOCIETY

(DEEMED TO BE UNIVERSITY), KOLHAPUR - 416 006

YEAR - 2020

DECLARATION

I hereby declare that the thesis entitled **"DEPOSITION OF NICKEL COBALT PHOSPHATE THIN FILMS ON CONDUCTING SUBSTRATE FOR SUPERCAPACITOR APPLICATION"** submitted for the award of degree of **Doctor of Philosophy** in **Physics** under the faculty of **Interdisciplinary studies** of D. Y. Patil Education Society (Deemed to be University), Kolhapur is completed and written by me, has not previously formed the basis for the award of any Degree or Diploma or other similar title of this or any other University in India or any other country or examining body to the best of my knowledge. Further, I declare that I have not violated any of the provisions under Copyright and Piracy/Cyber/IPR Act amended by UGC from time to time.

Place: Kolhapur   **Research Student**

Date: Miss Supriya Jaykumar Marje

D. Y. Patil Education Society
(Deemed to be University), Kolhapur

Centre for Interdisciplinary Research

Certificate

This is to certify that the thesis entitled *"Deposition of nickel cobalt phosphate thin films on conducting substrate for supercapacitor application"* which is being submitted herewith for the award of the Degree of *Doctor of Philosophy (Ph.D.)* in *Physics* of *D. Y. Patil Education Society (Deemed to be University), Kolhapur,* is the result of the original research work completed by *Miss Supriya Jaykumar Marje* under my supervision and guidance and to the best of my knowledge and belief the work embodied in this thesis has not formed earlier the basis for the award of any Degree or similar title of this or any other University or examining body.

Place: Kolhapur

Date:

Research Guide

Dr. Umakant M. Patil

Forwarded through Dean and Research Director

Centre for Interdisciplinary Studies

ACKNOWLEDGEMENT

It gives me great pleasure to express my sincere gratitude towards my research guide Dr. Umakant M. Patil (DST-INSPIRE Faculty, Centre for Interdisciplinary Studies, D. Y. Patil Education Society (Deemed to be University), Kolhapur) for his guidance, support and encouragement. His keenness, high-quality research work and integral view on research, has made a profound impression on me. His guidance helped me at all the time of research and writing of my thesis. I honestly thank him for his valuable advice, constructive criticism and his extensive discussions about my work. I gratefully acknowledge for his understanding and personal attention, which have provided good and smooth basis for my Ph.D. tenure. His flexibility in scheduling, gentle encouragement and relaxed demeanor made for a good working relationship and the impetus for me to finish the work. I find in him a real researcher, who through his own example and devotion for scientific work inspired me towards a common goal of achieving scientific knowledge and pursuit it.

I sincerely thankful to Prof. C. D. Lokhande, Dean and Research Director, Centre for Interdisciplinary Studies, D. Y. Patil Education Society (Deemed to be University), Kolhapur for generous support and constructive compliments helped me to achieve the goal. He provided a very fruitful discussion and helpful guidance for time management regarding my Ph.D. progress.

I would like to express my sincere thanks to Vice-chancellor Prof. Rakesh Mudgal, Pro vice-chancellor Dr. Shimpa Sharma and Registrar Dr. V. V. Bhosale for the inspiration and support. I am also thankful to Dr. J. L. Gunjakar, Dr. Vishwajeet

SUMMARY OF RESEARCH WORK LIST OF PUBLICATIONS

Papers Accepted at International Journals

1**. Supriya J. Marje**, Pranav K. Katkar, Sachin S. Pujari, Suraj A. Khalate, Prashant R. Deshmukh, Umakant M. Patil, "Effect of phosphate (anion) precursor on structural and morphology behavior of nickel phosphate thin films and its supercapacitive performance" Materials Science & Engineering B 261 (2020) 114641 (**I.F. - 4.7**).

2. **Supriya J. Marje**, Pranav K. Katkar, Sachin S. Pujari, Suraj A. Khalate, Abhishek C. Lokhande, Umakant M. Patil, "Regulated micro-leaf like nickel pyrophosphate as a cathode electrode for asymmetric supercapacitor" Synthetic Metals 259 (2020) 116224 (**I.F. - 3.286**).

3. **Supriya J. Marje**, Pranav K. Katkar, Shital B. Kale, Abhishek C. Lokhande, Chandrakant D. Lokhande, Umakant M. Patil, "Effect of phosphate variation on morphology and electrocatalytic activity (OER) of hydrous nickel pyrophosphate thin films" Journal of Alloys and Compounds 779 (2019) 49-58 (**I. F. - 4.65**).

4. S. S. Pujari, S. A. Kadam, Y. R. Ma, S. A. Khalate, P. K. Katkar, **S. J. Marje**, U. M. Patil, "Highly sensitive hydrothermally prepared nickel phosphate electrocatalyst as non-enzymatic glucose sensing electrode", Journal of Porous Material (2020) (**I.F-1.91**).

5. Pranav K. Katkar, **Supriya J. Marje**, Sachin S. Pujari, Suraj A. Khalate, Prashant R. Deshmukh, Umakant M. Patil, "Single-pot hydrothermal synthesis of manganese phosphate microrods as a cathode material for highly stable flexible solid-state symmetric supercapacitors" Synthetic Metals 267 (2020) 116446 (**I.F. - 3.286**).

6. Sachin S. Pujari, Sujit A. Kadam, Yuan-Ron Ma, Pranav K. Katkar, **Supriya J. Marje**, Suraj A. Khalate, Abhishek C. Lokhande, Umakant M. Patil, "Facile Synthesis of Microstrip-Like Copper Phosphate Hydroxide Thin Films for Supercapacitor Applications" Journal of Electronic Materials 49 (2020) 3890-3901 (**I.F. - 1.774**).

7. Shital B. Kale, Vaibhav C. Lokhande, **Supriya J. Marje**, Umakant M. Patil, Jin H. Kim, Chandrakant D. Lokhande, "Chemically deposited Co_3S_4 thin film: morphology dependant electrocatalytic oxygen evolution reaction" Applied Physics A 126 (2020) 206 (**I.F. - 1.81**).

8. Suraj A. Khalate, Sujit A. Kadam, Yuan-Ron Ma, Sachin S. Pujari, **Supriya J. Marje**, Pranav K. Katkar, Abhishek C. Lokhande, Umakant M. Patil, "Hydrothermally synthesized Iron Phosphate Hydroxide thin film electrocatalyst for electrochemical water splitting" Electrochimica Acta 319 (2019) 118-128 (**I.F. - 6.215**).

9. Pranav K. Katkar, **Supriya J. Marje**, Sachin S. Pujari, Suraj A. Khalate, Abhishek C. Lokhande, Umakant M. Patil, "Enhanced Energy Density of All-Solid-State Asymmetric Supercapacitors Based on Morphologically Tuned Hydrous Cobalt Phosphate Electrode as Cathode Material" ACS Sustainable Chemistry and Engineering 7 (2019) 11205-11218 (**I.F. - 7.632**).

10. Pranav K. Katkar, **Supriya J. Marje**, Shital B. Kale, Abhishek C. Lokhande, Chandrakant D. Lokhande, Umakant M. Patil, "Synthesis of hydrous cobalt phosphate electrocatalysts by a facile hydrothermal method for enhanced oxygen evolution reaction: effect of urea variation" CrystEngComm 21 (2019) 884-893 (**I.F. -3.382**).

11. Umakant M. Patil, Pranav K. Katkar, **Supriya J. Marje**, Chandrakant D. Lokhande, Seong C. Jun, "Hydrous nickel sulphide nanoparticle decorated 3D graphene foam electrodes for enhanced supercapacitive performance of an asymmetric device" New Journal of Chemistry 42 (2018) 20123-20130 (**I.F. - 3.288**).

Published (Indian) Patents

1. Vishwanath V. Bhosale, Umakant M. Patil, Pranav K. Katkar, **Supriya J. Marje**, Chandrakant D. Lokhande, "A chemical synthesis process of cobalt-manganese phosphate thin films on conducting substrates", (2018), Application No.- 201821018918.

2. Vishwanath V. Bhosale, Umakant M. Patil, Pranav K. Katkar, **Supriya J. Marje**, Chandrakant D. Lokhande, "A new chemical method to coat cobalt phosphate onto solid substrates", (2020), Application No.- 202021003019.

Papers/Poster Presented at National/International Conferences

1. **Supriya J. Marje**, Pranav K. Katkar, Girish S. Gund, Chandrakant D. Lokhande, Umakant M. Patil, Supercapacitive behaviour of electrodeposited Polyaniline thin films on carbon nanofiber paper, IC-NACMBM-2017, D. Y. Patil Education Society (Deemed to be University), Kolhapur.

2. **Supriya J. Marje**, Pranav K. Katkar, Sachin S. Pujari, Suraj A. Khalate, Abhishek C. Lokhande, Chandrakant D. Lokhande, Umakant M. Patil, Deposition of Hydrous Nickel Pyrophosphate Electrocatalyst for Oxygen Evolution Reaction, AMSCA-2018, Savitribai Phule Pune University, Pune.

3. **Supriya J. Marje**, Pranav K. Katkar, Sachin S. Pujari, Suraj A. Khalate, Abhishek C. Lokhande, Chandrakant D. Lokhande, Umakant M. Patil, Synthesis and Characterization of Hydrous Nickel Pyrophosphate Thin Film for Supercapacitor Application, MAS-2019, K. N. Bhise Arts, Commerce and Vinayakrao Patil Science College, Bhosare (Kurduwadi), Solapur.

4. **Supriya J. Marje**, Pranav K. Katkar, Sachin S. Pujari, Suraj A. Khalate, Abhishek C. Lokhande, Chandrakant D. Lokhande, Umakant M. Patil, Deposition and Characterization of Hydrous Nickel Pyrophosphate Thin Film for Supercapacitor Application, 4th ICPM-MDF-2019, Shivaji University, Kolhapur.

CONTENTS

CHAPTER – I

GENERAL INTRODUCTION AND LITERATURE SURVEY

CHAPTER - I

GENERAL INTRODUCTION AND LITERATURE SURVEY

1.1 General introduction

1.1.1 Necessity of supercapacitor

Whole world is dealing with big energy crises because of every single activity of human needed electrical energy and this energy produced from natural resources which are limited globally [1]. The worldwide increasing gasoline prices responsible for rise of ecofriendly and fuel efficient transportation development. To deal with this problem, clean and sustainable energy immediately needed. Easy and free availability of renewable energy sources may resolve this problem, so they got an extraordinary opportunity in development. There are numerous renewable energy sources, between that wind, solar and hydropower are most promising energy sources for energy generation. So, the problem can be resolved using renewable energy resources for continuous generation of energy. However, the main issue with the renewable energy sources is their irregular disposal [2]. So, the efficient energy storage devices should be develop since they can store the energy when it is available and retrieve when it needed. For the clean and green energy, the modern society moved towards development and improvement in efficiency of energy storage devices through variety of power sources. Presently, electrochemical energy systems are one and only who successively offers high power for the portable electronics and hybrid vehicles. As compare to fuel combustion system, electrochemical energy systems are more beneficial due to clean, economical and ecofriendly nature and are important in environmental point of view. The electrochemical energy storage technologies are most favorable choice for automobiles between various alternative energy sources. Batteries, fuel cells and supercapacitors are different types of power sources in electrochemical energy storage devices. Also, more capable and active than fuel combustion system with higher conversion efficiency [3].

Numerous applications requisite electrical energy storage devices such as cell phones, computers, solar cell, hybrid vehicles, etc. In the area of domestic and industrial, electric machines are widely used and are an important part of our day-to-day life. Also, electrical energy can easily converted into heat, light and mechanical energy as per requirement. However, electrical energy is difficult to available all time as in required form. So, there is need of efficient energy storage device which store large amount of energy. However, there are also some conditions in the application of energy storage devices like specific application required particular energy and power values. So, we need an energy storage devices who meet requirements of specific applications. For the application in portable electronics and electric vehicles, capacitors and batteries attracted attention among electrochemical energy storage technologies. Batteries are the common and most applicable electrical energy storage devices because they use small volume of active material for storing large amount of energy with appropriate amount of power as required for several applications. Batteries are filled with chemicals where electrochemical reactions take place at two electrodes which are separated by electrolyte, and it can be liquid or solid, but mostly dry powder used in ordinary batteries. In battery, energy stored in electrode by chemical reaction, when electrochemical reaction take place in electrode material by the electrolytic ions and released through load across it. Electrolyte act as ion transporter in charge storage reaction in battery. In recent years, storage capability of batteries improved by using standard design because of their increasing demand in numerous applications. Still, there is no any alternate available to deal with the problem of batteries like its low life span and less power. Hence, in present situation one needs to develop a design of device which has special abilities such as high power, energy density along with long cycle life [4].

Also, capacitor is another kind of energy storage device and basically it is used as filter in electronic circuits, it stores electric energy in the order of microfarads. Capacitors made up of with two electrically conducting plates separated by non-conducting material called a dielectric. One plate positively and other negatively charged when potential applied across it, after removing applied potential the charges releases via load [5]. It plays two crucial roles in the electronic circuits. In that, one is charging or discharging the electricity, which does numerous things in the circuits such as, smoothing the circuits of power supplies, for microcomputers act as backup circuits and for easier organization of electricity flow time for charging or discharging periods managed by timer circuits. Another role of capacitors is blocking of DC flow in the circuits. It is useful to remove or eliminate specific frequencies and very suitable where only specific frequency appearance is essential. However, the problem with a capacitor is, it stores a little amount of energy in the form of electricity [6]. So, it is not useful for applications that requires high energy.

The modern high power equipment demands a large amount of energy along with quick delivery, batteries and capacitors are unable to provide such requirement. Supercapacitors are developed in last few decades to fulfill major requirements of conventional energy storage devices (batteries and capacitors). Supercapacitors also known as electrochemical capacitors or ultracapacitors. As compare to conventional capacitors, supercapacitors achieve higher capacitance value by using high surface area electrode material and thin electrolytic dielectrics. So, they are capable to store high energy (compare with capacitor) along with high power (compare with batteries). Therefore, they are applicable in such applications that want high energy in a shorter time with good cycle life [7].
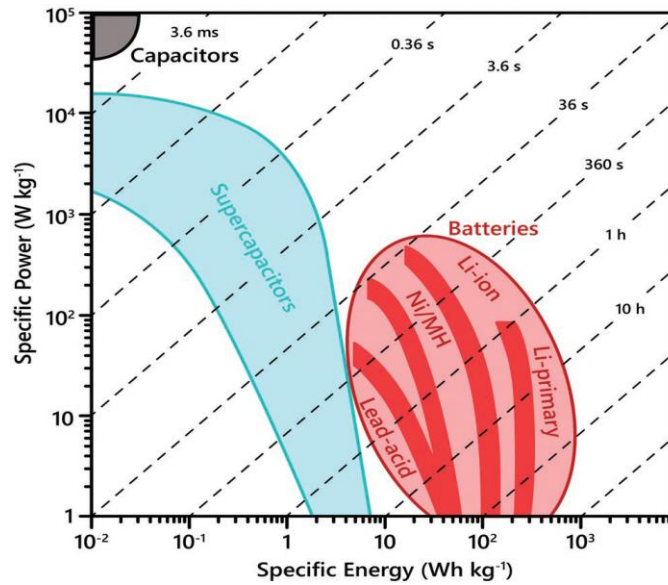
Fig. 1.1 Comparative Ragone plot of different energy storage devices with average

discharge time [8].

The performance of different energy storage devices is plotted in Ragone plot

and shown in Fig. 1.1. This graph explains how much energy (Wh kg^{-1}) is delivered by

different devices with respective power (W kg^{-1}), which means how rapidly they

delivers energy. This comparison clears that, supercapacitor getting much attention due

to high specific power (> 10 kW kg^{-1}) with moderate specific energy ($\sim$10 Wh kg^{-1})

[9]. Also, it is seen that supercapacitor lay between batteries and capacitors, which

means it bridges the gap between battery and conventional capacitor. Fast recharge

capability, high power density, and exceptionally long cycle lifetime of supercapacitors

have attracted significant attention in the field of power source applications such as

hybrid electric vehicles and portable electronics [10]. Also, they attracted for high

power applications such as backup system for computer memory, camera flash, lasers,

pulsed light generators, etc.

1.1.2 Background and development of supercapacitor

The next generation of capacitor is electrolytic capacitor. Their construction is

similar to batteries but they have same anode and cathode material, and they separated

by solid/liquid electrolytes. The electrochemical double layer capacitor is the third generation of capacitor, charge is stored at the interface of metal/electrolyte [6]. The electric double layer charge storage technology was well known in the 19th century but its first practical use in double layer capacitor was patented by H. I. Becker in 1957 using carbon electrodes in aqueous electrolyte [11]. However, it's impractical working mechanism in which electrodes need to be perfectly dipped in electrolyte container restricts commercialization. Furthermore, in 1966 the energy storage device successively developed using high surface area carbon material in a non-aqueous electrolyte by the Standard Oil Company of Ohio (SOHIO) [12]. First commercial double-layer capacitor called "Supercapacitors" was developed by Nippon Electric Company (NEC) under the license of SOHIO and applied for memory backup systems in 1978. At same time, "Goldcap" was invented by Matsushita Electric Industrial Co. (Panasonic) and used in memory backup systems. NECs developed supercapacitors using aqueous electrolyte and non-aqueous electrolyte was used in Panasonics Goldcap, this usage of electrolyte is main difference between them. Furthermore, a new principle for charge storage developed by B. E. Conway in 1975-1985 to replace coin cell batteries in memory backup systems. The fast and reversible redox reaction in bulk electrode material i.e. pseudocapacitive material used for the storage mechanism like ruthenium oxide (RuO_2) and this invention opened new trends in energy storage development. In 1982, the first high-power double-layer capacitors "PRI Ultracapacitor" prepared by PRI using metal oxide electrodes. Then "Dynacap" (double-layer capacitor) was established by ELNA in 1987. From 1990, the whole research world concentrated to develop high performance supercapacitor devices to replace battery technology. Now, there are numerous companies all over the world like ELTON, CAP-XX, Nippon Chemi-Con Corporation, NessCap, etc., manufacturing

supercapacitor devices for commercial applications. Currently, the high surface area carbon and transition metal oxide materials based supercapacitors are commercially manufactured and other metal sulphides, phosphides, phosphates and their composites are under investigation for supercapacitor application.

1.1.3 Recent trends in supercapacitor

Battery delivers high energy but suffers from low power than capacitor. However, supercapacitors deliver high power with a considerable amount of energy and long lifetime, and are easy to fabricate with low maintenance [13]. These features of supercapacitor used in present multifunctional technologies where battery technologies are limited, but their commercial applications restricted due to self-discharging rate [14]. So, nowadays all the researchers focuses on how to improve energy density of supercapacitor by manipulating various factors with maintaining all other properties. Basically, electrochemical double-layer capacitors (EDLCs), pseudocapacitors and hybrid capacitors are three types of supercapacitors. Generally, EDLCs fabricated using carbon based material which delivers high power density and pseudocapacitors by conducting polymers, metal oxide/hydroxides/sulphides/phosphates which delivers high energy density. Carbon based materials used as EDLC electrodes due to good electrical conductivity and high surface area [15]. Nevertheless, less capacitance of EDLCs limits their commercial use. On other hand, pseudocapacitive materials are beneficial for supercapacitive applications because of their low cost, low resistance and earth abundancy. Also, their fast and reversible redox reaction at the surface of electrode provides high capacitance and energy density values [16] but dissolution of active material in aqueous electrolyte limits cyclic stability. The issue of less stability can be resolved by replacing an aqueous electrolyte with a solid one, also it overcomes the electrolyte leakage problem with flexible and handy nature [17]. Different types of

ionic liquid electrolytes were invented to improve the electrochemical performance and operational potential window of the supercapacitor. They have several advantages such as non-flammability, non-toxicity and thermal stability. Moreover, they can extend applicable potential window of supercapacitor up to 4-6 V [18]. However, not only good electrode material improves total capacitance of supercapacitor but also other elements such as current collector, separator, electrolyte and other practical factors influence final electrochemical performance of supercapacitor. A high value of energy and power density can be obtained by employing pseudocapacitive electrode with a suitable electrolyte [19]. Nontoxicity and biocompatibility, lightweight are some advantages of flexible solid state devices which can be used in implantable medical devices. Furthermore, small and lightweight solid state supercapacitor devices can be used in portable electronic devices [20].

1.1.4 Working principle of supercapacitor

Electrochemical double-layer capacitor is the third generation of conventional capacitor. In conventional capacitor, two electrically conducting electrodes separated by insulating dielectric material and charge is stored electrostatically. As like conventional capacitor, electrochemical double layer capacitor store electric charge at metal/electrolyte interface and opposite ions on the surface of electrode forms an electric double layer. The schematic representation of charge storage mechanism in electrochemical capacitor is shown in Fig. 1.2. Electrochemical capacitors offer high energy density than conventional capacitors and longer life than batteries. For the higher capacitance, the electrochemical capacitor required a high surface area electrode and a smaller thickness of double layer.
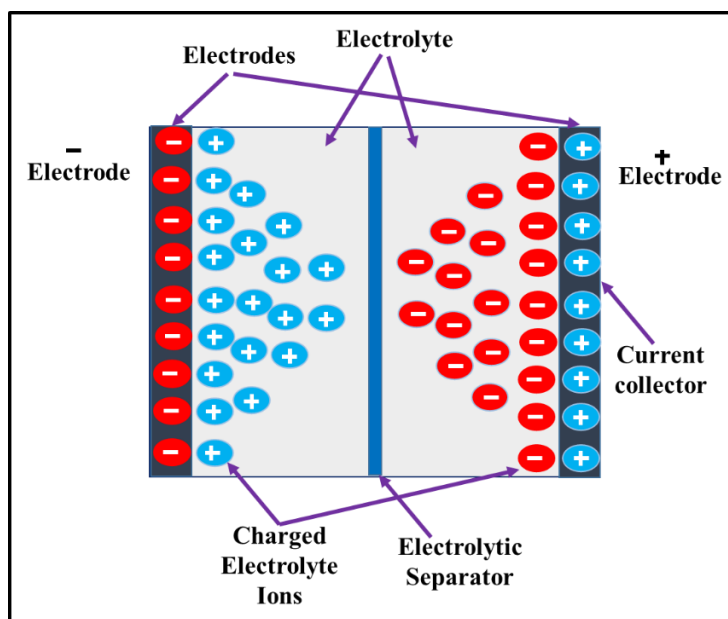
Fig. 1.2 Schematic of charge storage mechanism of electrochemical capacitor.

The capacitance of electrochemical capacitor C is calculated by following equation,

$$C = \varepsilon_r \frac{A}{d} \tag{1.1}$$

where, ε_r, A and d are the relative permittivity, surface area of active material and thickness of double layer, respectively. The energy density (E) of the electrochemical capacitor is calculated as follows,

$$E = \frac{CV^2}{2} \tag{1.2}$$

where, C is capacitance and V is the operational potential window of electrochemical capacitor.

1.2 Classification of supercapacitor

Unique storage mechanism and usage of electrode material distinguish supercapacitors into three categories as electric double-layer capacitors (EDLCs), pseudocapacitors and hybrid capacitors. A non-faradaic mechanism is used for charge storage in EDLCs, means charge stored by forming a double layer between electrode surface and electrolyte and carbon based electrode materials are used for the construction of EDLCs [21, 22]. Charge storage mechanism in pseudocapacitor

involves exchange of electrons and used materials have a number of oxidation states like metal oxides/hydroxides/sulphides/phosphides/phosphates, conducting polymers, etc. [23, 24]. Hybrid capacitors are fabricated by combining EDLCs and pseudocapacitive materials and they stores energy by both faradaic and non-faradaic mechanisms [25, 26]. The schematic presentation of classification of supercapacitor is shown in chart 1.

1.2.1 Electrochemical double-layer capacitors (EDLCs)

EDLCs consists of two carbon electrodes, electrolyte and separator, and charge stored electrostatically or non-faradaically as like conventional capacitor (Fig. 1.3 (a)). So, no charge transfer between electrode and electrolyte take place. Following the opposite charge attraction, ions diffuses through separator from electrolyte towards oppositely charged electrodes and adsorbs on the surface of electrode when voltage is applied. At the surface of each electrode, recombination of ions prevented by electrodes produces double-layer of ions.
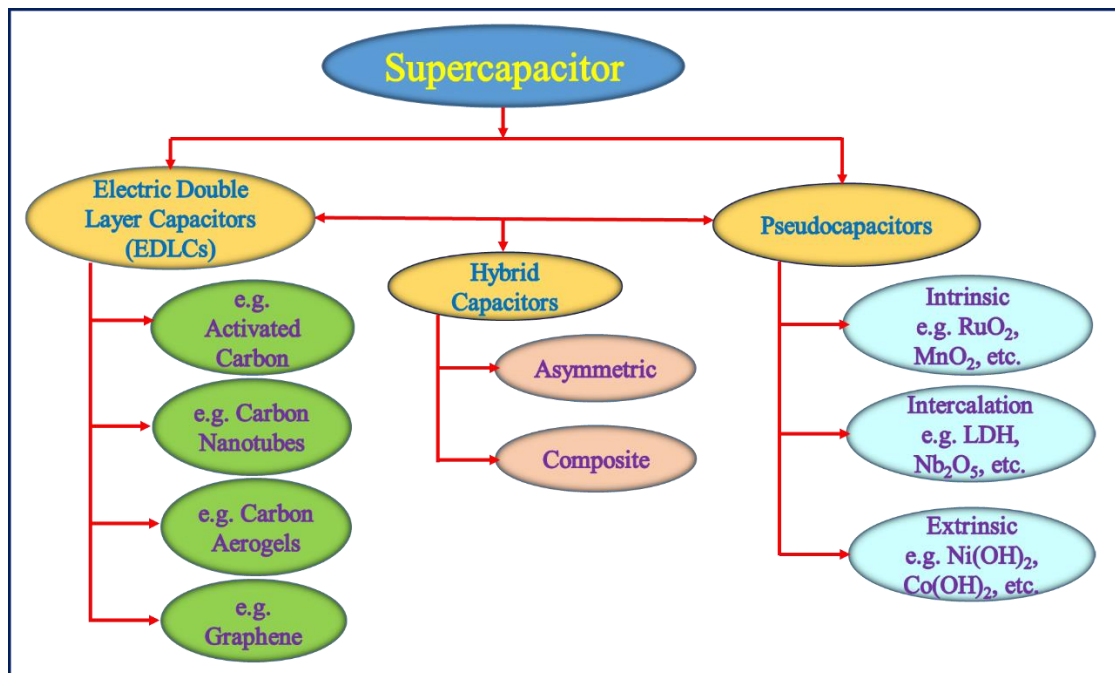

Chart 1: Classification of supercapacitor.

There is no chemical reaction or phase transformation due to no charge transfer between electrode and electrolyte. This non-faradaic reaction offers high reversibility in charge storage that responsible for higher cyclic stability of EDLC electrodes. So, EDLCs shows stable performance of charge-discharge cycles and it is upto 10^6 cycles. Due to higher cyclic stability, EDLCs are applicable at non-user serviceable locations such as on mountains and deep sea locations. Also, the low price, higher surface area and well established production techniques of the carbon electrode materials increases their importance than other electrode materials. For the charge storage in EDLC electrode different forms of carbon materials are used such as, activated carbon, carbon aerogels, carbon nanotubes, and recently new form of carbon is graphene which attracted much attention.

1.2.2 Pseudocapacitors

In pseudocapacitors charge is stored by faradaic mechanism, where charge transferred between electrode and electrolyte by fast and reversible redox surface reactions. The schematic representation of charge storage mechanism in pseudocapacitor is shown in Fig. 1.3 (b). The faradaic process allows high capacitance and energy densities for pseudocapacitors than the EDLCs. Less number of ions involved in double layer as compared to exchange of ions between electrolyte and electrode. Particle size, material conductivity, area of active material and also electrolyte type are important factors which affects on performance of pseudocapacitors. The charge storage procedure contains and able to do electrosorption, oxidation-reduction reaction, and intercalation/deintercalation processes, that labeled as pseudocapacitors. On the basis of charge storage mechanisms, pseudocapacitor further divided into three categories such as, i) intrinsic pseudocapacitor (on or near material surface faradaic reactions), b) intercalation-type pseudocapacitor (charge

stored in tunnels or layers of materials), and c) extrinsic pseudocapacitor (faradaic reaction at surface of nano sized battery materials).
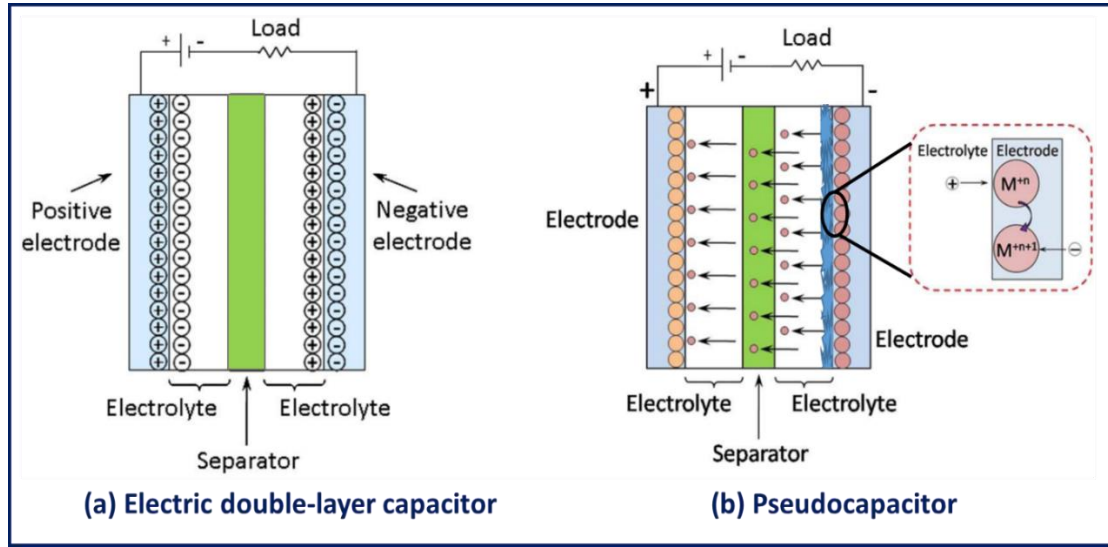

Fig. 1.3 Charge storage mechanism of (a) EDLC and (b) pseudocapacitor [26].

1.2.2.1 Intrinsic or surface redox pseudocapacitors

Trasatti and Buzzanca [27] firstly discovered pseudocapacitive nature of RuO_2 from its quasi-rectangular curves of cyclic voltammetry (CV) as like EDLC materials. In intrinsic material, charges are stored by double layer as well as surface redox mechanism on the surface of material or near the surface of material. Due to number of valance states, some transition metal oxides (e.g. RuO_2, MnO_2) exhibit intrinsic pseudocapacitive nature and their redox reaction at the surface of electrode makes them better than EDLCs. Also, they have capability of high energy storage with excellent charging-discharging rate.

1.2.2.2 Intercalation pseudocapacitors

The charge can be stored in material by faradaically via intercalation of electrolytic ions into tunnels and layers of material without changing its phase, such type of charge storage mechanism is investigated by Augustyn et. al. [28] and defined as "intercalation pseudocapacitors". The important property of intercalation

pseudocapacitor is that, the electrode material does not change its structural phase during electrochemical reaction [29]. In intercalation pseudocapacitor, charge storage process is not only restricted to surface but also utilizes bulk of material for electrochemical reactions. Some layered materials (e.g. Layer Double Hydroxide (LDH), Nb_2O_5) having wide interplanar spacing exhibits the intercalation pseudocapacitive type nature.

1.2.2.3 Extrinsic pseudocapacitors

The materials, who shows battery like nature in CV (strong redox peaks) and charge-discharge curves (with plateau) in their bulk form and transformed in pseudocapacitive nature by decreasing its particle size (in nanosize) was investigated by Augustyn et. al. [28] and defined as "extrinsic pseudocapacitors". The battery type materials overcome their phase change property when it goes in nanosize, decreases ion diffusion length and demonstrate pseudocapacitive nature. After reducing dimensions of material, typical battery type material serves a pseudocapacitive nature by promoting surface dominant ion storage. The nanosized nickel and cobalt hydroxides are examples of extrinsic pseudocapacitive materials [30].

1.2.3 Hybrid capacitors

In comparison between EDLCs and pseudocapacitors, merit of one type of material is demerit of other. So, the combination of both systems supposed to give the merits of both and resolve all problems of supercapacitor [31]. This can be done by merging one electrode material based on pure EDLC type and another pure pseudocapacitive type, such a combination is largely studied to take advantage of both mechanisms. Simultaneously both mechanism occurs in this kind of system and is called as hybrid capacitor [32]. Carbon based material combined with metal oxide or conducting polymer means both mechanism combines in single electrode and termed

as composite electrode. By using composite type electrodes fabricated capacitor called as composite hybrid capacitor. In asymmetric hybrid capacitor, hybrid capacitor is prepared by combining one battery type electrode and another capacitive type electrode. This combination offers high energy of batteries and power like a capacitor with improved cycle life. These devices may able to bridge the gap between batteries and supercapacitors [33]. They are attractive for improved energy and cyclic stability than EDLCs and pseudocapacitors, respectively.

1.3 Electrode materials for supercapacitors

The higher supercapacitive performance can be achieved by selecting active material with desired properties. The features of active material plays important role in achieving high supercapacitive performance. The required features of supercapacitor electrode materials are listed below,

❖ Electrode should have a high specific surface area.

❖ To control rate capability and power density electrical conductivity must be high.

❖ Controlled porosity can improve performance.

❖ Non-toxic and low cost precursor materials are required.

❖ Thermal and chemically stable active materials are required.

❖ Easy and economic preparation method of material.

1.3.1 Carbon based materials

In carbon based material, with high surface area and less expensive activated carbon material is the most prime choice for EDLCs. There is a correlation between surface area and capacitance, since surface area is directly proportional to capacitance. However, activated carbon could not achieve high capacitance due to the inaccessibility of surface area. So, researchers focused on development of optimal porous material for easy accessibility of electrolyte ions, which can improve total capacitance of activated

carbon. Recently, carbon aerogels getting much attention due to low electrochemical series resistance (ESR) than activated carbon because of binderless electrode preparation as an EDLC material. It has ability to chemically link with current collector and continuous structure of carbon aerogels does not require any additional binding agent. In contrast with other carbon materials, carbon nanotubes (CNT) have one dimensional structure that offers continuous charge distribution and fast transfer, and uses almost all active area for electrosorption. Therefore, efficient use of surface area of CNT material delivers high capacitance than activated carbon. Also, their mesoporous network is important for easy diffusion of electrolyte ions and lower ESR than activated carbon. Recently, interest increased in the use of graphene oxide and reduced graphene oxide based material as an EDLC electrode material because of their high surface area and conductivity. Graphene has a large theoretical surface area (2600 $m^2 g^{-1}$), high intrinsic mobility, high Young's modulus and thermal stability (1500-5000 $W m^{-1} K^{-1}$) with good electrical conductivity catches attention for particularly EDLC application among their various application [34].

1.3.2 Conducting polymers

Out of various conducting polymers polyaniline (PANI) [35], polypyrrole (PPy) [36] and polythiophene (PTh) [37] are mostly used for supercapacitor application. Good electrical conductivity, high porosity and wide operating potential window are the main advantages of conducting polymer materials. However, additional potential converts phase of conducting polymer (into non-conducting) and also causes mechanical degradation of material that reduces supercapacitive performance. Therefore, for better performance operative potential range is very important in case of conducting polymers.

1.3.3 Metal oxides

Metal oxide based electrodes are promising electrodes for supercapacitor application due to high energy density and electrochemical stability as compare to conducting polymers. Fast and reversible redox reaction at electrode/electrolyte interface responsible for high energy density value. They offer multiple oxidation states for charge storage and a wide operational potential window. The various metal oxides such as MnO_2 [38, 39], RuO_2 [40], Co_3O_4 [41], NiO [42] and Fe_2O_3 [43] were explored for supercapacitor application. Among these materials, RuO_2 is widely investigated for supercapacitor application due to its high electrical conductivity, different oxidation state and wide potential window. However, high cost and toxicity restrict their commercialization in supercapacitors.

1.3.4 Metal phosphates

Metal phosphate based materials attracted attention in recent years for application in energy storage devices due to their low cost, environment friendly and earth abundant nature. They also have numerous additional important properties such as unique chemical/physical characteristics and tunable multifunctionality [44]. Open structure of metal phosphate material with hollow wide channel offers good ionic conductivity and strong P-O covalent bond offers good chemical stability [48]. The structural stability of phosphate materials during charge-discharge makes them best candidate in energy storage applications. Therefore, many metal phosphates are commercially used in battery manufacturing [45-47]. The numerous metal phosphates were investigated for the supercapacitor application as, Ag_3PO_4 [49, 50], $BiPO_4$ [51-54], $Co_3(PO_4)_2$ [55], $Ni_3(PO_4)_2$ [56], $Mn_3(PO_4)_2$ [57], $VOPO_4$ [58, 59], etc. Among these metal phosphates, nickel and cobalt based phosphate materials are the best candidate as cathode and widely used for energy storage devices.

1.4 Literature survey on nickel phosphate, cobalt phosphate and nickel cobalt phosphate

1.4.1   Literature survey on nickel phosphate

In recent years, nickel based materials are highly investigated for energy storage applications due to its low cost, rich redox behaviour, high specific capacitance, high corrosion resistance and good stability. Different polymorphs of nickel phosphate prepared and investigated for supercapacitor application such as, $Ni_3(PO_4)_2$ [56, 60-64], $Ni_{20}[(OH)_{12}(H_2O)_6][(HP_4)_8(PO_4)_4].12H_2O$ [65, 66] and $Ni_2P_2O_7$ [67-73]. Various structures of nickel phosphate and their composite materials were prepared using different synthesis methods such as hydrothermal, co-precipitation, sonochemical and calcination. Different structures with morphologies and corresponding supercapacitive performance of nickel phosphate material are summarized in table 1.1. The different electrochemical performance observed for different structure and morphologies such as, nanoparticles of $Ni_3(PO_4)_2$ prepared via sonochemical method by Omar et. al [56] and observed phase transformation of nickel phosphate material after calcined at different temperature. The nickel phosphate material calcined at 300 ℃ delivered highest capacitance of 1771 F g^{-1} at 0.4 A g^{-1} current density. The microwave-assisted chemical method employed for the preparation of microflowers of $Ni_3(PO_4)_2.8H_2O$ by Peng et. al. [60]. The prepared nickel phosphate material offered maximum specific capacitance of 1301 F g^{-1} at 2 A g^{-1} current density with 83.59 % capacitance retention after 1000 cycles. The nanoparticles of $Ni_3(PO_4)_2$ composite with GO synthesized by Li et. al. [61] via precipitation method and obtained specific capacitance of 1392.59 F g^{-1} at 0.5 A g^{-1} current density with 93.5 % capacitive retention after 1000 cycles. Mirghni et. al. [62] synthesized $Ni_3(PO_4)_2$/GF composite material via hydrothermal method delivered highest specific capacity of 48 mAh g^{-1} at 0.5 A g^{-1} current density.

Omar et. al. [63] deposited silver phosphate nanoparticles (Ag_3PO_4 NPs) on amorphous $Ni_3(PO_4)_2$ by precipitation method followed by calcination, it offered maximum specific capacity of 478 C g^{-1} at 1 A g^{-1} current density in 1 M KOH electrolyte.

Zhao et. al. [64] prepared $Ni_3(PO_4)_2/RGO/Co_3(PO_4)_2$ composite material via hydrothermal method, which delivered specific capacitance of 1137.5 F g^{-1} at 0.56 A g^{-1} current density with 117.8 % capacitive retention over 14000 cycles. Zhao et. al. [65] prepared nanorods of $Ni_{20}[(OH)_{12}(H_2O)_6][(HP_4)_8(PO_4)_4].12H_2O$ by simple hydrothermal method and reported specific capacitance of 1494 F g^{-1} at 1.25 A g^{-1} current density. The nanocrystal of VSB-5 ($Ni_{20}[(OH)_{12}(H_2O)_6][(HP_4)_8(PO_4)_4].12H_2O$) prepared by Yang et. al. [66] via hydrothermal method and it delivered highest specific capacitance of 2740 F g^{-1} at 3 A g^{-1} current density. Pramanik et. al. [67] synthesized amorphous nature of $Ni_2P_2O_7$ via hydrothermal method followed by calcination offers a specific capacitance of 265 F g^{-1} at 20 mV s^{-1} scan rate. Amorphous nickel pyrophosphate ($Ni_2P_2O_7$) microstructures was synthesized by calcining ammonium nickel phosphate hydrate microstructures in air by Pang et. al. [68], and it exhibited specific capacitance of 1050 F g^{-1} at 0.5 A g^{-1} current density. Senthilkumar et. al. [69] synthesized nanograins of $Ni_2P_2O_7$ by simple co-precipitation technique and tested as cathode material, which delivered a maximum specific capacitance of 1893 F g^{-1} at 2 A g^{-1} current density. Sankar et. al. [70] prepared nanorods of $Ni_2P_2O_7$ by simple hydrothermal method and offered maximum capacitance of 5753 mF cm^{-2} at 5 mA cm^{-2} current density with addition of $K_3[Fe(CN)_6]$ redox additive in 1 M KOH electrolyte. Nanosheets of $Ni_2P_2O_7$ decorated by NiCo-OH composite material prepared by Chodanakar et. al. [71] on nickel foam and delivered highest specific capacitance of 2529 F g^{-1} at 1 mA cm^{-2} current density with high stability (92.59 %). A core-shell structured $MnO_2@Ni_2P_2O_7$ prepared by Chodanakar et. al. [72] using hydrothermal

followed by a chemical bath deposition method and delivered specific capacity of 309 mAh g^{-1} at 1 A g^{-1} current density with excellent stability (94 %) over 12000 cycles. Na doped Ni$_2$P$_2$O$_7$ hexagonal tablets are synthesized by Wei et. al. [73] via hydrothermal method, offered maximum capacitance of 557.5 F g^{-1} at 1.2 A g^{-1} current density. Nickel phosphite (Ni$_{11}$(HPO$_3$)$_8$(OH)$_6$) hexagonal polyhedrons were successfully synthesized under hydrothermal conditions by Pang et. al. [74]. Also, the nanotubes and nanocrystals of nickel phosphite (Ni$_{11}$(HPO$_3$)$_8$(OH)$_6$) prepared by Li et. al. [75] and Gao et. al. [76], respectively. Moreover, the Co-doped bouquet-like nickel phosphite (Ni$_{11}$(HPO$_3$)$_8$(OH)$_6$) material synthesized by Li et. al. [77] via a simple solvothermal method.

Table 1.1: Electrochemical performance of nickel phosphate based electrodes.

Sr. No.	Material and morphology	Substrate	Method of deposition	Electrolyte	Capacitance (F g^{-1}) at current density (A g^{-1})	Stability at cycles	Ref.
1.	Ni$_3$(PO$_4$)$_2$ (Nanoparticles)	Nickel Foam	Sonochemical	1 M KOH	1771 at 0.4	-	56
2.	Ni$_3$(PO$_4$)$_2$.8H$_2$O (Microflowers)	Nickel Foam	Microwave-assisted	KOH	1301 at 2	83.59%, 1000	60
3.	Ni$_3$(PO$_4$)$_2$@GO (Nanoparticles)	Nickel Foam	Chemical precipitation	2 M KOH	1392.59 at 0.5	93.5%, 1000	61
4.	Ni$_3$(PO$_4$)$_2$/GF (Nanorods)	Nickel Foam	Hydrothermal	6 M KOH	48 mAh g^{-1} at 0.5	92%, 2000	62
5.	Ni$_3$(PO$_4$)$_2$-Ag$_3$PO$_4$ (Nanoparticles)	Nickel Foam	Sonochemical & Calcination	1 M KOH	478 C g^{-1} at 1	-	63
6.	Ni$_3$(PO$_4$)$_2$/RGO/ Co$_3$(PO$_4$)$_2$ (Roe shaped)	Cobalt Foam	Hydrothermal	1 M KOH	1137.5 at 0.56	117.8%, 14000	64
7.	Ni$_{20}$[(OH)$_{12}$ (H$_2$O)$_6$] [(HP$_4$)$_8$(PO$_4$)$_4$]. 12H$_2$O (Nanorods)	Nickel Foam	Hydrothermal	3 M KOH	1497 at 1.25	-	65
8.	Ni$_{20}$[(OH)$_{12}$ (H$_2$O)$_6$] [(HP$_4$)$_8$(PO$_4$)$_4$]. 12H$_2$O (Nanocrystal)	Nickel Foam	Hydrothermal	1 M KOH	2740 at 3	-	66
9.	Ni$_2$P$_2$O$_7$ (Nano spheres)	Graphite	Hydrothermal & Calcination	3 M KOH	265 at 20 mV s^{-1}	97%, 1000	67
10.	Ni$_2$P$_2$O$_7$ (Microstructures)	Nickel Foam	Stirring & Calcination	3 M KOH	1050 at 500 mA g^{-1}	90.5%, 6000	68

11.	$Ni_2P_2O_7$ (Nanograins)	Carbon Paper	Co-precipitation	1 M NaOH	1893 at 2	-	69
12.	$Ni_2P_2O_7$ (Nanorods)	Nickel Foam	Hydrothermal	1 M KOH	5753 mF cm^{-2} at 5 mA cm^{-2}	83.59%, 5000	70
13.	$Ni_2P_2O_7$/NiCo-OH (Nanosheets, micro-sheets)	Nickel Foam	Hydrothermal & Electrodeposition	2 M KOH	2529 at 1 mA cm^{-2}	92.59%, 10000	71
14.	$MnO_2@Ni_2P_2O_7$ (Nanoflakes, micro-sheets)	Nickel Foam	Hydrothermal & Chemical bath deposition	2 M KOH	309 mAh g^{-1} at 1	94%, 12000	72
15.	$Na-Ni_2P_2O_7$ (Hexagonal tablets)	Nickel Foam	Hydrothermal	3 M NaOH	557.5 at 1.2	97.3%, 1000	73
16.	$(Ni_{11}(HPO_3)_8 (OH)_6)$ (Hexagonal polyhedron)	Nickel Foam	Hydrothermal	3 M KOH	295 at 0.625	99.3%, 1000	74
17.	$Ni_{11}(HPO_3)_8 (OH)_6$ (Nanotubes)	Nickel Foam	Hydrothermal	3 M KOH	1876 at 0.625	95%, 2000	75
18.	$(Ni_{11}(HPO_3)_8 (OH)_6)$ (Nanocrystals)	Nickel Foam	Hydrothermal	3 M KOH	588 at 0.5	97.7%, 10000	76
19.	$Co-(Ni_{11}(HPO_3)_8 (OH)_6)$ (Bouquet-like)	Nickel Foam	Solvothermal	3 M KOH	751.5 at 1	92.8%, 8000	77

The asymmetric devices were fabricated using different phases of nickel phosphate as a cathode for evaluation of practical applicability and summarized in table 1.2. Omar et. al. [56] fabricated an asymmetric device by comprising $Ni_3(PO_4)_2$ as a positive electrode and activated carbon (AC) as a negative electrode in 1 M KOH electrolyte. The device delivered specific capacity of 355 C g^{-1} at 0.4 A g^{-1} current density with energy density of 76 Wh kg^{-1} at power density of 599 W kg^{-1}. Also, device retained 88.5 % initial capacity after 3000 cycles. The $Ni_3(PO_4)_2.8H_2O$//rGO device prepared by Peng et. al. [60] delivered highest specific capacity of 122.3 C g^{-1} at 1 A g^{-1} current density with energy density of 25.48 Wh kg^{-1} at power density of 750 W kg^{-1}, and retained 84.23 % capacity after 1000 cycles. The asymmetric device $Ni_3(PO_4)_2@GO$//$Fe_2O_3@GO$ fabricated by Li et. al. [61] and observed maximum

capacitance of 189 F g^{-1} at 0.25 A g^{-1} current density with 85 % cyclic stability after 1000 cycles. Also, it achieved maximum energy density of 67.2 Wh kg^{-1} at power density of 200.43 W kg^{-1}. Mirghni et. al. [62] fabricated asymmetric device ($Ni_3(PO_4)_2$/90 mg GF//C-FP) by combining $Ni_3(PO_4)_2$/90 mg graphene foam (GF) as the cathode and carbonized iron (Fe^{3+}) adsorbed on polyaniline (PANI) (C-FP) as the anode material and it achieved maximum energy density of 49 Wh kg^{-1} at power density of 499 W kg^{-1} with 53 % cyclic stability. Omar et. al. [63] fabricated $Ni_3(PO_4)_2$-Ag_3PO_4//AC based supercapattery and it exhibited an energy density of 32.4 Wh kg^{-1} at 399.5 W kg^{-1} power density, and excellent cyclic stability after 5000 cycles. The asymmetric device $Ni_3(PO_4)_2$/RGO/$Co_3(PO_4)_2$//AC fabricated by Zhao et. al. [64] delivered capacitance of 115.4 F g^{-1} at 0.12 A g^{-1} current density with 91.9 % cyclic stability over 18000 cycles. Also, it achieved energy density of 44.82 Wh kg^{-1} at 428.6 W kg^{-1} power density. A solid state device $Ni_{20}[(OH)_{12}(H_2O)_6][(HP_4)_8(PO_4)_4].12H_2O$ //graphene fabricated by Zhao et. al. [65] using PVA-KOH electrolyte delivered highest volumetric energy density of 0.445 mWh cm^{-3} at power density of 44 mW cm^{-3} with 97.4 % capacitive retention over 5000 cycles.

Senthilkumar et. al. [69] fabricated $Ni_2P_2O_7$//HPGC asymmetric device delivered capacitance of 183 F g^{-1} and it achieved energy density of 65 Wh kg^{-1} at 800 W kg^{-1} power density with 83 % capacitive retention. Sankar et. al. [70] assembled $Ni_2P_2O_7$//rGO hybrid supercapacitor device and it delivered a high specific capacitance of 224 F g^{-1} at 1 A g^{-1} current density. Also, it delivered high energy density of 70 Wh kg^{-1} at a power density of 750 W kg^{-1} with high coulombic efficiency (96 %) over 5000 cycles. $Ni_2P_2O_7$/NiCo-OH//AC device fabricated by Chodanakar et. al. [71] using PVA-KOH gel electrolyte delivered specific capacitance of 221 F g^{-1} at 3 mA cm^{-2} current density with 91.83 % cyclic stability over 10000 cycles. Also, it exhibited high

energy density of 78 Wh kg^{-1} at a power density of 444 W kg^{-1}. Chodanakar et. al. [72] fabricated MnO$_2$@NPO//AC solid-state device using PVA-KOH gel electrolyte and it exhibits specific capacity of 82 mAh g^{-1} at a current density of 1 A g^{-1} and excellent specific energy of 66 Wh kg^{-1} at specific power of 640 W kg^{-1}. The solid state device fabricated by Wei et. al. [73] using Na doped Ni$_2$P$_2$O$_7$ and graphene as positive and negative electrodes, respectively. The fabricated device achieved maximum specific capacitance of 32.6 mF cm^{-2} at current density of 0.5 mA cm^{-2} with maximum energy density of 23.4 Wh kg^{-1} at power density of 1.29 kW kg^{-1}. A flexible solid-state asymmetric supercapacitor device fabricated using nanocrystal of Ni$_{11}$(HPO$_3$)$_8$(OH)$_6$ (cathode) and graphene nanosheets (anode) by Gao et. al. [76] using PVA-KOH gel electrolyte. The device exhibited specific capacitance of 1.64 F cm^{-2} at current density of 5 mA cm^{-2} with energy density of 0.45 mWh cm^{-3} at power density of 33 mW cm^{-3} and 93.3 % initial capacitance retention after 10000 cycles. Li et. al. [77] prepared aqueous and solid state devices using Co doped nickel phosphite (Ni$_{11}$(HPO$_3$)$_8$(OH)$_6$) and activated carbon as positive and negative electrodes, respectively. The aqueous device with 3 M KOH electrolyte delivered specific capacitance of 83.1 mF cm^{-2} at 0.5 mA cm^{-2} current density, also exhibits energy density of 15.48 mWh cm^{-2} at power density of 600 W cm^{-2} with 94 % cyclic stability over 5000 cycles. The solid state device with PVA-KOH gel electrolyte delivered specific capacitance of 77.1 mF cm^{-2} at 0.5 mA cm^{-2} current density, also exhibits energy density of 14.72 mWh cm^{-2} at power density of 600 W cm^{-2} with 91.2 % cyclic stability over 5000 cycles.

Table 1.2: Electrochemical performance of nickel phosphate based supercapacitor devices.

Sr. No.	Positive electrode (cathode)	Negative electrode (anode)	Electrolyte	Capacitance ($F g^{-1}$) at current density ($A g^{-1}$)	Energy density (Wh kg^{-1})	Power density (W kg^{-1})	Stability at cycles	Ref.
1.	$Ni_3(PO_4)_2$/NF	AC/NF	1 M KOH	355 C g^{-1} at 0.4	76	599	88.5%, 3000	56
2.	$Ni_3(PO_4)_2.8H_2O$	rGO	-	122.3 C g^{-1} at 1	25.48	750.02	84.23%, 1000	60
3.	$Ni_3(PO_4)_2$@GO/ NF	Fe_2O_3@ GO/NF	-	189 at 0.25	67.2	200.43	85%, 1000	61
4.	$Ni_3(PO_4)_2$/GF/ NF	C-FP/NF	-	48 mAh g^{-1} at 0.5	49	499	53%, 10000	62
5.	$Ni_3(PO_4)_2$- Ag_3PO_4/NF	AC/NF	1 M KOH	146 C g^{-1} at 0.5	32.4	399.5	82%, 5000	63
6.	$Ni_3(PO_4)_2$/RGO /$Co_3(PO_4)_2$/ Cobalt Foam	AC/NF	-	115.4 at 0.12	44.82	428.6	91.9%, 18000	64
7.	$Ni_{20}[(OH)_{12}(H_2O)_6][(HP_4)_8(PO_4)_4].12H_2O$/ PET	Graphene/ PET	PVA-KOH	148.3 F cm^{-2} at 0.5 mA cm^{-2}	0.445 mWh cm^{-3}	44 mW cm^{-3}	97.4%, 5000	65
8.	$Ni_2P_2O_7$/CP	HPGC/ CP	1 M NaOH	183	65	800	83%, 2000	69
9.	$Ni_2P_2O_7$/NF	rGO/NF	1 M KOH	224 at 1	70	750	73%, 5000	70
10.	$Ni_2P_2O_7$/ NiCo-OH/NF	AC/NF	PVA-KOH	221 at 3 mA cm^{-2}	78	444	91.83%, 10000	71
11.	MnO_2@ $Ni_2P_2O_7$	AC/NF	PVA-KOH	82 mAh g^{-1} at 1	66	640	93%, 10000	72
12.	Na-$Ni_2P_2O_7$	Graphene	PVA-NaOH	32.6 mF cm^{-2} at 0.5 mA cm^{-2}	23.4	1292.2	98.5%, 5000	73
13.	$(Ni_{11}(HPO_3)_8(OH)_6)$/PET	Graphene/ PET	PVA-KOH	1.64 F cm^{-3} at 0.5 mA cm^{-2}	0.45 mW h cm^{-3}	33 mW cm^{-3}	93.3%, 10000	76
14.	Co- $(Ni_{11}(HPO_3)_8(OH)_6)$	AC/NF	3 M KOH	83.1 mF cm^{-2} at 0.5 mA cm^{-2}	15.48 mWh cm^{-2}	600 W cm^{-2}	94%, 5000	77
		AC/PET	PVA-KOH	77.1 mF cm^{-2} at 0.5 mA cm^{-2}	14.72 mWh cm^{-2}	600 W cm^{-2}	91.2%, 5000	

Specifications: AC - activated carbon, NF - nickel foam, GO - graphene oxide, GF – Graphene foam, C-FP - carbonized iron cations adsorbed onto polyaniline, PET - polyethylene terephthalate, CP - carbon paper, HPGC - highly porous graphitic carbon, rGO - reduced graphene oxide.

1.4.2 Literature survey on cobalt phosphate

Also cobalt phosphate is highly investigated material for supercapacitor application along with nickel phosphate. Cobalt based materials are abundant in nature, low cost, non-toxic and have multiple oxidation states, so they catch attention in every field. Cobalt phosphate material getting much attention in energy storage field due to its excellent redox behavior and conductivity. Different methods are used to develop cobalt phosphate material such as green precipitation, hydrothermal, solvothermal, co-precipitation, solid state sintering and sonication. These different methods are used to prepare various polymorphs of cobalt phosphate material as $Co_3(PO_4)_2$ [78-87], $Co_3P_2O_8$ [88], $Co_2P_2O_7$ [89, 90], $CoHPO_4$ [91], $Co_{11}(HPO_3)_8(OH)_6$ [92-94], $Co_2P_4O_{12}$ [95], $Co_7(PO_4)_2(HPO_4)_4$ [96] and along with pure phase of cobalt phosphate, NH_4 [97-99] and K [100] rich cobalt phosphate materials also prepared and their study is summarized in table 1.3. Different structure of cobalt phosphate material offers different electrochemical properties as briefly discussed herein. Li et. al. [78] prepared flower like $Co_3(PO_4)_2.8H_2O$ using green-precipitate method and it delivered maximum specific capacitance of 350 F g^{-1} at 1 A g^{-1} current density with 102 % cyclic stability. Sankar et. al. [79] prepared 1D $Co_3(PO_4)_2$ nanograsses on Ni foam via simple hydrothermal method at different reaction times and achieved maximum capacitance of 15,687 mF cm^{-2} at 6 A g^{-1} current density with 89 % cyclic stability over 6000 cycles. Theerthagiri et. al. [80] prepared nanoflakes of $Co_3(PO_4)_2$ using co-precipitation method and it offered maximum capacitance of 188 F g^{-1} at 3 A g^{-1} current density. Shao et. al. [81] synthesized nanoflakes of $Co_3(PO_4)_2.8H_2O$ by simple hydrothermal method, it offered highest specific capacitance of 1578.7 F g^{-1} at 5 A g^{-1} current density with 72.8 % capacitive retention over 1000 cycles. Xi et. al. [82] developed nanowires of $Co_3(PO_4)_2$ via solvothermal method and obtained highest capacitance of 1174 F g^{-1} at 2

A g^{-1} current density in 3 M KOH electrolyte. Mao et. al. [83] used hydrothermal method for the preparation of leaf and nanoflakes like $Co_3(PO_4)_2$, which delivered capacitance of 410 F g^{-1} at 1 A g^{-1} current density with 96.1 % cyclic stability. Mirghni et. al. [84] used hydrothermal method and prepared $Co_3(PO_4)_2.4H_2O$/GF composite and it offered maximum capacity of 39.8 mAh g^{-1} at 10 A g^{-1} current density. Katkar et. al. [85] synthesized $Co_3(PO_4)_2.8H_2O$ and studied effect of various amounts of hydrolyzing agent on morphology and supercapacitive performance. The prepared electrode exhibited highest specific capacitance of 800 F g^{-1} at 2 mA cm^{-2} current density.

Li et. al. [88] prepared nanoparticles of $Co_3P_2O_8.8H_2O$ via precipitation and it delivered maximum capacitance of 446 F g^{-1} at 0.5 A g^{-1} current density with 100 % cyclic stability over 1000 cycles. The nanorods and nanosheets of $Co_2P_2O_7$ prepared by Hou et. al. [89] and Khan et. al. [90] via stirring and hydrothermal methods, respectively. The nanorods of $Co_2P_2O_7$ delivered maximum capacitance of 483 F g^{-1} at 1 A g^{-1} current density with 90 % cyclic stability over 3000 cycles and the nanosheets of $Co_2P_2O_7$ delivered maximum capacitance of 580 F g^{-1} at 1 A g^{-1} current density with 96 % cyclic stability over 5000 cycles. Pang et. al. [91] prepared nanosheets of $CoHPO_4.3H_2O$ via hydrothermal method and tested in 3 M KOH electrolyte, and prepared electrode offered maximum capacitance of 413 F g^{-1} at 1.5 A g^{-1} current density. Pang et. al. [92] and Lee et. al. [93] prepared nanoribbons and dumbbell shapes of $Co_{11}(HPO_3)_8(OH)_6$ using hydrothermal method. The nanoribbons like $Co_{11}(HPO_3)_8(OH)_6$ offered capacitance of 312 F g^{-1} at 1.25 A g^{-1} current density and dumbbell shaped $Co_{11}(HPO_3)_8(OH)_6$ exhibited capacitance of 226 F g^{-1} at 1 A g^{-1} current density. Also, Dan et. al. [94] prepared nanowires of Ni-doped $Co_{11}(HPO_3)_8(OH)_6$ via solvothermal method and it delivered capacity of 159 mAh g^{-1} at 0.5 A g^{-1} and 71.1 % cyclic stability over 8000 cycles. Patil et. al. [95] synthesized

nanoparticles of $Co_2P_4O_{12}$ delivered specific capacitance of 437 F g^{-1} at 2.5 A g^{-1} current density with 90 % cyclic stability. Wang et. al. [96] developed rod-shaped $Co_7(PO_4)_2(HPO_4)_4$ using organic solvent reflux method and prepared electrode delivered highest specific capacitance of 345 F g^{-1} at 1 A g^{-1} current density in 3 M KOH electrolyte. The chemical precipitation and hydrothermal method were used for the preparation of microflowers and microbundles of $NH_4CoPO_4.H_2O$ and its supercapacitive performance evaluated in KOH electrolyte [97-99]. Also, the nanocrystals of $K_2Co_3(P_2O_7)_2\cdot 2H_2O$ were prepared via hydrothermal method by Pang et. al. [100].

Table 1.3: Electrochemical performance of cobalt phosphate based electrodes.

Sr. No.	Material and morphology	Substrate	Method of deposition	Electrolyte	Capacitance (F g^{-1}) at current density (A g^{-1})	Stability at cycles	Ref.
1.	$Co_3(PO_4)_2.8H_2O$ (Flower like)	Nickel Foam	Green-precipitate	3 M KOH	350 at 1	102 %, 1000	78
2.	$Co_3(PO_4)_2$ (Nanograss)	Nickel Foam	Hydrothermal	1 M KOH	15,687 mF cm^{-2} at 6	89 %, 6000	79
3.	$Co_3(PO_4)_2$ (Nanoflakes)	Carbon Paper	Co-precipitation	3 M KOH	188 at 3	95 %, 800	80
4.	$Co_3(PO_4)_2.8H_2O$ (Nanoflakes)	Nickel Foam	Hydrothermal	1 M NaOH	1578.7 at 5	72.8 %, 1000	81
5.	$Co_3(PO_4)_2$ (Nanowires)	Nickel Foam	Solvothermal	3 M KOH	1174 at 2	4000	82
6.	$Co_3(PO_4)_2$ (Leaf like, Nanoflakes)	Nickel Foam	Hydrothermal	3 M KOH	410 at 1	96.1%, 2000	83
7.	$Co_3(PO_4)_2.4H_2O/GF$ (Flakes)	Nickel Foam	Hydrothermal	6 M KOH	39.8 mAh g^{-1} at 10	-	84
8.	$Co_3(PO_4)_2.8H_2O$ (Microflowers)	Stainless Steel	Hydrothermal	1 M KOH	800 at 2 mA cm^{-2}	83%, 3000	85
9.	$Co_3(PO_4)_2$ (Anisotropic nano/ micro rectangular)	Nickel Foam	Sonochemical	1 M KOH	203.4 C g^{-1} at 2	-	86
10.	$Co_3(PO_4)_2$ (Nanoflakes/Flower)	Nickel Foam	Hydrothermal	3 M KOH	1990 at 5 mA	80.4%, 2000	87
11.	$Co_3P_2O_8.8H_2O$ (Nanoparticles)	Nickel Foam	Chemical precipitation	3 M KOH	446 at 0.5	100%, 1000	88

12.	$Co_2P_2O_7$ (Nanorods)	Nickel Foam	Stirring	3 M KOH	483 at 1	90%, 3000	89
13.	$Co_2P_2O_7$ (Nanosheets)	Carbon Paper	Hydrothermal	3 M KOH	580 at 1	96%, 5000	90
14.	$CoHPO_4.3H_2O$ (Nanosheets)	Nickel Foam	Hydrothermal	3 M KOH	413 at 1.5	58.1%, 3000	91
15.	$Co_{11}(HPO_3)_8$ $(OH)_6$ (Nano-ribbons)	Nickel Foam	Hydrothermal	3 M KOH	312 at 1.25	89.4%, 3000	92
16.	$Co_{11}(HPO_3)_8$ $(OH)_6$ (Dumbbell shape)	Nickel Foam	Hydrothermal	3 M KOH	226 at 1	-	93
17.	Ni-doped $Co_{11}(HPO_3)_8$ $(OH)_6$ (Nanowire arrays)	Nickel Foam	Solvothermal	2 M KOH	159 mAh g^{-1} at 0.5 A g^{-1}	71.1%, 8000	94
18.	$Co_2P_4O_{12}$ (Nanoparticles)	Carbon Cloth	Solid-state sintering	2 M KOH	437 at 2.5	90%, 3000	95
19.	$Co_7(PO_4)_2$ $(HPO_4)_4$ (Rod-shaped)	Nickel Foam	Organic solvent reflux	3 M KOH	345 at 1	80.14%, 2000	96
20.	$NH_4CoPO_4.H_2O$ (Nano/Micro flowers/ plates)	Nickel Foam	Chemical precipitation	3 M KOH	369.4 at 0.625	99.7%, 4000	97
21.	$NH_4CoPO_4.H_2O$ (Microflowers)	Nickel Foam	Chemical precipitation	1 M KOH	525 at 0.625	99.4%, 4000	98
22.	$NH_4CoPO_4.H_2O$ (Microbundles)	Nickel Foam	Hydrothermal	3 M KOH	662 at 1.5	92.7%, 3000	99
23.	$K_2Co_3(P_2O_7)_2 \cdot 2H_2O$ (Nanocrystal whiskers)	Nickel Foam	Hydrothermal	3 M KOH	1100 mF cm^{-2} at 1.0 mA cm^{-2}	-	100

Few reports are available on fabrication of asymmetric devices using cobalt phosphate material as a cathode for high energy and power density and tabulated in table 1.4. Sankar et. al. [79] prepared asymmetric device using 1D $Co_3(PO_4)_2$ nanograsses as a cathode and activated carbon (AC) as an anode electrode, and it exhibited specific capacitance of 85 F g^{-1} at a current density of 1 A g^{-1} and specific energy of 26.66 Wh kg^{-1} at specific power of 750 W kg^{-1}. Shao et. al. [81] fabricated $Co_3(PO_4)_2.8H_2O$//AC device, which delivered highest capacitance of 111.2 F g^{-1} at a current density of 5 mA cm^{-2}, specific energy of 29.29 Wh kg^{-1} at specific power of 468.75 W kg^{-1} with 77.9 % initial capacitance retention over 1000 cycles. Xi et. al. [82]

developed asymmetric device of $Co_3(PO_4)_2$//AC. The prepared device exhibited maximum capacitance of 169.35 F g^{-1} at a current density of 2 A g^{-1} with excellent cyclic stability. Mirghni et. al. [84] developed $Co_3(PO_4)_2.4H_2O/GF$//C-FP device and tested in 6 M KOH electrolyte. The device exhibited highest specific capacity of 24 mAh g^{-1} at 0.5 A g^{-1} with excellent cyclic stability (99 % over 10000 cycles). Also, it delivered specific energy of 24 Wh kg^{-1} at a specific power of 468 W kg^{-1}. Katkar et. al. [85] fabricated aqueous and flexible solid state devices using $Co_3(PO_4)_2.8H_2O$ and CuS as positive and negative electrodes, respectively. The $Co_3(PO_4)_2.8H_2O$//CuS aqueous device offered highest specific capacitance of 163 F g^{-1} at current density of 2 mA cm^{-2} with 58.1 Wh kg^{-1} energy density at power density of 3520 W kg^{-1} and 94 % initial capacitance retention after 4000 cycles. The solid state device fabricated using PVA-KOH gel electrolyte, which delivered highest specific capacitance of 70 F g^{-1} (at current density of 2 mA cm^{-2}) with high energy density (24.91 Wh kg^{-1}) and power density (2630 W kg^{-1}). $Co_3P_2O_8.8H_2O$//AC device prepared by Li et. al. [88] delivered capacitance of 55 F g^{-1} at current density of 0.5 A g^{-1}. Also, the device exhibited energy density of 15 Wh kg^{-1} at power density of 350 W kg^{-1} and 100 % capacitive retention after 3000 cycles. Dan et. al. [94] prepared Ni-doped $Co_{11}(HPO_3)_8(OH)_6$//AC device and tested in 2 M KOH electrolyte, it offered capacitance of 55 F g^{-1} at current density of 0.5 A g^{-1} with 58.7 Wh kg^{-1} energy density at 532 W kg^{-1} power density and excellent cyclic retention (90.5 %) after 10000 cycles. Patil et. al. [95] fabricated $Co_2P_4O_{12}$//AC device and used KI added KOH electrolyte for the performance evaluation. The device delivered specific capacitance of 156 F g^{-1} at current density of 2.5 A g^{-1} and energy density of 70 Wh kg^{-1} at power density of 2300 W kg^{-1} with superior cyclic retention (94 % over 5000 cycles). Wang et. al. [96] developed $Co_7(PO_4)_2(HPO_4)_4$//AC device and tested in 3 M KOH electrolyte. The device offered 84.3 F g^{-1} specific capacitance

at current density of 0.5 A g^{-1} and energy density of 26 Wh kg^{-1} (power density of 372.75 W kg^{-1}) with good cyclic performance.

Table 1.4: Electrochemical performance of cobalt phosphate based supercapacitor devices.

Sr. No.	Positive electrode (cathode)	Negative electrode (anode)	Electrol yte	Capacitance (F g^{-1}) at current density (A g^{-1})	Energy density (Wh kg^{-1})	Power density (W kg^{-1})	Stability at cycles	Ref.
1.	Co$_3$(PO$_4$)$_2$/ NF	AC/NF	1 M KOH	85 at 1	26.66	750	86%, 6000	79
2.	Co$_3$(PO$_4$)$_2$. 8H$_2$O/NF	AC/NF	1 M NaOH	111.2 at 5 mA cm^{-2}	29.29	468.75	77.9%, 1000	81
3.	Co$_3$(PO$_4$)$_2$/ NF	AC/NF	3 M KOH	169.35 at 2	-	-	86%, 4000	82
4.	Co$_3$(PO$_4$)$_2$. 4H$_2$O/GF	C-FP	6 M KOH	24 mAh g^{-1} at 0.5	24	468	99%, 10000	84
5.	Co$_3$(PO$_4$)$_2$. 8H$_2$O/SS	CuS/SS	1 M KOH	163 at 2 mA cm^{-2}	58.12	3520	94%, 4000	85
			PVA-KOH	70 at 2 mA cm^{-2}	24.91	2630	-	
6.	Co$_3$P$_2$O$_8$. 8H$_2$O/NF	AC/NF	-	55 at 0.5	15	350	100%, 3000	88
7.	Ni-doped Co$_{11}$ (HPO$_3$)$_8$ (OH)$_6$/NF	AC/NF	2 M KOH	55 at 0.5	58.7	532	90.5%, 10000	94
8.	Co$_2$P$_4$O$_{12}$/ CC	AC/CC	KI-KOH	156 at 2.5	70	2300	94%, 5000	95
9.	Co$_7$(PO$_4$)$_2$ (HPO$_4$)$_4$ /NF	AC/NF	3 M KOH	84.34 at 0.5	26.04	372.75	93.08%, 2500	96
10.	K$_2$Co$_3$ (P$_2$O$_7$)$_2$· 2H$_2$O/PET	Graphene/ PET	PVA-KOH	6.0 F cm^{-3} at 10 mA cm^{-3}	0.96 mWh cm^{-3}	-	94.4%, 5000	100

Specifications: SS – Stainless steel, CC – Carbon cloth.

1.4.3 Literature survey on nickel cobalt phosphate

The mixed metal compounds delivered high specific capacitance than single metals due to synergetic effects between two metal species. The ratio of two metal species plays important role in electrochemical properties of bimetals. So, for better results ratio of nickel and cobalt is varied in preparation of nickel cobalt based bimetals. Different methods were used for synthesis of nickel cobalt phosphate material like

hydrothermal, co-precipitation, irradiation of microwave, solvothermal, etc. Generally, the nickel cobalt based phosphate material obtained by calcination of ammonium based nickel cobalt phosphate precursors. Chen et. al. [101] prepared microplates of nickel cobalt pyrophosphate material from calcination of ammonium nickel cobalt pyrophosphate material at different temperatures and effect of calcination temperature on material properties were studied. Microplates of $Co_{0.4}Ni_{1.6}P_2O_7$ delivered specific capacitance of 1259 F g^{-1} at current density of 1.5 A g^{-1}. Li et. al. [102] studied influence of variation of different parameters in synthesis process of nickel cobalt phosphate on the structure, morphology and electrochemical performance like Ni/Co ratio, reaction temperature, reaction time, solvent quantity, surface active agent, etc. The prepared nanosheets of $NiCoPO_4$ offer highest specific capacitance of 1132.5 F g^{-1} at a current density of 1 A g^{-1}. Liu et. al. [103] also studied effect of Ni/Co ratio variation in the synthesis of $Ni_3P_2O_8$-$Co_3P_2O_8.8H_2O$ and compared their capacitive performance with $Ni_3P_2O_8$ and $Co_3P_2O_8$. The prepared $Ni_3P_2O_8$-$Co_3P_2O_8.8H_2O$ exhibits specific capacitance of 1980 F g^{-1} at 0.5 A g^{-1} current density. Similarly, ratio variation study was done by Tang et. al. [104] and obtained nanospheres with honeycomb-like mesoporous nickel cobalt phosphate material, and dehydration process effect also studied. The prepared nanospheres of $Co_{0.86}Ni_{2.14}(PO_4)_2$ delivered capacitance of 1409 F g^{-1} at 0.25 A g^{-1} current density. Hollow shells of $NiCo_2(PO_4)_2$ prepared by Zhang et. al. [105] using microwave assisted method and shell to sheet morphological evolution was observed and it delivered 940.4 F g^{-1} capacitance at 1 A g^{-1} current density. Microplates of $Ni(Co)NH_4PO_4$ coated by rGO nanosheets composite prepared using hydrothermal method by Zhang et. al. [106] and used as a supercapacitor electrode which offered specific capacitance of 1451 F g^{-1} (at current density 1 A g^{-1}). Zhao et. al. [107] prepared hybridized phosphate material by adding NH_4 in

$(Ni,Co)_3(PO_4)_2.8H_2O$ and studied their electrochemical properties. The prepared microplates of $(NH_4)(Ni,Co)PO_4 \cdot 0.67H_2O$ delivered capacitance of 1128 F g^{-1} at current density of 0.5 A g^{-1}. A nanospherical hollow nickel cobalt phosphate nanocages prepared by Xiao et. al. [108] using template of metal-organic framework (ZIF-67) via shell coating followed with controlled etching process and it offered high specific capacitance of 1616 F g^{-1} (at current density of 1 A g^{-1}). Also, Liu et. al. [109] prepared Na-rich nickel cobalt phosphate material using microwave synthesis method, the $NaNi_{0.33}Co_{0.67}PO_4.H_2O$ exhibited specific capacitance of 828 F g^{-1} at 1 A g^{-1} current density. Similarly, K-rich microplates of nickel cobalt phosphate were synthesized by Liang et. al. [110] via hydrothermal method and exhibited maximum specific capacitance of 1166 F g^{-1} at 1.5 A g^{-1} current density. Hun et. al. [111] prepared Ni_xCo-P-O using hydrothermal method, different Ni/Co ratios were used in the synthesis process to determine optimum ratio of Ni/Co for good electrochemical performance and prepared Ni_xCo-P-O exhibited maximum specific capacitance of 952 F g^{-1} at 1 A g^{-1} current density. Chen et. al. [112] converted $Ni_xCo_{1-x}(CO_3)_{0.5}OH$ precursor in to Ni-Co-P/POx by low temperature phosphating process and combination of phosphate and phosphide is observed in final material due to low temperature process.

Table 1.5: Electrochemical performance of nickel cobalt phosphate based electrodes.

Sr. No.	Material and morphology	Substrate	Method of deposition	Electrolyte	Capacitance (F g^{-1}) at current density (A g^{-1})	Stability at cycles	Ref.
1.	$Co_{0.4}Ni_{1.6}P_2O_7$ (Microplates)	Nickel Foam	Hydrothermal	3 M KOH	1259 at 1.5	88.9%, 1000	101
2.	$NiCoPO_4$ (Nanosheets)	Nickel Foam	Hydrothermal	3 M KOH	1132.5 at 1	93%, 8000	102
3.	$Ni_3P_2O_8$-$Co_3P_2O_8.8H_2O$ (Nanoparticle)	Nickel Foam	Co-precipitation	6 M KOH	1980 at 0.5	90.9%, 1000	103
4.	$Co_{0.86}Ni_{2.14}$ $(PO_4)_2$ (Nanospheres)	Nickel Foam	Hydrothermal	2 M KOH	1409 at 0.25	-	104

5.	$NiCo_2(PO_4)_2$ (Hollow shells)	Nickel Foam	Microwave assisted	3 M KOH	940.43 at 1	84.5%, 1000	105
6.	$Ni(Co)NH_4$ $PO_4@rGO$ (Microplates)	Nickel Foam	Hydrothermal	6 M KOH	1451 at 1	125%, 5000	106
7.	$(NH_4)(Ni,Co)$ $PO_4 \cdot 0.67H_2O$ (Microplates)	Nickel Foam	Hydrothermal	6 M KOH	1128 at 0.5	-	107
8.	ZIF-67-LDH-$NiCoPO_4$ (Nanocages)	Nickel Foam	Solvothermal	6 M KOH	1616 at 1	72.46%, 2000	108
9.	$NaNi_{0.33}Co_{0.67}$ $PO_4.H_2O$ (Particles)	Nickel Foam	Microwave	1 M KOH	828 at 1	83.1%, 3000	109
10.	$KCo_{0.33}Ni_{0.67}$ $PO_4.H_2O$ (Microplates)	Nickel Foam	Hydrothermal	1 M KOH	1166 at 1.5	94%, 1000	110
11.	$Ni_xCo-P-O$ (Nanoflowers)	Nickel Foam	Hydrothermal & Annealing	6 M KOH	952 at 1	-	111
12.	$NiCoP/PO_x$ (Sea-urchin-like)	Nickel Foam	Hydrothermal & Phosphorization	6 M KOH	647 C g^{-1} at 1	94%, 1000	112

The practical applicability of electroactive material is tested by preparing supercapacitor device. The electrochemical performance of nickel cobalt phosphate based devices is tabulated in table 1.6. Chen et. al. [101] fabricated asymmetric device by combining $Co_{0.4}Ni_{1.6}P_2O_7$ and AC as positive and negative electrodes, respectively. The $Co_{0.4}Ni_{1.6}P_2O_7$//AC device delivered highest capacitance of 119 F g^{-1} at 1 A g^{-1} current density in 3 M KOH electrolyte. Also, it exhibited energy density of 42.2 Wh kg^{-1} at 800 W kg^{-1} power density with 80 % cyclic stability after 2000 cycles. Li et. al. [102] prepared aqueous and solid state devices using $NiCoPO_4$ and AC as positive and negative electrodes, respectively. The aqueous device performance tested in 3 M KOH electrolyte, which delivered high capacitance of 162.8 F g^{-1} at 1 A g^{-1} current density along with energy density of 32.5 Wh kg^{-1} at 600 W kg^{-1} power density. The solid state device performance was tested in PVA-KOH gel electrolyte and it achieved maximum capacitance of 129.6 F g^{-1} at 1 A g^{-1} current density along with energy density of 35.8

Wh kg^{-1} at 700 W kg^{-1} power density. Liu et. al. [103] fabricated $Ni_3P_2O_8$-$Co_3P_2O_8.8H_2O$//AC device provided capacitance of 94 F g^{-1} at current density of 0.5 A g^{-1} with 33.4 Wh kg^{-1} energy density at 399 W kg^{-1} power density. Tang et. al. [104] used $Co_{0.86}Ni_{2.14}(PO_4)_2$ as cathode and AC as anode for device fabrication and prepared device provided capacitance of 149.6 F g^{-1} at 0.7 mA current and 45.8 Wh kg^{-1} energy density at power density of 42.4 W kg^{-1}. Zhao et. al. [107] used ammonium nickel phosphate $((NH_4)(Ni,Co)PO_4·0.67H_2O)$ and hierarchical porous carbon (HPC) for asymmetric device fabrication. The $(NH_4)(Ni,Co)PO_4·0.67H_2O$//HPC device delivered specific capacitance of 88 F g^{-1} at 0.01 A g^{-1} current density and 35.3 Wh kg^{-1} energy density at power density of 101 W kg^{-1}.

The ZIF-67-LDH-NiCoPO$_4$//AC device prepared using PVA-KOH electrolyte by Xiao et. al. [108] offered 116.67 F g^{-1} capacitance at 0.1 A g^{-1} current density with 33.29 Wh kg^{-1} energy density at power density of 150 W kg^{-1}. The $NaNi_{0.33}Co_{0.67}PO_4.H_2O$ (cathode) and graphene (anode) electrodes combined by Liu et. al. [109] for asymmetric device fabrication. The $NaNi_{0.33}Co_{0.67}PO_4.H_2O$//graphene device exhibited specific capacitance of 95.52 F g^{-1} at current density of 0.5 A g^{-1}, with high energy and power density of 29.85 Wh kg^{-1} and 374.95 W kg^{-1}, respectively. Liang et. al. [110] fabricated $KCo_{0.33}Ni_{0.67}PO_4.H_2O$//AC device which delivered capacitance of 227 F g^{-1} at 1.5 A g^{-1} current density and 80.64 Wh kg^{-1} energy density at power density of 1200 W kg^{-1}. Hu et. al. [111] prepared $Ni_xCo-P-O$//AC device which provided specific capacitance of 424 F g^{-1} at 1 A g^{-1} current density and energy density of 47.68 Wh kg^{-1} at power density of 884.78 W kg^{-1}. Chen et. al. [112] fabricated $NiCoP/PO_x$//rGO device, delivered specific capacity of 182 C g^{-1} at 1 A g^{-1} current density with energy density of 36.84 Wh kg^{-1} at power density of 727.8 W kg^{-1}.

Table 1.6: Electrochemical performance of nickel cobalt phosphate based

supercapacitor devices.

Sr. No.	Positive electrode (cathode)	Negative electrode (anode)	Electrolyte	Capacitance ($F\ g^{-1}$) at current density ($A\ g^{-1}$)	Energy density (Wh kg^{-1})	Power density (W kg^{-1})	Stability at cycles	Ref.
1.	$Co_{0.4}Ni_{1.6}P_2O_7/NF$	AC/NF	3 M KOH	119 at 1	42.2	800	80%, 2000	101
2.	$NiCoPO_4/NF$	AC/NF	3 M KOH	162.8 at 1	32.5	600	80.4%, 5000	102
			PVA-KOH	129.6 at 1	35.8	700	90.5%, 5000	
3.	$Ni_3P_2O_8$-$Co_3P_2O_8$.$8H_2O/NF$	AC/NF	6 M KOH	94 at 0.5	33.4	399	83%, 5000	103
4.	$Co_{0.86}Ni_{2.14}(PO_4)_2/NF$	AC/NF	-	149.6 at 0.7 mA	45.8	42.4	57.8%, 2500	104
5.	$(NH_4)(Ni,Co)PO_4\cdot0.67H_2O/NF$	HPC/NF	6 M KOH	88 at 0.01	35.3	101	95.6%, 5000	107
6.	ZIF-67-LDH-$NiCoPO_4$	AC	PVA-KOH	116.67 at 0.1	33.29	150	67.24%, 10000	108
7.	$NaNi_{0.33}Co_{0.67}PO_4.H_2O/NF$	Graphene/NF	1 M KOH	95.52 at 0.5	29.85	374.95	76.9%, 10000	109
8.	$KCo_{0.33}Ni_{0.67}PO_4.H_2O$	AC/NF	1 M KOH	227 at 1.5	80.64	1200	82%, 5000	110
9.	Ni_xCo-P-O/NF	AC/NF	6 M KOH	424 at 1	47.68	884.78	69.3%, 8000	111
10.	$NiCoP/PO_x$	rGO	-	182 $C\ g^{-1}$ at 1	36.84	727.8	86%, 7000	112

From literature survey, it is found that binary metal phosphate based electrode shows good electrochemical capacitive performance than single metal phosphate based electrodes. Also, the binary metal phosphate based fabricated asymmetric device delivered high energy and power density with excellent cyclic stability. However, these materials couldn't achieve their theoretical capacitance values. So, there is still scope for improvement in capacitance, energy density and cyclic stability of device, and can be achieved by preparing binder-free electrodes of binary metal phosphate thin films along with manipulating material properties.

1.5 Orientation and purpose of dissertation

In recent years, researchers all over the world concentrated on improvement of electrochemical performance of supercapacitor by means of enhanced energy density, power density, long cycle life and preparation of cost effective electrodes, which are the important four pillars of energy storage systems. A supercapacitor device with outstanding electrochemical activity and low cost may raises its usage over widespread applications. The active electrode material and electrolyte are key factors and influence the performance of supercapacitor in terms of capacitance and energy density. However, the energy densities of supercapacitor are still low, to overcome the challenges in field of supercapacitor, have to develop efficient active material with high capacitance. Previously reported major types of supercapacitor materials are carbon based, conducting polymers, metal oxides and transition metal phosphates. Recently, transition metal phosphates attract more attention among those active materials for energy storage applications.

In a literature study, it is observed that single metal phosphate materials were effective with good electrochemical performance, but they have some drawbacks such as low stability and conductivity. These problems can be resolved easily by finding efficient method to prepare electrode material with improved properties (surface area, conductivity, porosity, etc.). So, it is reported that, doping or addition of proper metal ions can hopefully change physical and chemical properties of material. Therefore, binary material preparation is noble solution to resolve drawbacks of single metal based materials where weakness of one material solved by another. In binary materials, multiple oxidation states of both material reduces resistance of electrode and participate in electrochemical redox reactions. However, co-incorporation of two transition metals offer an effective method to tailor electrochemical performance of binary metal for

supercapacitor application. In literature, nickel and cobalt based phosphate materials investigated widely for energy storage devices. They both together shows better performance than pure nickel phosphate or cobalt phosphate, because bimetallic materials benefit from the synergistic effect of two materials and exhibit enhanced capacitance behavior.

The fundamental requirement for supercapacitor electrodes include high conductivity, chemical and mechanical stability, high surface area with appropriate pore sizes optimal for an electrolyte. To improve conductivity of the electrode binder-free deposition approach is generally used for thin film electrode preparation. It is accepted that, directly grown (binder-free) nanostructures of materials on conducting substrate possess better mechanical and structural stability compared to composite powder attached on substrate by conventional way (drop casting). Hence, binder-free approach became the choice for preparing supercapacitor electrode. For the preparation of binder free and additive less nickel cobalt phosphate thin films, simple and cost effective chemical methods can be used than physical methods. Among various chemical methods, electrodeposition and chemical bath deposition methods were selected for the thin film synthesis. These two methods are easy to handle, cheap and useful to deposit materials on large scale. Preparative parameters such as pH of solution, concentration of precursor, deposition temperature and deposition time can be easily controlled in these chemical methods.

So, the present work is focused on synthesis of nickel cobalt phosphate thin films by simple chemical bath deposition and electrodeposition methods. These methods offer required material properties such as crystal structure, surface morphology and film thickness. The physical and chemical properties of prepared thin films studied by various characterizations. The phase identification of material is carried out by X-ray

diffraction (XRD) technique. Chemical bonding in material is studied by Fourier Transform Infrared spectroscopy analysis (FT-IR). The surface morphology of prepared thin films is evaluated by Field Emission Scanning Electron Microscopy (FE-SEM) technique. Elemental composition of thin films is detected by Energy-Dispersive X-ray Spectroscopy (EDS) technique. Prepared material confirmation, available oxidation states and chemical composition of thin film are done with X-ray Photoelectron Spectroscopy (XPS) technique. The supercapacitive properties of prepared thin films (using electrodeposition and chemical bath deposition methods) are investigated by cyclic voltammetry (CV), galvanostatic charge-discharge (GCD) and electrochemical impedance spectroscopy (EIS) techniques. Three electrode system used for the electrochemical study of single electrodes in 1 M KOH electrolyte, prepared thin films used as working electrode, platinum as a counter and saturated calomel electrode (SCE) as a reference electrode. Furthermore, the performance of prepared thin films evaluated in terms of specific capacitance and cyclic life.

The main aim of this work, fabrication of aqueous and flexible solid state supercapacitor device using nickel cobalt phosphate thin films as an active cathode material with KOH and PVA-KOH gel electrolyte, respectively. The activity of electrode material and usefulness of electrolytes are investigated by fabricating aqueous and solid state devices. The performances of asymmetric devices are studied in terms of capacitance, energy and power density, and cyclic stability. Finally, conclusions are assessed on the basis of the performance of nickel cobalt phosphate based devices.

1.6 References

1.   H. Zhao, Z. Yuan, Catal. Sci. Technol., 7 (2017) 330-347.
2.   S. Zheng, X. Li, B. Yan, Q. Hu, Y. Xu, X. Xiao, H. Xue, H. Pang, Adv. Energy Mater., 7 (2017) 1602733 (1-27).

3. A. Shukla, S. Sampath, K. Vijayamohanan, Curr. Sci., 79 (2000) 1656-1661.

4. A. Burke, J. Power Sources, 91 (2000) 37-50.

5. A. Nishino, J. Power Sources, 60 (1996) 137-147.

6. M. Jayalakshmi, K. Balasubramanian, Int. J. Electrochem. Sci., 3 (2008) 1196-1217.

7. M. Halper, J. Ellenbogen, MITRE (2006) 1-34.

8. T. Mathis, N. Kurra, X. Wang, D. Pinto, P. Simon, Y. Gogotsi, Adv. Energy Mater., 9 (2019) 1902007 (1-13).

9. U. Patil, S. Lee, S. Kulkarni, J. Sohn, M. Nam, S. Han, S. Jun, Nanoscale, 7 (2015) 6999-7021.

10. S. Liu, S. Lee, U. Patil, I. Shackery, S. Kang, K. Zhang, J. Park, K. Chung, S. Jun, J. Mater. Chem. A, 5 (2017) 1043-1049.

11. H. Becker, Low voltage electrolytic capacitors, U. S. Patent 2800616 (1957).

12. R. Rightmire, Electrical energy storage apparatus, U. S. Patent 3288641 (1966).

13. S. Kim, S. Kim, K. Jung, J. Kim, J. Jang, Nano Energy, 24 (2016) 17-24.

14. J. Niu, W. Pell, B. Conway, J. Power Sources, 156 (2006) 725-740.

15. Z. Fan, J. Yan, T. Wei, L. Zhi, G. Ning, T. Li, F. Wei, Adv. Funct. Mater., 21 (2011) 2366-2375.

16. C. Lokhande, D. Dubal, O. Joo, Curr. Appl. Phys., 11 (2011) 255-270.

17. H. Pang, X. Li, Q. Zhao, H. Xue, W. Lai, Z. Hu, W. Huang, Nano Energy, 35 (2017) 138-145.

18. L. Miao, H. Duan, M. Liu, W. Lu, D. Zhu, T. Chen, L. Li, L. Gan, Chem. Eng. J., 317 (2017) 651-659.

19. G. Wang, H. Wang, X. Lu, Y. Ling, M. Yu, T. Zhai, Y. Tong, Y. Li, Adv. Mater., 26 (2014) 2676-2682.

20. X. Lu, M. Yu, G. Wang, Y. Tong, Y. Li, Energy Environ. Sci., 7 (2014) 2160-2181.

21. Y. Zhu, S. Murali, M. Stoller, K. Ganesh, W. Cai, P. Ferreira, A. Pirkle, R. Wallace, K. Cychosz, M. Thommes, D. Su, E. Stach, R. Ruoff, Science, 332 (2011) 1537-1541.

22. D. Pech, M. Brunet, H. Durou, P. Huang, V. Mochalin, Y. Gogotsi, P. Taberna, P. Simon, Nat. Nanotechnol., 5 (2010) 651-654.

23. M. Mastragostino, C. Arbizzani, F. Soavi, Solid State Ion., 148 (2002) 493-498.

24. S. Gowda, A. Reddy, X. Zhan, P. Ajayan, Nano Lett., 11 (2011) 3329-3333.

25. W. Chen, R. Rakhi, L. Hu, X. Xie, Y. Cui, H. Alshareef, Nano Lett., 11 (2011) 5165-5172.

26. M. Vangari, T. Pryor, L. Jiang, J. Energy Eng., 139 (2013) 72-79.

27. N. Chodankar, H. Pham, A. Nanjundan, J. Fernando, K. Jayaramulu, D. Golberg, Y. Han, D. Dubal, Small, 16 (2020) 2002806 (1-35).

28. V. Augustyn, P. Simon, B. Dunn, Energy Environ. Sci., 7 (2014) 1597-1614.

29. P. Simon, Y. Gogotsi, B. Dunn, Science, 343 (2014) 1210-1211.

30. H. Li, M. Yu, F. Wang, P. Liu, Y. Liang, J. Xiao, C. Wang, Y. Tong, G. Yang, Nat. Commun., 4 (2013) 1-7.

31. D. Dubal, R. Holze, P. Romero, Sci. Rep., 4 (2014) 7349 (1-10).

32. T. Lin, C. Dai, K. Hung, Sci. Rep., 4 (2014) 7274 (1-10).

33. D. Cericol, R. Kotz, Electrochim. Acta, 72 (2012) 1-17.

34. L. Zhang, R. Zhou, X. Zhao, J. Mater. Chem., 20 (2010) 5983-5992.

35. A. Sumboja, X. Wang, J. Yan, P. Lee, Electrochim. Acta, 65 (2012) 190-195.

36. L. Fan, J. Maier, Electrochem. Commun., 8 (2006) 937-940.

37. S. Gnanakan, M. Rajasekhar, A. Subramania, Int. J. Electrochem. Sci., 4 (2009) 1289-1301.

38. D. Malavekar, V. Lokhande, V. Mane, S. Ubale, U. Patil, C. Lokhande, J. Phys. Chem. Solids, 141 (2020) 109425 (1-11).

39. L. Yuan, X. Lu, X. Xiao, T. Zhai, J. Dai, F. Zhang, B. Hu, X. Wang, L. Gong, J. Chen, C. Hu, Y. Tong, J. Zhou, Z. Wang, ACS Nano, 6 (2012) 656-661.

40. C. Hu, K. Chang, M. Lin, Y. Wu, Nano Lett., 6, (2006) 2690-2695.

41. S. Meher, G. Rao, J. Phys. Chem. C, 115 (2011) 15646-15654.

42. D. Wang, F. Li, H. Cheng, J. Power Sources, 185 (2008) 1563-1568.

43. P. Kulal, D. Dubal, C. Lokhande, V. Fulari, J. Alloys Compd., 509 (2011) 2567-2571.

44. H. Zhao, Z. Yuan, ChemCatChem, 12 (2020) 3797-3810.

45. T.V.S.L. Satyavani, A. Kumar, P.S.V.S. Rao, Eng. Sci. Technol. Int. J., 19 (2016) 178-188.

46. Y. Ye, Y. Shi, A. Tay, J. Power Sources, 217 (2012) 509-518.

47. J. Li, Y. Cheng, M. Jia, Y. Tang, Y. Lin, Z. Zhang, Y. Liu, J. Power Sources, 255 (2014) 130-143.

48. X. Li, A. Elshahawy, C. Guan, J. Wang, Small, 13 (2017) 1701530 (1-24).

49. C. Zheng, H. Yang, Y. Yang, Mater. Trans., 58 (2017) 298-301.

50. S. Li, F. Teng, M. Chen, N. Li, X. Hua, K. Wang, M. Li, Chem. Phys. Lett., 601 (2014) 59-62.

51. V. Nithya, L. Vasylechko, R. Selvan, RSC Adv., 4 (2014) 65184-65194.

52. S. Vadivel, D. Maruthamani, M. Kumaravel, B. Saravanakumar, B. Paul, S. Dhar, K. Saravanakumar, V. Muthuraj, J. Taibah Univ. Sci., 11 (2017) 661-666.

53. S. Vadivel, A. Naveen, J. Theerthagiri, J. Madhavan, T. Priya, N. Balasubramanian, Ceram. Int., 42 (2016) 14196-14205.

54. V. Nithya, R. Selvan, L. Vasylechko, J. Phys. Chem. Solids, 86 (2015) 11-18.

55. B. Mahmoud, A. Mirghni, K. Oyedotun, D. Momodu, O. Fasakin, N. Manyala, J. Alloys Compd., 818 (2020) 1-36.

56. F. Omar, A. Numan, N. Duraisamy, S. Bashir, K. Ramesh, S. Ramesh, RSC Adv., 6 (2016) 76298-76306.

57. X. Ma, W. Zhang, L. Kong, Y. Luo, L. Kang, RSC Adv., 6 (2016) 40077-40085.

58. Y. He, X. Yang, Y. Bai, J. Zhang, L. Kang, Z. Lei, Z. Liu, Electrochim. Acta, 178 (2015) 312-320.

59. N. Chen, J. Zhou, Q. Kang, H. Ji, G. Zhu, Y. Zhang, S. Chen, J. Chen, X. Feng, W. Hou, J. Power Sources, 344 (2017) 185-194.

60. X. Peng, H. Chai, Y. Cao, Y. Wang, H. Dong, D. Jia, W. Zhou, Mater. Today Energy, 7 (2018) 129-135.

61. J. Li, M. Liu, L. Kong, D. Wang, Y. Hu, W. Han, L. Kang, RSC Adv., 5 (2015) 41721-41728.

62. A. Mirghni, M. Madito, K. Oyedotun, T. Masikhwa, N. Ndiaye, S. Ray, N. Manyala, RSC Adv., 8 (2018) 11608-11621.

63. F. Omar, A. Numan, S. Bashir, N. Duraisamy, R. Vikneswaran, Y. Loo, K. Ramesh, S. Ramesh, Electrochim. Acta, 273 (2018) 216-228.

64. C. Zhao, S. Wang, Z. Zhu, P. Ju, C. Zhao, X. Qian, J. Mater. Chem. A, 5 (2017) 18594-18602.

65. J. Zhao, S. Wang, Z. Run, G. Zhang, W. Du, H. Pang, Part. Part. Syst. Charact., 32 (2015) 880-885.

66. J. Yang, J. Tan, D. Ma, J. Power Sources, 260 (2014) 169-173.

67. M. Pramanik, R. Salunkhe, M. Imura, Y. Yamauchi, ACS Appl. Mater. Interfaces, 8 (2016) 9790-9797.

68. H. Pang, Y. Zhang, Z. Run, W. Lai, W. Huang, Nano Energy, 17 (2015) 339-347.

69. B. Senthilkumar, Z. Khan, S. Park, K. Kim, H. Ko, Y. Kim, J. Mater. Chem. A, 3 (2015) 21553-21561.

70. K. Sankar, Y. Seo, S. Lee, S. Jun, ACS Appl. Mater. Interfaces, 10 (2018) 8045-8056.

71. N. Chodankar, D. Dubal, S. Ji, D. Kim, Small, 15 (2019) 1901145 (1-11).

72. N. Chodankar, D. Dubal, S. Patil, G. Raju, S. Karekar, Y. Huh, Y. Han, Electrochim. Acta, 319 (2019) 435-443.

73. C. Wei, C. Cheng, S. Wang, Y. Xu, J. Wang, H. Pang, Chem. Asian J., 10 (2015) 1731-1737.

74. H. Pang, Z. Yan, Y. Wei, X. Li, J. Li, L. Zhang, J. Chen, J. Zhang, H. Zheng, Part. Part. Syst. Charact., 30 (2013) 287-295.

75. H. Pang, C. Wei, Y. Ma, S. Zhao, G. Li, J. Zhang, J. Chen, S. Li, ChemPlusChem, 78 (2013) 546-553.

76. Y. Gao, J. Zhao, Z. Run, G. Zhang, H. Pang, Dalton Trans., 43 (2014) 17000-17005.

77. B. Li, Y. Shi, K. Huang, M. Zhao, J. Qiu, H. Xue, H. Pang, Small, 14 (2018) 1703811 (1-7).

78. H. Li, H. Yu, J. Zhai, L. Sun , H. Yang, S. Xie, Mater. Lett., 152 (2015) 25-28.

79. K. Sankar, S. Lee, Y. Seo, C. Ray, S. Liu, A. Kundu, S. Jun, J. Power Sources, 373 (2018) 211-219.

80. J. Theerthagiri, K. Thiagarajan, B. Senthilkumar, Z. Khan, R. Senthil, P. Arunachalam, J. Madhavan, M. Ashokkumar, ChemistrySelect, 2 (2017) 201-210.

81. H. Shao, N. Padmanathan, D. McNulty, C. O' Dwyer, K. Razeeb, ACS Appl. Mater. Interfaces, 8 (2016) 28592-28598.

82. Y. Xi, B. Dong, Y. Dong, N. Mao, L. Ding, L. Shi, R. Gao, W. Liu, G. Su, L. Cao, Chem. Mater., 28 (2016) 1355-1362.

83. H. Mao, F. Zhang, X. Liu, J. Qiu, B. Li, Z. Jin, J. Mater. Sci.: Mater. Electron., 29 (2018) 16721-16729.

84. A. Mirghni, D. Momodu, K. Oyedotun, J. Dangbegnon, N. Manyala, Electrochim. Acta, 283 (2018) 374-384.

85. P. Katkar, S. Marje, S. Pujari, S. Khalate, A. Lokhande, U. Patil, ACS Sustain. Chem. Eng., 7 (2019) 11205-11218.

86. N. Duraisamy, N. Arshid, K. Kandiah, J. Iqbal, P. Arunachalam, G. Dhanaraj, K. Ramesh, S. Ramesh, J. Mater Sci: Mater. Electron., 30 (2019) 7435-7446.

87. H. Shao, N. Padmanathan, D. McNulty, C. O' Dwyer, K. Razeeb, ACS Appl. Energy Mater., 2 (2019) 569-578.

88. J. Li, M. Liu, L. Kong, M. Shi, W. Han, L. Kang, Mater. Lett., 161 (2015) 404-407.

89. L. Hou, L. Lian, D. Li, J. Lin, G. Pan, L. Zhang, X. Zhang, Q. Zhang, C. Yuan, RSC Adv., 3 (2013) 21558-21562.

90. Z. Khan, B. Senthilkumar, S. Lim, R. Shanker, Y. Kim, H. Ko, Adv. Mater. Interfaces, 4 (2017) 1700059 (1-7).

91. H. Pang, S. Wang, W. Shao, S. Zhao, B. Yan, X. Li, S. Li, J. Chen, W. Du, Nanoscale, 5 (2013) 5752-5757.

92. H. Pang, Y. Liu, J. Li, Y. Ma, G. Li, Y. Ai, J. Chen, J. Zhang, H. Zheng, Nanoscale, 5 (2013) 503-507.

93. D. Lee, M. Kang, S. Paek, H. Jung, Bull. Korean Chem. Soc., 37 (2016) 192-199.

94. H. Dan, K. Tao, Q. Zhou, Y. Gong, J. Lin, ACS Appl. Mater. Interfaces, 10 (2018) 31340-31354.

95. D. Patil, B. Koteswararao, K. Begari, A. Yogi, M. Moussa, D. Dubal, ACS Appl. Energy Mater., 2 (2019) 2972-2981.

96. D. Wang, Y. Xu, W. Sun, X. Guo, L. Yang, F. Wang, Z. Yang, Electrochim. Acta, 337 (2020) 135827 (1-10).

97. H. Pang, Z. Yan, W. Wang, J. Chen, J. Zhang, H. Zheng, Nanoscale, 4 (2012) 5946-5953.

98. X. Wang, Z. Yan, H. Pang, W. Wang, G. Li, Y. Ma, H. Zhang, X. Li, J. Chen, Int. J. Electrochem. Sci., 8 (2013) 3768-3785.

99. S. Wang, H. Pang, S. Zhao, W. Shao, N. Zhang, J. Zhang, J. Chen, S. Li, RSC Adv., 4 (2014) 340-347.

100. H. Pang, Y. Zhang, W. Lai, Z. Hu, W. Huang, Nano Energy, 15 (2015) 303-312.

101. C. Chen, N. Zhang, Y. He, B. Liang, R. Ma, X. Liu, ACS Appl. Mater. Interfaces, 8 (2016) 23114-23121.

102. B. Li, P. Gu, Y. Feng, G. Zhang, K. Huang, H. Xue, H. Pang, Adv. Funct. Mater., 27 (2017) 1605784 (1-11).

103. M. Liu, J. Li, Y. Hu, Q. Yang, L. Kang, Electrochim. Acta, 201 (2016) 142-150.

104. Y. Tang, Z. Liu, W. Guo, T. Chen, Y. Qiao, S. Mu, Y. Zhao, F. Gao, Electrochim. Acta, 190 (2016) 118-125.

105. J. Zhang, Y. Yang, Z. Zhang, X. Xu, X. Wang, J. Mater. Chem. A, 2 (2014) 20182-20188.

106. S. Zhang, H. Gao, J. Zhou, J. Alloys Compd., 746 (2018) 549-556.

107. Y. Zhao, Z. Chen, D. Xiong, Y. Qiao, Y. Tang, F. Gao, Sci. Rep., 6 (2016) 17613 (1-10).

108. Z. Xiao, Y. Bao, Z. Li, X. Huai, M. Wang, P. Liu, L. Wang, ACS Appl. Energy Mater., 2 (2019) 1086-1092.

109. M. Liu, N. Shang, X. Zhang, S. Gao, C. Wang, Z. Wang, J. Alloys Compd., 791 (2019) 929-935.

110. B. Liang, Y. Chen, J. He, C. Chen, W. Liu, Y. He, X. Liu, N. Zhang, V. Roy, ACS Appl. Mater. Interfaces, 10 (2018) 3506-3514.

111. J. Hu, P. Yang, S. Wang, J. Shi, ChemElectroChem, 6 (2019) 928-936.

112. H. Chen, S. Jiang, B. Xu, C. Huang, Y. Hu, Y. Qin, M. He, H. Cao, J. Mater. Chem. A, 7 (2019) 6241-6249.

CHAPTER – II

THEORETICAL BACKGROUND OF ELECRODEPOSITION, CHEMICAL BATH DEPOSITION METHOD AND THIN FILM CHARACTERIZATION TECHNIQUES

CHAPTER – II

THEORETICAL BACKGROUND OF ELECRODEPOSITION, CHEMICAL BATH DEPOSITION METHOD AND THIN FILM CHARACTERIZATION TECHNIQUES

2.1 Introduction: Thin films

Interest in the study of science and technology of thin films enhances due to its applicability, properties, technical values, and curiosity in two-dimensional solids. Thin films have been developed to study the change in physical properties and their connection with structure of solids. Also, thin films are used in many devices such as, optical instruments, electrical circuits, magnetic information storage devices, etc [1]. In the formation of thin film, material deposited on surface of clean substrate up to certain thickness of film.

"A surface bounded between two parallel planes extending infinitely in two directions restricted in the dimension along third direction."

Changes in physico-chemical properties are observed due to alteration of structure (bulk to thin film) of material, which dependent on the order and periodicity. The system of thin film possesses at most two-dimensional order or periodicity, that highly influences the physico-chemical properties and also responsible for change in properties than bulk material. Thin film technology highly developed in the fields like optics, magnetism, sensors, electronics and energy storage devices. Many of these applications required nanocrystalline form of material for enhancement in the properties. Materials in nanometer scale offer several advantages such as large surface area, improved diffusivity, high electrical resistivity and high mechanical properties than their bulk counterpart [2]. Nanomaterials can be prepared by two ways, first way is top-down approach, where nanomaterials prepared by breaking of bulk material into nanoscale pieces via chemical or mechanical processes. Another way is bottom-up approach, in which material allows to grow from atomic or molecular species. Most of the research has been devoted to developing capability to control shape, size and

structure of material. Nanocrystalline form of materials have been prepared via numerous chemical synthesis methods and also some novel methods are developed.

Thin film properties depend on deposition method and preparative conditions, and by selecting the proper method desired properties can be achieved. Basically, thin film deposition methods divided into the class of physical and chemical methods [3, 4]. In physical method, there are two branches, one is vacuum evaporation and other is sputtering [5], where material required to transfer in a gaseous state for evaporation method and impact processes for sputtering deposition. In chemical method, there are also two branches. One branch is gas phase chemical process and it contains different deposition methods such as, conventional chemical vapor deposition (CVD), laser CVD, photo CVD, metal organo-chemical vapor deposition (MOCVD) and plasma enhanced CVD. Another branch is liquid phase chemical methods which include electrodeposition, chemical bath deposition (CBD), successive ionic layer adsorption and reaction (SILAR), spray pyrolysis, liquid phase epitaxy, sol gel process, reflux method, spin coating, dip coating, etc. In chemical methods, growth of material obtained through chemical solutions [6]. Physical methods have many drawbacks such as high working temperature, small area deposition, requires sophisticated instruments, costly system, material wastage, high vacuum, etc. In comparison with physical methods, chemical methods are simple, economic, and suitable for large area deposition over any kind of substrate [3, 5, 6]. Also, preparative parameters are easy to control like concentration of solution, pH of solution, temperature, complexing agent, etc. Various chemical methods operate at low temperature that eliminates issue of corrosion and oxidation of metallic substrate. Also, these deposition methods are capable to deposit uniform and pinhole free thin films. So, the chemical processes are advantageous in the

preparation of various materials in thin film form. The classification of thin film deposition techniques is summarized in chart 2.1.

This chapter contains three major parts: first part deals with theoretical background of electrodeposition, second part deals with theoretical background of chemical bath deposition method and third part deals with working principle of characterization techniques (structural, morphological and electrochemical) for thin films.
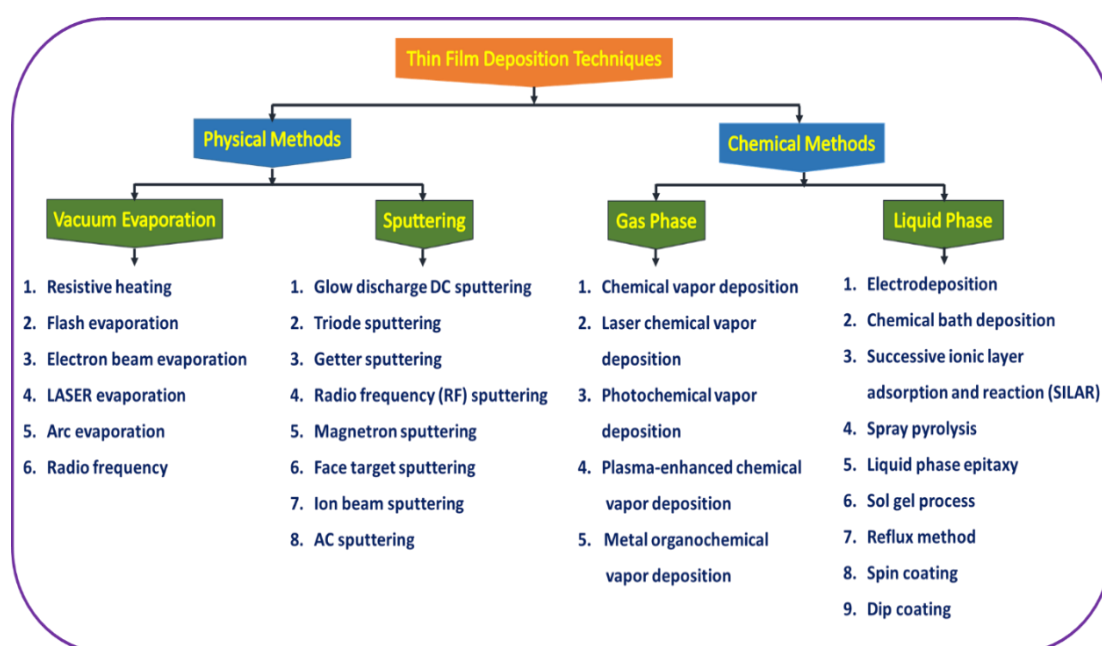
Chart 2.1: Classification of thin film deposition techniques.

2.2 Electrodeposition method

In electrodeposition process, a layer of one metal simply coated on the other metal only by exchanging electrons with ions (oxidation-reduction reaction) in the electrolyte. Easy and economic process for fabrication of metallic coating makes it famous in the field of coating (galvanization/electroplating). Also, it used to prepare numerous nanostructured materials in thin film form. This method is widely used for soft and hard coatings for decorative and protective purposes, so it is explored in electronic industry for new emerging applications [7].

Electrodeposition is easy, attractive and well known technique in comparison with the other physical and chemical methods due to several advantages. By this method, many properties can be controlled easily with accuracy like conductivity of semiconductor (n- or p-type), variation in band gap, control over stoichiometry and doping, etc. Up to now, several materials in the thin film form have been deposited using electrodeposition method such as, ceramics [8], metals [9], semiconductors [10], superconductors [11], oxides [12], hydroxides [13], etc., for different applications. There is an incredible difference in the electrodeposition compared with chemical reaction based methods, where electrodeposition produces a chemical substance in a controlled manner.

2.2.1 Fundamentals of electrodeposition

An exchange of ions or atoms among the electrolyte and electrode occurs in electrochemical deposition processes [14]. In electrodeposition process, generally direct current delivered through a metal ion containing solution for the deposition of metal atoms on a conducting substrate. The schematic of electrodeposition process is shown in Fig. 2.1. The main components in the typical electrodeposition set up are as follow,

1. Working electrode (WE) (Cathode)

2. Auxiliary electrode (Counter electrode (CE)) (Anode)

3. Reference electrode (RE)

4. Electrolyte (Precursor salt solution)

5. Electrochemical workstation (Potentiostat)

As shown in Fig. 2.1, cathode, anode and reference electrode are dipped in the metal ions containing electrolyte, when direct current is passed through anode and cathode then positively charged metal ions attracted towards cathode, and deposited by

becoming electrically neutralized [15]. By controlling charge amount and charge rate passing through electrolyte, the process of deposition can be organised. Thus, chemical changes can be observed over the substrate or in electrolyte due to electrical energy.
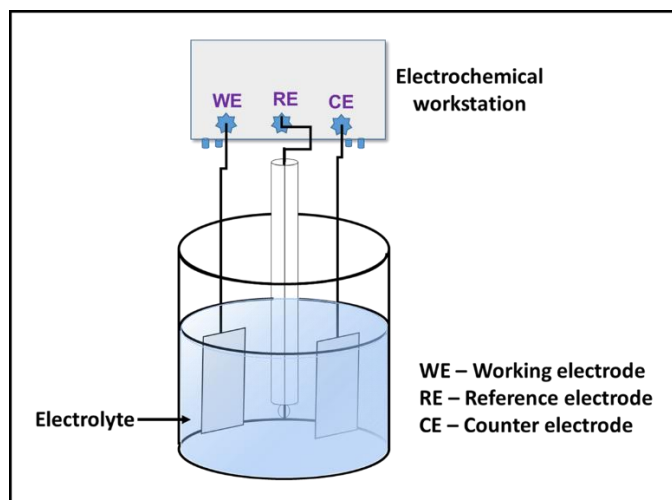
Fig. 2.1 Schematic diagram of electrodeposition.

The deposition of metal on the cathode from the electrolyte containing metal ions takes place as per following reaction [16].

$$M^{n+} + ne^- \longrightarrow M \tag{2.1}$$

where, M^{n+} is metal ions, e^- is electron and n is number of charges.

On the other hand, electrolyte containing more than one cationic species, cations get deposited on cathode simultaneously. For two different cationic species, the reaction in electrodeposition process can be written as below,

$$M^+ + e^- \longrightarrow M \tag{2.2}$$

$$N^+ + e^- \longrightarrow N \tag{2.3}$$

Or $$M^+ + N^+ + 2e^- \longrightarrow MN \tag{2.4}$$
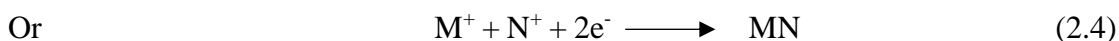
where, N^+ is another metal ion. The amount of deposition can be determined according to Faraday's law.

Faraday's laws of electrolysis

In 1834, Michael Faraday established relationship between the chemical changes in electrolyte solution and electricity passed through it for deposition or liberation of material at electrode.

Faraday's first law

"The amount of substance liberated or deposited on the electrode is proportional to the quantity of electricity passed" and mathematically it can be written as,

$$W \propto Q$$

where, W is amount of substance liberated (g), and Q is the quantity of electricity passed through electrolyte (coulomb). If current (I) transfer for the time (t) then the quantity of electricity is,

$$\text{Quantity of electricity} = \text{Current (I)} \times \text{time (t)}$$

$$Q = I \times t \tag{2.5}$$

$$W \propto I\,t \quad \text{or} \quad W = z\,I\,t \tag{2.6}$$

Here, z is the proportionality constant, known as 'Electrochemical equivalent'. It can be defined as, "The amount of substance liberated (g) on the electrode on passing a current 1 A for 1 sec or passing 1 coulomb of electricity" [17].

Faraday's second law

"If same quantity of electricity is passed through different electrolytes, then the amount of substance liberated on the respective electrodes will be in the ratio of their equivalent weights". An important implication of Faraday's second law is that, the ratio of mass of electrodeposit to its gram-equivalent weight is a constant equivalent to 1 Faraday or 96,500 Coulombs (C) or 26.3 ampere-hour (Ah) [18].

2.2.2 Various steps associated with electrodeposition process

Following successive steps are involved in the electrodeposition process of ionic species from the electrolyte solution as shown in Fig. 2.2.

1. Ionic transport

2. Discharge

3. Breaking of ion-ligand bond (if the bath is complexed)

4. Incorporation of adatoms onto the substrate followed by nucleation and growth.
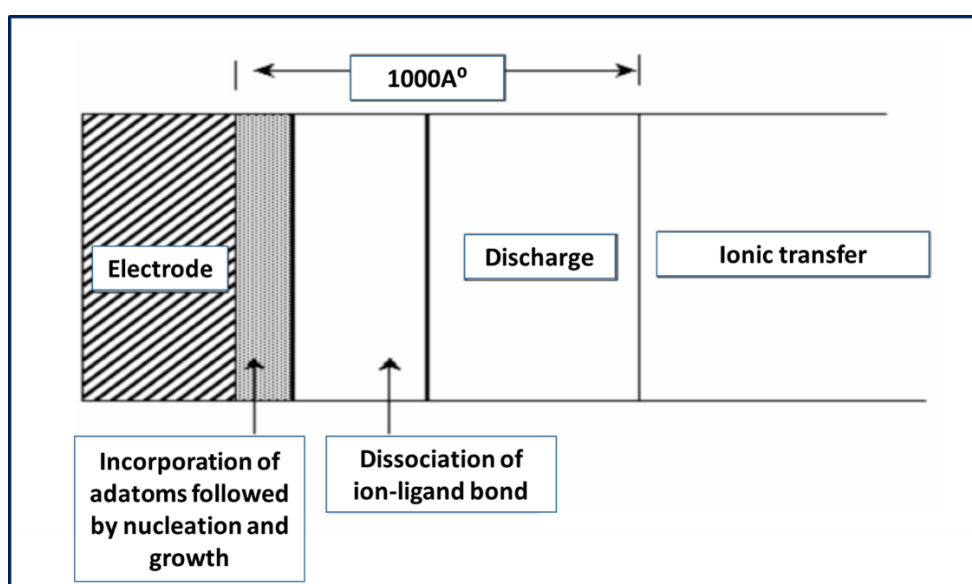
Fig. 2.2 Regions in which various stages of ion transport occur leading to electrodeposition [19].

All steps occur in the range of 1-1000 A⁰ from the substrate and every step has a specific region for the operation. These steps can be classified into three processes with respect to distance from the electrode as [20]:

a. In the electrolyte

b. Near the electrode

c. At the electrode surface

a. Process in the electrolyte

Ions moved towards the electrode in electrolyte due to the influence of

1. Potential gradient, dɸ/dx

2. Concentration gradient, dc/dx

3. Density convective current, dρ/dx.

Above all processes can be expressed in the Nernst-Planck equation,

$$j = zF \frac{D_c}{RT}\frac{d\varphi}{dx} + D\frac{dc}{dx} + cv \qquad (2.7)$$

Where, F, *v*, R and D are the Faraday's constant, electrolyte viscosity, gas constant and diffusion coefficient, respectively. There are three terms responsible for the transport of mass towards the electrode as migration, diffusion and convection processes.

b. Process near the electrode

Generally, electrolyte contains a hydration sheath or complex formed or ligand bounded ionic species. These bounded ions with surrounding moves like individuals and reach near the electrode surface, at that place system can gain the electrons from cathode or losses electrons to anode. This region denoted as discharge and available between 10 to 1000 A⁰ from the electrode.

c. Process at the electrode surface

Electrons are lighter than ions, so they easily cross the solution layer of 5-10 A⁰ thick, but ions do not cross it at room temperature. The ion can reach metal surface from the solution after breaking solvation cage and then subsequent deposition takes place as presented in schematic Fig. 2.3.
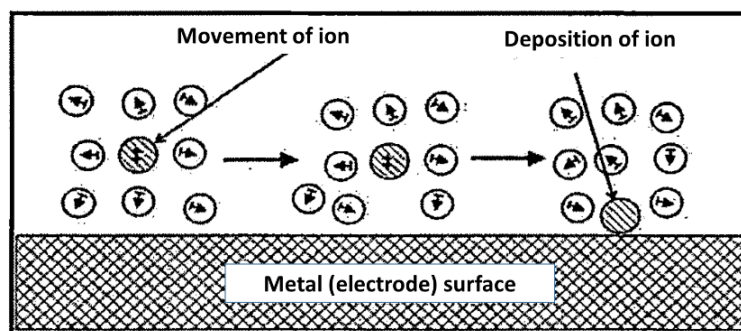
Fig. 2.3 Schematic of ion transfer from solution onto the electrode surface.

The electrically neutral (discharged) ions reach near the electrode surface and form

solid phase by nucleation and growth process through adatom. Transport, discharge,

nucleation and growth are interlinked steps in electrodeposit development.

2.2.3 Pathways for the growth of an electrodeposit

The surface of a solid metal offers various sites for metal deposition as shown in

schematic Fig. 2.4. On the plane of flat surface, a single atom signified as an adatom;

several adatom combination forms as an adatom cluster. Missing of single atom

assigned as vacancy; several vacancies combinely called as vacancy cluster. Steps and

kink sites are important for crystal growth. The addition and removal of atoms at the

kink site create new kink sites.
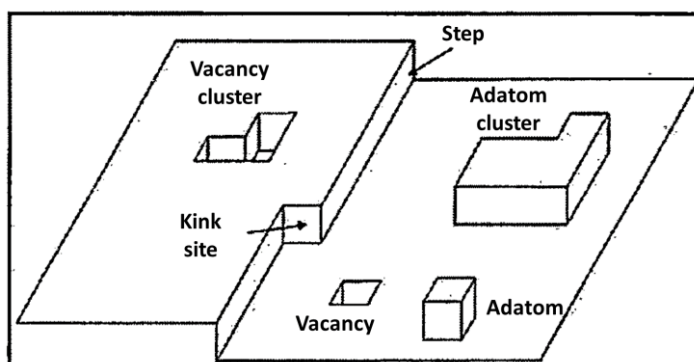
Fig. 2.4 Schematic diagram for a metal surface with few characteristic features [21].

There are two paths for the deposition of metal: (1) direct deposition on the

growth site from solution and (2) formation of adatom by surface diffusion to edges.

Growth of material can be divided into following steps,

1. Ions are transported near the interface in bulk electrolyte.

2. Adatoms are generated by discharged ions on the electrode surface.

3. Nucleation and subsequent growth, here also different routes are possible as,

    i. Surface diffusion directed growth.

    ii. Clusters formation and critical nuclei based growth.

    iii. Formation of monolayer and final growth of electrodeposit.

2.2.4 Initial stages of electrodeposition

There are several principle mechanisms for deposition of metal on flat metal substrate. The initial stage of deposition started by formation of islands or atomic clusters on the surface of substrate which is highly mobile but small in size. In beginning, size of nuclei decided by change in Gibbs free energy and the further growth decides the form, shape and morphology of electrodeposit [22]. There are two kinds of interactive forces are responsible for growth of electrodeposit as, stronger interaction between (1) metal atoms and (2) metal atom and substrate.

2.2.4.1. Stronger interaction between metal atoms

The nucleation clusters are formed in beginning and this process can't take place at underpotentials. In other words, overpotential is required to start the nucleation for deposition process. The process called "Volmer-Weber or three-dimensional island growth" (as shown in Fig. 2.5 (a)), where the connection between atom-atom is stronger than atom-substrate, it leads to nucleate three dimensional islands and then it grows on the substrate surface [19].

2.2.4.2 Stronger interaction between metal atom and substrate

If the interaction between deposited atoms and substrate is stronger, a monolayer of metal atoms on surface of substrate can be deposited at underpotential. There are two subcases,

a) If mismatch available between the lattice structure of metal and substrate atoms then the first layer can form with uneven structure and accordingly then three-dimensional clusters are formed. Such a growth is mentioned as Stranski-Krastanov growth mode and shown in Fig. 2.5 (b).

b) If no mismatch present between the structure of metal atoms and substrate then the uniform monolayer is formed. The layer is also epitaxic and material deposit (Fig.

2.5 (c)) layer-by-layer and it is known as Frank-van-der-Merwe growth mode. The substrate influence is negligible after two or three layers and then deposition continuous like on the bulk metal atoms.
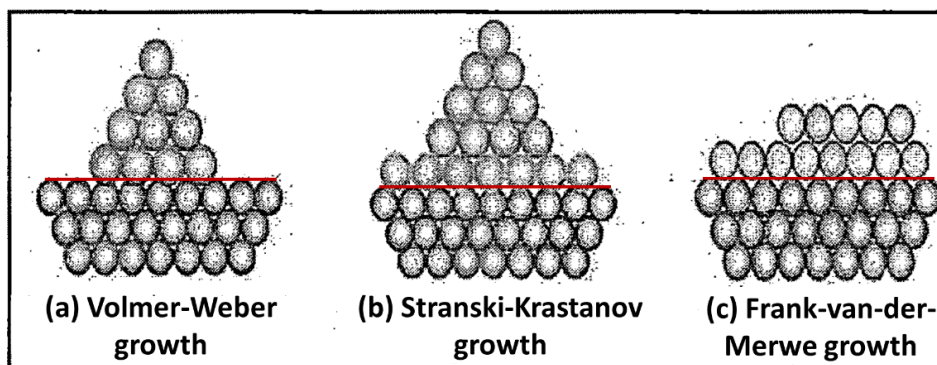
Fig. 2.5 Schematic of three growth modes (a) Volmer-Weber (3-D island) growth, (b) Stranski-Krastanov growth, (c) Frank-van-der-Merwe (layer-by-layer) growth [22].

2.2.5 Various modes of electrodeposition

In electrodeposition method, three different modes can be used for deposition of material as,

1. Potentiostatic (At constant potential)

2. Galvanostatic (At constant current)

3. Potentiodynamic (Potential and current varies with time)

2.2.5.1 Potentiostatic (At constant potential)

In potentiostatic mode, the deposition is carried out at constant dc voltage. In this mode, different charge transfer reactions carried at constant interfacial overpotential in steady-state condition and exchange current density. The selection of overpotential depends on different preparative parameters such as, substrate nature, composition of bath and reversible potential of deposited species. Approximate possible potential required to electrodeposit particular species and it can be discovered with the guidance of standard electrode potential (reference electrode). Nevertheless, the actual potential

for the deposition influences by several factors like interaction between substrate and depositant, overpotential of hydrogen evolution, the bath polarization characteristics and interaction between the various compounds in case of compound electrodeposition. The deposition is done in pure activation, diffusion, or mixed, it dependant on selection of deposition potential. In potentiostatic deposition following features are important,

i)   In this method working electrode potential is controlled with respect to reference electrode.

ii) To develop required potential across the working electrode, the potential is driven through counter electrode.

iii) The cell current varies with respect to time as the output waveform.

2.2.5.2 Galvanostatic (At constant current)

In galvanostatic mode, the deposition is carried out at constant dc current. In this method, during deposition process current between working and counter electrodes kept constant and this is important for uniform deposition. The rate of deposition is proportional to the corresponding current densities. Following features are important in the galvanostatic deposition,

i)   At selected current density, current between the counter and working electrode should able to drive electrolyte ions.

ii) Required cell current is generated by essential potential applied through the counter electrode.

iii) Current is not controlled by reference electrode, the reference electrode only used to measure potential in the electrochemical cell.

iv) The cell potential varies with respect to time as the output waveform.

2.2.5.3 Potentiodynamic (Potential and current varies with time)

In potentiodynamic method, current of electrolysis is measured as a function of applied potential. In potentiodynamic mode, cyclic voltammetry and linear sweep voltammetry can be used. The cyclic voltammetry technique used to study electrochemical processes that take place through electrolysis like, charge transfer, electrode kinetics, etc. Also, it provides qualitative information of electrochemical reactions. Redox potential values of electroactive species present in the solution can be determined using cyclic voltammogram (i.e. an electrochemical hysteresis). In this method, the redox reaction of electroactive species can prepare new material on the substrate. In single step, metal oxides can be easily deposited by this method. A film can be formed on the metal substrate by the reduction of metal ions (at reduction potential) followed by oxidation (at oxidation potential) of metal ions. The desired thickness of film can be obtained by several repeated deposition cycles. Important features of potentiodynamic deposition method are as follows,

i) Measures current during triangular potential sweep and both responses can be observed (anodic and cathodic).

ii) Information about electroactivity of solution and electrode provides by output waveform which has forward and reverse peaks (redox peaks).

2.2.6 Effect of preparative parameters

The properties of material (structural, optical and morphological) directly depend upon preparative parameters of the electrodeposits. Smooth, uniform and stoichiometric film of electrodeposits obtained by controlling preparative parameters like nature of substrate, applied electric field, bath temperature, complexing agents and pH of the bath, etc., [23, 24]. Among these preparative parameters, some are discussed below.

❖ **Substrate**

In electrodeposition method substrate plays a significant role, acts as backbone and mechanical support for the electrodeposit, and also influences the morphology of growing material. Also, modifies optical and electronic properties of material. Following criteria of substrate is important for uniform electrodeposition [25].

i) Substrate should have excellent conductivity.

ii) Thermal expansion coefficient of substrate should matches with electrodeposit.

iii) Good mechanical strength.

iv) Substrate should be stable in electrodeposit precursor solution.

Generally, metal substrates have been widely used for electrodeposit material due to their high conductivity, low cost, easy availability and handling.

❖ **Bath temperature**

The ionic mobility and diffusion rate enhances with increasing temperature of electrodeposit bath. Higher temperature of electrodeposit bath raises current density and that increases nucleation rate, so smooth and fine grained particles can be obtained in thin film form. Also, at higher temperatures, the precipitation of salts and gas evolution potential can be decreased. So, the optimum temperature of bath is difficult to predict and it can be optimized by performing experiments.

❖ **Current density/Overpotential**

The rate of deposition depends upon the applied current density/overpotential. At lower current density/overpotential, slow discharge of ions occurs that decreases growth rate and forms closely packed structure of material. On the other hand, at higher current density/overpotential rate of nuclei formation increases resulted in a fine grain and favours perpendicular deposition of material. However, at very high current density/overpotential rate of hydrogen evolution is very fast that influences the growth

of material and deposited material can be porous and spongy in nature. Also, it responsible for salt precipitation. So, the applied current density/overpotential can control the thickness and structure of deposited material.

❖ **Complexing agent**

The positively charged complex ion formed by chemical combination of unstable metal ions with neutral molecules. Complex compound offers two advantages as, continuous supply of ions for the deposition process and maintain a high concentration of metal complex but low metal ion concentration. The complex formation responsible for growth of small grain and also decreases precipitate formation.

❖ **pH of solution**

The pH of electrodeposit bath need to control high efficiency and desired properties of deposit material. High pH may leads to growing hydroxide ions near the cathode, that resulted in precipitation of basic salt and may participate in electrodeposition, thus it alters properties of electrodeposit. Also, at low pH bath required high current density for the deposition of electrodeposit with high efficiency.

2.2.7 Advantages of electrodeposition method

There are several mesmerizing advantages of electrodeposition method for thin films as follows,

1. Numerous structures, alloys and compounds with tailored composition can be deposited, which is difficult to prepare by other deposition methods.

2. By using potential and charge (current) like electrochemical parameters, morphology and thickness of thin film can be easily controlled.

3. Uniform deposition of material on a complex shape substrate is possible.

4. Precursors like toxic gases are not required (like gas phase methods).

5. Required equipments are inexpensive.

6. Compared to other gas phase methods, reaction in the deposition process arise closer to equilibrium so it is easy to control with accuracy.

7. Avoids high temperature effects like contamination, dopant redistribution and interdiffusion due to low temperature energy saving deposition process.

2.3 Chemical bath deposition (CBD) method

In chemical synthesis methods, thin film formation is based on a thermodynamic equilibrium approach and kinetic approach. In general, CBD method is based on the thermodynamic approach. Synthesis process in thermodynamic approach consist steps of (i) supersaturation generation, (ii) nucleation, and (iii) subsequent growth. For synthesis of nanomaterial in thin film form, the CBD method is very popular. In CBD method, nanomaterial deposited by starting nucleation of depositant on surface of substrate from the liquid phase [26].

Reproducibility, handy nature, large area deposition and commercial production by CBD method underline its importance for thin film preparation [27]. In CBD method, only hot plate and stirrer like simple and easily available instruments are required for the deposition of thin film. By using such simple instruments, pinhole free and uniform thin films can be prepared. Also, nanomaterials with controlled size, shape and composition can be produced with the help of economic CBD method. Thin film properties are relies upon the preparative parameters and they can be easily controlled in CBD method. The review article published by Mane and Lokhande [28] describes thin film formation using economic CBD method in detail. Also, there are many review articles available in literature on the CBD method for thin film preparation [29, 30].

2.3.1 CBD: basic principle

Controlled precipitation of required compound over substrate surface is the basic principle of CBD method for thin film preparation. Basically, formation of thin films through controlled precipitation contains three steps: (i) formation of species, (ii) transport of species and (iii) condensation of species [3, 4]. For precipitate formation in CBD method, the ionic product should exceed than solubility product [3]. Ionic product and solubility product concepts are described below; when sparingly soluble salt AB added in water, a saturated solution containing A⁺ and B⁻ ions along with undissolved solid AB is obtained and equilibrium is established between the solid phase and ions in the solution as,

$$AB(S) \longleftrightarrow A^+ + B^- \tag{2.8}$$
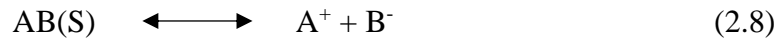
By the law of mass action to equilibrium condition,

$$K = \frac{C_A^+ C_B^-}{C_{AB}(S)} \tag{2.9}$$

Where, C_A^+, C_B^- and C_{AB} are the concentrations of A⁺, B⁻ ions and AB compound in solution.

The pure solid phase concentration is a constant number, i.e. $C_{AB}(S) = $ constant $= K'$

$$K = \frac{C_A^+ C_B^-}{K'} \tag{2.10}$$

$$KK' = C_A^+ C_B^- \tag{2.11}$$

Here, K, K' is constant and product of KK' is also constant, and denoted by K_s then the above equation can be written as,

$$K_s = C_A^+ C_B^- \tag{2.12}$$

K_s and $C_A^+ C_B^-$ are called solubility product (SP) and the ionic product (IP), respectively. At the saturated condition, ionic product is equal to solubility product of ions in

solution. But when IP exceeds SP i.e. IP/SP = S > 1, solution gets supersaturated and precipitation occurs, which leads formation of nuclei in the solution (homogeneous) as well as on the substrate surface (heterogeneous) [28].

In the CBD method, substrate dipped in the solution where solution is the combination of source of cations and anions, then these ions form nuclei on the substrate surface by heterogeneous reaction at supersaturated state. For the formation of thin film by nucleation and growth, a supersaturation state must be created in solution.

2.3.2 Theoretical background of nucleation and growth

2.3.2.1 Fundamentals of nucleation and growth

In chemical deposition, the film formed on substrate due to reaction occurs in a solution. There are several steps in the preparation of film such as nucleation, crystal growth and thin film growth [26].

1) Nucleation

There are two types of nucleation depending upon deposition mechanism such as, homogeneous and heterogeneous nucleation. Homogeneous nucleation occurs when concentration of anions and cations are exceeded than solubility product. On the other hand, heterogeneous nucleation occurs when individual ions/subcritical embryos adsorbed on the substrate surface. The process of adsorption of ion/subcritical embryo on the surface of substrate is shown in schematic Fig. 2.6. The energy required for the formation of an interface between individual ion and substrate surface is usually less than required for interface between ions. Heterogeneous nucleation preferred for formation of thin layer of material on the surface of substrate.
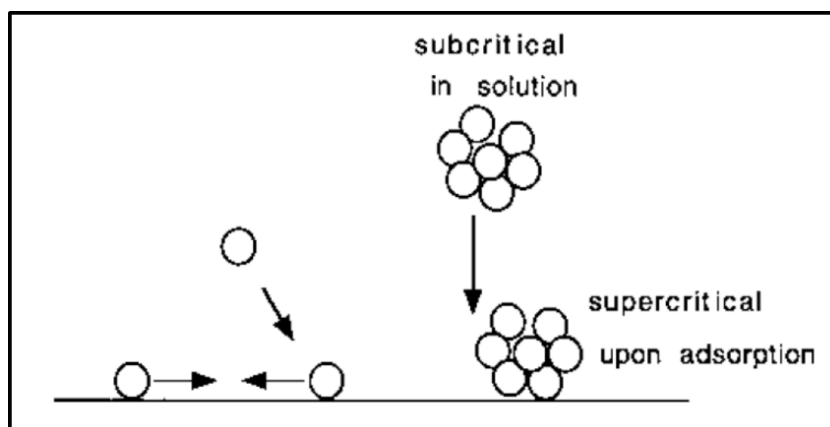
Fig. 2.6 Processes involved in heterogeneous nucleation on a surface of substrate.

2) Crystal growth

In several ways growth can occurs, one is based on self-assembling process and other is disintegration and reconstruction. In first process, after formation of nuclei, growth can be carried out by self-assembling process. On the other hand, growth occurs by rearrangement process of particle due to aggregation and coalescence process (second process) called as Ostwald ripening. The process of aggregation is the adsorption of individual particles on one another and coalescence is reunion of the particles where smaller or unstable nuclei near to large crystal start to dissolve and becomes even smaller, and eventually disappeared which resulted in larger crystal, as shown in Fig. 2.7.
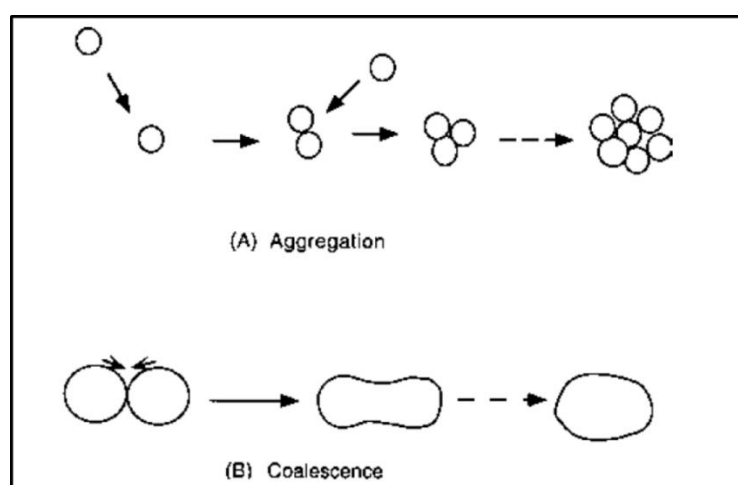
Fig. 2.7 Particle growth by (A) aggregation and (B) coalescence process.

3) Thin film growth

Chemical methods are suitable for deposition of uniform and adherent thin films. In chemical methods growth carried out by ion-by-ion or hydroxide cluster mechanisms separately.

i) Ion-by-ion growth mechanism

High degree of saturation required for the homogenous nucleation in ion-by-ion growth mechanism. Degree of heterogeneity introduced by surface and available free particles helps for nucleation. Surface of substrate act as a catalyst for nucleation. Once nucleation starts on substrate surface, it helps to grow the film, so the deposition rate of film is greater at the nucleated site than the other part of substrate. The growth of material continued until it stopped by some processes or interrupted by some substances.

ii) Hydroxide cluster mechanism

Generally, it is used to describe growth of metal chalcogenide film. The hydroxide cluster process is very simple, since the metal hydroxide is already present in solid phase and the process proceeds by only substitution of hydroxide by chalcogenide on that solid phase.

2.3.3 Preparative parameters of CBD

The deposition of thin film with adherent and uniform nature by CBD method depends upon rate of chemical reaction. Supersaturation of solution and availability of nucleation centres are responsible for deposition rate and thickness of film. Different factors are responsible for growth kinetics of film such as pH, temperature, complexing agent and so on. Effect of preparative parameters on growth mechanism is discussed below;

❖ **Complexing agent**

Deposition in the CBD method generally takes place in a supersaturated solution. Therefore, complexing agents are used to prevent rapid precipitation of material by reducing free metal ions concentration in the solution through complex formation. An increase in complexing agent decreases the free metal ions in the solution and subsequently reaction rate reduces that controls the particle size of material.

❖ **pH of solution**

Rate of reaction and deposition is controlled by supersaturation condition. A complex of metal ion becomes more stable with increasing pH of reaction bath by sacrificing free metal ions availability. That influences reaction rate and it can resulted into change in thickness of film.

❖ **Temperature of the solution**

Temperature of bath is one more parameter that influences rate of reaction. Increase in solution temperature, complex dissociates more efficiently and increases kinetic energy of molecules, and improves interaction between ions. A degree of supersaturation with temperature influences the terminal thickness (increment or decrement) of thin film.

❖ **Nature of substrate**

Film adhesion and reaction kinetics are greatly influenced by nature of substrate. Availability of nucleation centers on the substrate surface is important for nucleation and further growth. Therefore, cleaning process of substrate is an important step for thin film deposition. Substrates lattice parameters also play considerable role in film growth, when it well matches with deposited material then a high rate of deposition and terminal thickness can be obtained.

2.3.4 Advantages of CBD

❖ A variety of substrate can be used (conducting or non-conducting).

❖ Feasible for large area deposition.

❖ Low temperature reaction process.

❖ Stoichiometric deposition can be obtained.

❖ High reproducibility.

❖ Safe with less environmental hazards.

❖ Thickness of film can be easily controlled using deposition time or other preparative parameters.

❖ Pinhole free and uniform deposition of a thin film can be achieved.

2.4 Thin film characterization techniques

The physico-chemical properties of thin film material responsible for their usage in respective applications. So, for the achievement of excellent performance of thin film for the desired application, it is necessary to characterize the prepared material by different techniques like structural, morphological and surface analyses with XRD, FT-IR, FE-SEM, EDS and XPS techniques.

2.4.1 X-ray diffraction (XRD)

XRD technique is used for the confirmation of phase and crystal structure of prepared material. XRD is a non-destructive technique and it is based on scattering of X-rays from the structures [31]. For the identification of unknown substance, XRD technique is very important. Diffraction data of identifying material is compared with available data in Joint Committee on Powder Diffraction Standards (JCPDS) or American Standard for Testing of Materials (ASTM) [32]. Commercial monochromators with micro focused intense X-ray assembled in XRD technique which improves detection limit of system and can be used for identification of material in thin

film form. Accurate quantitative information of interfacial atomic arrangements (i.e. structural information, d-spacing, lattice parameters) can be obtained from XRD patterns. Schematic presentation of diffractometer is shown in Fig. 2.8, where 2θ is the angle between the incident and diffracted X-ray. Typically, diffraction pattern is provided by orientation of specimen and diffracted intensity with function of 2θ. The wavelength of X-ray is in the range of 0.7-2 A⁰ with corresponding energies.
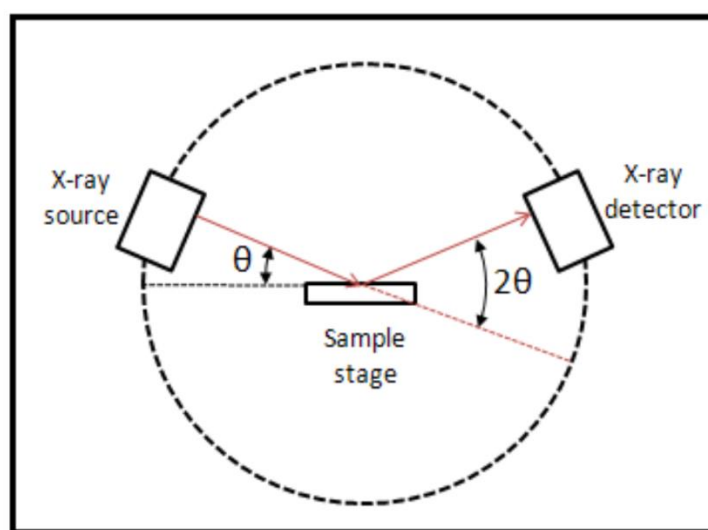
Fig. 2.8 The schematic diagram of XRD diffractometer [33].

Chromator in the XRD technique is used as a source of diffraction beam and X-ray beam diffracts from the surface of film and detected by oscillating detector around the mean position of diffraction. Monochromatic radiation is important in XRD technique for the determination of accurate d-spacing from observed diffraction angles. The basic phenomenon of XRD technique is the X-ray reflection from the crystallographic planes and is directed by Bragg's equation;

$$2d \sin\theta = n\lambda \qquad\qquad (2.13)$$

where, d, λ, n and θ are the lattice spacing, wavelength of the monochromatic X–ray, order of diffraction and diffraction angle, respectively. When the values of θ, λ and n are known then the value of 'd' can be calculated using above equation [34].

2.4.2 Fourier Transform-Infrared Spectroscopy (FT-IR)

For the information of atomic arrangement and interatomic forces in material, infrared spectroscopy can be used. In an electromagnetic field, two energy levels (E_1 and E_2) are present in a material where energy level difference is equal to 'h' times of incident radiation frequency (ν) and it is written as,

$$\Delta E = h\nu \qquad (2.14)$$

In above equation, ΔE is positive when energy is absorbed by molecule and negative when radiation emitted. A unique spectrum for the molecule is found when above equation satisfied. The plot of intensity versus frequency called as a spectrum and peaks observed after the satisfaction of equation (2.14). In FT-IR analysis, a small region of spectrum (close to visible) can be investigated, which contains UV, visible and IR regions (10^{-6} to 10^{-3} cm). Different spectra raise by atoms or molecules depends on the energy levels involved in the transition. In atom, transition between different levels of orbital electron signifies absorption and the whole molecule rotate or vibrate when atoms vibrate within the molecule. Therefore, the energy contribution can be represented by the following equation [35],

$$E_{tot} = E_{elect} + E_{vib} + E_{rot} + E_{trans} \qquad (2.15)$$

where, E_{elect}, E_{vib}, E_{rot} and E_{trans} are the electronic energy, vibrational energy, rotational energy and translation energy, respectively.

The basic ray diagram of FT-IR spectrometer is shown in Fig. 2.9. Electronic, vibrational and rotational energies are possible only for certain transitions due to quantized energy levels and because of small quantity translational energy can be ignored. In the support of XRD technique for material characterization, infrared spectrum can be used as a fingerprint for identification of material.
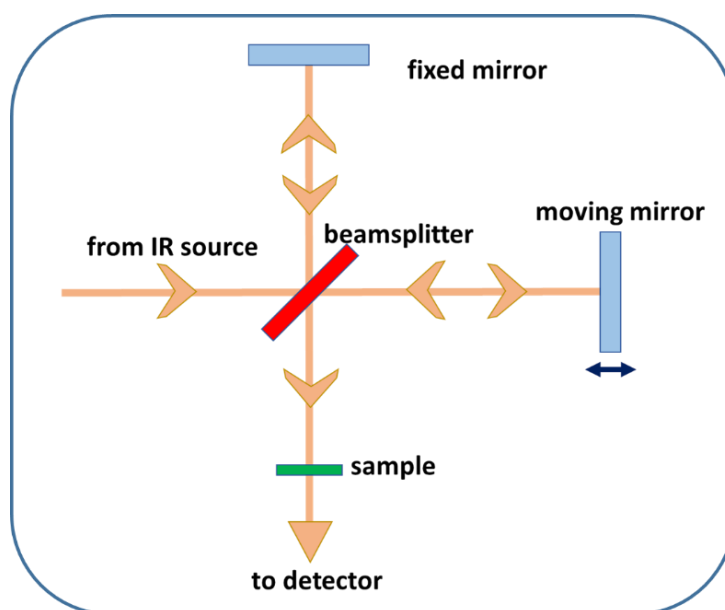
Fig. 2.9 Basic ray diagram of FT-IR spectrometer [36].

2.4.3 X-Ray Photoelectron Spectroscopy (XPS)

The surface properties of material or thin film can be identified by the X-ray photoelectron spectroscopy (XPS) technique and it also called as electron spectroscopy for chemical analysis (ESCA). This technique based on photoelectric effect and X-rays are used as a source of photons. Electrons escape from the material surface when the beam of X-ray incident on the surface of material. The escaped electron mentioned as photoelectrons and using the kinetic energies of photoelectrons elemental identification can be done directly. Also, the intensities of photoelectrons help to determine the relative composition of elements in the material. The ejected electrons kinetic energy can be calculated by the relation [37],

$$\text{K.E.} = h\nu - \text{B.E.} - \varphi_s \qquad (2.16)$$

where, K.E., $h\nu$, B.E. and φ_s are ejected photoelectrons kinetic energy, X-ray photons characteristic energy, binding energy of the atomic orbital from which the electrons originated and spectrometer work function, respectively.

Ionization and emission of electrons in inner shell happen due to absorption of photons by the atom present in a molecule. Each element represents a characteristic

peak in the spectrum of photoelectron due to each core level atomic orbital having characteristic binding energy. In XPS, very firstly the survey scan is done, in that all available energies measurement are carried out and confirm present elements in the sample. In XPS study, energy spectrum is created by plotting binding/kinetic energies of emitted electrons and plot informs amount of elements present in the sample.
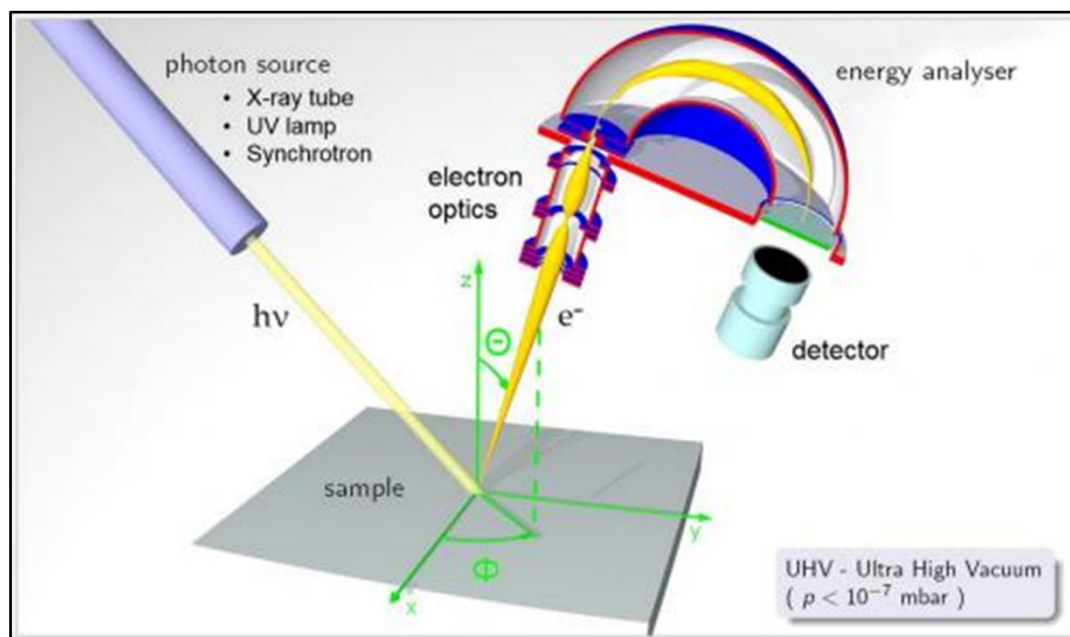
Fig. 2.10 Ray diagram of XPS [38].

The peaks at particular energies denotes presence of specific element and these peaks are related to electronic configuration of elements. This instrument is useful to identify oxidation state of elements. Ray diagram of XPS technique is shown in Fig. 2.10. XPS cannot provide a complete chemical analysis, since it is a surface phenomenon where signals used for analysis, originates generally from a few atomic layers of surface and very few from the deeper part of solids.

2.4.4 Field Emission–Scanning Electron Microscopy (FE-SEM)

High energy focussed electron beam is used, for scanning of the specimen surface in FE-SEM for better visualization. It has better (3 to 6 times) resolution than conventional SEM technique and more clear images (resolution around 1 nm) can be

obtained, which is used for elemental, compositional and topographical study of specimen [39]. Ray diagram of FE-SEM is shown in Fig. 2.11.
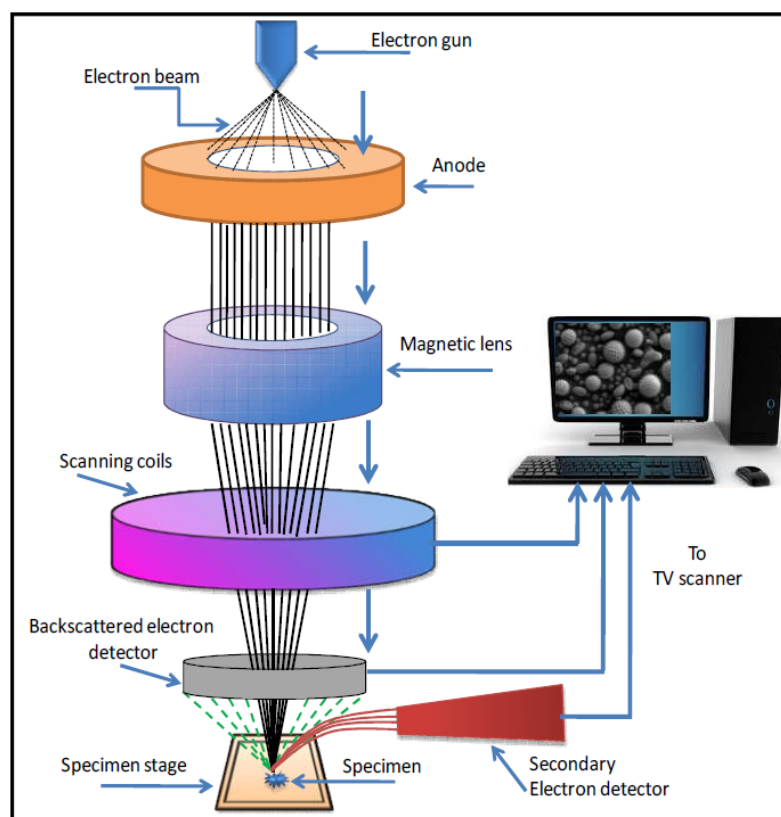
Fig. 2.11 Ray diagram of FE-SEM [40].

Electrons emitted from the source of field emission called as primary electrons are accelerated in high vacuum and electric field gradient. A narrow beam of primary electrons is produced by focusing and deflecting it through electronic lenses to bombard on the specimen. This beam incident over the specimen surface and due to the number of interaction between beam and specimen, electrons ejects from the specimen. Possible emission of electrons after interaction of primary electrons with specimen is shown in Fig. 2.12. The secondary electrons, backscattered electrons, transmitted electrons, auger electrons and X-rays are produced during the interaction between beam and specimen and they are separated on the basis of energies. A digital image of specimen surface is produced from secondary electrons detected by detector. A detector produces an electronic signal and further it amplified and display as an image on a monitor. When

electrons interact with specimen atoms then there is a possibility of elastic or inelastic scattering. In scattering, if transferred energy is small then electron cannot emit from the specimen, and transferred energy is more than work function of specimen material then electron emits from the specimen surface. Specific information of specimen such as topography, surface characteristics, specimen composition, etc. can be obtained from each signals.
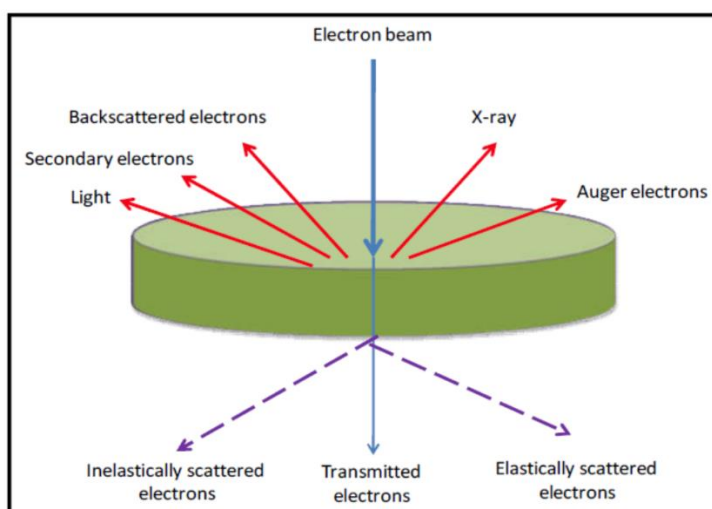
Fig. 2.12 Ray diagram of the emitted different types of electrons during interaction between specimen and beam [41].

2.4.5 Energy Dispersive X-ray Spectroscopy (EDS)

Energy dispersive X-ray spectroscopy (EDS) is generally used for elemental analysis or chemical characterization of samples and also called as energy dispersive X-ray analysis (EDAX) or energy dispersive X-ray microanalysis (EDXMA). The principle used in the EDS is that, every element has a specific atomic structure and gives a unique set of peaks in the emission spectrum.

For the emission of characteristic X-rays from the sample, a charged particle beam or high-energy X-ray beam is focused on specimen. Ground state electrons are present in the atom of specimen in different energy levels. Electrons in the inner shell are excited or eject after beam incident on it and the hole is created after ejection of

electron. Then, the electron from higher shell occupies the vacant space, so energy difference between the shells released in the form of X-ray (shown ray diagram in Fig. 2.13). The energy dispersive spectrometer calculates energy and released number of X-rays from the specimen. The energies of X-rays are characteristics of atomic structure and energy difference between two shells. Hence, elemental composition of the specimen can be measured by EDS [42].
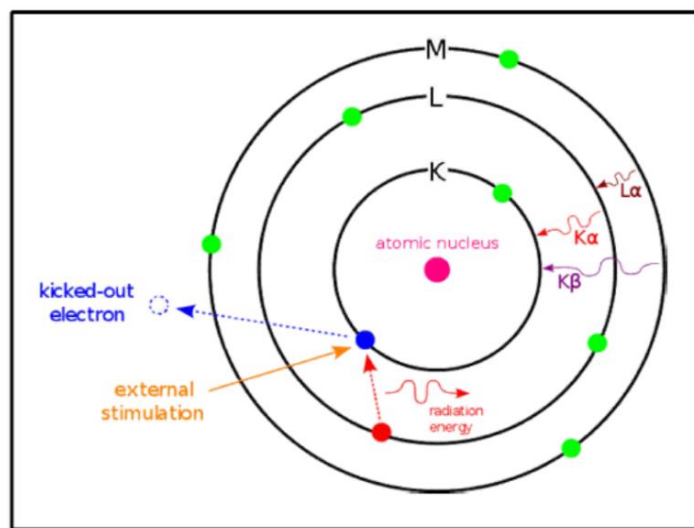
Fig. 2.13 Ray diagram of emission of X-ray in EDS [43].

Following components are embedded in the EDS equipment;

1. The excitation source (X-ray beam or electron beam)

2. The X-ray detector

3. The pulse processor

4. The analyzer

When emitted X-rays incident on the detector, charged pulses create. The detector converts that charged pulse into voltage signals with the help of amplifier. Charged pulse further deliver to a pulse processor, which measures signals and forward to the analyzer for data display. Elemental composition of the specimen is analyzed using spectrum from number of counts against the X-rays energy.

2.5 Electrochemical Techniques

As discussed in chapter I, supercapacitor generally categorized into EDLCs (charge stored by non-faradaic mechanism) and pseudocapacitors (charge stored by faradaic mechanism). Ion permeable electrodes and suitable electrolytes are comprised in the supercapacitor devices. Following equation is used for the calculation of specific capacitance of supercapacitor device,

$$C_S = \frac{1}{mv(V_{max} - V_{min})} \int_{V_{min}}^{V_{max}} I(V)dV \qquad \text{(F g}^{-1}\text{)} \qquad (2.17)$$

where, C_s, v, $(V_{max} - V_{min})$, I(V) and m are the specific capacitance (F g^{-1}), potential scan rate (V s^{-1}), operational potential window (V), current response (A) and deposited mass of material (g) on electrodes, respectively. Then energy density (ED) and power density (PD) of supercapacitor are calculated using the following equations,

$$ED = \frac{0.5 \times C_S \times (V_{max} - V_{min})}{3.6} \qquad \text{(Wh kg}^{-1}\text{)} \qquad (2.18)$$

And $\quad PD = \frac{ED \times 3600}{t_d} \qquad\qquad \text{(W kg}^{-1}\text{)} \qquad (2.19)$

where, ED, PD and t_d are energy density, power density and discharge time of supercapacitor.

The maximum value of energy and power density can be achieved by large capacitance value and wide operating potential window of supercapacitor. Active electrode material and electrolyte are accountable for large capacitance and wide potential window of supercapacitor. The electrochemical capacitor stores charges at the interface of electrode/electrolyte. The opposite charges accumulate via different charge storage mechanisms (discussed in chapter I), when potential is applied to the electrodes [44-46]. Electrical charges stored in supercapacitor devices are represented as follows,

$$E_s1 + E_s2 + K^+ + A^- \Leftrightarrow E_s1^- // K^+ + E_s2^+ // A^- \qquad (2.20)$$
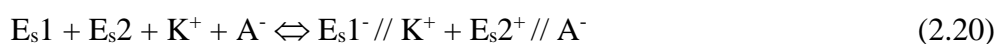
where, E_s1 and E_s2 are the specific surface area of negative and positive electrodes. The symbol // indicates charges stored on both electrodes, where K^+ and A^- are cations and anions present in the electrolyte. To understand the electrochemical behavior of electrode, CV, GCD and EIS techniques are required. Therefore, these electrochemical characterizations of electrode are important for successful implementation in supercapacitor device.

2.5.1 Cyclic voltammetry (CV)

Information about electroactivity of electrode in solution of electrolyte can be provided by the fundamental electrochemical characterization technique CV. In this experiment, electrodes dipped into electrolyte solution and three electrode system preferred for investigation with minimized ohmic resistance. Potential is applied with respect to reference electrode, and current is measured across working and counter electrode in three electrode system [47, 48].

In CV, potential varied in fixed potential window with respect to time. During first scan when voltage achieves V_2 point then scan reversed and reaches point V_1. This flow of voltage schematically presented in Fig. 2.14 (a). Typical CV curve of reversible reaction for the single electrode is shown in Fig. 2.14 (b). In this figure, V_1 and V_2 represent starting and final potentials, I_pc and I_pa are the cathodic and anodic peak currents and E_pc and E_pa are cathodic and anodic peak voltages of resulted voltammogram.
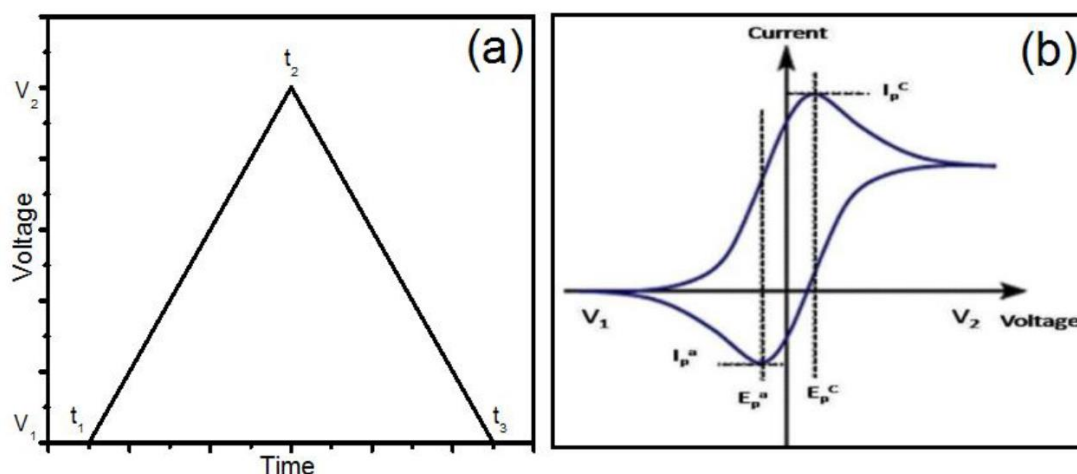
Fig. 2.14 (a) Ramping applied voltage with time (b) a typical cyclic voltammogram

for a reversible single electrode transfer reaction.

In forward scan, potential increases from V_1 to V_2, initially cathodic current increases and further decreases as decreasing concentration of reduced analyte. In reverse scan potential decreases from V_2 to V_1 and reduced analyte will start to re-oxidized which delivers reverse polarity current, called as anodic current. Selection of initial and final potential in the CV measurement is very important. The working potential of electrode depends upon redox and electrolytes decomposition potential.

2.5.2 Galvanostatic charge-discharge (GCD)

The GCD technique is used for the testing capacitive performance of supercapacitor. In this technique, constant current is applied to working electrode and its potential measured as a function of time with respect to reference electrode. The schematic of GCD curve is shown in Fig. 2.15. When constant current is applied, initially potential quickly develops because of internal resistance and further it develops gradually due to the exhaustion of reactant concentration at the electrode surface. Similarly, potential drop occurs while discharging due to IR (internal resistance) and it is related to electrode and solution resistance. Constant current is used to achieve the set/required voltage during charge and discharge [49].
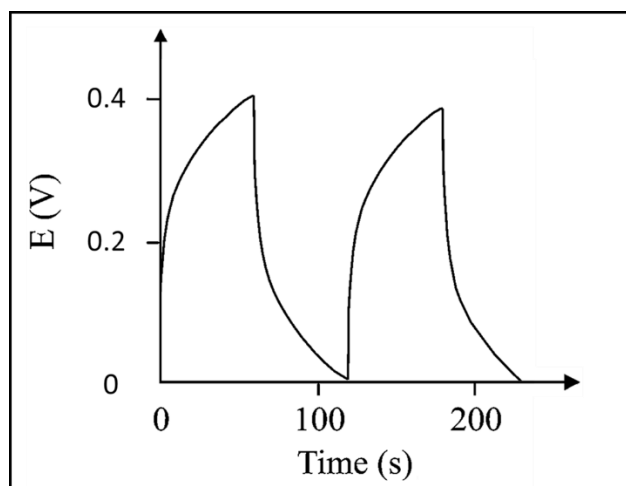
Fig. 2.15 Plot of charge-discharge curve [50].

To sustain the applied current, redox reactions take place at the surface of working electrode. Confirmation of charge storage mechanism of prepared electrode is possible from the nature of charge-discharge curve. Linear nature of charge-discharge curve confirms the electric double-layer mechanism and non-linear nature confirms pseudocapacitive mechanism used for charge storage [51]. Importantly, GCD technique is useful for determination of energy and power density of supercapacitor device.

2.5.3 Electrochemical impedance spectroscopy (EIS)

In EIS technique, electrochemical impedance and response of current are measured by applying AC signal of potential in wide range of frequencies to a system. Impedance is nothing but the AC resistance of the cell, which consists of imaginary and real parts. The electrochemical cell contains resistive, capacitive and inductive properties. Resistive properties involve in real part, while capacitive and inductive properties involve in the imaginary part. As the capacitor acts open circuit for DC and inductor acts as a straight conductor wire in DC, however both appear as imaginary resistors in an AC circuit. A wide range of frequencies (sweeping from high to low) allows reaction steps to be separated with different rate constants such as, charge transfer, mass transport and chemical reaction. Electrochemical reactions are

responsible for flow of current at the electrified interface, which always contains Faradaic/non-faradaic components.

$$O + ne^{-} \rightarrow R \tag{2.21}$$

where, O, n and R are the oxidant, number of electrons transferred and reduced species, respectively. The accumulation of ions across the electrified interface are shown in Fig. 2.16 (a). In Fig. 2.16 (a), the counter cations united beside the electrified surface due to negatively polarized electrode. The equivalent circuit (Fig. 2.16 (b)) contains low and high frequency components, where, CE, C_d, R_p, R_s, Z_W and WE are counter electrode, the double-layer capacitor, polarization resistance, solution resistance, Warburg impedance and working electrode, respectively. The electrochemical impedance can arise from both faradaic and non-faradaic components.
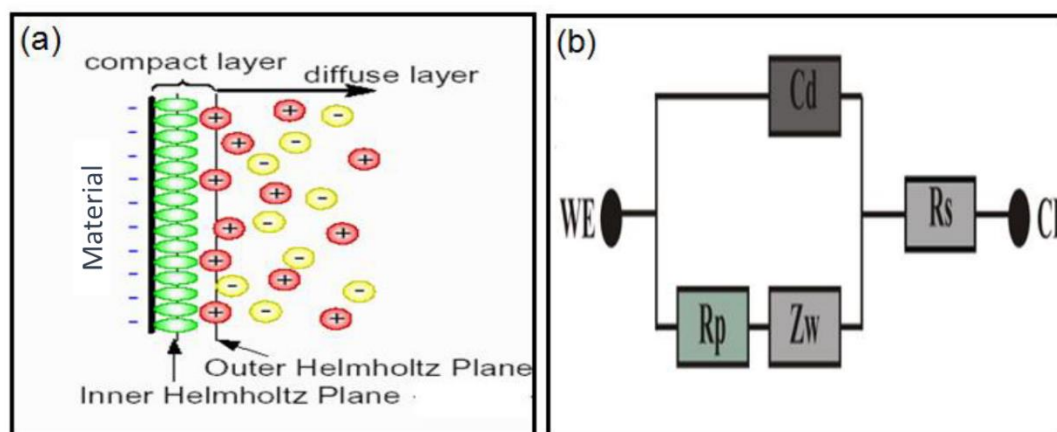
Fig. 2.16 (a) Schematic of electrified interface at negative electrode of cell and (b) equivalent electrical circuit for the electrode/electrolyte interface [52].

Redox reaction is responsible for rising of faradaic components and double layer capacitor (C_d) responsible for the rise of non-faradaic components. Availability of oxidants and creation of reductants near the electrode surface controls rate of charge transfer. All these characterization techniques are used to find out operating potential

window, specific capacitance, energy density, power density and cyclic stability of supercapacitor.

2.6 References

1. https://en.wikipedia.org/wiki/Thin_film
2. I. Gurrapp, L. Binder, Sci. Technol. Adv. Mater., 9 (2008) 043001 (1-11).
3. J. George, "Preparation of Thin Films", Marcel Dekker, Inc., New York, (1992) 13-19.
4. K. Chopra, I. Kaur, "Thin film Device Application", Plenum Press, (1983) 101-102.
5. T. Niesen, M. De Guire, Solid State Ion., 151 (2002) 61-68.
6. C. Lokhande, Mater. Chem. Phys., 27 (1991) 1-43.
7. P. Andricacos, Electrochem. Soc. Interface, 8 (1999) 32-37.
8. I. Zhitomirsky, L. Gal-or, A. Kohn, J. Mater. Sci., 30 (1995) 5307-5312.
9. M. Jeske, J. Schultze, M. Thonissen, H. Munder, Thin Solid Films, 255 (1995) 63-66.
10. G. Fulop, R. Taylor, Ann. Rev. Mater. Sci., 15 (1985) 197-210.
11. G. Yi, W. Schwarzacher, Appl. Phys. Lett., 74 (1999) 1746-1748.
12. S. Peulon, D. Lincot, Adv. Mater., 8 (1996) 166-170.
13. C. Natarajan, H. Matsumoto, G. Nogami, J. Electrochem. Soc., 144 (1997) 121-125.
14. A. Bard, L. Faulkner, "Electrochemical methods: fundamentals and applications", New York: Wiley, Second edition, (2000) 586-587.
15. A. Karatutlu, A. Barhoum, A. Sapelkin, "Emerging Applications of Nanoparticles and Architecture Nanostructures", Elsevier, (2018) 1-28.
16. R. Pandey, S. Sahu, S. Chandra, "Handbook of Semiconductor Electrodeposition", Marcel Dekker, Inc., (1996) 3-4.
17. Y. Gamburg, G. Zangari, "Theory and Practice of Metal Electrodeposition" Springer-Verlag New York, (2011) 2-3.
18. https://www.electrical4u.com/faradays-first-and-second-laws-of electrolysis/
19. https://eng.thesaurus.rusnano.com/wiki/article1171

20.   W. Schmickler, E. Santos, "Interfacial Electrochemistry", Oxford University Press, New York, Second Edition, (2010) 145-149.

21.   S. Saha, M. Johnson, F. Altayaran, Y. Wang, D. Wang, Q. Zhang, Electrochem, 1 (2020) 286-321.

22.   F. Nasirpouri, "Electrodeposition of Nanostructured Materials", Springer Series in Surface Sciences, (2017) 35-36.

23.   D. Sarkar, X. Zhou, A. Tannous, M. Louie, K. Leung, Solid State Comm., 125 (2003) 365-368.

24.   N. Gaikwad, V. Nikale, C. Bhosale, J. Phys. Chem. Solids, 64 (2003) 723-730.

25.   J. Min, J. Wu, J. Cho, Q. Liu, J. Lee, Y. Ko, J. Chung, J. Lee, Y. Kim, J. Magn. Mater., 304 (2006) e100-e102.

26.   G. Hodes, "Chemical Solution Deposition of Semiconductor Films", Marcel Dekker Inc., New York, (2001).

27.   D. Dubal, R. Holze, P. Gomez-Romero, Sci. Rep., 4 (2014) 7349 (1-10).

28.   R. Mane, C. Lokhande, Mater. Chem. Phys., 65 (2000) 1-31.

29.   S. Pawar, B. Pawar, J. Kim, O. Joo, C. Lokhande, Curr. Appl. Phys., 11 (2011) 117-161.

30.   B. Ezekoye, P. Offor, V. Ezekoye, F. Ezema, IJSR, 2 (2013) 452-456.

31.   C. Hu, X. Dang, S. Hu, J. Electroanal. Chem., 572 (2004) 161-171.

32.   B. Cullity, S. Stock, "Elements of X-rays Diffraction", 3rd Edition, Prentice Hall, (2014) 284-285.

33.   http://xrd.co/component-parts-x-ray-diffractometer/

34.   http://chemwiki.ucdavis.edu/Analytical_Chemistry/Instrumental_Analysis/Diffraction/Powder_X-ray_Diffraction

35.   R. Nyquist, R. Kagel, "Infrared Spectra of Inorganic Compounds", Academic Press INC, New York, (1971) 2-6.

36.   https://lab-training.com/2015/05/08/contributions-of-michelson-interferometer-to-ft-ir-spectroscopy/

37.   S. Kerber, T. Barr, G. Mann, W. Brantley, E. Papazoglou, J. Mitchell, J. Mater. Eng. Perform., 7 (1998) 329-333.

38.   http://ywcmatsci.yale.edu/sites/default/files/resize/images/XPS-1-500x294.JPG.

39. http://www.stcloudstate.edu/cmia/documents/Invitation_to_the_SEM_World.pdf

40. https://icme.hpc.msstate.edu/mediawiki/index.php/Scanning_Electron_Microscopes.html

41. http://web.eng.fiu.edu/wangc/electron%20microscopy%201%202009.pdf

42. http://www.wikiwand.com/en/Energy-dispersive_X ray spectroscopy

43. http://en.wikipedia.org/wiki/Electric_double-layer_capacitor

44. A. Burke, J. Power Sources, 91 (2000) 37-50.

45. Y. Volfkovich, T. Serdyuk, Russ. J. Electrochem., 38 (2002) 935-959.

46. http://en.wikipedia.org/wiki/Pseudocapacitor

47. A. Mabbot, J. Chem. Educ., 60 (1983) 697-702.

48. P. Kissinger, W. Heineman, J. Chem. Educ., 60 (1983) 702-706.

49. http://www.michaelsharris.com/electronics/images/capRCcurve.gif.

50. D. Kampouris, X. Ji, E. Randviir, C. Banks, RSC Adv., 5 (2015) 12782-12791.

51. S. Dai, Y. Xi, C. Hu, X. Yue, L. Cheng, G. Wang, J. Power Sources, 274 (2015) 477-482.

52. http://web.nmsu.edu/snsm/classes/chem435/Lab14/double_layer.html

82

CHAPTER – III

SYNTHESIS, CHARACTERIZATION AND SUPERCAPACITIVE PERFORMANCE EVALUATION OF CHEMICAL BATH DEPOSITED NICKEL COBALT PHOSPHATE THIN FILMS

SYNTHESIS, CHARACTERIZATION AND SUPERCAPACITIVE PERFORMANCE EVALUATION OF CHEMICAL BATH DEPOSITED NICKEL COBALT PHOSPHATE THIN FILMS

3.1 Introduction

In recent years, supercapacitors (SCs) getting much attention due to their several properties like longer life span and high power with considerable amount of energy as well as easy fabrication process with low maintenance [1]. Still, the energy density values of supercapacitor couldn't match with current requirement of the electrical appliances or portable devices, which is prime need of improved life style and economic development [2]. To reach required values, numerous efforts have been taken by researchers and number of materials are studied as electrode material for supercapacitor application like, metal oxides [3, 4], hydroxides [5] and sulfides [6]. However, poor stability, poor conductivity and low specific capacitance of existing materials limit their application in supercapacitor [7, 8]. The effective and high performing device can be developed using the electrode material which has higher specific capacitance, good cycling ability and cost effective synthesis process [9].

Among numerous materials, the metal phosphate based materials attract much attention due to excellent conductivity, several active sites, wide and open structural channels are helpful for ion transformation and P-O covalent bond offers highly stable structure [10]. In all metal phosphates, nickel and cobalt mostly used in energy storage application due to earth abundant nature and excellent redox reaction. However, still there is a gap between predicted theoretical and achieved performance of phosphate electrodes [11]. Moreover, the mixed metal compounds studied for the improvement in the performance of material, mixed metal compounds deliver high specific capacitance than single metals due to synergetic effect between two metal species [12]. This aspect proved by some researchers by preparing binary metal compounds and evaluating their electrochemical performance. Yang et. al. [13] prepared nanowire arrays of Ni-Co oxides and obtain maximum capacitance of 2282 F g^{-1} at 0.5 A g^{-1} than the single metal

oxides like CoO (257 F g^{-1}) and NiO (807 F g^{-1}) electrodes. Also, Patil et. al. [14] synthesized nanorods of $Co_{0.67}Ni_{0.33}(OH)_2$ which offers high capacitance of 1280 F g^{-1} at 60 A g^{-1} than the $Co(OH)_2$ (1120 F g^{-1}) and $Ni(OH)_2$ (130 F g^{-1}) electrodes.

A similar approach was considered for the synthesis of binary metal phosphate thin films. So, for the first time low temperature simple chemical bath deposition (CBD) method was used for the binder-free synthesis of nickel cobalt phosphate thin film electrodes for supercapacitor application with different nickel and cobalt molar ratio. Effect of chemical composition variation on structure and morphology are studied and analyzed. Furthermore, influence on supercapacitive performance (specific capacitance) due to variation in morphology is studied. The present chapter is divided into two sections (section A and B). Section 'A' deals with the synthesis of nickel cobalt phosphate thin films by simple CBD method and their characterization. Section 'B' is associated with the supercapacitive performance evaluation of chemical bath deposited nickel cobalt phosphate thin films.

SECTION – A

SYNTHESIS AND CHARACTERIZATION OF NICKEL COBALT PHOSPHATE THIN FILMS BY CBD METHOD

3.2.A.1 Introduction

The architecture of prepared material majorly depends on deposition process and composition of precursors. The composition affects on the morphology of material and change in corresponding results can be observed in the physico-chemical properties and electrochemical performance. The variation in morphology is observed by Patil et. al. [14] with variation of nickel and cobalt ratio in nickel cobalt hydroxide. The nanorod size of $Co(OH)_2$ reduces with increase in nickel content and is converted into fuzzy nanoparticle like structure at zero cobalt content ($Ni(OH)_2$). Similarly, in the

preparation of $Co_{0.4}Ni_{1.6}P_2O_7$ using hydrothermal method by Chen et. al. [9] observed decrement in size of microplates from $Co_2P_2O_7$ to $Ni_2P_2O_7$. Li et. al. [15] observed variation in thickness of $Co_3(PO_4)_2$ nanosheets after addition of nickel content and finally converted into nanosheets with nanoparticles for $Ni_3(PO_4)_2$. Conversion of porous nanospheres structure of $Co_3(PO_4)_2$ to non-porous irregular nanospheres like structure of $Ni_3(PO_4)_2$ was observed by Tang et. al. [16] with increasing nickel content. Also, Zhang et. al. observed pompon-shaped hollow shells of $Co_3(PO_4)_2$ covered by flexible nanosheets and gradual increase in nickel content, the pompon-shaped hollow shells eventually develop into nanosheets at zero cobalt content [17]. A similar approach is followed and nickel cobalt phosphate thin films are prepared with tuned morphologies to achieve better electrochemical results.

Directed to commercialization of supercapacitor, the main and unsacrificial requirements are high energy and power density, a cost effective preparation and electrochemical stability of electrodes. To fulfill one above mentioned requirement, simple, binder-free and eco-friendly CBD method is used for the synthesis of cost effective nickel cobalt phosphate thin film electrodes. In the synthesis method, preparative parameters like reaction temperature, reaction time, concentration of solution, etc. are optimized for the deposition of good quality nickel cobalt phosphate thin films. The prepared films are characterized by different techniques as, XRD, FT-IR, XPS, FE-SEM and EDS. By varying nickel and cobalt molar ratio in the synthesis process, different morphologies of nickel cobalt phosphate thin films are achieved.

3.2.A.2 Experimental details

3.2.A.2.1 Substrate

In the development of supercapacitor electrodes, the substrate properties play a key role. The flexibility and mechanical strength of electrode are depended upon the

substrate material. Up to now, various flexible, eco-friendly and cost-effective substrates are used for the fabrication of light weight flexible devices such as metals, carbon foam, sponge, textiles, carbon papers, cables, etc., and they acts as a supporter for the active material [18].

The carbon based substrates offer high surface area and deliver high capacitance but processing methods for material preparation are sluggish and costly, also they have less conductivity. The textiles substrate used for flexible, wearable and bendable device purposes, but they have naturally low capacitance and it is main limitation in the practical application [19]. The carbon papers have high flexibility and low weight but they suffers from low conductivity and surface area. The sponge like substrate restricted in most applications due to its larger volume. The cable type substrates caught huge attraction due to their versatility of shapes, but they limit in practical application because of low energy density and, high processing and preparation cost [18].

Metal based current collectors are investigated mostly for the practical application of the active material due to their high conductivity. The performance of supercapacitor can be enhanced by using a conducting substrate. The metallic substrates like Al, Ti, Cu, Ni foam and stainless steel (SS) are investigated for the preparation of bendable supercapacitor. Among them, the SS substrate is a promising candidate in terms of higher stability and low cost due its natural abundance. Also, the SS substrate is stable in acidic and basic conditions than the other metallic substrates [19]. Moreover, the flexibility and lightweight nature of SS substrate are important factors for the fabrication of flexible supercapacitors. Overall, the SS substrate is preferred as a supporting substrate due to its high conductivity, high flexibility and low cost. Also, the direct growth of material on SS substrate enhances electrochemical performance by avoiding the usage of additives and resistive binders, and eliminate dead volume. The

efficient electrochemical reaction may offer high capacitive performance because of direct electrical contact between active material and substrate.

3.2.A.2.2 Substrate cleaning

The major requirement for thin film deposition is ultraclean substrate. Substrate with an impurity responsible for the uncontrolled growth of material and resulted in the creation of non-uniform thin film. The basic requirement of supercapacitor electrode is a conducting substrate, so low cost and highly conductive SS is used as a substrate. Procedure used for the SS substrate cleaning is as follow,

1. The SS substrate was mirror polished using zero grade polish paper.

2. After polishing, substrate was cleaned with detergent and double distilled water (DDW).

3. Then, ultrasonically cleaned for 15 minutes and dried at room temperature, and further used for the deposition.

3.2.A.2.3 Chemicals

Nickel chloride ($NiCl_2.6H_2O$), cobalt chloride ($CoCl_2.6H_2O$), potassium dihydrogen orthophosphate (KH_2PO_4) and urea (NH_2CONH_2) were purchased from Sigma Aldrich (AR grade) and used as received without any purification.

3.2.A.2.4 Synthesis of nickel cobalt phosphate thin films

In the nickel cobalt phosphate material synthesis nickel chloride, cobalt chloride and potassium dihydrogen orthophosphate were used as a source of nickel, cobalt and phosphate, respectively. For the controlled reaction process, urea is added and it acts as a hydrolyzing agent in the synthesis. Nickel (0.033M), cobalt (0.033M) and phosphate (0.066M) sources were dissolved in 50 ml of double distilled water with hydrolyzing agent (0.075M), sequentially. The above mixture was stirred vigorously up to preparation of homogenous solution then it was used for further nickel cobalt phosphate

thin film preparation. The effect of variation in nickel and cobalt content studied via varying the ratio between them. Herein, the molar ratio of nickel and cobalt varied as 1:0, 0.8:0.2, 0.75:0.25, 0.66:0.34, 0.5:0.5, 0.34:0.66, 0.25:0.75, 0.2:0.8 and 0:1 (Ni:Co), and named as C-NCP1, C-NCP2, C-NCP3, C-NCP4, C-NCP5, C-NCP6, C-NCP7, C-NCP8 and C-NCP9, respectively.
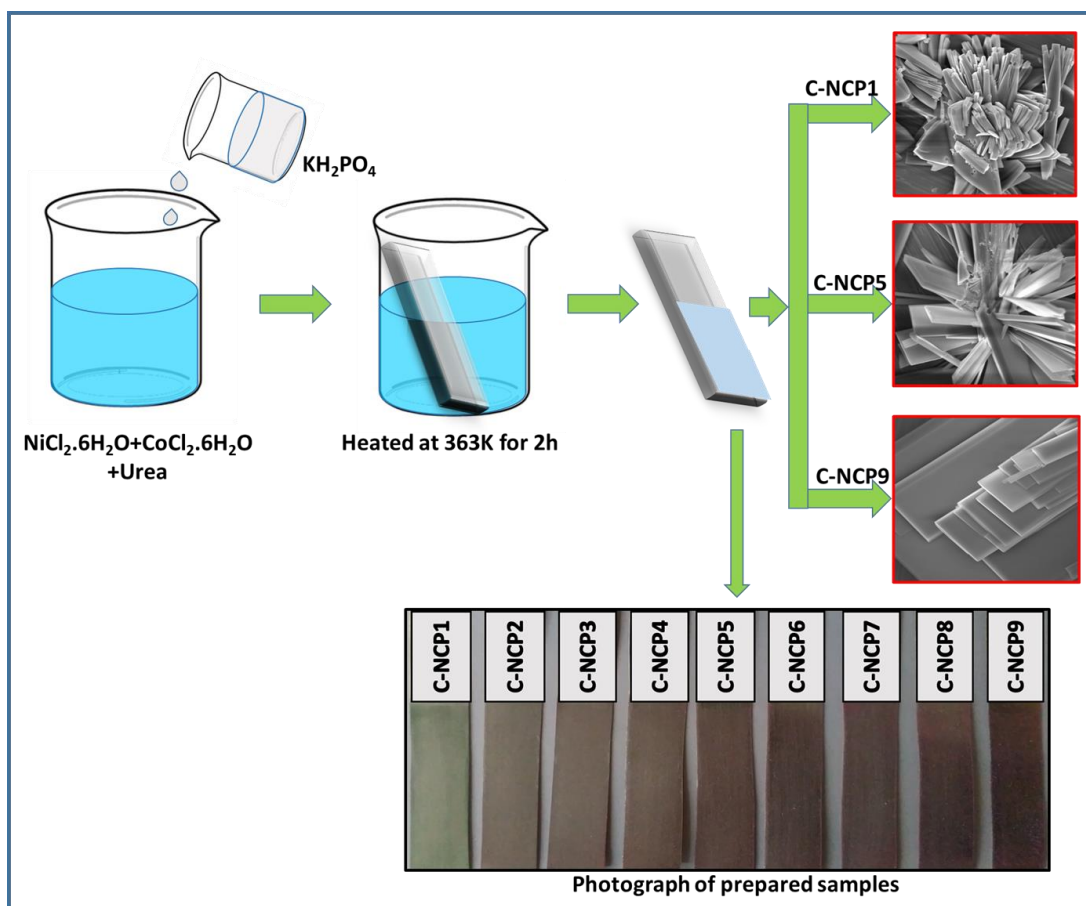
Fig: 3.1 Schematic presentation of nickel cobalt phosphate thin films preparation by CBD method at different nickel and cobalt molar ratio.

In prepared solution baths with different nickel and cobalt molar ratio (mentioned above), well cleaned SS substrates were immersed vertically. After immersing the substrate, the solution baths put into the water bath and kept at a constant 363 K temperature for 2h. The schematic presentation of thin film preparation by CBD method is shown in Fig. 3.1. After continuous 2h heating, the reaction bath was removed from

water bath and substrate with deposited material taken out from solution. The substrates with material rinsed 2-3 times in DDW for removal of residues from the surface. After that, the prepared thin films dried at ambient conditions and used for different characterization.

3.2.A.2.5 Materials characterization

The crystal structure analysis of prepared material was characterized using X-ray diffractometer (XRD) from Rigaku miniflex-600 with Cu Kα (λ=0.15425 nm) radiation. Alpha (II) Bruker unit was used to record Fourier transform-infrared spectrometry (FT-IR) for the detection of functional groups in the prepared material. A Thermoscientific ESCALAB 250 (Thermo Fisher Scientific, UK) instrument was used for X-ray photoelectron spectroscopy (XPS) measurement. Field emission scanning electron microscopy (FE-SEM, JSM-7001 F, JEOL) was used to investigate morphology of material and energy dispersive spectrometer (EDS) for elemental analysis. Electrochemical activities were measured using ZIVE MP1 multichannel electrochemical workstation. All electrochemical analysis of prepared thin film electrodes were measured in three electrode system at ambient conditions. Prepared nickel cobalt phosphate thin films with various Ni:Co molar ratio used as a working electrode, platinum plate and saturated calomel electrode (SCE, with saturated KCl solution) as a counter and reference electrode, respectively. Supercapacitive performance of prepared thin film electrodes was tested using cyclic voltammetry (CV), galvanostatic charge-discharge (GCD) and electrochemical impedance spectroscopy (EIS).

3.2.A.3 Results and discussion

3.2.A.3.1 Film formation and reaction mechanism

The binder-free synthesis process is preferred and used for the synthesis of nickel cobalt phosphate thin films on SS substrate. Basically, there are two types of growth mechanisms in CBD method for the formation of thin film. One is ion-by-ion mechanism where ions are deposited on the surface of substrate at the nucleation sites and then further growth of material takes place. Another mechanism is the formation of nuclei due to adsorption of colloidal particles and growth of thin film followed by aggregation and coalescence, and observed like cluster-by-cluster growth mechanism [20].

To study the effect of combination of two metal species with phosphate, nickel cobalt phosphate thin films with different nickel and cobalt ratio (C-NCP1, C-NCP2, C-NCP3, C-NCP4, C-NCP5, C-NCP6, C-NCP7, C-NCP8 and C-NCP9) are prepared. In the synthesis process, urea is used as a hydrolyzing agent and reaction bath is heated at 363 K temperature for 2h. At 363 K urea decomposes gently and releases CO_2 and NH_3 as the following reaction,

$$NH_2CONH_2 + H_2O \rightarrow 2NH_3 + CO_2\uparrow \qquad (3.1)$$

Furthermore, released ammonia reacts with water as follow,

$$NH_3 + H_2O \rightarrow NH_4OH \qquad (3.2)$$
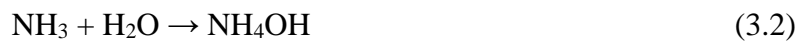
Urea decomposition is responsible for the alkaline pH of solution and such alkaline condition is favorable to form complex with metal ions as [14],

$$NiCl_2.6H_2O + CoCl_2.6H_2O + 2NH_4OH \rightarrow [Ni(NH_3)]^{2+} + [Co(NH_3)]^{2+} + 14H_2O + 4Cl^-$$

$$(3.3)$$
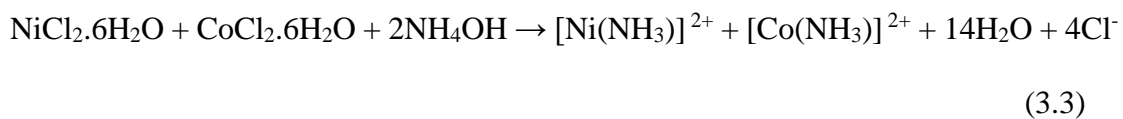
On other hand, phosphate decomposes as follows,

$$KH_2PO_4 \rightarrow K^+ + H_2PO_4^- \qquad (3.4)$$

Moreover, as shown in equation (3.3) the amine complexes of Ni and Co as $[Ni(NH_3)]^{2+}$ and $[Co(NH_3)]^{2+}$ are unstable due to unbalanced ions and react with $H_2PO_4^-$ ions, and finally resulted into the film formation of nickel cobalt phosphate $(Ni_xCo_{(3-x)}(PO_4)_2)$. The possible reaction mechanism is,

$$x[Ni(NH_3)]^{2+} + (3-x)[Co(NH_3)]^{2+} + 2H_2PO_4^- \rightarrow Ni_xCo_{(3-x)}(PO_4)_2 + 3NH_3\uparrow + 2H_2\uparrow$$

$$(3.5)$$
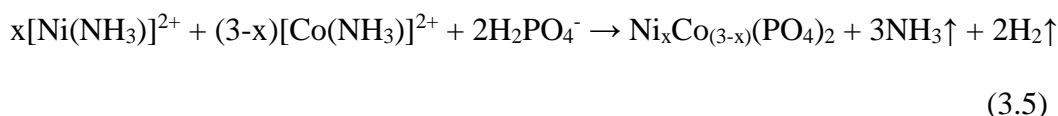
Reaction time (2h) and reaction temperature (363 K) are optimized for the uniform coating of material on SS substrate. Before 2h deposition time, the film was not uniform. However, if deposition time exceeds than 2h, then the film becomes powdery due to overgrowth of material and it leads to peel off from the substrate. In the synthesis process, NH_3 released from urea acts as a complexing agent and controls the release of metal ions. So, released NH_3 controls the rate of reaction and the availability of metal ions for the reaction. The gravimetric weight difference method is used to measure deposited mass of material at different compositions.
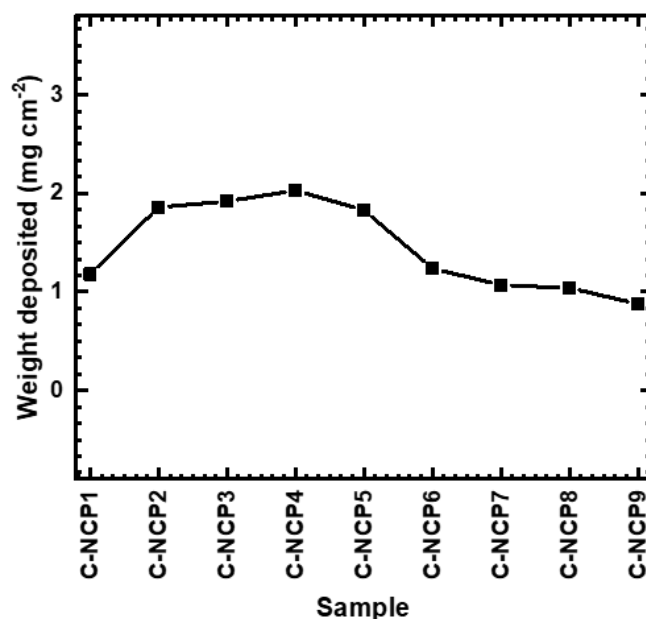
Fig. 3.2 Nickel cobalt phosphate thin film thickness for different compositions (C-NCP1 to C-NCP9) of $NiCl_2.6H_2O:CoCl_2.6H_2O$.

The deposited mass of material increases with increase in cobalt content up to 0.66:0.34 composition (C-NCP1 to C-NCP4, 1.18 to 2.03 mg cm^{-2}) and then it decreases continuously up to 0:1 composition (C-NCP9, 0.88 mg cm^{-2}) as shown in Fig. 3.2. The growth rate of material is quicker due to mixing of transition metals (Ni and Co) and may influence the terminal thickness of thin films [21].

3.2.A.3.2 XRD studies

The XRD analysis was used for the determination of structural phase of the synthesized thin films of nickel cobalt phosphate. The XRD patterns of C-NCP series samples are shown in Fig. 3.3 (a). The XRD pattern of C-NCP1 matches with the JCPDS card no. 33-0951 and confirms the formation of $Ni_3(PO_4)_2.8H_2O$. In C-NCP1 XRD pattern, diffraction peaks at angles of 11.78, 13.8, 18.88, 20.36, 22.6, 23.9, 28.7, 31.02, 34.14, 36.49, 38.11, 39.96 and 56.08⁰ are ascribed to the (110), (020), (200), (011), (130), (101), (031), ($\bar{3}$01), ($\bar{1}$41), (141), (301), ($\bar{1}$12) and (080) crystal planes. Similarly, the XRD pattern of C-NCP9 matches with JCPDS card no. 33-0432 and confirms the formation of $Co_3(PO_4)_2.8H_2O$. In C-NCP9, diffraction peaks at an angle of 10.89, 13.6, 21.66, 33.87, 55.49 and 70.93⁰ corresponds to the (110), (020), (130), ($\bar{3}$21), (501) and (291) crystal planes of cobalt phosphate.

The peaks marked with '*' are corresponds to SS substrate in XRD patterns. The low angle XRD pattern, peak along with the (020) plane of samples is shown in Fig. 3.3 (b). Shifting of peak towards lower diffraction angle is clearly observed in Fig. 3.3 (b) as increase in cobalt content in nickel cobalt phosphate samples. The shift observed due to combination of Ni and Co atoms during the material formation [22]. Since, Co atom has higher atomic radius (2 A⁰) than the Ni atom (1.63 A⁰), the interplanar spacing increases with the addition of Co atoms [23].
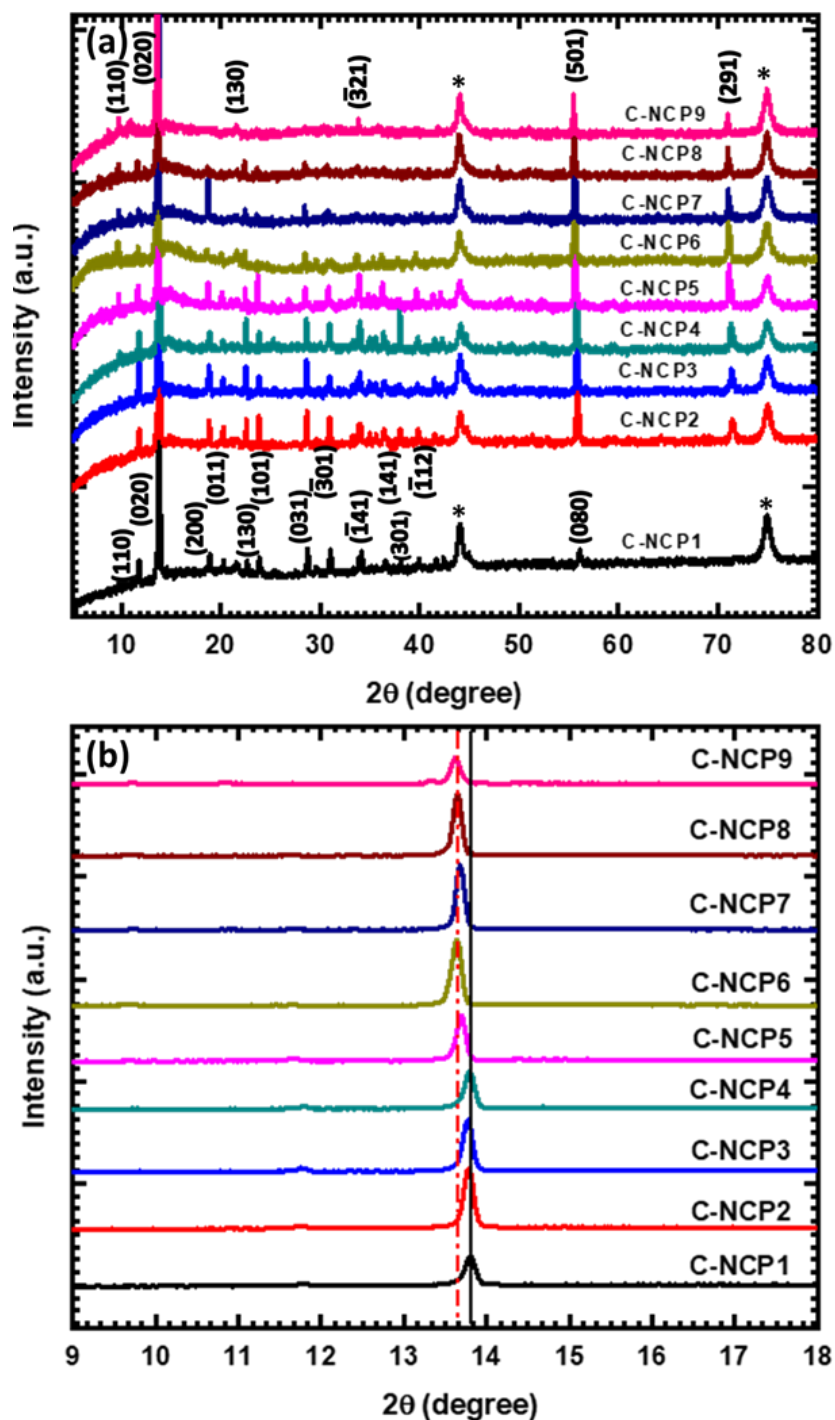
Fig. 3.3 (a) Full scan and (b) low angle XRD patterns of nickel cobalt phosphate thin

films (C-NCP1 to C-NCP9).

The shifting of major peak from the angle of 13.8 to 13.6º with increase in cobalt

content confirm that compositions of C-NCP2, C-NCP3, C-NCP4, C-NCP5, C-NCP6,

C-NCP7 and C-NCP8 are nickel cobalt phosphate. Similar results of peak shifting in

XRD pattern by the addition of atom in the formation of binary material observed by Li. et. al. [24], the XRD peaks of $NH_4CoPO_4.H_2O$ were shifted towards higher diffraction angle with the addition of nickel ($NH_4NiPO_4.H_2O$). In present case, the narrow and intense diffraction peaks demonstrated good crystallinity of nickel cobalt phosphate material which can improve the electrochemical stability of the material in electrochemical testing [25].

3.2.A.3.3 FT-IR studies

The FT-IR analysis of prepared thin films was carried out in the region of 400-4000 cm^{-1} and displayed in Fig. 3.4. The chemical composition and available bonding in electrodes were analyzed by FT-IR analysis. Fig. 3.4 reveals the peak in the range of 571-583 cm^{-1} corresponds to metal-oxygen bonding, peak (γ_1) at 582 cm^{-1} in C-NCP1 reveals Ni-O [26] and peak at 571 cm^{-1} in C-NCP9 reveals Co-O bonding in the prepared thin films [27, 28]. The peak (γ_2) in the range of 706-731 cm^{-1} corresponds to symmetric stretching of P-O-P linkage [29]. The absorption peaks (γ_3, γ_4) in the region of 855-1075 cm^{-1} represent P-O stretching vibrational mode of PO_4^{3-} anions [30-34]. The peaks (γ_5) at 1409 cm^{-1} and (γ_6) in the range of 1594-1649 cm^{-1} corresponds to bending mode of water molecule (H-O-H) [31, 34, 35]. Furthermore, the peaks (γ_7, γ_8) observed in the region of 3067-3459 cm^{-1} represents the content of absorbed water (O-H bonding) in the prepared material [31, 34, 35]. Peaks of samples from C-NCP2 to C-NCP9 show a slight shift as compared to C-NCP1 sample may be due to the coordination interaction between nickel and cobalt linkages in the bimetal sample [36]. Also, the samples show peaks in the similar range confirms a similar chemical bondings are present in the samples. The overall FT-IR result confirms that, phosphate and water content are present in the samples. The above result supports XRD analysis and confirms the formation of hydrous nickel cobalt phosphate material in thin film form.
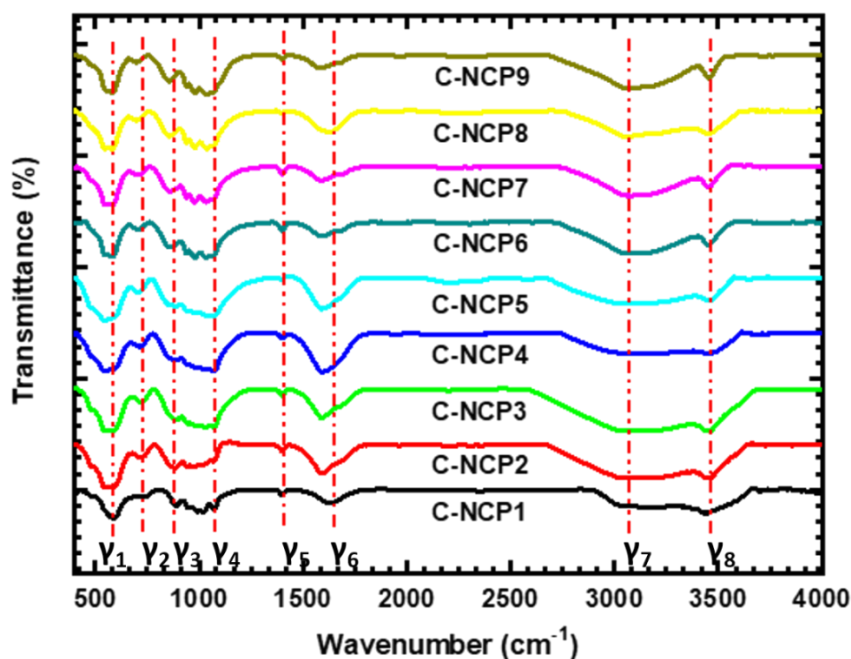
Fig. 3.4 FT-IR spectra of nickel cobalt phosphate thin film samples (C-NCP1 to C-NCP9).

3.2.A.3.4 Surface morphological studies

Herein, FE-SEM is used to observe morphological evolution in nickel cobalt phosphate with nickel and cobalt ratio variation in synthesis process. The expected change in morphology is observed due to nickel and cobalt molar ratio variation and shown in Fig. 3.5. The nickel phosphate material (C-NCP1 sample) shows microflower like structure, that formed by combining willow leafs which have average length of 32 μm. The image shows a compact connection between the willow like leafs (Fig. 3.5 (a)). The willow leaf like structure changes after addition of cobalt content in synthesis in molar ratio (0.8:0.2) of nickel and cobalt (sample C-NCP2). The microflower like structure by combining microsheets observed in Fig. 3.5 (b) and the average length of microsheets is 24 μm. With increase in cobalt content shape of willow like microsheets changes into more rectangular shape and average length of microsheets increases continuously. From the nickel and cobalt molar ratio of 0.75:0.25 to 0.5:0.5 (C-NCP3

to C-NCP5 sample), the material shows microflower like structure with the combining hexagonal and rectangular sheets with the increasing average length from 29 to 49 µm. The increase in sharpness of edge in the structure with increasing cobalt content is found in Fig. 3.5 (c), (d) and (e). Moreover, at 0.34:0.66 molar ratio of nickel and cobalt (C-NCP6 sample), the microsheets fully converted into rectangular sheets (average length of 65 µm) with sharp edges, as displayed in Fig. 3.5 (f). For the samples C-NCP7 and C-NCP8 (with molar ratio of 0.25:0.75 and 0.2:0.8), length of the microsheets continuously increases (from∼71 to∼80 µm) as increase in cobalt content in material (Fig. 3.5 (g) and (h)).
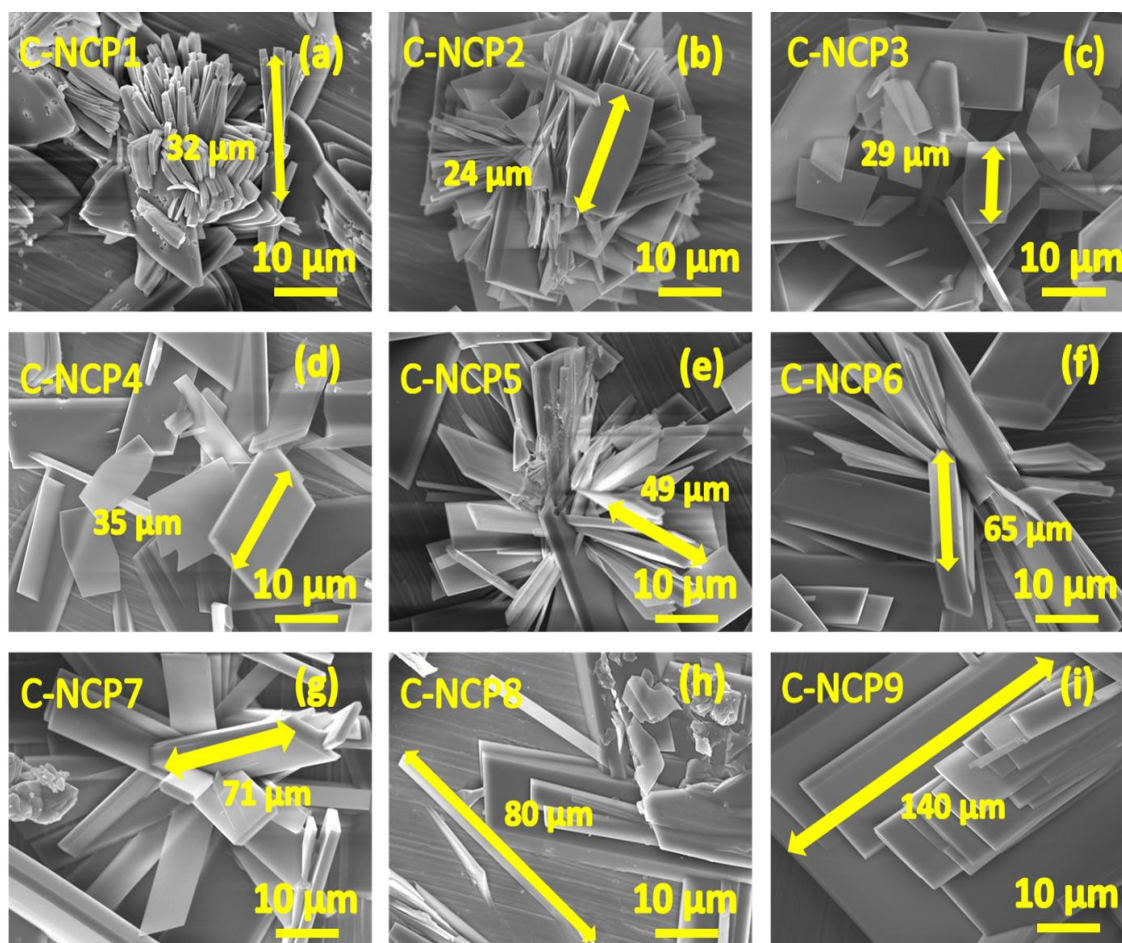
Fig. 3.5 FE-SEM images of sample (a) C-NCP1, (b) C-NCP2, (c) C-NCP3, (d) C-NCP4, (e) C-NCP5, (f) C-NCP6, (g) C-NCP7, (h) C-NCP8 and (i) C-NCP9 at the magnification of X2000.

Total conversion from microflower to rectangular microsheets is observed for sample C-NCP8 in Fig. 3.5 (h). The individual cobalt phosphate sample (C-NCP9) shows perfect rectangular microsheets like structure with few layers stacked on each other (Fig. 3.5 (i)).

In summary it is found that, the length of microsheets increases (from 32 to 140 µm) as increase in cobalt content in the sample and it is attributed to transformation in microstructure from willow leaf like microplates to rectangular microsheets. Such evolution in morphology can be correlated with the XRD results, the oriented growth along (020) leads to two dimensional growth. The reaction rate depends upon available quantities of nickel and cobalt content that alters the morphology from willow leaf to microsheet. It demonstrates that, the molar ratio influences the microstructure (leaf and sheets) and corresponding morphology of the material.

The chemical composition of the samples was investigated by EDS analysis as shown in Fig. 3.6. The C-NCP1 sample shows nickel, phosphorous and oxygen elements, and confirms formation of nickel phosphate. Similarly, the C-NCP9 sample shows cobalt, phosphorous and oxygen elements and confirms formation of cobalt phosphate material. The other samples (C-NCP2 to C-NCP8) show nickel, cobalt, phosphorous and oxygen elements in the EDS spectra, which confirm successful preparation of nickel cobalt phosphate material. Approximately constant phosphorous and oxygen atomic percentage is found in all samples, only difference is observed in the nickel and cobalt atomic ratio and it is quite similar to experimental ratio.
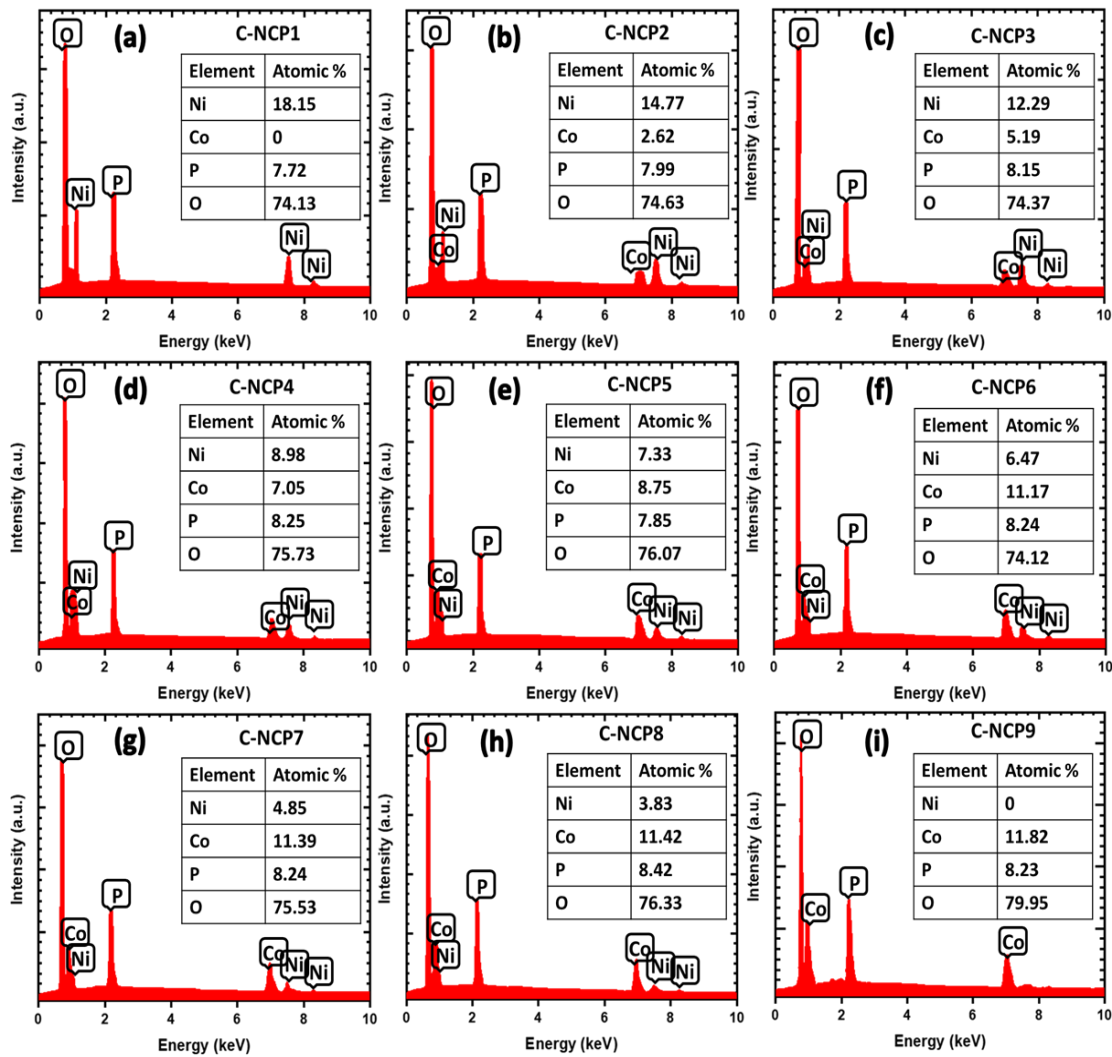
Fig. 3.6 EDS spectra of nickel cobalt phosphate thin film samples (a) C-NCP1, (b) C-NCP2, (c) C-NCP3, (d) C-NCP4, (e) C-NCP5, (f) C-NCP6, (g) C-NCP7, (h) C-NCP8 and (i) C-NCP9.

As observed in table 3.1, the atomic percentage of cobalt in the prepared material increases as per synthesis and atomic percentage of nickel decreases. Also, the observed atomic ratios are very close to the experimental molar ratios of the materials. The EDS result confirms change in molar ratio of nickel and cobalt, and it is responsible for structural and morphological evolution. Also, only nickel, cobalt, phosphorous and oxygen elements are observed in samples confirm the formation of nickel cobalt phosphate material in thin film form.

Sample name	Experimental ratio (Ni:Co)	Observed ratio (Ni:Co)	Obtained phase
C-NCP1	1:0	1:0	$Ni_3(PO_4)_2$
C-NCP2	0.80:0.20	0.85:0.15	$Ni_{2.55}Co_{0.45}(PO_4)_2$
C-NCP3	0.75:0.25	0.70:0.30	$Ni_{2.1}Co_{0.9}(PO_4)_2$
C-NCP4	0.66:0.34	0.56:0.44	$Ni_{1.68}Co_{1.32}(PO_4)_2$
C-NCP5	0.50:0.50	0.46:0.54	$Ni_{1.38}Co_{1.62}(PO_4)_2$
C-NCP6	0.34:0.66	0.37:0.63	$Ni_{1.11}Co_{1.89}(PO_4)_2$
C-NCP7	0.25:0.75	0.30:0.70	$Ni_{0.9}Co_{2.1}(PO_4)_2$
C-NCP8	0.20:0.80	0.25:0.75	$Ni_{0.75}Co_{2.25}(PO_4)_2$
C-NCP9	0:1	0:1	$Co_3(PO_4)_2$

Table 3.1: Experimental and observed nickel and cobalt atomic ratio with obtained

phase of nickel cobalt phosphate thin film samples (C-NCP1 to C-NCP9).

3.2.A.3.5 XPS studies

The valance state and the chemical environment of elements in the material were

investigated by XPS analysis. The survey spectrum of XPS for sample C-NCP5 is

shown in Fig. 3.7 (a), the survey spectrum confirms nickel, cobalt, phosphorous and

oxygen elements are present in the sample. The high resolution spectrum of Ni2p is

shown in Fig. 3.7 (b), intense peaks at the binding energies of 856.7 and 874.5 eV

correspond to Ni2p$_{3/2}$ and Ni2p$_{1/2}$, respectively along with two satellite peaks at 862.1

and 880.2 eV, indicates oxidation state of Ni (Ni^{2+}), which are located at the surface

[37, 38]. Fig. 3.7 (c) shows high resolution XPS spectrum of Co2p region, the peak at

781.8 eV binding energy corresponds to Co2p$_{3/2}$ along with satellite peak at 785.6 eV

binding energy, indicates the +2 valence state of the cobalt. Similarly, the intense peak

at 797.8 eV binding energy signifies Co2p$_{1/2}$ orbits and the satellite peak at 802.9 eV

further proves the same assumption [39]. The high resolution XPS spectrum of P2p

region is shown in Fig. 3.7 (d), only one intense peak is observed at 133.3 eV of binding

energy and represents P-O bonding and pentavalent state of the phosphorous [40].

Furthermore, the O1s region shown in Fig. 3.7 (e) and it is deconvoluted in two peaks.
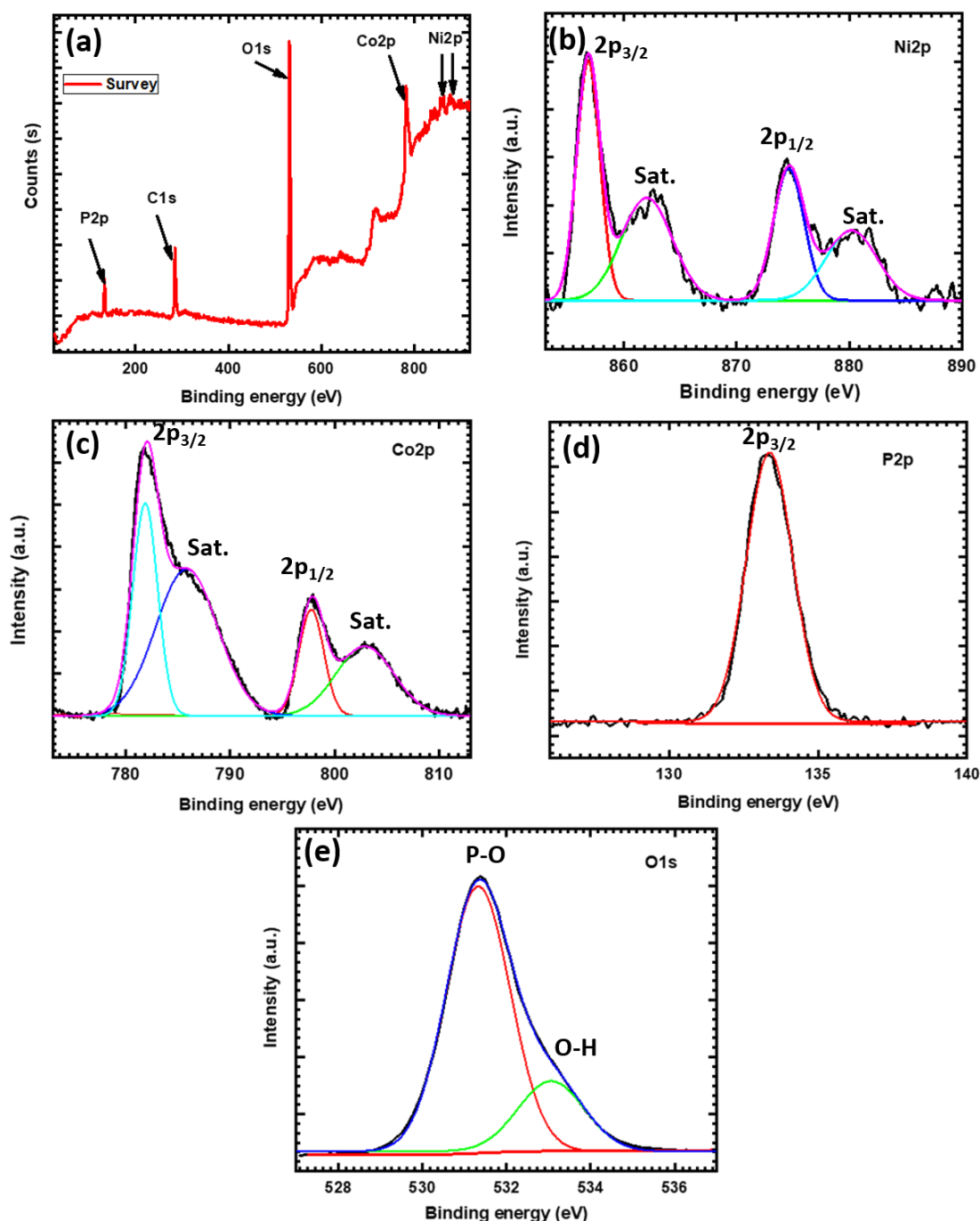
Fig. 3.7 (a) Survey, (b) Ni2p, (c) Co2p, (d) P2p and (e) O1s XPS spectrum of sample

C-NCP5.

First peak at 531.3 eV and second at 533.1 eV binding energies correspond to core level

of oxygen in phosphate species and adsorbed water in the material, respectively [40-

43]. Therefore, XPS spectrum confirms the successful preparation of nickel cobalt phosphate material on SS substrate by simple CBD method.

3.2.A.4 Conclusions

In conclusion, nickel cobalt phosphate thin films on stainless steel substrate are successfully prepared by a simple chemical bath deposition method. XRD analysis confirms the successful formation of nickel cobalt phosphate material in thin film form. FT-IR, EDS and XPS result confirms formation of nickel cobalt phosphate ($Ni_xCo_{(3-x)}(PO_4)_2$) material by observing metal phosphate content and their corresponding bonds in the prepared samples. Also, the composition variation (molar ratio of nickel and cobalt species) influences the reaction kinetics, and that ultimately alters the morphology (microflower to microsheet) of thin films. The above results complement each other and confirms the successful preparation of hydrous nickel cobalt phosphate material in thin film form.

SECTION – B

SUPERCAPACITIVE PERFORMANCE EVALUATION OF NICKEL COBALT PHOSPHATE THIN FILMS

3.2.B.1 Introduction

Some research groups reported the morphology of single metal compounds (like NiS, $Ni(OH)_2$) is altered when a another metal compound added and such morphologically tuned binary metal compounds (like NiCoS, $NiCo(OH)_2$) shows a high electrochemical performance than the single metal compound due to synergistic effect. A similar strategy is applied for the preparation of binary metal phosphate for the improvement in supercapacitive performance. Chen et. al. [9] synthesized microplates of $Co_{0.4}Ni_{1.6}P_2O_7$ by hydrothermal method and it delivered high capacitance of 1259 F g^{-1} at 1.5 A g^{-1} with 88.9 % capacitive retention after 1000 cycles than the $Co_2P_2O_7$ (358

F g^{-1}) and Ni$_2$P$_2$O$_7$ (945 F g^{-1}). Li. et. al. [15] prepared nanosheets of NiCoPO$_4$ by hydrothermal method and achieved high capacitance of 1132.5 F g^{-1} at 1 A g^{-1} with 93 % capacitive retention after 8000 cycles than the Co$_3$(PO$_4$)$_2$ (417 F g^{-1}). Tang et. al. [16] prepared nanospheres of Co$_{0.86}$Ni$_{2.14}$(PO$_4$)$_2$ by hydrothermal method and exhibited high capacitance of 1409 F g^{-1} at 0.25 A g^{-1} than the Co$_3$(PO$_4$)$_2$ (247.7 F g^{-1}) and Ni$_3$(PO$_4$)$_2$ (1149.2 F g^{-1}). Zhang et. al. [17] developed hollow shells of NiCo$_2$(PO$_4$)$_2$ by microwave assisted method and obtained high capacitance of 940.43 F g^{-1} at 1 A g^{-1} with 84.5 % capacitive retention after 1000 cycles than the Co$_3$(PO$_4$)$_2$ (239.31 F g^{-1}). A similar insights are considered in this study for preparation of nickel cobalt phosphate thin film electrodes.

In this section, the electrochemical performance of chemically deposited nickel cobalt phosphate thin films (C-NCP1 to C-NCP9) in 1 M KOH electrolyte is studied. The effect of scan rate and current density on electrochemical performance of nickel cobalt phosphate thin film electrodes (C-NCP1 to C-NCP9) is studied.

3.2.B.2 Experimental setup for electrochemical performance measurements

The conventional three electrode system is used for the electrochemical measurements of nickel cobalt phosphate thin film electrodes in 1 M KOH electrolyte solution. For the three electrode system, nickel cobalt phosphate thin films used as a working electrode, platinum plate as a counter electrode and saturated calomel electrode (SCE) as a reference electrode. The 1 cm^2 area of working electrode was immersed in the electrolyte for accurate electrochemical measurement. The setup of the experiment for the electrochemical performance evaluation is shown in Fig. 3.8. The electrochemical studies are carried out using the ZIVE MP1 workstation.

The CV considered a good technique for the measurement of redox potentials and involved electron-transfer redox reactions. The specific capacitance (C_s) is calculated from CV curves using equation 2.17.
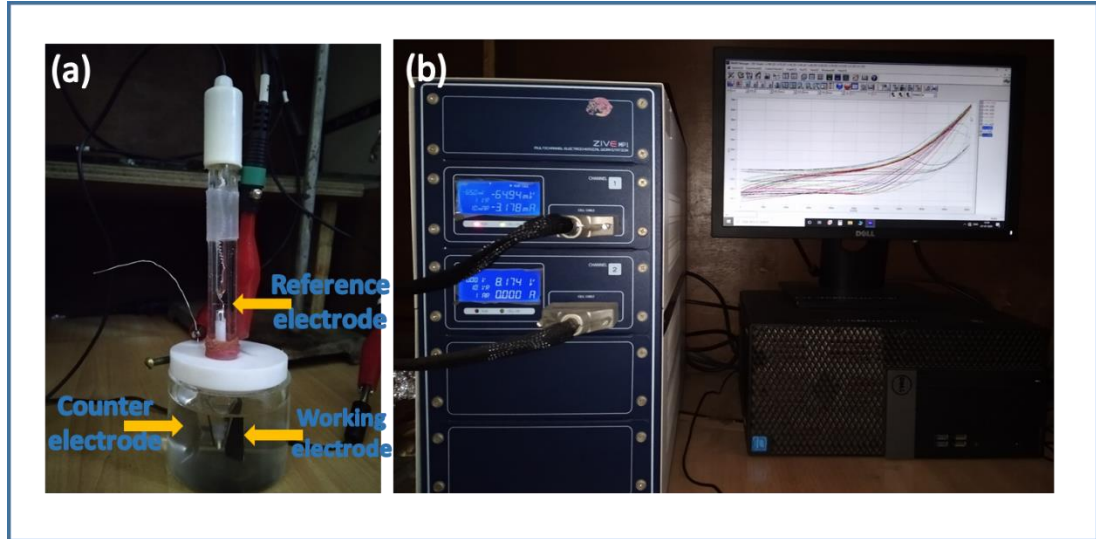
Fig. 3.8 Photograph of (a) three electrode system and (b) experiment setup consist of battery cycler with CV graphs on monitor.

The GCD technique is employed to estimate the rate capability of electrode material in terms of specific capacitance, specific energy and power density of the electrode. Also, the capacitive behavior of the electrode material is determined from the nature of GCD curves.

The C_s of electrode material is calculated using following equation,

$$C_S = \frac{I \times t_d}{\Delta V \times m} \tag{3.6}$$

where, I, t_d, m and ΔV are the current density, discharging time, deposited mass and potential window, respectively. The specific energy density (ED) and power density (PD) are calculated from the discharging curve according to equation 2.18 and 2.19, respectively.

3.2.B.3 Results and discussion

3.2.B.3.1 Cyclic voltammetry (CV) studies

The morphology altered due to molar ratio variation of nickel and cobalt in nickel cobalt phosphate material and its influence on supercapacitive performance was investigated in electrochemical cell of three electrode system. Fig. 3.9 shows CV curves of C-NCP series electrodes in the optimized potential window of 0 to 0.5 V (vs SCE). The comparative CV curves of some electrodes (C-NCP1, C-NCP3, C-NCP5, C-NCP7 and C-NCP9) at 20 mV s^{-1} scan rate are displayed in Fig. 3.9 (a). The area under CV curve of electrode C-NCP5 is higher than the nickel phosphate (C-NCP1), cobalt phosphate (C-NCP9) and other nickel cobalt phosphate electrodes. Combined microstructure of microflower with microsheets show higher area under the curve than single microflower and microsheets like structure due to large number of electrochemical active cites. The intercalation of OH$^-$ ions from the electrolyte to the surface of nickel cobalt phosphate material takes place at the time of charging and deintercalate during discharging. This can be explained by the following reaction mechanism [9, 16]

$$Ni_xCo_{3-x}(PO_4)_2 + OH^- \leftrightarrow Ni_xCo_{3-x}(OH)*(PO_4)_2 + e^- \tag{3.7}$$

CV curves of C-NCP series electrodes at various scan rates from 1-20 mV s^{-1} are shown in Fig. 3.9 (b-j). The nickel phosphate electrode (C-NCP1) shows well established redox peaks (Fig. 3.9 (b)) and that confirm pseudocapacitive nature of material. On the other hand, cobalt phosphate electrode (Fig. 3.9 (j)) shows the CV nature quite different than the nickel phosphate electrode. Increasing cobalt content influences the morphology that ultimately affect on the electrochemical performance. The shifting of CV nature from nickel phosphate to cobalt phosphate electrode (C-NCP1 to C-NCP9) is very clearly observed in the Fig. 3.9 from (b) to (j). Area under the curve increases

for every sample as increasing scan rates from 1-20 mV s^{-1}, shows that the voltammetric

currents are directly proportional to the scan rate. At the higher scan rate, only the outer

surface of material is used for the storage of electrolytic ions, but at lower scan rate,

due to the availability of more time for the diffusion process it goes in inner surface of

the material which increases the utilization of electrode material.
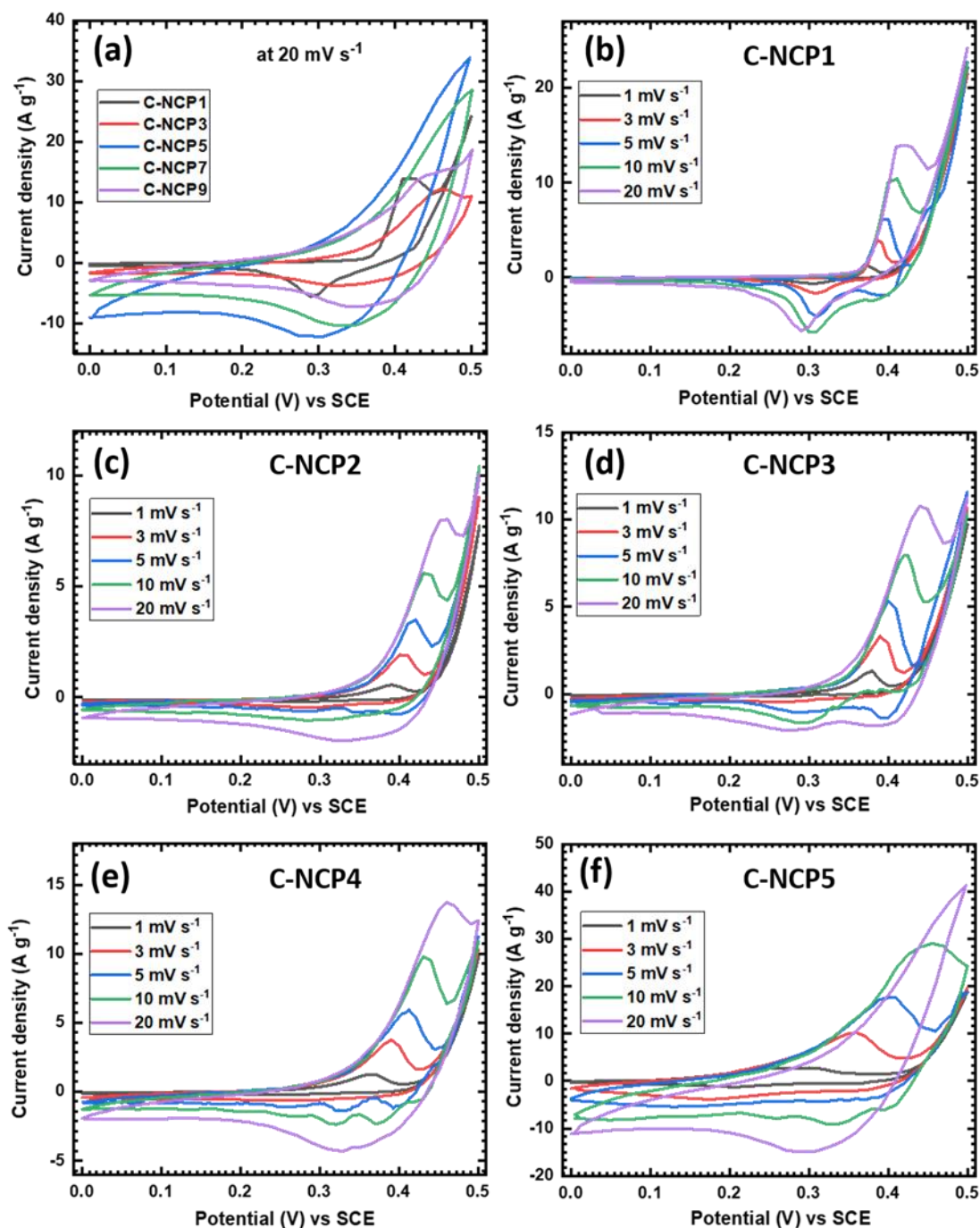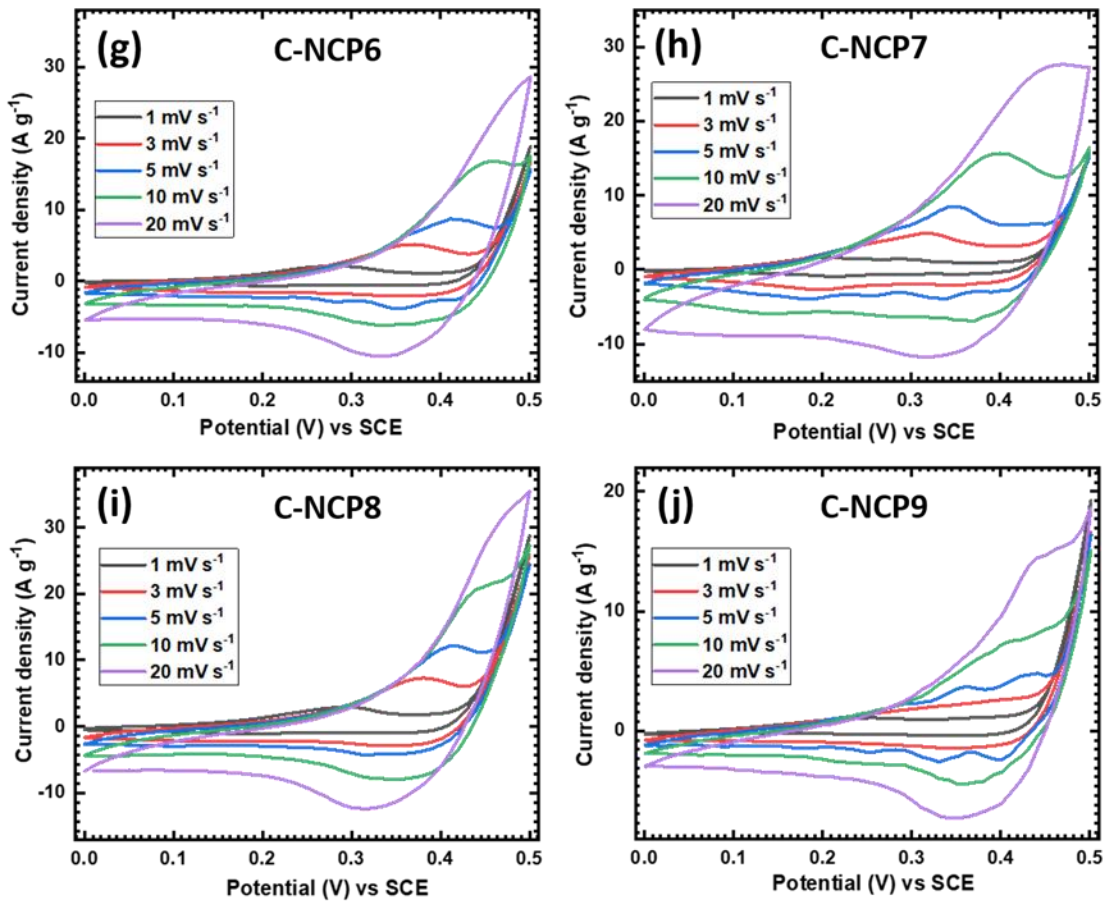
Fig. 3.9 (a) Comparative CV curves at 20 mV s^{-1} scan rate, CV curves at various scan

rates from 1-20 mV s^{-1} of (b) C-NCP1, (c) C-NCP2, (d) C-NCP3, (e) C-NCP4, (f) C-

NCP5, (g) C-NCP6, (h) C-NCP7, (i) C-NCP8 and (j) C-NCP9 electrode.

Capacitive and intercalation processes are contributed in total charge storage of

electrode. According to Power's law, CV current is dependent on scan rate and can be

expressed as follows,

$$i_p(v) = a v^b \qquad (3.8)$$

where, i_p, v, a and b are represent the peak current, scan rate and adjustable parameters.

The slope of log (i) vs log (v) represents the b value. For C-NCP series electrode, graph

of log (i) vs log (v) plotted in Fig. 3.10 and calculated their b values. The basic criteria

for the b value is, when it is 0.5 then the electrochemical process is diffusive and it is 1

then the electrochemical process is capacitive [44]. The prepared electrodes C-NCP1,

C-NCP2, C-NCP3, C-NCP4, C-NCP5, C-NCP6, C-NCP7, C-NCP8 and C-NCP9 exhibits b values of 0.79, 0.70, 0.89, 0.81, 0.88, 0.88, 0.83, 0.84 and 0.86, respectively. The values of b for C-NCP series electrodes ranging from 0.5 to 1 that demonstrate the capacitive and diffusive both type of processes contributed in charge storage mechanism.
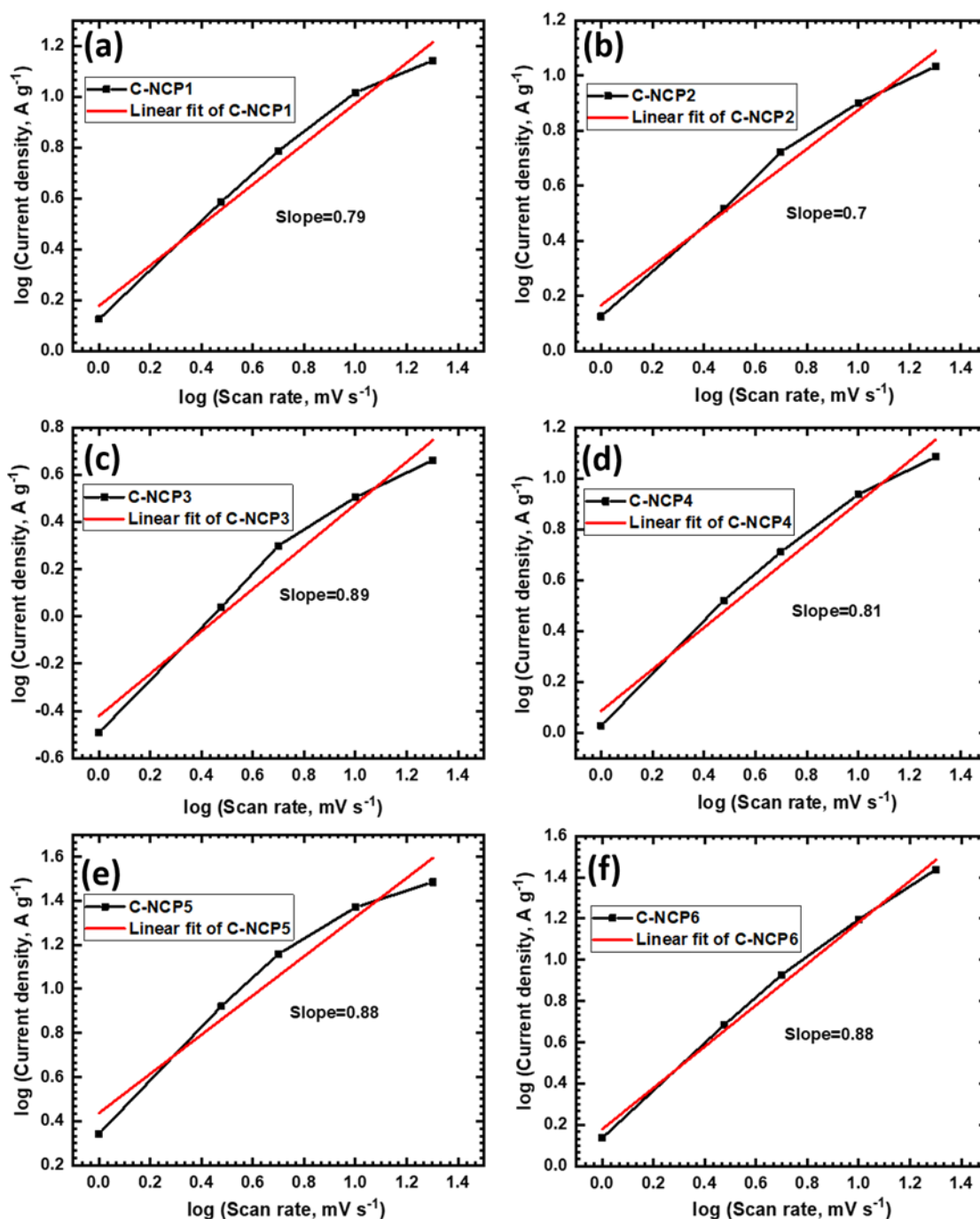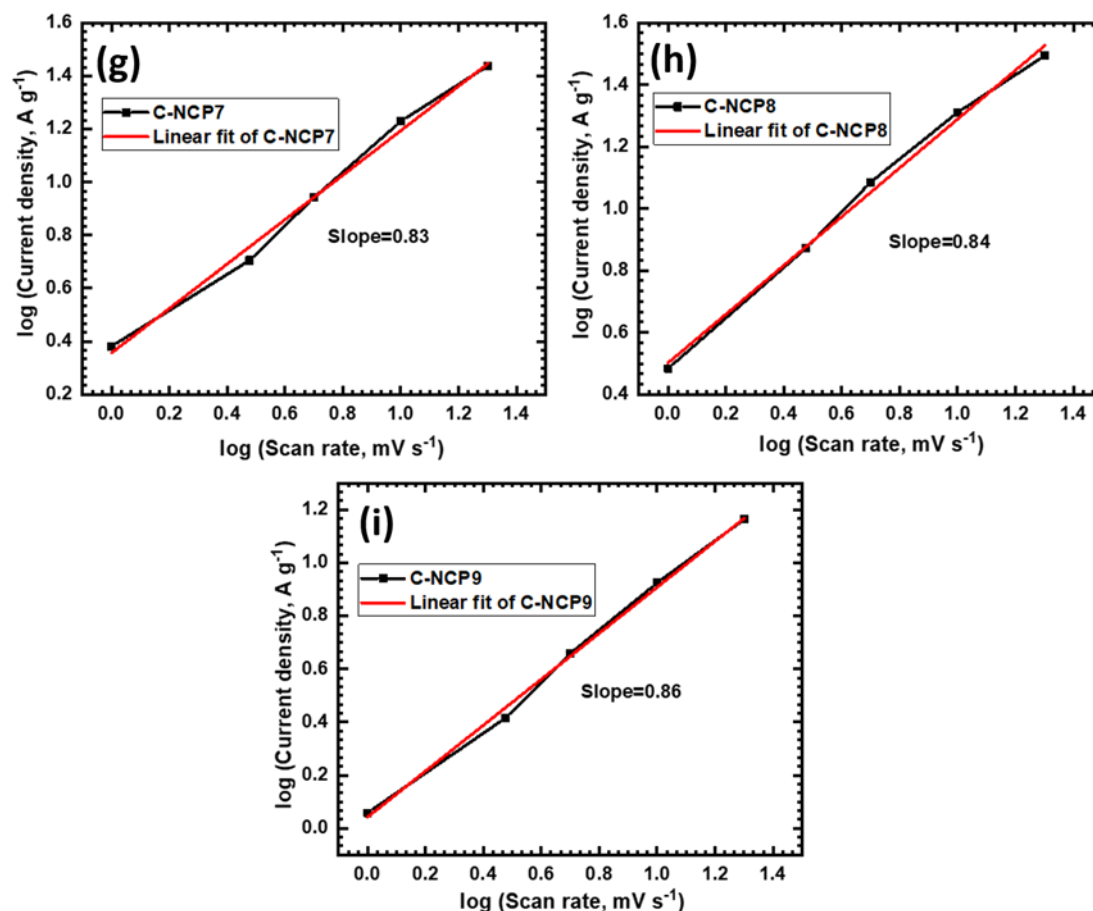
Fig. 3.10 Plot of log (current density, A g^{-1}) versus log (scan rate, mV s^{-1}) for electrode (a) C-NCP1, (b) C-NCP2, (c) C-NCP3, (d) C-NCP4, (e) C-NCP5, (f) C-NCP6, (g) C-NCP7, (h) C-NCP8 and (i) C-NCP9.

The modified Power's law used for the calculation of respective current contribution from the battery like bulk and pseudocapacitive process as given below [45-47],

$$I_p = I_{surface} + I_{bulk} = C_{surface}v + C_{bulk}v^{1/2} \qquad (3.9)$$

Where, I_p, v, $C_{surface}v$ and $C_{bulk}v^{1/2}$ represents the peak current density, scan rate, surface pseudocapacitive process ($I_{surface}$) current contribution and bulk process (I_{bulk}) current contribution, respectively. Current contributions from pseudocapacitive and bulk process for prepared electrodes are calculated from above equation and plotted in Fig. 3.11.

It observed that, the contribution from pseudocapacitive surface process increases with increasing scan rate, which concluded that, diffusive process is dominant at low scan rate and capacitive process dominant at high scan rate. So, the active material shows battery like nature at low scan rate and more capacitive nature at high scan rates. The C-NCP9 electrode (cobalt phosphate) shows highest capacitive contribution (~ 84 %) than the other samples.
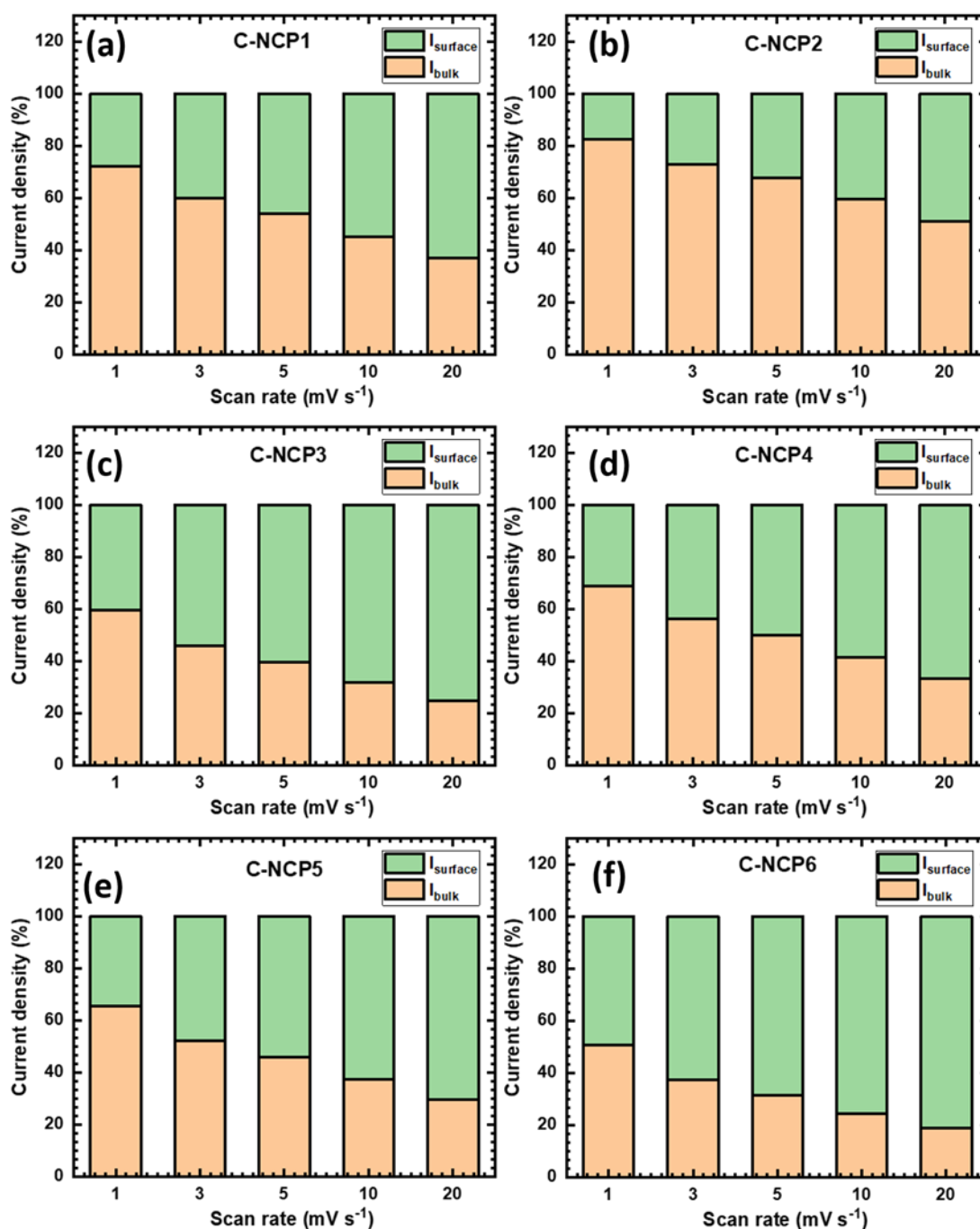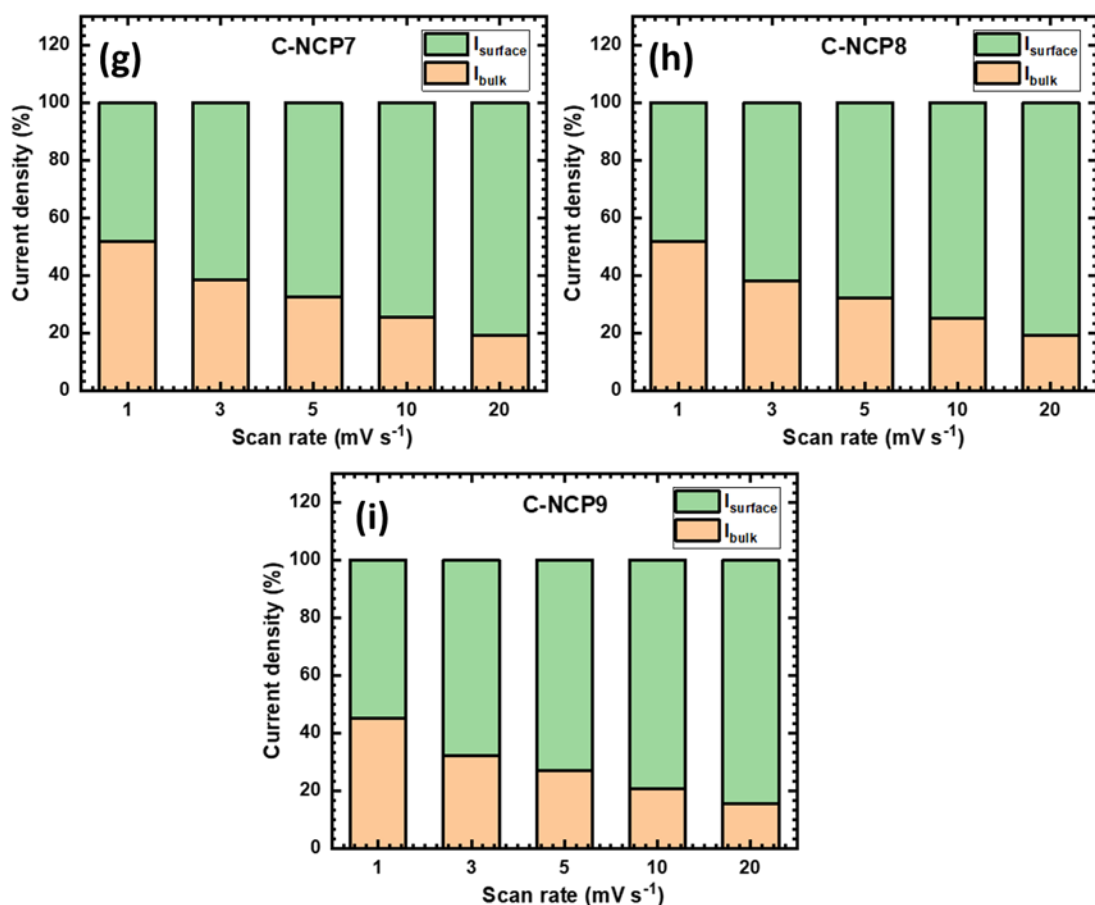
Fig. 3.11 Graphs of calculated contribution of pseudocapacitive (surface current) and

battery type (bulk current) current density at various scan rates (1 to 20 mV s^{-1}) of

electrode (a) C-NCP1, (b) C-NCP2, (c) C-NCP3, (d) C-NCP4, (e) C-NCP5, (f) C-

NCP6, (g) C-NCP7, (h) C-NCP8 and (i) C-NCP9.

Conversely, the nickel phosphate electrode (C-NCP1) shows ̴63 % capacitive current

contribution in total current. The C-NCP5 electrode shows moderate capacitive current

contribution of ̴70 % and other sample shows different values of current contribution

may be due to different morphology and chemical composition (nickel and cobalt).

3.2.B.3.2 Galvanostatic charge-discharge (GCD) studies

The GCD measurement is very significant method for calculating the specific

capacitance of supercapacitor electrodes at different current densities. The GCD curves

of C-NCP series electrodes at different current densities in the optimized potential

window of 0 to 0.4 V (vs SCE) are shown in Fig. 3.12. Comparative GCD curves of C-NCP series electrodes at 0.5 A g^{-1} current density are shown in Fig. 3.12 (a). As like the nature of CV curve, nickel phosphate (C-NCP1) and cobalt phosphate (C-NCP9) electrodes shows different nature of charge-discharge curve, and change in nature of GCD curves observed from nickel phosphate to cobalt phosphate electrode as shown in Fig. 3.12 (b-j).
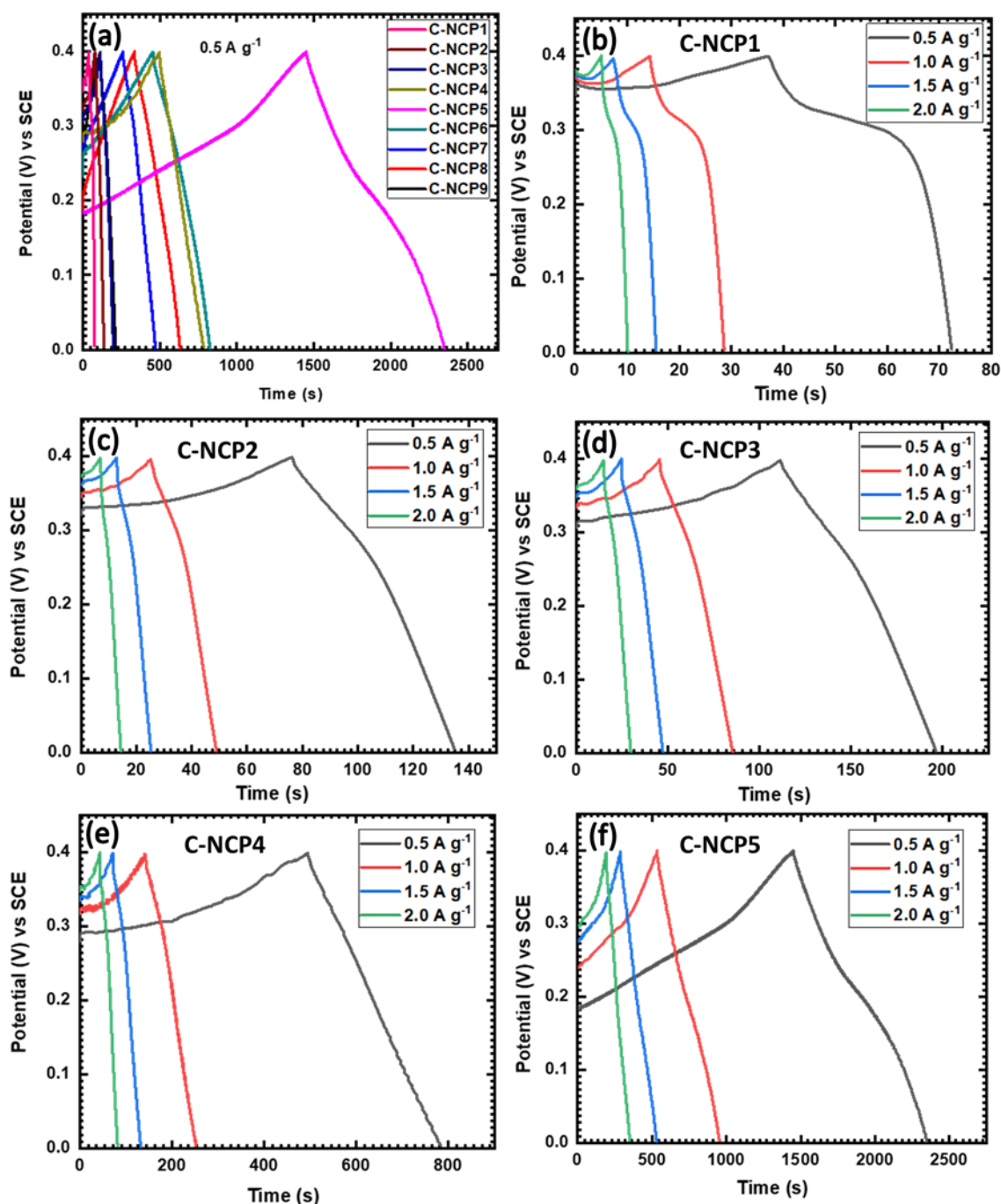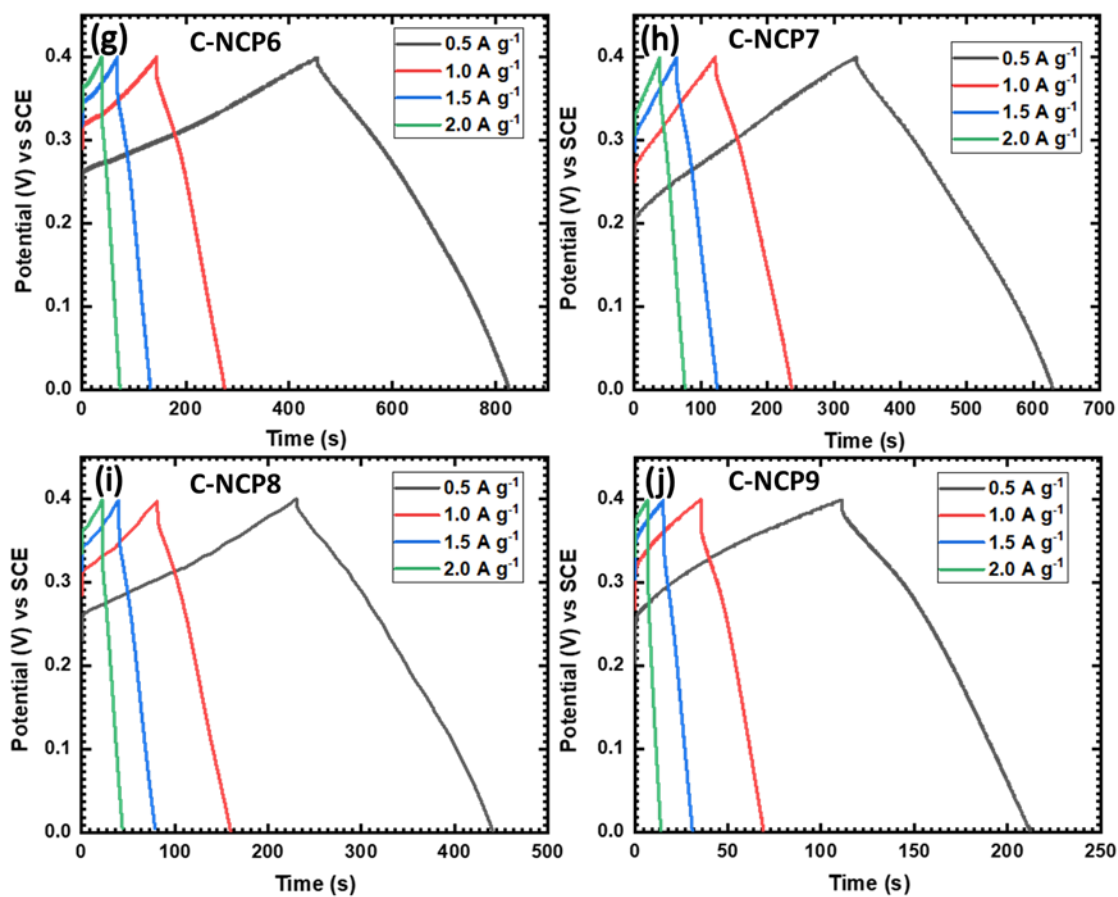
Fig. 3.12 (a) Comparative GCD curves of C-NCP series electrodes at 0.5 A g^{-1} current density, GCD curves at various current densities from 0.5-2.0 A g^{-1} of (b) C-NCP1, (c) C-NCP2, (d) C-NCP3, (e) C-NCP4, (f) C-NCP5, (g) C-NCP6, (h) C-NCP7, (i) C-NCP8 and (j) C-NCP9 electrode.

The non-linear curve during discharge obtained due to deep ion intercalation and redox reaction, indicates pseudocapacitive behavior of the material [48-50]. In consistent with CV analysis, the C-NCP5 electrode shows higher discharging time as compared to other compositions and it demonstrates material with optimum composition of nickel and cobalt shows superior electrochemical performance.

The specific capacitance from the GCD plots are calculated for C-NCP series electrodes using the equation 3.6 and plotted in Fig. 3.13. The C-NCP5 electrode with high discharging time and optimum active material shows higher specific capacitance

than other electrodes. The C-NCP5 electrode shows maximum specific capacitance of 1116 F g^{-1} at 0.5 A g^{-1} current density and it decreases up to 806 F g^{-1} at 2 A g^{-1} current density. Similarly, the C-NCP1, C-NCP2, C-NCP3, C-NCP4, C-NCP6, C-NCP7, C-NCP8 and C-NCP9 thin film electrodes show maximum specific capacitance of 44, 73, 103, 360, 462, 366, 262 and 126 F g^{-1}, respectively at 0.5 A g^{-1} current density. It is observed that, at high current density specific capacitance value decreases due to fast charging-discharging rate. On the other hand, at lower current density maximum utilization of active material is possible due to more penetration time for electrolyte ions in the interior surface of the material which contributes in the high capacitance [51]. The microstructure of C-NCP5 electrode (a microflowers consisting of rectangular microsheets) with optimum size is good for the easy accessibility of electrolyte ions, which offer high electrochemical active area and result in higher capacitive performance.
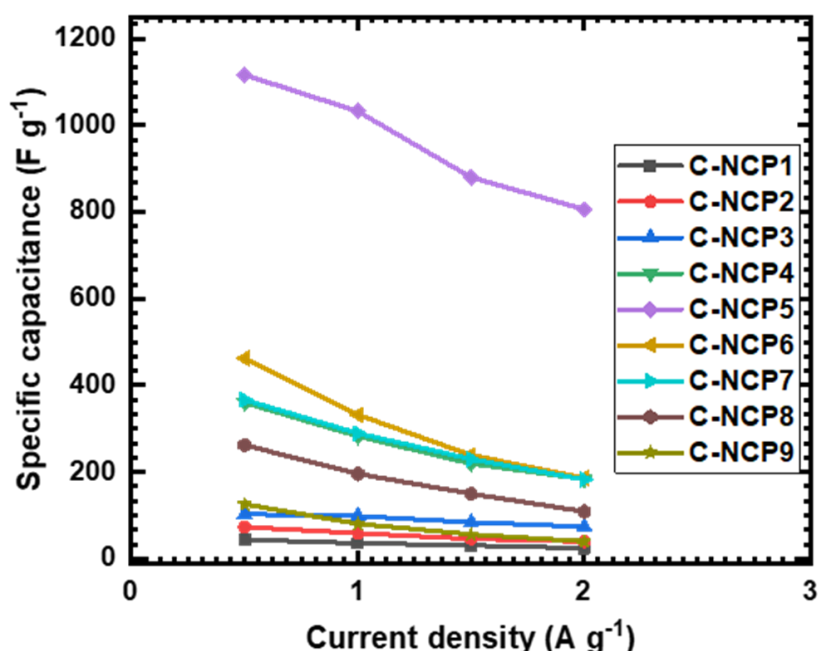
Fig. 3.13 The plots of specific capacitance at various current densities of nickel cobalt phosphate electrodes (C-NCP1 to C-NCP9).

3.2.B.3.3 Stability studies

The stability (in terms of capacitive retention) was investigated for best performing nickel cobalt phosphate (C-NCP5) electrode. The electrochemical stability of C-NCP5 electrode tested for 3000 GCD cycles at 6 A g^{-1} current density and shown in Fig. 3.14.
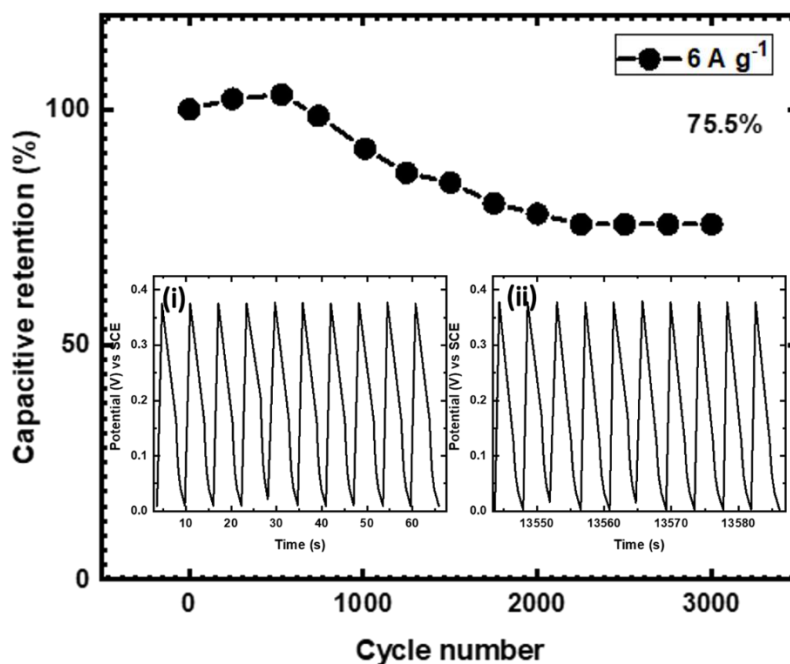
Fig. 3.14 The plot of capacitive retention of C-NCP5 electrode at 6 A g^{-1} current

density for 3000 cycles (inset: GCD curves of (i) initial and (ii) final 10 cycles).

The C-NCP5 electrode exhibits 75.5 % capacitive retention after 3000 cycles. The GCD curves of initial 10 cycles and final 10 cycles are shown in inset of Fig. 3.14 as (i) and (ii), respectively. The decrement in charge-discharge time is observed in initial and final GCD cycles (inset Fig. 3.14). The little increment in specific capacitance is observed in initial cycles due to volume expansion of active material by insertion and extraction of ions [52]. Then decrement in capacitance is detected may be due to depletion of minute active material during cycling.

3.2.B.3.4 EIS studies

The electrochemical impedance and ion transfer features of thin film electrodes are investigated with the help of EIS study. The EIS study was carried out in the range of 10mHz to 1MHz with an ac amplitude of 10 mV at open circuit potential. The Nyquist plots of C-NCP series electrodes are displayed in Fig. 3.15 (a). In Nyquist plot, semicircle appears in high frequency region and straight line in low frequency region. The semicircle in the high frequency region represents the charge transfer resistance arises due to faradaic reactions and double-layer capacitance at the interface of electrode/electrolyte. The electrolytic ion diffusion in the active material is responsible for the straight line in the low frequency region and it corresponds to Warburg impedance. The solution resistance (R_s) obtained by pointing the intersection of Nyquist plot to real axis, which is combination of electrolyte resistance and contact resistance at the interface between electrode and electrolyte. Diameter of semicircle at high-frequency region gives the charge transfer resistance (R_{ct}) value and it is related to the faradaic leakage current [53].
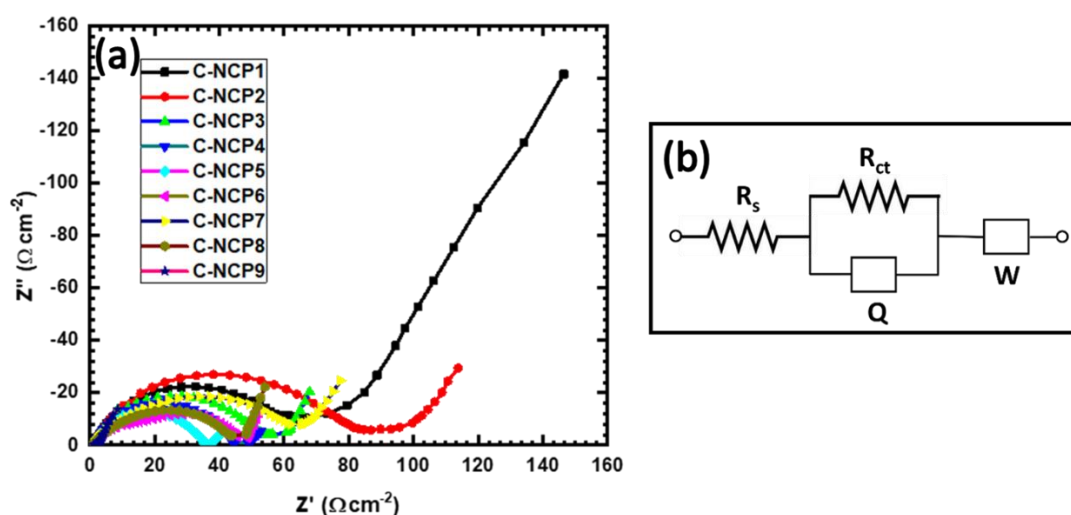
Fig. 3.15 (a) The Nyquist plots of C-NCP series electrodes (C-NCP1 to C-NCP9) and (b) the fitted equivalent circuit for the EIS data.

The C-NCP series electrodes show solution resistance (R_s) in between 1.03 and 1.4 Ω, such smaller value show feasible interaction between electrolyte and active material. The cobalt phosphate electrode (C-NCP9) show very low charge transfer resistance of 1.48 Ω and nickel phosphate (C-NCP1) show high charge transfer resistance value of 69.1 Ω. The high performing C-NCP5 electrode shows lower charge transfer resistance (34.94 Ω) than other electrodes (except C-NCP9). The microflowers with rectangular microsheets like structure (C-NCP5 electrode) provides pathways for easy charge transfer. The sheet like microstructure of C-NCP series electrodes with tunnels and open channel crystal structure offers easy penetration to ions in the inner surface of microstructure which are responsible for maximum usage of active material and increases electrochemical performance and supports the results obtained from CV and GCD studies.

The fitted equivalent circuit for the EIS data of C-NCP series electrodes is shown in Fig. 3.15 (b). The circuit consist of R_s, R_{ct}, W and Q are the solution resistance, charge transfer resistance, Warburg impedance and constant phase element, respectively. The Q obtained due to inhomogeneities present at electrode/electrolyte interface, porosity, nature of electrode and disorder associated with diffusion, and when n=1 then Q=C [54-56]. The values of each fitted circuit parameter is tabulated in table 3.2. The best performing C-NCP5 electrode show fitted values of R_s, R_{ct}, W and Q are 1.1 Ω, 34.9 Ω, 0.5 Ω and 0.35 mF, respectively.

Sample Name	R_s (Ω)	R_{ct} (Ω)	Q (mF)	n	W (Ω)
C-NCP1	1.03	69.1	0.610	0.781	0.031
C-NCP2	1.4	85.3	0.479	0.703	0.250
C-NCP3	1.3	52.2	0.692	0.796	0.267
C-NCP4	1.3	43.2	0.082	0.801	0.503
C-NCP5	1.1	34.9	0.355	0.804	0.527
C-NCP6	1.3	45.2	1.039	0.940	0.411
C-NCP7	1.2	63.3	2.249	0.786	0.264
C-NCP8	1.2	43.6	1.584	0.885	0.504
C-NCP9	1.2	1.5	0.080	0.863	0.850

Table 3.2: Electrochemical impedance spectroscopic fitted circuit parameters for Nyquist plots of C-NCP series electrodes.

3.2.B.4 Conclusions

Different morphology exhibited different electrochemical performance, the microflowers containing rectangular microsheets show high supercapacitive performance than the individual microflower and microsheet like structure. The $Ni_{1.38}Co_{1.62}(PO_4)_2$ electrode (C-NCP5) with microflowers containing rectangular microsheets like structure exhibits high specific capacitance of 1116 F g^{-1} at 0.5 A g^{-1} current density and offered 75 % capacitive retention over 3000 cycles. The good electrochemical results suggest that, $Ni_{1.38}Co_{1.62}(PO_4)_2$ thin film can be used as a cathode material in asymmetric supercapacitor devices.

3.3 References

1. S. Kim, S. Kim, K. Jung, J. Kim, J. Jang, Nano Energy, 24 (2016) 17-24.
2. A. Bello, K. Makgopa, M. Fabiane, D. Dodoo-Ahrin, K. Ozoemena, N. Manyala, J. Mater. Sci., 48 (2013) 6707-6712.
3. U. Patil, S. Kulkarni, V. Jamadade, C. Lokhande, J. Alloys Compd., 509 (2011) 1677-1682.
4. X. Han, K. Tao, Q. Ma, L. Han, J. Mater. Sci. Mater. Electron., 29 (2018) 14697-14704.

5.   U. Patil, K. Gurav, J. Kim, C. Lokhande, S. Jun, Bull. Mater. Sci., 37 (2014) 27-33.

6.   X. Yu, L. Yu, H. Wu, X. Lou, Angew. Chem. Int. Ed., 54 (2015) 5331-5335.

7.   F. Shi, L. Li, X. Wang, C. Gu, J. Tu, RSC Adv., 4 (2014) 41910-41921.

8.   G. Snook, P. Kao, A. Best, J. Power Sources, 196 (2011) 1-12.

9.   C. Chen, N. Zhang, Y. He, B. Liang, R. Ma, X. Liu, ACS Appl. Mater. Interfaces, 8 (2016) 23114-23121.

10.   X. Li, A. Elshahawy, C. Guan, J. Wang, Small, 13 (2017) 1701530-1701554.

11.   L. Tao, J. Li, Q. Zhou, H. Zhu, G. Hu, J. Huang, J. Alloys Compd., 767 (2018) 789-796.

12.   C. Yuan, H. Wu, Y. Xie, X. Lou, Angew Chem. Int. Ed., 53 (2014) 1488-1504.

13.   F. Yang, J. Yao, F. Liu, H. He, M. Zhou, P. Xiao, Y. Zhang, J. Mater. Chem. A, 1 (2013) 594-601.

14.   U. Patil, J. Sohn, S. Kulkarni, S. Lee, H. Park, K. Gurav, S. Jun, ACS Appl. Mater. Interfaces, 6 (2014) 2450-2458.

15.   B. Li, P. Gu, Y. Feng, G. Zhang, K. Huang, H. Xue, H. Pang, Adv. Funct. Mater., 27 (2017) 1605784-1605795.

16.   Y. Tang, Z. Liu, W. Guo, T. Chen, Y. Qiao, S. Mu, Y. Zhao, F. Gao, Electrochim. Acta, 190 (2016) 118-125.

17.   J. Zhang, Y. Yang, Z. Zhang, X. Xu, X. Wang, J. Mater. Chem. A, 2 (2014) 20182-20188.

18.   D. Dubal, J. Kim, Y. Kim, R. Holze, C. Lokhande, W. Kim, Energy Technol., 2 (2014) 325-341.

19.   S. Palchoudhury, K. Ramasamy, R. Gupta, A. Gupta, Front. Mater., 5 (2019) 1-9.

20.   G. Hodes, "Chemical Solution Deposition of Semiconductor Films", Marcel Dekker Inc., New York, (2001).

21.   R. Bacsa, J. Kiwi, T. Ohno, P. Albers, V. Nadtochenko, J. Phys. Chem. B, 109 (2005) 5994-6003.

22.   K. Ikeda, S. Orimo, A. Zuttel, L. Schlapbach, H. Fujii, J. Alloys Compd., 280 (1998) 279-283

23. H. Gao, G. Wang, M. Yang, L. Tan, J. Yu, Nanotechnology, 23 (2012) 015607 (1-8).

24. Q. Li, Y. Li, H. Peng, X. Cui, M. Zhou, K. Feng, P. Xiao, J. Mater. Sci., 51 (2016) 9946-9957.

25. H. Pang, S. Wang, W. Shao, S. Zhao, B. Yan, X. Li, S. Li, J. Chen, W. Du, Nanoscale, 5 (2013) 5752-5757.

26. S. Navale, V. Mali, S. Pawar, R. Mane, M. Naushad, F. Stadler, V. Patil, RSC Adv., 5 (2015) 51961-51965.

27. H. Wen, M. Cao, G. Sun, W. Xu, D. Wang, X. Zhang, C. Hu, J. Phys. Chem. C, 112 (2008) 15948-15955.

28. T. Nguyen, V. Nguyen, R. Deivasigamani, D. Kharismadewi, Y. Iwai, J. Shim, Solid State Sci., 53 (2016) 71-77.

29. H. Liu, T. Chin, S. Yung, Mater. Chem. Phys., 50 (1997) 1-10.

30. N. Prokopchuk, V. Kopilevich, L. Voitenko, Russ. J. Appl. Chem., 81 (2008) 386-391.

31. M. Al-Omair, A. Touny, M. Saleh, J. Power Sources, 342 (2017) 1032-1039.

32. D. Yang, Q. Yu, L. Gao, L. Mao, J. Yang, Appl. Surf. Sci., 416 (2017) 503-510.

33. C. Lee, F. Omar, A. Numan, N. Duraisamy, K. Ramesh, S. Ramesh, J. Solid State Electrochem., 21 (2017) 3205-3213.

34. N. Priyadharsini, A. Shanmugavani, L. Vasylechko, R. Selvan, Ionics, 24 (2018) 2073-2082.

35. P. Noisong, C. Danvirutai, T. Srithanratana, B. Boonchom, Solid State Sci., 10 (2008) 1598-1604.

36. Y. Zhu, Y. Liu, T. Ren, Z. Yuan, Nanoscale, 6 (2014) 6627-6636.

37. J. Chang, Q. Lv, G. Li, J. Ge, C. Liu, W. Xing, Appl. Catal. B, 204 (2017) 486-496.

38. W. Bian, Y. Huang, X. Xu, M. Din, G. Xie, X. Wang, ACS Appl. Mater. Interfaces, 10 (2018) 9407-9414.

39. H. Shao, N. Padmanathan, D. McNulty, C. Dwyer, K. Razeeb, ACS Appl. Mater. Interfaces, 8 (2016) 28592-28598.

40. N. Jiang, B. You, M. Sheng, Y. Sun, ChemCatChem, 8 (2016) 106-112.

41. T. Sun, L. Xu, Y. Yan, A. Zakhidov, R. Baughman, J. Chen, ACS Catal., 6 (2016) 1446-1450.

42. P. Feng, X. Cheng, J. Li, X. Luo, ChemistrySelect, 3 (2018) 760-764.

43. J. Li, W. Xu, D. Zhou, J. Luo, D. Zhang, P. Xu, L. Wei, D. Yuan, J. Mater. Sci., 53 (2018) 2077-2086.

44. M. Sathiya, A. Prakash, K. Ramesha, J. Tarascon, A. Shukla, J. Am. Chem. Soc., 133 (2011) 16291-16299.

45. P. Katkar, S. Marje, S. Pujari, S. Khalate, A. Lokhande, U. Patil, ACS Sustain. Chem. Eng., 7 (2019) 11205-11218.

46. B. Senthilkumar, K. Sankar, L. Vasylechko, Y. Lee, R. Selvan, RSC Adv., 4 (2014) 53192-53201.

47. W. Xing, S. Qiao, X. Wu, X. Gao, J. Zhou, S. Zhuo, S. Hartono, D. Jurcakova, J. Power Sources, 196 (2011) 4123-4127.

48. S. Kandalkar, H. Lee, S. Seo, K. Lee, C. Kim, J. Mater. Sci., 46 (2011) 2977-2981.

49. F. Omar, A. Numan, S. Bashir, N. Duraisamy, R. Vikneswaran, Y. Loo, K. Ramesh, S. Ramesh, Electrochim. Acta, 273 (2018) 216-228.

50. K. Sankar, Y. Seo, S. Lee, S. Jun, ACS Appl. Mater. Interfaces, 10 (2018) 8045-8056.

51. J. Cherusseria, K. Kar, J. Mater. Chem. A, 4 (2016) 9910-9922.

52. Y. Jiang, L. Jiang, Z. Wu, P. Yang, H. Zhang, Z. Pan, L. Hu, J. Mater. Chem. A, 6 (2018) 16308-16315.

53. Z. Huang, G. Natu, Z. Ji, P. Hasin, Y. Wu, J. Phys. Chem. C, 115 (2011) 25109-25114.

54. P. Deshmukh, S. Pusawale, V. Jamadade, U. Patil, C. Lokhande, J. Alloys Compd., 509 (2011) 5064-5069.

55. D. Dubal, D. Dhawale, R. Salunkhe, C. Lokhande, J. Electrochem. Soc., 157 (2010) A812-A817.

56. M. Singh, S. Semwal, A. Kumar, S. Singh, Turk J. Elec. Eng. & Comp. Sci., 23 (2015) 2208-2214.

CHAPTER – IV

SYNTHESIS, CHARACTERIZATION AND SUPERCAPACITIVE PERFORMANCE EVALUATION OF ELECTRODEPOSITED NICKEL COBALT PHOSPHATE THIN FILMS

SYNTHESIS, CHARACTERIZATION AND SUPERCAPACITIVE PERFORMANCE EVALUATION OF ELECTRODEPOSITED NICKEL COBALT PHOSPHATE THIN FILMS

4.1 Introduction

The characteristic of supercapacitors in terms of energy density and power density is higher than conventional capacitors and batteries, respectively. The supercapacitors are used to fill the gap between them (batteries and capacitors) and generally used in electronic devices, electric vehicles and back-up power storage [1-4]. To improve the performance of supercapacitors, efficient electrodes are required. So, the main focus is shifted towards development of efficient electrodes using low cost and simple environmental friendly preparative methods [5, 6]. Open and wide channel structured metal phosphate materials catch attention in the energy storage field as a cathode material due to their excellent properties like large active sites for reaction, excellent conducive nature and higher stability due to P-O covalent bond [7]. For the synthesis of metal phosphate material different methods were used as hydrothermal [8], microwave assisted [9] and co-precipitation [10].

The different morphologies and phases of metal phosphates are obtained using various synthesis processes. The various polymorphs of nickel phosphate such as, $Ni_2P_2O_7$ [11], $Ni_3(PO_4)_2$ [9], $Ni_{11}(HPO_3)_8(OH)_6$ [12], etc. were synthesized for supercapacitor application. Similarly, the polymorphs of cobalt phosphate such as $Co_3(PO_4)_2 \cdot 8H_2O$ [13], $CoHPO_4 \cdot 3H_2O$ [14], $Co_3P_2O_8 \cdot 8H_2O$ [15], $Co_2P_2O_7$ [16], $Co_2P_4O_{12}$ [17], etc. were prepared and investigated for supercapacitor application. It is known that, the synergistic effect between the nickel and cobalt species can offer high electrochemical response for nickel cobalt binary phosphate material [18-21].

So considering advantage of synergistic effect, nickel and cobalt species are combined and binder-free nickel cobalt phosphate thin film electrodes are prepared by electrodeposition method. The simple electrodeposition method (potentiostatic mode) was employed for the preparation of nickel cobalt phosphate thin films on stainless steel

substrate. The ratio of nickel and cobalt species varied in nickel cobalt phosphate to achieve better performance by tuning structural and morphological properties of electrodes. The present chapter is divided into two sections (section A and B). Section 'A' deals with the synthesis of nickel cobalt phosphate thin films by electrodeposition method and their characterization. Section 'B' is associated with the supercapacitive performance evaluation of electrodeposited nickel cobalt phosphate thin film electrodes.

SECTION – A

SYNTHESIS AND CHARACTERIZATION OF NICKEL COBALT PHOSPHATE THIN FILMS BY ELECTRODEPOSITION METHOD

4.2.A.1 Introduction

The combination of two metal compounds offers excellent properties than the single metal compound due to the synergistic effect. So, this strategy used by several researchers and prepared different morphologies with different phases of nickel cobalt phosphate material and hydrothermal method is mostly used for the preparation. The microplates of $Co_{0.4}Ni_{1.6}P_2O_7$ by Chen et. al. [22], nanosheets of $NiCoPO_4$ by Li. et. al. [23], nanospheres of $Co_{0.86}Ni_{2.14}(PO_4)_2$ by Tang et. al. [24] prepared using hydrothermal method and, also hollow shells of $NiCo_2(PO_4)_2$ synthesized by Zhang et. al. [25] via microwave assisted chemical method. There are only a few reports found in the literature on the preparation of nickel cobalt phosphate for supercapacitor application. All researchers prepared nickel cobalt phosphate material in powder form and pasted it on the substrate via the casting method to fabricate supercapacitor electrode. Still, there is no report available on employing electrodeposition (potentiostatic) method for the preparation of nickel cobalt phosphate thin film electrode.

Therefore, a binder-free and eco-friendly electrodeposition method is employed for the synthesis of nickel cobalt phosphate thin films. The electrodeposition method is famous for the preparation of material with accurate composition and controlled deposition. In this synthesis method, preparative parameters like reaction time, reaction potential and concentration of the solution, etc. are optimized for the deposition of well adherent and uniform nickel cobalt phosphate thin films. Then, different techniques were used for the characterization of prepared films like XRD, FT-IR, FE-SEM, EDS, XPS, etc. The change in composition and corresponding morphologies of nickel cobalt phosphate thin films are obtained by varying nickel and cobalt molar ratio in the synthesis process.

4.2.A.2 Experimental details

4.2.A.2.1 Chemicals

Nickel chloride ($NiCl_2.6H_2O$), cobalt chloride ($CoCl_2.6H_2O$) and potassium dihydrogen orthophosphate (KH_2PO_4) were purchased from Sigma Aldrich (AR grade) and used as received without any purification.

4.2.A.2.2 Experimental setup for nickel cobalt phosphate thin film deposition

In electrodeposition method, the conventional three electrode system is used as an electrochemical cell in cylindrical container. In this setup, intentionally the glass cylindrical cell was used because of transparency and chemical inertness during deposition. The electrochemical cell consists of stainless steel as a working electrode, graphite as a counter electrode and SCE (with saturated KCl solution) as a reference electrode and all are fitted in bakelite holder on the cylindrical cell. The photograph of experimental setup for electrodeposition of nickel cobalt phosphate thin films is shown in Fig. 4.1. Electrodeposition synthesis processes were carried out using ZIVE MP1 multichannel electrochemical workstation.
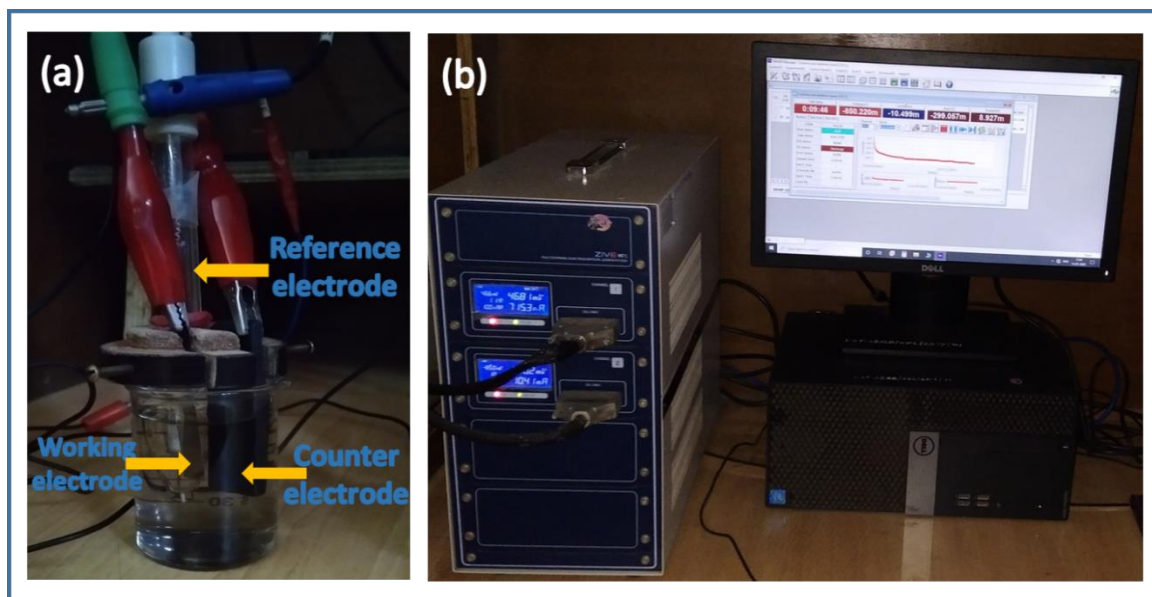
Fig. 4.1 Photograph of (a) electrochemical deposition cell and (b) experimental setup
consisting of battery cycler with potentiostatic (current versus time) graph on monitor.

4.2.A.2.3 Synthesis of nickel cobalt phosphate thin films

The synthesis of nickel cobalt phosphate thin films is carried out by potentiostatic

mode in aqueous solution of precursors containing nickel chloride ($NiCl_2.6H_2O$), cobalt

chloride ($CoCl_2.6H_2O$) and potassium dihydrogen orthophosphate (KH_2PO_4). For the

synthesis of nickel cobalt phosphate thin films, the nickel chloride and cobalt chloride

precursors concentration were varied from 0.045-0 M and 0-0.025 M, respectively. The

phosphate precursor (potassium dihydrogen orthophosphate) concentration was kept

constant (0.125 M) for variations in nickel and cobalt precursor, intentionally higher

concentration of phosphate precursor used for the deposition. The deposition potential

is varied and optimized between -0.85 to -1.1 V/SCE at room temperature. In between

the various potential, well adherent with uniform film was obtained at -0.85 V/SCE

potential from 0.045 M nickel chloride and 0.125 M potassium dihydrogen

orthophosphate precursors bath. The composition of precursors

($NiCl_2.6H_2O:CoCl_2.6H_2O$) is varied as 1:0, 0.85:0.15, 0.75:0.25, 0.5:0.5, 0.25:0.75,

0.15:0.85 and 0:1 for nickel cobalt phosphate thin film deposition on stainless steel substrate and denoted by E-NCP1, E-NCP2, E-NCP3, E-NCP4, E-NCP5, E-NCP6 and E-NCP7, respectively. The optimized preparative parameters for thin film deposition of nickel cobalt phosphate by potentiostatic mode are described in table 4.1.

Parameters	Condition						
Film	Nickel cobalt phosphate						
Medium	Aqueous						
Bath composition	(0.045-0M):(0-0.025M)						
$NiCl_2.6H_2O$: $CoCl_2.6H_2O$	1:0	0.85:0.15	0.75:0.25	0.5:0.5	0.25:0.75	0.15:0.85	0:1
KH_2PO_4	0.125M						
Total quantity of solution	50 ml						
pH	~3.5						
Potential	-0.85 V/SCE						
Time	5400 s						
Temperature	300 K						
Substrate	Stainless steel (1 X 3 cm^2)						

Table 4.1 Optimized preparative parameters for potentiostatic deposition of nickel cobalt phosphate thin films (E-NCP1 to E-NCP7).

4.2.A.3 Results and discussion

4.2.A.3.1 Film formation

For the electrodeposition process of material, formal deposition potential, redox reactions and film formation are examined by linear sweep voltammetry (LSV) study. Fig. 4.2 shows LSV curves of $NiCl_2.6H_2O$, $CoCl_2.6H_2O$ and $NiCl_2.6H_2O+CoCl_2.6H_2O$ with KH_2PO_4 aqueous precursor solutions at compositions ($NiCl_2.6H_2O:CoCl_2.6H_2O$) as 1:0, 0:1 and 0.5:0.5, respectively. The LSV is scanned from 0 to -1.2 V/SCE at a scan rate of 20 mV s^{-1}. In this scan, nickel precursor solution does not show any increment in current at initial potential, but both cobalt precursor and combined (nickel

and cobalt) precursor solution shows a well defined cathodic peak at initial potential.

Then, as increase in negative potential almost no current observed until the potential

reaches up to -0.7 V/SCE. After that, the reduction of solution starts and the reduction

current increases rapidly from -0.7 V/SCE due to the starting of nucleation process. Fig.

4.2 shows that, Ni precursor solution has lower current response and more negative

reduction potential than individual Co and combined Co+Ni precursor solution.

However, they have approximately similar reduction potential, so deposition can take

place at same potential from uncomplexed ions [26].
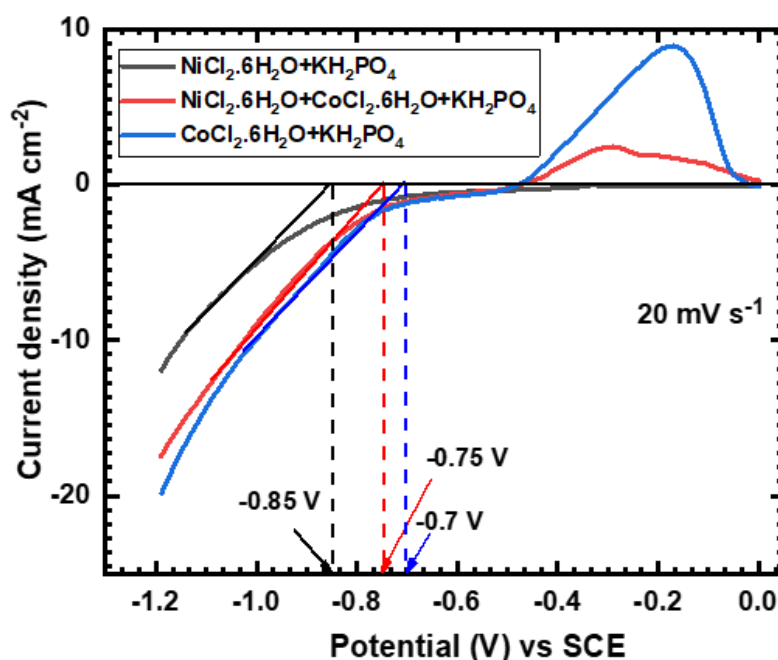
Fig 4.2 LSV curves for precursor solution of $NiCl_2.6H_2O$, $CoCl_2.6H_2O$ and

$NiCl_2.6H_2O+CoCl_2.6H_2O$ (with KH_2PO_4) with composition 1:0, 0:1 and 0.5:0.5

$(NiCl_2.6H_2O:CoCl_2.6H_2O)$, respectively at 20 mV s^{-1} sweep rate.

Based on LSV study, it is possible to obtain tentative deposition potential to

encourage potentiostatic deposition of nickel cobalt phosphate thin films. The reduction

potentials of cobalt precursor and nickel cobalt precursor solutions were determined by

plotting tangent on the X-axis and found to be -0.7 and -0.75 V/SCE, respectively.

Similarly, the reduction potential for nickel precursor solution is measured and found to be -0.85 V/SCE. For the deposition of nickel and cobalt species simultaneously with phosphate species, the overpotential of -0.85 V/SCE is applied, since the reduction potential of cobalt and nickel cobalt precursor solution is less than nickel precursor. The potentiostatic curves of prepared compositions during nickel cobalt phosphate thin film formation on SS substrate at -0.85 V/SCE are shown in Fig. 4.3. Potentiostatic deposition curves can be classified in to two regions, first region explains nuclei formation and second region corresponds to film growth. The observed initial surge in current response is depends upon number of available cation species at the interface of electrode which discharge immediately after the polarization of electrode and leads to birth of nuclei (region-I). After the initial increment, the current decreases sharply and shows almost steady state after achieving minimum current (region-II). In second region, the growth process is slow which responsible for the cluster formation due to the process like adsorption and coalescence.
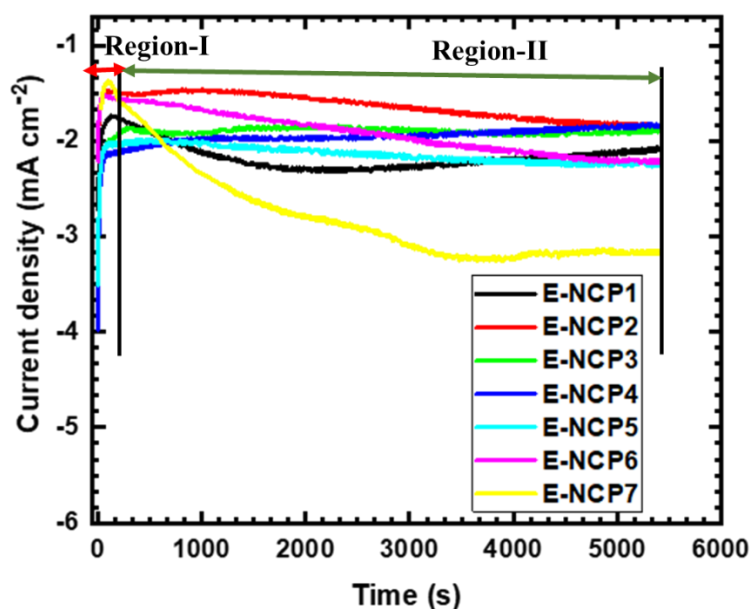
Fig. 4.3 A potentistatic curves of nickel cobalt phosphate (E-NCP1 to E-NCP7) for various bath compositions at potential of -0.85 V/SCE on stainless steel substrate.

The steady nature of current after the nucleation corresponds to uniform growth of material. After achieving minimum current response, little increment in current observed for E-NCP1 sample may be due to higher conductivity of nickel phosphate material. On the other hand, continuous decrement (compare to other solutions) and then steady response in the current density is observed with increasing time for E-NCP7 sample suggest faster growth kinetics of cobalt phosphate.
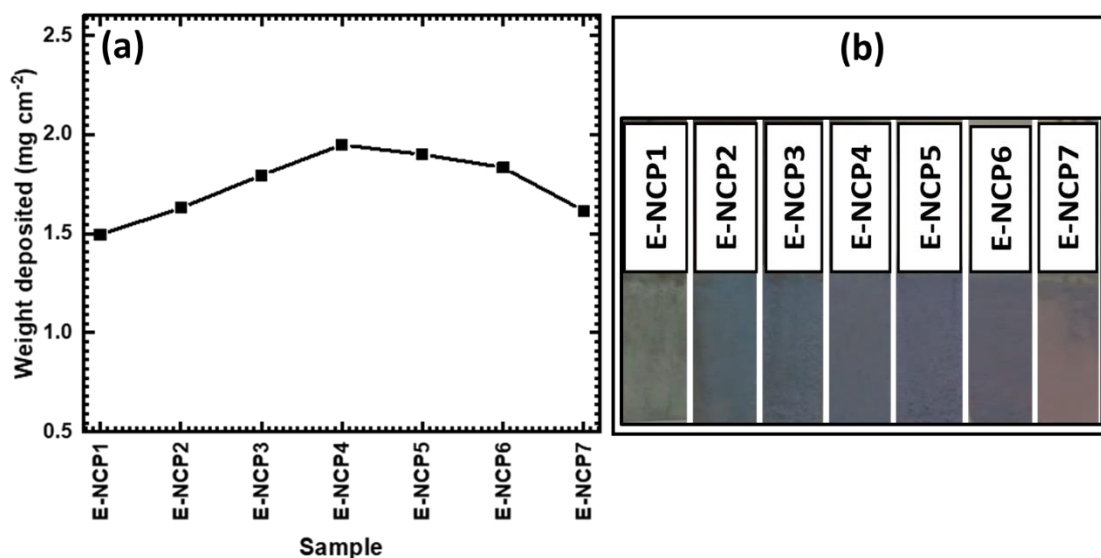
Fig. 4.4 (a) Nickel cobalt phosphate thin film thickness at different compositions of $NiCl_2.6H_2O:CoCl_2.6H_2O$ and (b) photograph of prepared thin film electrodes.

Variation observed in the weight of the deposited nickel cobalt phosphate for the different bath compositions of $NiCl_2.6H_2O:CoCl_2.6H_2O$. The electrodeposition (potentiostatic) method is used for the deposition of nickel cobalt phosphate thin films at constant potential of -0.85 V/SCE for 5400 s at room temperature. Thickness of film varies from 1.5 to 1.95 mg cm^{-2} with respect to bath composition as shown in Fig. 4.4 (a). The well adherent and uniform film of nickel cobalt phosphate with various compositions are obtained and photograph is shown in Fig. 4.4 (b). The lowest thickness observed for the bath composition of 1:0 i.e. nickel phosphate (E-NCP1). As increase in Co content, the deposited weight increases up to sample E-NCP4

(composition of 0.5:0.5) and decreases up to sample E-NCP7 (composition of 0:1) i.e. cobalt phosphate. It concludes that, the deposition rate increases by increasing Co content up to optimum limit at constant deposition time and potential.

4.2.A.3.2 XRD studies

The structural study of synthesized thin films was investigated by XRD analysis. The XRD patterns of prepared E-NCP series samples are shown in Fig. 4.5. The peaks denoted by '*' correspond to stainless steel. The XRD pattern of E-NCP1 sample shows only stainless steel peaks and confirms amorphous nature of prepared material. On the other hand, XRD pattern of E-NCP7 sample matches with the JCPDS card no. 34-0844 and confirms the formation of $Co_3(PO_4)_2.4H_2O$ material in thin film form. The XRD pattern of E-NCP7 sample shows diffraction peaks at an angle of 14.5, 24.19, 28.96, 31.52 and 34.55º ascribed to the (020), (101), (310), ($\bar{2}$31) and (330) crystal planes, respectively.
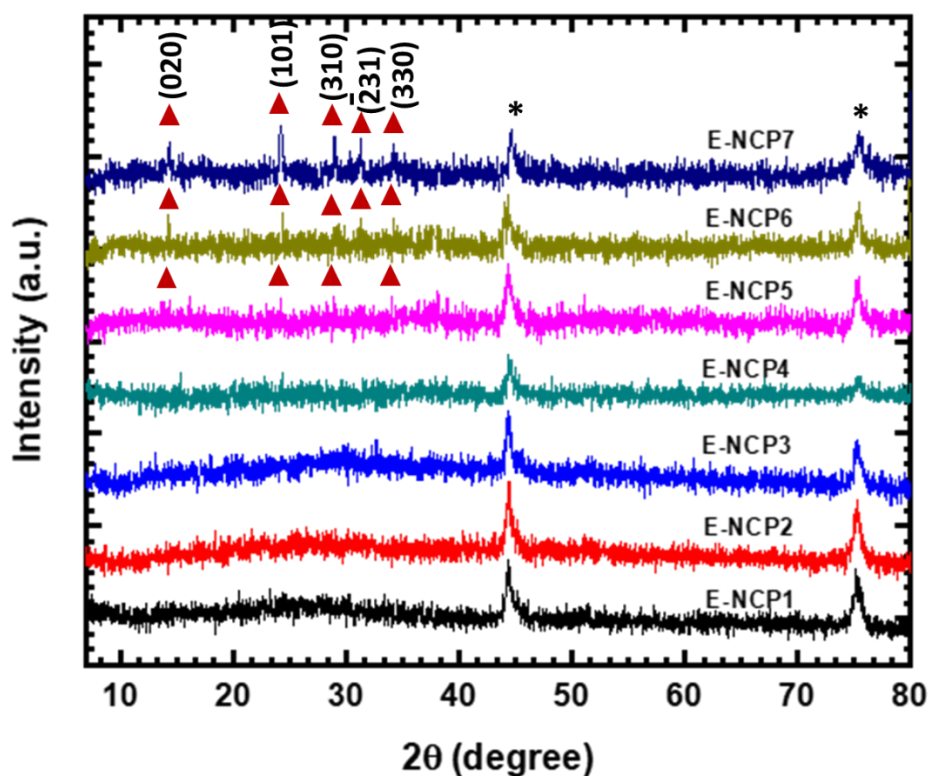
Fig. 4.5 XRD patterns of nickel cobalt phosphate thin films (E-NCP1 to E-NCP7).

The E-NCP1 sample shows pure amorphous nature in XRD analysis. As like E-NCP1, the other sample with less cobalt content shows amorphous nature up to E-NCP4 sample. With increase in cobalt content, the structure of composition changes and some peaks are observed in XRD. Further increase in cobalt content, samples after E-NCP4 show peaks which match with cobalt phosphate. The XRD result confirms, amorphous nature of nickel phosphate totally converted in to crystalline phase (at lowest nickel content) after addition of cobalt. Also, it confirms the prepared material is nickel cobalt phosphate in thin film form over SS substrate.

4.2.A.3.3 FT-IR studies

The FT-IR spectra of E-NCP series thin films was carried out in the region of 400-4000 cm^{-1} and displayed in Fig. 4.6. The presence of functional groups of material in electrodes is analyzed by FT-IR analysis. Peaks (γ_1) in the range of 568-595 cm^{-1} represent the metal-oxygen bonding in samples. The peak at 595 cm^{-1} ascribed to Ni-O bonding [27] and peak at 571 cm^{-1} ascribed Co-O bonding in thin films [28, 29].
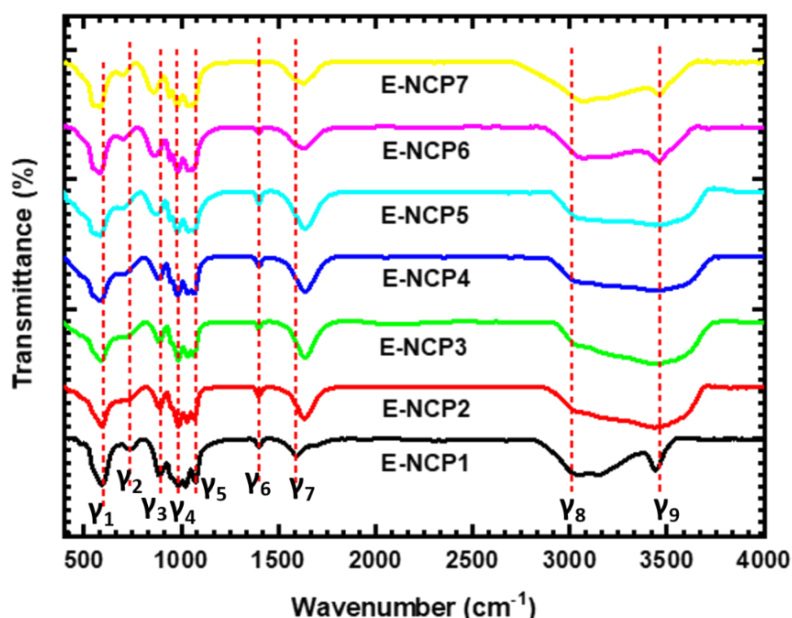
Fig. 4.6 FT-IR spectra of nickel cobalt phosphate thin films (E-NCP1 to E-NCP7).

The symmetric stretching of P-O-P linkage observed at the absorption peak (γ_2) in the range of 708-741 cm^{-1} [30]. The symmetric and asymmetric P-O stretching vibrational mode of PO_4^{3-} anions are confirmed by the peaks (γ_3, γ_4, γ_5) observed in the region of 857-1076 cm^{-1} [31-35]. The absorption peaks (γ_6, γ_7) in the region of 1400-1644 cm^{-1} are corresponds to bending mode of water molecule (H-O-H) [32, 35, 36]. Moreover, the peaks (γ_8, γ_9) in the region of 3000-3464 cm^{-1} are corresponds to O-H stretching vibration mode of adsorbed water content in the material [32, 35, 36]. Moreover, the slight shifting in peaks from sample E-NCP1 to E-NCP7 confirm the coordination interaction between nickel and cobalt elements [37]. The FT-IR results confirm successful preparation of hydrous nickel cobalt phosphate material in thin film form.

4.2.A.3.4 Surface morphological studies

FE-SEM analysis is used for the investigation of surface morphology of electrodeposited nickel cobalt phosphate thin films. Fig. 4.7 shows the morphologies of electrodeposited thin films at different magnifications (20,000X and 50,000X). The morphological evolution is observed from E-NCP1 to E-NCP7 sample due to variation in nickel and cobalt composition. Fig. 4.7 (a1, a2) shows the surface architecture of nickel phosphate thin film (E-NCP1). The E-NCP1 sample shows microsphere like structure and it grows on one another due to the overgrowth of material. The average diameter of the microspheres is 3.5 µm and rough surface of microsphere (Fig. 4.7 (a2)) is observed due to number of nanoparticles exists in it. Addition of cobalt content influences the morphology of thin film (E-NCP2 sample) through decrease in diameter of microspheres, in the range of 2.5-2.9 µm as observed in Fig. 4.7 (b1). As like sample E-NCP1, the E-NCP2 sample shows rough surface of microspheres and it shows larger size of pores than E-NCP1 (Fig. 4.7 (b2)). Again increase in cobalt content, highly merged microspheres are observed for sample E-NCP3 as shown in Fig. 4.7 (c1) and

they are ranging in diameter of 1.2-2.5 µm. At higher magnification, the merged structure of microspheres easily observed from Fig. 4.7 (c2). Also, some nanocracks are observed on the microsphere structure and shown in the inset of Fig. 4.7 (c2). Similar, merged microspheres are observed in E-NCP4 sample with different dimensions as shown in Fig. 4.7 (d1).
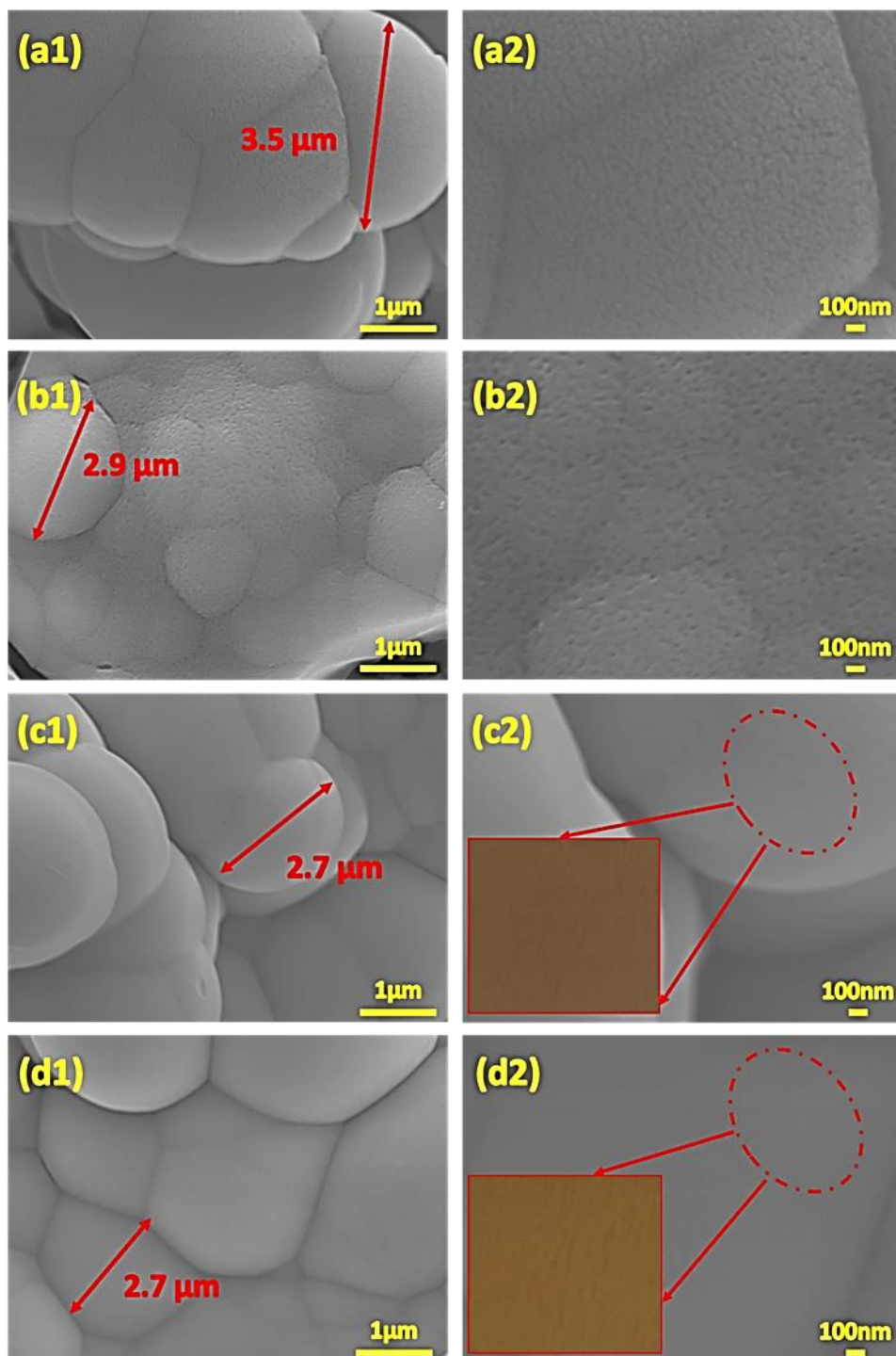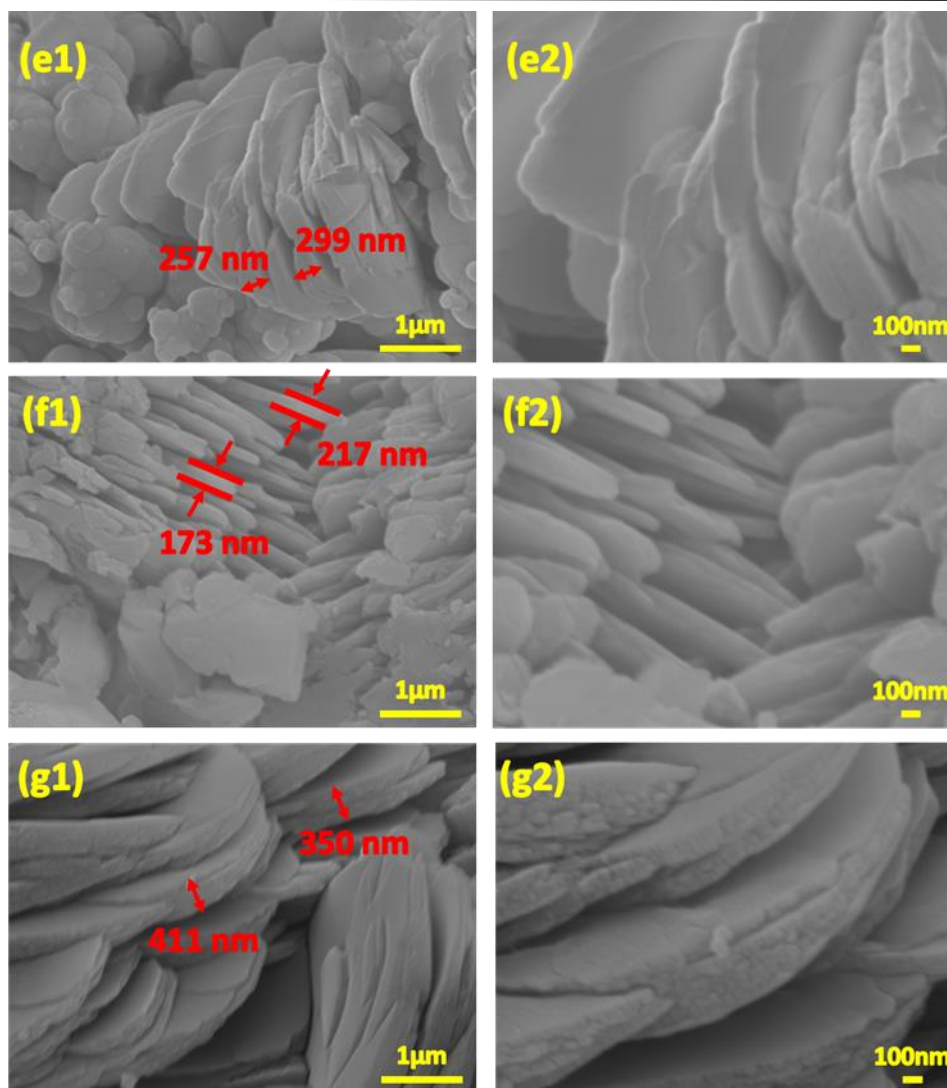
Fig. 4.7 FE-SEM images of sample E-NCP1 (a1, a2), E-NCP2 (b1, b2), E-NCP3 (c1, c2), E-NCP4 (d1, d2), E-NCP5 (e1, e2), E-NCP6 (f1, f2) and E-NCP7 (g1, g2) at the magnification of 20,000X and 50,000X, respectively.

Similar to sample E-NCP3, the sample E-NCP4 show nanocracks on the surface of the microspheres (inset of Fig. 4.7 (d2)) and higher content of cobalt may be responsible for formation of nanocracks on the surface of microspheres. The drastic change in microstructure is observed for the sample E-NCP5, which shows sheets like structure in combination with extremely merged microspheres and seems mud like structure (Fig. 4.7 (e1) and (e2)). The nanosheets with thickness of 257-299 nm are observed in Fig. 4.7 (e1). Further increase in cobalt content, microsphere like architecture is completely

vanished and displays extremely close packed nanosheets like architecture (Fig. 4.7 (f1) and (f2)) for sample E-NCP6. The decrement in thickness of nanosheets observed up to 173-217 nm (Fig. 4.7 (f1)). At the most higher cobalt content (zero content of nickel), sample E-NCP7 shows nanosheets like structure with curved edges (Fig. 4.7 (g1) and (g2)). The thickness of curve edged nanosheets is higher than the close packed nanosheets and has thickness of 350-411 nm (Fig. 4.7 (g1)). The variation in morphology observed with the change in precursor concentrations and confirms morphology of electrodeposited thin film is sample depend upon the Ni:Co composition.

Elemental mapping of E-NCP series thin film samples was carried out using energy dispersive spectroscopy (EDS) analysis and displayed in Fig. 4.8 (a-g). Thin films with different nickel and cobalt compositions formed by combining nickel, cobalt, phosphorous and oxygen elements (Fig. 4.8). The presence of nickel, cobalt, phosphorous and oxygen elements in the sample E-NCP2 to E-NCP6 confirm the successful deposition of nickel cobalt phosphate material on SS substrate in thin film form via electrodeposition method. Also, the absence of cobalt in E-NCP1 and nickel in E-NCP7 samples confirm formation of nickel phosphate and cobalt phosphate materials, respectively.
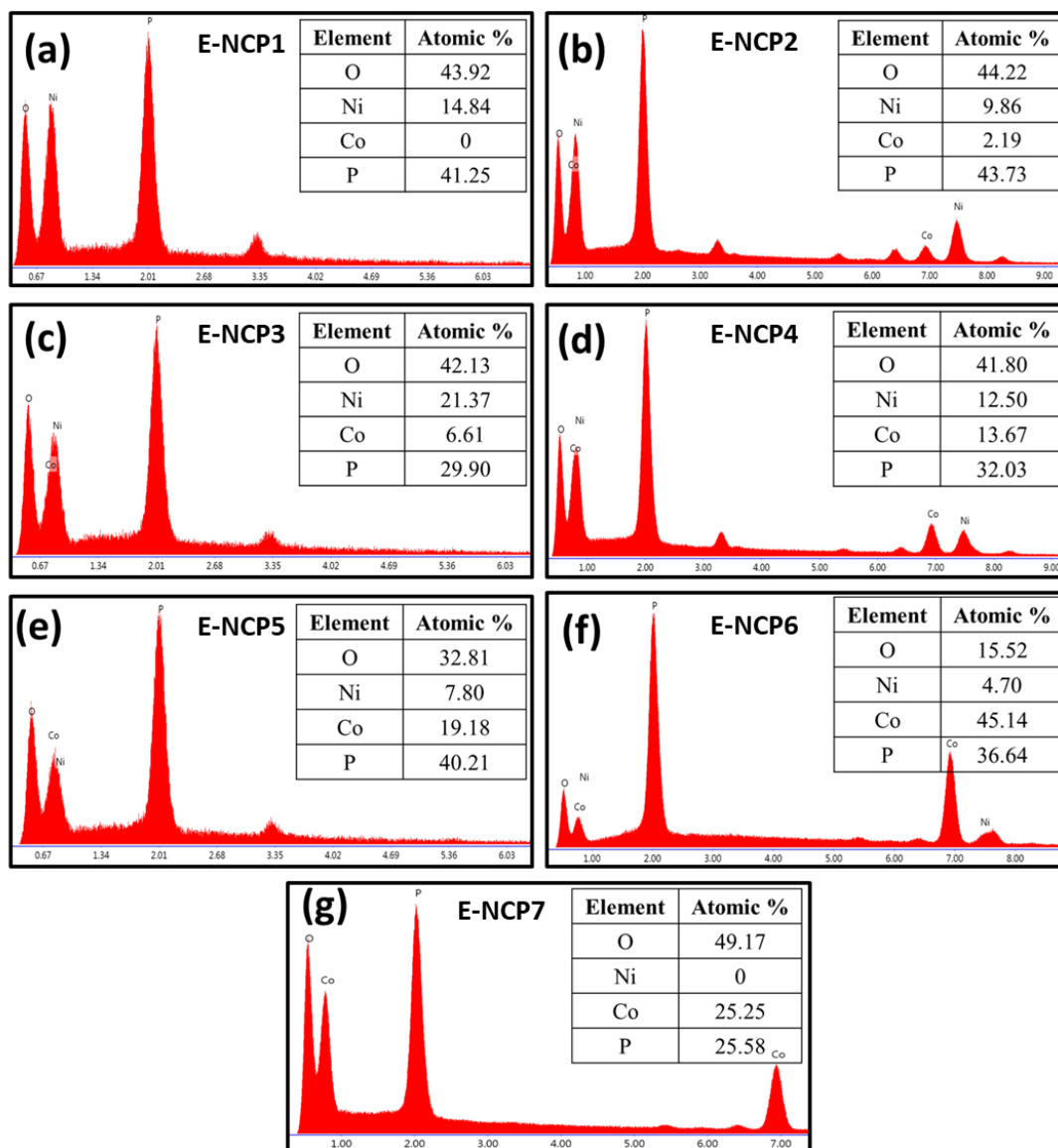
Fig. 4.8 EDS spectra of nickel cobalt phosphate thin film samples (a) E-NCP1, (b) E-

NCP2, (c) E-NCP3, (d) E-NCP4, (e) E-NCP5, (f) E-NCP6 and (g) E-NCP7.

The experimental and observed nickel and cobalt ratios for E-NCP series samples are

summarized in table 4.2. The observed and experimental ratios of nickel and cobalt

contents are nearly similar. So, the EDS and FE-SEM results confirm the composition

varied in the sample from E-NCP1 to E-NCP7, ultimately influences the morphology

of thin film samples. No other elements are observed in the EDS spectra that confirm

the formation of nickel cobalt phosphate material in thin film form.

Sample name	Experimental ratio (Ni:Co)	Observed ratio (Ni:Co)	Obtained phase
E-NCP1	1:0	1:0	$Ni_3(PO_4)_2$
E-NCP2	0.85:0.15	0.82:0.18	$Ni_{2.46}CO_{0.54}(PO_4)_2$
E-NCP3	0.75:0.25	0.76:0.24	$Ni_{2.28}CO_{0.72}(PO_4)_2$
E-NCP4	0.50:0.50	0.48:0.52	$Ni_{1.44}CO_{1.56}(PO_4)_2$
E-NCP5	0.25:0.75	0.29:0.71	$Ni_{0.87}CO_{2.13}(PO_4)_2$
E-NCP6	0.15:0.85	0.10:0.90	$Ni_{0.3}CO_{2.7}(PO_4)_2$
E-NCP7	0:1	0:1	$CO_3(PO_4)_2$

Table 4.2 Experimental and observed nickel and cobalt atomic ratio in nickel cobalt

phosphate thin film samples (E-NCP1 to E-NCP7).

4.2.A.3.5 XPS studies

The surface elements with existing valence states in the material was investigated

by XPS analysis. The XPS spectra of sample E-NCP4 is displayed in Fig. 4.9. The

nickel, cobalt, phosphorous and oxygen elements are observed in the XPS survey

spectrum of sample E-NCP4 (Fig. 4.9 (a)). The high resolution Ni2p XPS spectrum

confirms the $Ni2p_{3/2}$ and $Ni2p_{1/2}$ state by intense peaks at binding energies of 856.2 and

874 eV, respectively along with satellite peaks at 860.8 and 879.3 eV binding energies

present at surface of the material, indicates oxidation state of Ni (Ni^{2+}) (Fig. 4.9 (b))

[38, 39]. The high resolution XPS spectrum of Co2p region is shown in Fig. 4.9 (c), the

peak at 781.3 eV binding energy correspond to $Co2p_{3/2}$ along with satellite peak at

784.2 eV binding energy, correspond to +2 valence state of cobalt. Similarly, the intense

peak at 797.8 eV binding energy signifies $Co2p_{1/2}$ orbits along with satellite peak at

802.9 eV further proves the same assumption [40]. Fig. 4.9 (d) shows the high

resolution XPS spectrum of P2p region. In this region, only one intense peak is

observed at 133.2 eV binding energy represents P-O bonding and pentavalent state of

the phosphorous [41].
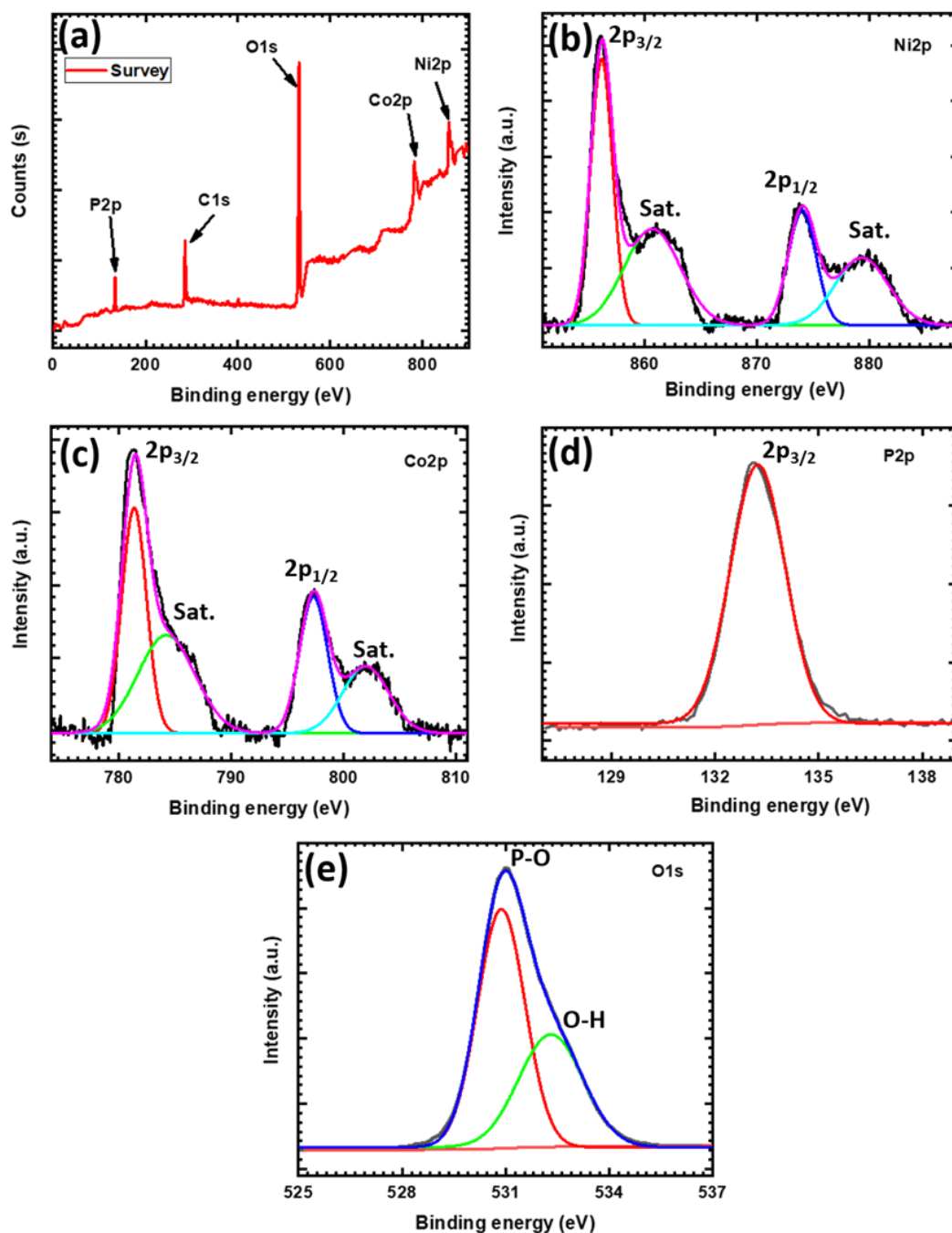
Fig. 4.9 (a) Survey, (b) Ni2p, (c) Co2p, (d) P2p and (e) O1s XPS spectrum of sample

E-NCP4.

Moreover, one broad peak is observed in the O1s region of XPS spectrum and

shown in Fig. 4.9 (e). The broad peak is deconvoluted into two peaks in O1s region at

531 eV and 532.3 eV binding energies which are correspond to core level of oxygen in

phosphate species and structural water in the material, respectively [42-44]. Thus, XPS

spectrum confirms the successful preparation of the nickel cobalt phosphate material on SS substrate by electrodeposition method.

4.2.A.4 Conclusions

In conclusion, electrodeposition (potentiostatic mode) method is feasible for successful deposition of nickel cobalt phosphate material on stainless steel substrate. Amorphous to crystalline phase conversion from nickel to cobalt phosphate is observed from XRD analysis and confirms formation of nickel cobalt phosphate material in thin film form. FT-IR, EDS and XPS analyses confirm the presence of nickel, cobalt, phosphate bonding in the prepared thin film samples. Also, the variation in nickel and cobalt content changes the morphology of nickel cobalt phosphate thin films from microspheres to nanosheets (with increase in cobalt content). The above result confirms the successful preparation of nickel cobalt phosphate material in thin film form.

SECTION – B

SUPERCAPACITIVE PERFORMANCE EVALUATION OF NICKEL COBALT PHOSPHATE THIN FILMS

4.2.B.1 Introduction

The electrode with high capacitive performance and higher stability is required to achieve best performance of supercapacitor device. The binary metal compounds like NiCoO, NiCoP and NiCoSe showed superior electrochemical performance than the single metal compounds, such as NiO (or P, Se) and CoO (or P, Se) materials, due to richer redox chemistry (Ni^{2+}, Ni^{3+}, Co^{2+}, Co^{3+}), the faster electrochemical kinetics and the strong synergistic effect between Ni and Co redox species [45]. Depend on these considerations, the proper ratio of nickel and cobalt with phosphate structure could effectively enhance the electrochemical performance than the single nickel or cobalt phosphate. However, very few reports are available on nickel cobalt phosphate

electrode material for supercapacitor application. So, the composition of nickel and cobalt varied in synthesis process and supercapacitive performance of prepared nickel cobalt phosphate electrodes is studied and discussed in this section.

Electrochemical measurements of electrodeposited nickel cobalt phosphate thin film samples E-NCP1 to E-NCP7 are discussed in this section. Also, the influence in electrochemical performance of E-NCP series thin films due to scan rates, current densities and electrochemical cycling are studied.

4.2.B.2 Results and discussion

4.2.B.2.1 Cyclic voltammetry (CV) studies

Electrochemical activity of E-NCP series electrodes in electrolyte (1 M KOH) was investigated by CV analysis. Typical CV curves of E-NCP series electrodes at 20 mV s^{-1} scan rate within potential window of 0 to 0.5 V/SCE are measured and plotted in Fig. 4.10 (a). The E-NCP4 electrode shows higher current area in the curve than other electrodes. Area under the CV curves increases with increasing cobalt content in the electrode up to E-NCP4 sample, furthermore area under curve decreases with increasing cobalt. Redox peaks in CV curve reveal pseudocapacitive (surface and bulk process) nature of the material [46]. The different nature of CV curves are obtained for nickel (E-NCP1) and cobalt (E-NCP7) phosphate electrodes. It is observed that, the nickel and cobalt ratio variation influences the morphology and that ultimately affects the electrochemical performance. The CV curves of electrodes (E-NCP1 to E-NCP7) at 1-20 mV s^{-1} sweep rates are shown in Fig. 4.10 (b-h) and area under the CV curve increases with increasing scan rate. It is observed that, the equal composition of nickel and cobalt in E-NCP4 sample having microspheres with nanocracks like morphology exhibits higher CV area than the other electrodes (microspheres or nanosheets like architectures). The higher CV current area is responsible for higher areal capacitance.

Chapter – IV

SYNTHESIS, CHARACTERIZATION AND SUPERCAPACITIVE PERFORMANCE EVALUATION OF ELECTRODEPOSITED NICKEL COBALT PHOSPHATE THIN FILMS
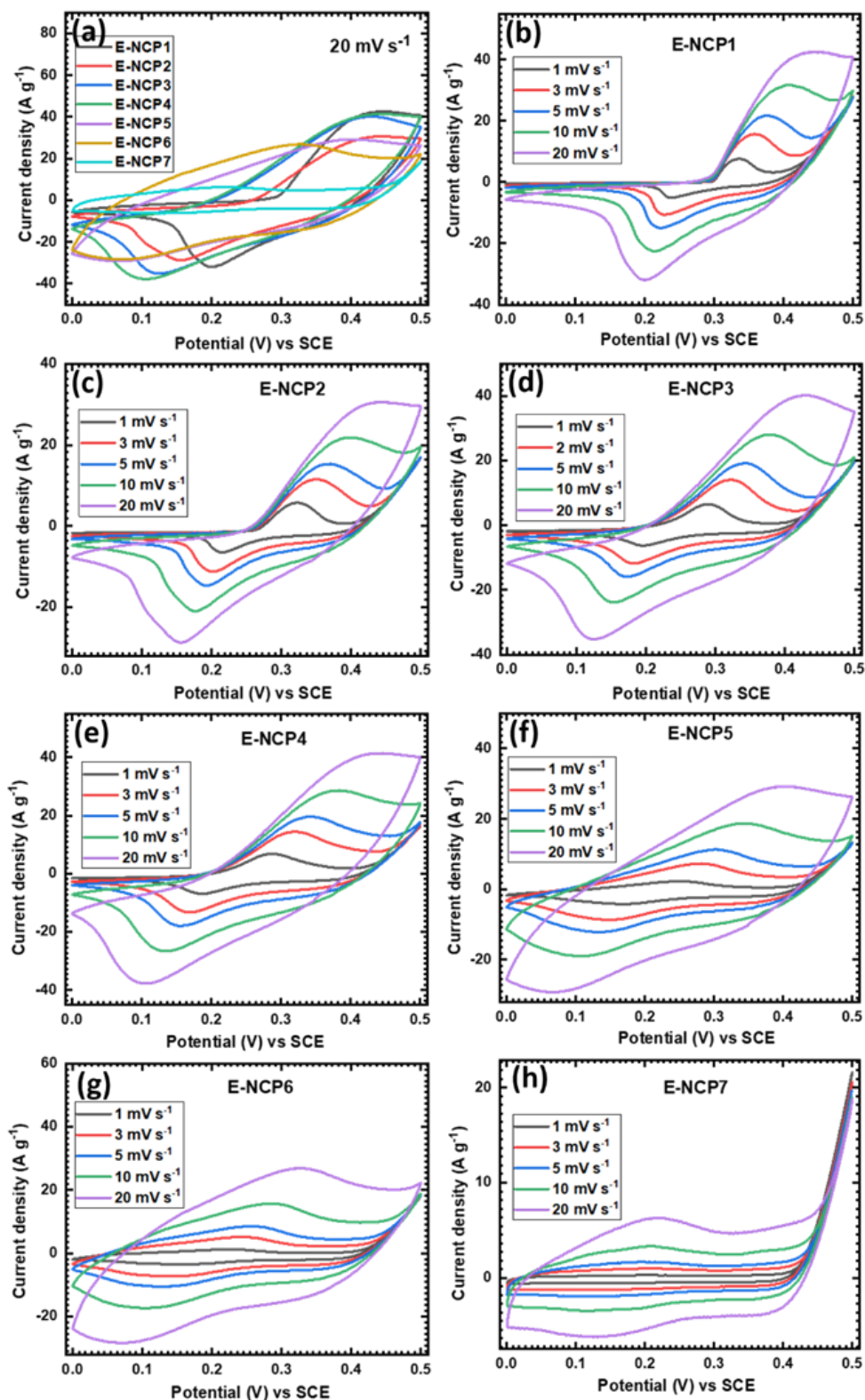
Fig. 4.10 (a) The comparative CV curves of E-NCP series electrodes at 20 mV s⁻¹ scan rate, the CV curves at various scan rates from 1-20 mV s⁻¹ for (b) E-NCP1, (c) E-NCP2, (d) E-NCP3, (e) E-NCP4, (f) E-NCP5, (g) E-NCP6 and (h) E-NCP7 electrode.

Charge stored in the electrode can be the combination of two mechanisms (battery type and electrochemical pseudocapacitive type) and it is investigated by Power's law using scan rate dependent CV curves. The b value of E-NCP series electrodes is calculated from the slope of graph log (i) vs log (v) [47] and shown in Fig. 4.11. Graphs represent b values of E-NCP1, E-NCP2, E-NCP3, E-NCP4, E-NCP5, E-NCP6 and E-NCP7 electrodes are 0.57, 0.55, 0.6, 0.61, 0.81, 0.88 and 0.90, respectively. The obtained b values for E-NCP series electrodes are greater than 0.5 and less than 1 suggests that total current is contributed from a combination of both battery and pseudocapacitive type. The b values of electrode increases from E-NCP2 to E-NCP7, it means as increase in cobalt content the electrode show more pseudocapacitive contribution.

Furthermore, modified Power's law was used to evaluate specific current density contribution from bulk battery type and surface pseudocapacitive type [48-50]. Pseudocapacitive and battery type current contribution for E-NCP series electrodes are calculated at different scan rates and displayed in Fig. 4.12. Figure reveals that, current contribution from surface pseudocapacitive process increases as increasing cobalt content in the sample. The contribution of surface pseudocapacitance is more for high scan rate and more bulk battery type at low scan rate. The result concludes that, at lower scan rate bulk battery current contribution is dominant over surface pseudocapacitive current and vice versa. The E-NCP4 electrode offers ~32 % capacitive current contribution at 20 mV s^{-1} scan rate and it is higher than nickel phosphate (E-NCP1) (~20%) and lower than cobalt phosphate (E-NCP7) (~87%) electrode. Also, other electrodes show different current contribution values due to different concentration of nickel and cobalt in the material.
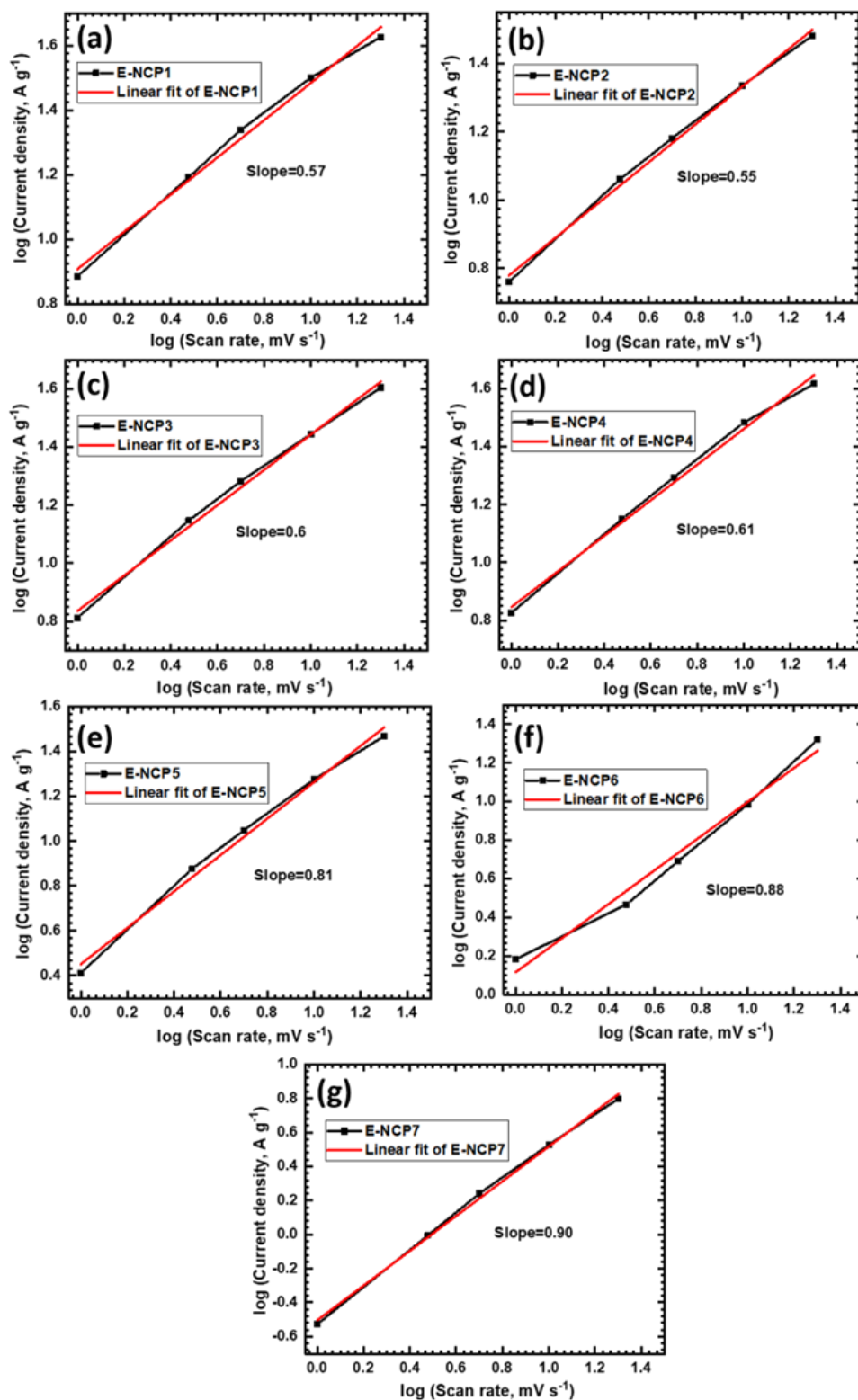
Fig. 4.11 Plot of log (current density, A g^{-1}) versus log (scan rate, mV s^{-1}) for (a) E-NCP1, (b) E-NCP2, (c) E-NCP3, (d) E-NCP4, (e) E-NCP5, (f) E-NCP6 and (g) E-NCP7 electrode.
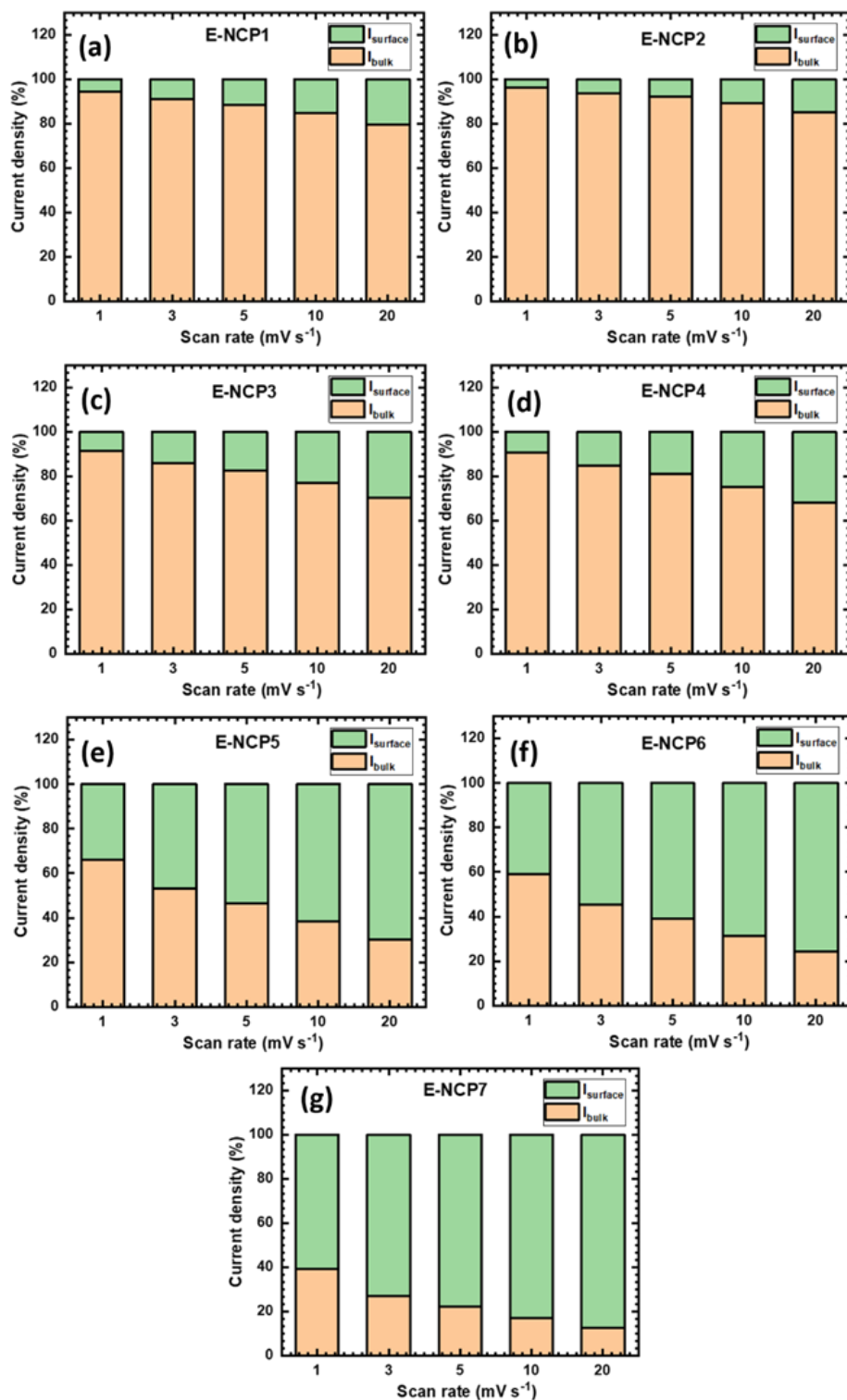
Fig. 4.12 Graph of calculated contribution of pseudocapacitive (surface current) and battery type (bulk current) current density at various scan rates (1 to 20 mV s^{-1}) for (a) E-NCP1, (b) E-NCP2, (c) E-NCP3, (d) E-NCP4, (e) E-NCP5, (f) E-NCP6 and (g) E-NCP7 electrode.

4.2.B.2.2 Galvanostatic charge-discharge (GCD) studies

GCD analysis is carried out within optimized potential window of 0 to 0.4 V (vs SCE) for E-NCP series electrodes. At constant current density of 1.5 A g^{-1}, GCD analysis of E-NCP series electrodes is studied and displayed in Fig. 4.13 (a). In a comparative study, E-NCP4 electrode shows large charging and discharging time than other electrodes. The GCD curves of E-NCP series electrodes at different current densities from 1.5-3.5 A g^{-1} are shown in Fig. 4.13 (b-h). Likewise CV curves, the nickel (E-NCP1) and cobalt (E-NCP7) phosphate electrode shows different charge-discharge curves like battery type and surface redox type, respectively. The E-NCP series electrodes show conversion in nature of GCD curve from E-NCP1 to E-NCP7 and it corresponds to battery-intercalation-surface redox type mechanism. Non-linear discharging curves of E-NCP series electrodes show deep ion intercalation and obtained due to redox reaction, and represents pseudocapacitive behavior of the material [51-53]. GCD study concludes that, the E-NCP4 electrode offers higher charge-discharge response may be due to high surface area by specific microstructure (microspheres consisting nanocracks) and optimum composition of nickel and cobalt.

From the GCD plots, the specific capacitance values of E-NCP series electrodes are calculated and plotted in Fig. 4.14. The E-NCP4 electrode shows higher discharging time that responsible for high specific capacitance than other electrodes. The E-NCP4 electrode shows maximum specific capacitance of 2228 F g^{-1} at 1.5 A g^{-1} current density and it decreases up to 1750 F g^{-1} at 3.5 A g^{-1} current density. Similarly, the E-NCP1, E-NCP2, E-NCP3, E-NCP5, E-NCP6 and E-NCP7 thin film electrodes offer maximum specific capacitance of 722, 926, 1563, 1575, 1299 and 211 F g^{-1}, respectively at 1.5 A g^{-1} current density. The decrement in specific capacitance observed with respect to
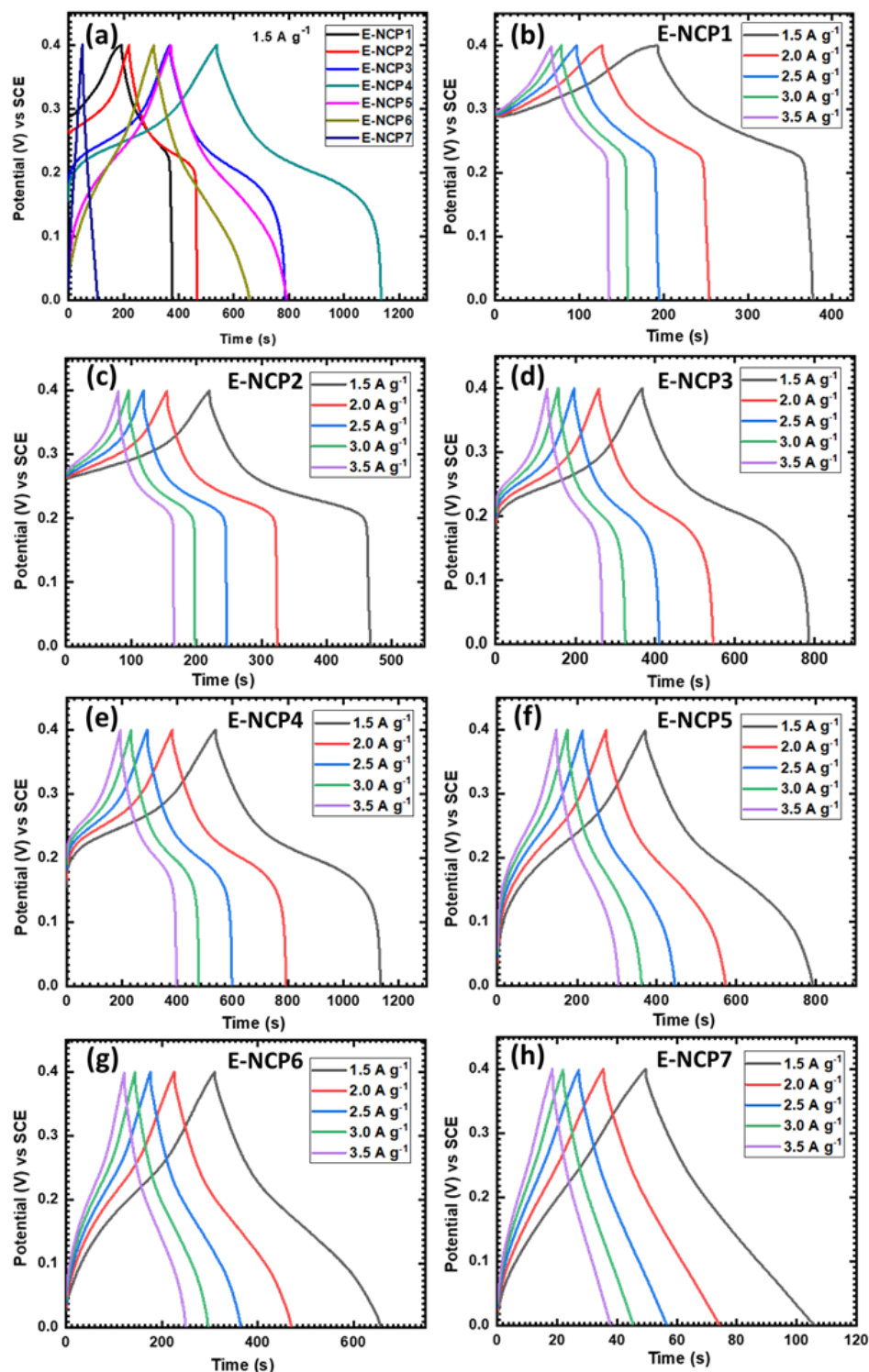
Fig. 4.13 (a) The comparative GCD curves of E-NCP series electrodes at current

density of 1.5 A g^{-1}. The GCD curves at various current densities from 1.5-3.5 A g^{-1}

for (b) E-NCP1, (c) E-NCP2, (d) E-NCP3, (e) E-NCP4, (f) E-NCP5, (g) E-NCP6 and

(h) E-NCP7 electrode.

increase in current density due to less time for electrochemical reaction and difficult to react with microstructures by electrolytic ion at high current density [54]. On the other hand, the longer interaction of electrolyte ions with the inner and outer surface of material at lower charge-discharge rate offers high specific capacitance values [55].
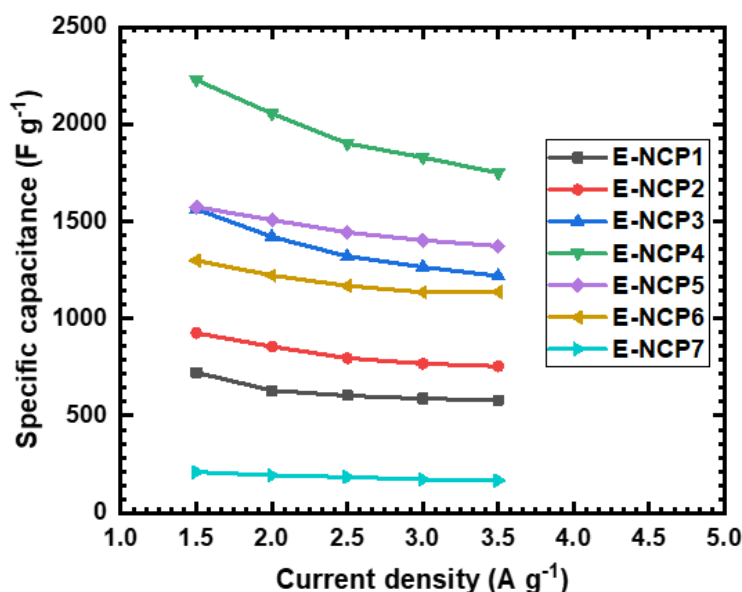
Fig. 4.14 The plots of specific capacitance at various current densities for nickel cobalt phosphate electrodes (E-NCP1 to E-NCP7).

4.2.B.2.3 Stability studies

The long term applicability of the electrode tested by stability and is an important parameter for the good supercapacitive electrode. The stability in terms of capacitive retention of best performed electrode (E-NCP4) carried out at 15 A g^{-1} current density for 3000 GCD cycles. The capacitive retention study of E-NCP4 electrode is shown in Fig. 4.15. The E-NCP4 electrode exhibits ~81 % capacitive retention at high current density over 3000 cycles. The GCD curves of initial and last 10 cycles are shown as inset of Fig. 4.15. The decrement in capacitance is observed due to minute depletion of active material after many charge-discharge cycles because of swelling and shrinking

of material. It concludes that, the microspheres with nanocracks like morphology of E-NCP4 electrode offer good cyclic life at high charge-discharge current density.
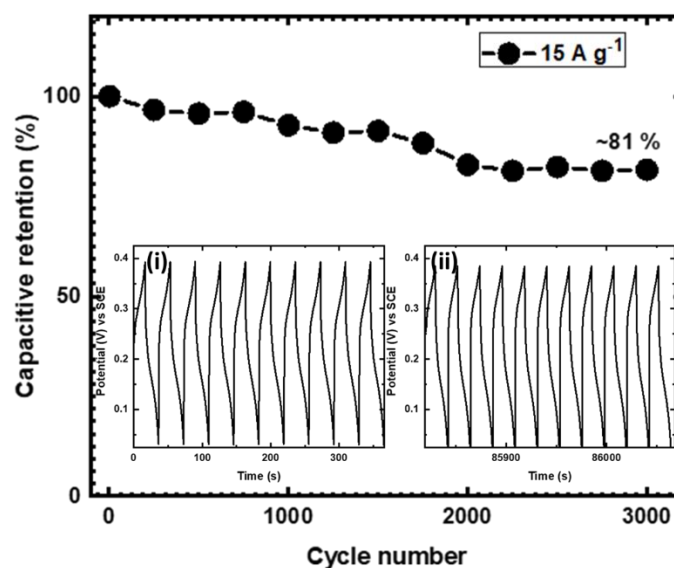
Fig. 4.15 The plot of capacitive retention of E-NCP4 electrode at 15 A g^{-1} current density for 3000 cycles (inset: GCD curve of (i) initial and (ii) final 10 cycles).

4.2.B.2.4 EIS studies

The Nyquist plots of E-NCP series electrodes are shown in Fig. 4.16 (a). The EIS technique is used to investigate electrochemical conductivity and ion transformation properties of electrodes [56].
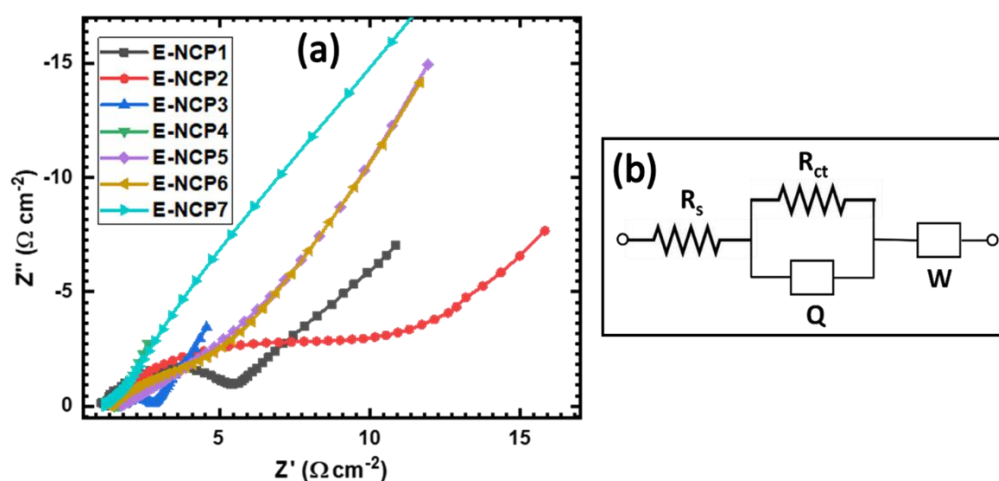
Fig. 4.16 (a) The Nyquist plots of E-NCP series electrodes (E-NCP1 to E-NCP7) and (b) the fitted equivalent circuit for the EIS data.

The fitted equivalent circuit of EIS data for E-NCP series electrodes is shown in Fig. 4.16 (b). In this figure, R_s, R_{ct}, W and Q are the solution resistance, charge transfer resistance, Warburg impedance and constant phase element, respectively. The values of each fitted circuit parameters are tabulated in table 4.3. The impedance of Q is defined as follows,

$$Z_Q = \frac{1}{Q(j\omega)^n} \qquad \text{(where } 0 < n > 1) \qquad (4.1)$$

The constant phase element arises due to inhomogeneities present at electrode/electrolyte interface, porosity and disorder associated with diffusion.

Sample Name	R_s (Ω)	R_{ct} (Ω)	Q (mF)	n	W (Ω)
E-NCP1	1.31	4.39	2.95	0.831	0.360
E-NCP2	1.44	11.19	0.422	0.895	0.233
E-NCP3	1.87	0.95	0.036	0.602	0.432
E-NCP4	1.47	0.2	9.449	0.771	0.222
E-NCP5	1.75	7.3	191.9	0.876	0.825
E-NCP6	1.33	99.6	229.5	0.842	0.009
E-NCP7	1.25	356.7	118.1	0.756	0.002

Table 4.3 Electrochemical impedance spectroscopic fitted circuit parameters for Nyquist plots of E-NCP series electrodes.

The Q value related to surface and electroactive species, n is the correction factor due to the roughness. The Q is considered as pure capacitance when n=1, resistance when n=0 and Warburg impedance when n=0.5. In table 4.3 the n values are higher than 0.5, so the Q is pseudocapacitor in present study [57-59]. The E-NCP4 electrode shows low charge transfer resistance (0.2 Ω) as compared to other electrodes. Less value of charge transfer resistance offered by E-NCP4 electrode due to good active material contact with substrate and microspheres with nanocracks like morphology, which may be responsible for high pseudocapacitive performance of electrode.

4.2.B.3 Conclusions

The CV and GCD analyses confirm that electrochemical response depends on morphologies of nickel cobalt phosphate electrodes. The microspheres with nanocracks like morphology of E-NCP4 electrode with lower charge transfer resistance (0.2 Ω) offers higher electrochemical response than other electrodes. The microspheres with nanocracks like morphology of $Ni_{1.44}Co_{1.56}(PO_4)_2$ thin film electrode exhibits maximum specific capacitance of 2286 F g^{-1} at current density of 1.5 A g^{-1} and good capacitive retention (~81 %) over 3000 cycles. The good electrochemical capacitive results suggest that, electrodeposited $Ni_{1.44}Co_{1.56}(PO_4)_2$ thin film can be excellent choice as a cathode for asymmetric supercapacitor device fabrication.

4.3 References

1. A. Arico, P. Bruce, B. Scrosati, J. Tarascon, W. Schalkwijk, Nat. Mater., 4 (2005) 366-377.
2. L. Zhang, X. Zhao, Chem. Soc. Rev., 38 (2009) 2520-2531.
3. C. Abbey, G. Joos, IEEE Trans. Ind. Appl., 43 (2007) 769-776.
4. Q. Lu, M. Lattanzi, Y. Chen, X. Kou, W. Li, X. Fan, K. Unruh, J. Chen J. Xiao, Angew. Chem. Int. Ed., 50 (2011) 6847-6850.
5. H. Chen, J. Jiang, Y. Zhao, L. Zhang, D. Guo, D. Xia, J. Mater. Chem. A, 3 (2015) 428-437.
6. J. Li, M. Liu, L. Kong, D. Wang, Y. Hu, W. Han, L. Kang, RSC Adv., 5 (2015) 41721-41728.
7. X. Li, A. Elshahawy, C. Guan, J. Wang, Small, 13 (2017) 1701530-1701554.
8. A. Mirghni, M. Madito, K. Oyedotun, T. Masikhwa, N. Ndiaye, S. Ray, N. Manyala, RSC Adv., 8 (2018) 11608-11621
9. X. Peng, H. Chai, Y. Cao, Y. Wang, H. Dong, D. Jia, W. Zhou, Mater. Today Energy, 7 (2018) 129-135.
10. B. Senthilkumar, Z. Khan, S. Park, K. Kim, H. Ko, Y. Kim, J. Mater. Chem. A, 3 (2015) 21553-21561

11. F. Omar, A. Numan, N. Duraisamy, S. Bashir, K. Ramesh, S. Ramesh, RSC Adv., 6 (2016) 76298-76306.

12. Y. Gao, J. Zhao, Z. Run, G. Zhang, H. Pang, Dalton Trans., 43 (2014) 17000-17005.

13. H. Li, H. Yu, J. Zhai , L. Sun, H. Yang, S. Xie, Mater. Lett., 152 (2015) 25-28.

14. H. Pang, S. Wang, W. Shao, S. Zhao, B. Yan, X. Li, S. Li, J. Chen, W. Du, Nanoscale, 5 (2013) 5752-5757.

15. M. Liu, J. Li, Y. Hu, Q. Yang, L. Kang, Electrochim. Acta, 201 (2016) 142-150.

16. Z. Khan, B. Senthilkumar, S. Lim, R. Shanker, Y. Kim, H. Ko, Adv. Mater. Interfaces, 4 (2017) 1700059 (1-7).

17. D. Patil, B. Koteswararao, K. Begari, A. Yogi, M. Moussa, D. Dubal, ACS Appl. Energy Mater., 2 (2019) 2972-2981.

18. M. Liu, L. Kong, C. Lu, X. Ma, X. Li, Y. Luo, L. Kang, J. Mater. Chem. A, 1 (2013) 1380-1387.

19. H. Chen, J. Jiang, L. Zhang, T. Qi, D. Xia, H. Wan, J. Power Sources, 248 (2014) 28-36.

20. F. Yang, J. Yao, F. Liu, H. He, M. Zhou, P. Xiao, Y. Zhang, J. Mater. Chem. A, 1 (2013) 594-601.

21. U. Patil, J. Sohn, S. Kulkarni, S. Lee, H. Park, K. Gurav, S. Jun, ACS Appl. Mater. Interfaces, 6 (2014) 2450-2458.

22. C. Chen, N. Zhang, Y. He, B. Liang, R. Ma, X. Liu, ACS Appl. Mater. Interfaces, 8 (2016) 23114-23121.

23. B. Li, P. Gu, Y. Feng, G. Zhang, K. Huang, H. Xue, H. Pang, Adv. Funct. Mater., 27 (2017) 1605784-1605795.

24. Y. Tang, Z. Liu, W. Guo, T. Chen, Y. Qiao, S. Mu, Y. Zhao, F. Gao, Electrochim. Acta, 190 (2016) 118-125.

25. J. Zhang, Y. Yang, Z. Zhang, X. Xu, X. Wang, J. Mater. Chem. A, 2 (2014) 20182-20188.

26. W. E. G. Hansal, B. Tury, M. Halmdienst, M. Varsanyi, W. Kautek, Electrochim. Acta, 52 (2006) 1145-1151.

27. S. Navale, V. Mali, S. Pawar, R. Mane, M. Naushad, F. Stadler, V. Patil, RSC Adv., 5 (2015) 51961-51965.

28. H. Wen, M. Cao, G. Sun, W. Xu, D. Wang, X. Zhang, C. Hu, J. Phys. Chem. C, 112 (2008) 15948-15955.

29. T. Nguyen, V. Nguyen, R. Deivasigamani, D. Kharismadewi, Y. Iwai, J. Shim, Solid State Sci., 53 (2016) 71-77.

30. H. Liu, T. Chin, S. Yung, Mater. Chem. Phys., 50 (1997) 1-10.

31. N. Prokopchuk, V. Kopilevich, L. Voitenko, Russ. J. Appl. Chem., 81 (2008) 386-391.

32. M. Al-Omair, A. Touny, M. Saleh, J. Power Sources, 342 (2017) 1032-1039.

33. D. Yang, Q. Yu, L. Gao, L. Mao, J. Yang, Appl. Surf. Sci., 416 (2017) 503-510.

34. C. Lee, F. Omar, A. Numan, N. Duraisamy, K. Ramesh, S. Ramesh, J. Solid State Electrochem., 21 (2017) 3205-3213.

35. N. Priyadharsini, A. Shanmugavani, L. Vasylechko, R. Selvan, Ionics, 24 (2018) 2073-2082.

36. P. Noisong, C. Danvirutai, T. Srithanratana, B. Boonchom, Solid State Sci., 10 (2008) 1598-1604.

37. Y. Zhu, Y. Liu, T. Ren, Z. Yuan, Nanoscale, 6 (2014) 6627-6636.

38. J. Chang, Q. Lv, G. Li, J. Ge, C. Liu, W. Xing, Appl. Catal. B, 204 (2017) 486-496.

39. W. Bian, Y. Huang, X. Xu, M. Din, G. Xie, X. Wang, ACS Appl. Mater. Interfaces, 10 (2018) 9407-9414.

40. H. Shao, N. Padmanathan, D. McNulty, C. Dwyer, K. Razeeb, ACS Appl. Mater. Interfaces, 8 (2016) 28592-28598.

41. N. Jiang, B. You, M. Sheng, Y. Sun, ChemCatChem, 8 (2016) 106-112.

42. T. Sun, L. Xu, Y. Yan, A. Zakhidov, R. Baughman, J. Chen, ACS Catal., 6 (2016) 1446-1450.

43. P. Feng, X. Cheng, J. Li, X. Luo, ChemistrySelect, 3 (2018) 760-764.

44. J. Li, W. Xu, D. Zhou, J. Luo, D. Zhang, P. Xu, L. Wei, D. Yuan, J. Mater. Sci., 53 (2018) 2077-2086.

45. X. Li, R. Ding, W. Shi, Q. Xu, E. Liu, Chem. Eur. J., 23 (2017) 6896-6904.

46. X. Bai, Q. Liu, Z. Lu, J. Liu, R. Chen, R. Li, D. Song, X. Jing, P. Liu, J. Wang, ACS Sustain. Chem. Eng., 5 (2017) 9923-9934.

47. M. Sathiya, A. Prakash, K. Ramesha, J. Tarascon, A. Shukla, J. Am. Chem. Soc., 133 (2011) 16291-16299.

48. H. Kim, J. Cook, H. Lin, J. Ko, S. Tolbert, V. Ozolins, B. Dunn, Nat. Mater., 16 (2017) 454-460.

49. P. Yang, Z. Wu, Y. Jiang, Z. Pan, W. Tian, L. Jiang, L. Hu, Adv. Energy Mater., 8 (2018) 1801392-1801402.

50. J. Duay, S. Sherrill, Z. Gui, E. Gillette, S. Lee, ACS Nano, 7 (2013) 1200-1214.

51. S. Kandalkar, H. Lee, S. Seo, K. Lee, C. Kim, J. Mater. Sci., 46 (2011) 2977-2981.

52. F. Omar, A. Numan, S. Bashir, N. Duraisamy, R. Vikneswaran, Y. Loo, K. Ramesh, S. Ramesh, Electrochim. Acta, 273 (2018) 216-228.

53. K. Sankar, Y. Seo, S. Lee, S. Jun, ACS Appl. Mater. Interfaces, 10 (2018) 8045-8056.

54. F. Butt, M. Tahir, C. Cao, F. Idress, R. Ahmed, W. Khan, Z. Ali, N. Mohmood, M. Tanveer, A. Mohmood, I. Aslam, ACS Appl. Mater. Interfaces, 16 (2014) 13635-13641.

55. J. Cherusseria, K. Kar, J. Mater. Chem. A, 4 (2016) 9910-9922.

56. Z. Huang, G. Natu, Z. Ji, P. Hasin, Y. Wu, J. Phys. Chem. C, 115 (2011) 25109-25114.

57. P. Deshmukh, S. Pusawale, V. Jamadade, U. Patil, C. Lokhande, J. Alloys Compd., 509 (2011) 5064-5069.

58. D. Dubal, D. Dhawale, R. Salunkhe, C. Lokhande, J. Electrochem. Soc., 157 (2010) A812-A817.

59. M. Singh, S. Semwal, A. Kumar, S. Singh, Turk. J. Elec. Eng. & Comp. Sci., 23 (2015) 2208-2214.

CHAPTER – V

ASYMMETRIC SUPERCAPACITOR DEVICE FABRICATION AND PERFORMANCE EVALUATION

5.1 Introduction

The supercapacitors and batteries are most liked energy storage devices and they are used in smart, portable and flexible technologies due to higher storage capacity [1, 2]. In comparison with batteries, the supercapacitors gain much attention because of high charge-discharge rate, high power and long cyclic stability [3, 4]. In case of supercapacitor, the terms of energy and power density are related to rate of charging-discharging, potential window and capacitance [5]. Still, low energy density values of supercapacitors than batteries restricts their usage in various applications. The energy density of supercapacitor is depended upon specific capacitance and operational potential window. So, the energy density can be enhanced by increasing either one of them or both and it can be achieved by developing electrode material with high capacitance, electrolytes with wide potential window or combined system [6]. The overall performance of device depends on the electrochemical properties of active electrode material and electrolyte. Therefore, the good active material needs to corroborate with proper electrolyte for higher performance of supercapacitor device.

According to requirement of energy density, two types of devices are generally fabricated such as symmetric and asymmetric. The same or different kinds (EDLCs and pseudocapacitive) of electrode materials are used to develop the symmetric and asymmetric supercapacitor devices. The asymmetric device is more beneficial than the symmetric one, since the electrodes in asymmetric device are based on the EDLC capacitive and pseudocapacitive mechanism which can provide large working voltage, higher energy density and long term stability [7]. For this purpose, the asymmetric devices were fabricated by combining electrodes with different working potential windows and charge storage mechanisms.

In present work, asymmetric aqueous and solid state supercapacitor devices are prepared using good performing nickel cobalt phosphate thin film as a cathode and rGO as an anode material to achieve high performance. This chapter is divided into three sections (A, B and C). Section 'A' deals with preparation and electrochemical performance evaluation of rGO electrode. Section 'B' explains the fabrication and electrochemical performance evaluation of aqueous asymmetric devices and section 'C' is related to fabrication and electrochemical performance evaluation of asymmetric flexible solid state devices.

<div align="center">

SECTION – A

SYNTHESIS, CHARACTERIZATION AND SUPERCAPACITIVE

PERFORMANCE EVALUTION OF REDUCED GRAPHENE OXIDE

</div>

5.2.A.1 Introduction

In the development of asymmetric supercapacitor devices, the carbon based materials are largely investigated because of their good specific capacitance, excellent electrical conductivity and high power density [8-11]. Generally, carbon based materials such as activated carbon, CNTs, carbon aerogels, graphene, etc. were used as negative electrode in the asymmetric devices [12, 13]. Among them, graphene is most promising material due to its unique physical, chemical, electrical and mechanical properties, which are useful to apply in various applications. So, various physical and chemical methods are used to produce graphene. Among them, the Hummer's method has been paid the most intensive attention due to its high efficiency and satisfying reaction safety [14]. Also, it is more prominent and suitable for mass production. Further, the reduction of graphene oxide improves its electrical conductivity and possesses large surface area. Among various reduction methods for graphene oxide, chemical reduction of graphene oxide is feasible and attractive method, to produce

single layered reduced graphene oxide in large scale at relatively low cost. Present section describes the preparation of reduced graphene oxide by modified Hummer's method followed by hydrothermal reduction. Further, the reduced graphene oxide films are characterized by different techniques and supercapacitive performance is evaluated in 1 M KOH electrolyte.

5.2.A.2 Experimental details

5.2.A.2.1 Chemicals

Graphite flakes, sulfuric acid (H_2SO_4), potassium permanganate ($KMnO_4$), sodium nitrate ($NaNO_3$), hydrogen chloride (HCl) and hydrogen peroxide (H_2O_2) were purchased from Sigma Aldrich and used as received to synthesize graphene oxide.

5.2.A.2.2 Synthesis of graphene oxide (GO)

The graphene oxide (GO) was synthesized by modified Hummer's method [15]. In primary step, graphite flakes (3 g) and $NaNO_3$ (1.5 g) mixture was prepared then H_2SO_4 (69 ml) added slowly in mixture, maintained at 273 K. Then, $KMnO_4$ (9 g) was added slowly in the mixture with stirring and temperature maintained below 293 K. After that, the prepared mixture was stirred for 12h at room temperature. Later, double distilled water (420 ml) with 30 % H_2O_2 (3 ml) was added slowly (30 min) maintaining temperature below 308 K. Furthermore, HCl (50 ml) with DDW (500 ml) was added in the mixture for washing purpose. Then, resultant mixture was centrifuged at low rpm (2000) to remove unreacted graphite flakes and further centrifuged at high rpm (10000) to collect GO nanosheets. The resulting GO suspension solution was washed and centrifuged until supernatant becomes neutral (pH~7).

5.2.A.2.3 Synthesis of reduced graphene oxide (rGO)

For the preparation of graphene hydrogel, the well dispersed 50 ml GO solution (4 mg ml^{-1}) was heated in hydrothermal autoclave at 433 K for 12h. Prepared hydrogel

was cooled using liquid nitrogen for solidification and freeze dried for 70h. Finally, the reduced graphene oxide foam was obtained and crushed into powder. Then, the slurry coating technique is adapted to prepare rGO electrode (anode).

5.2.A.3 Results and discussion

5.2.A.3.1 XRD studies

The XRD patterns of GO and rGO are shown in Fig. 5.1. The intense characteristic peak at 11^0 in the XRD of GO confirms the successful preparation of GO by modified Hummer's method [16]. The broad peak at 24.9^0 observed in the XRD pattern of rGO, confirms stacking of GO sheets due to removal of oxygen containing groups and also it indicates formation of multilayered rGO nanosheets [17]. A change in peak from 11 to 24.9^0 confirms successful reduction of GO to rGO.
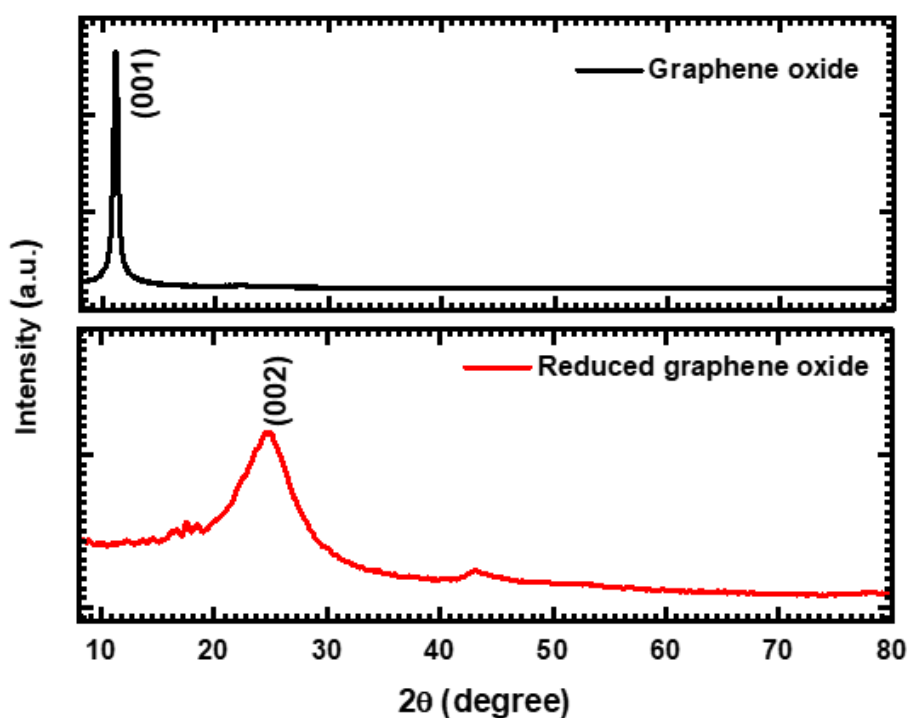
Fig. 5.1 XRD patterns of GO and rGO samples.

5.2.A.3.2 Raman studies

The structural and electronic properties of graphene were characterized by Raman spectroscopy, which is popular for the identification of defects and disordered

structures of graphene. Raman spectroscopy is mostly useful for carbon based material characterization. The two characteristic peaks of GO in Raman spectra are G-band and D-band. The D-band arises due to breaking translational symmetry or defects and the G-band arises due to first-order scattering of sp^2 domain of graphite. The relative response of D and G-bands depend on the quantity of disorder present in the graphitic material [17]. The Raman spectra of GO and rGO samples are shown in Fig. 5.2. The G-band and D-band for GO and rGO samples arise at 1342 and 1604 cm^{-1}, respectively. The ratio of D/G intensity increases after reduction of GO sample.
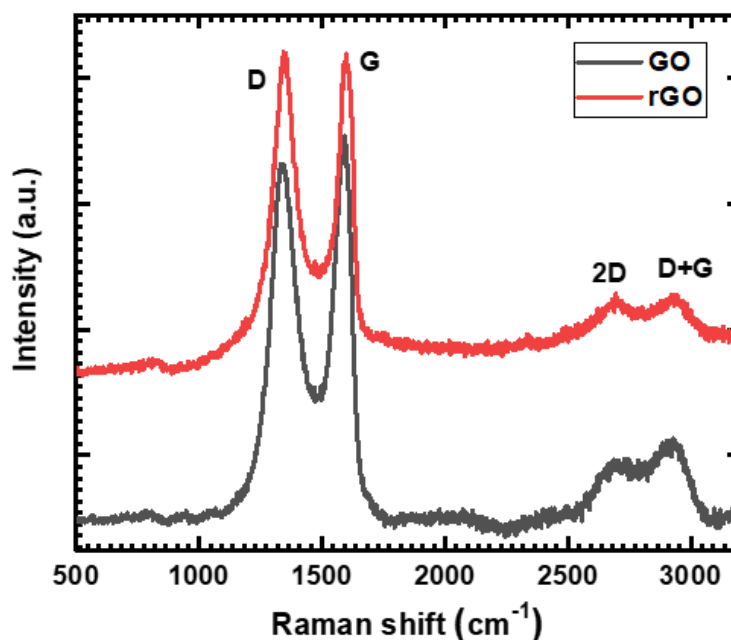
Fig. 5.2 Raman spectra of GO and rGO samples.

Interestingly, the D/G intensity ratio increased from 0.92 to 1.01, indicates that during reduction some defects are introduced in the structure of GO [16]. Also, it reveals change in electronic conjugation state due to reduction process. Furthermore, the peaks at 2697 and 2934 cm^{-1} correspond to 2D and D+G bands, which correspond to better graphitization and no charge transfer due to absence of impurities [18]. The XRD and Raman results confirm the successful conversion of GO to rGO by hydrothermal reduction.

5.2.A.4 Supercapacitive performance of reduced graphene oxide electrode

5.2.A.4.1 Preparation of reduced graphene oxide (rGO) electrode

The electrode of rGO is prepared by slurry coating technique, combining 75% rGO, 20% carbon black, 5% polyvinylidene fluoride (PVDF) with N-methyl 2-pyrrolidone (NMP) for making slurry. The prepared slurry coated on stainless steel substrate (1 X 1 cm^2) and dried at 333 K for an hour. The prepared thin film electrode was used for further electrochemical characterization.

5.2.A.4.2 Cyclic voltammetry (CV) studies

The CV curves of rGO electrode at various scan rates from 5-100 mV s^{-1} in the optimized potential window of -1 to 0 V/SCE in 1 M KOH electrolyte are shown in Fig. 5.3. The quasi-rectangular shape of CV curves confirms EDLC based capacitive nature of rGO electrode. Also, large and symmetric current response in anodic and cathodic direction is observed which represents EDLC capacitive nature of material. The area under the CV curve increases with increasing scan rate, this shows voltammetric current is proportional to the scan rate of CV and represents typical EDLC capacitive feature of electrode.
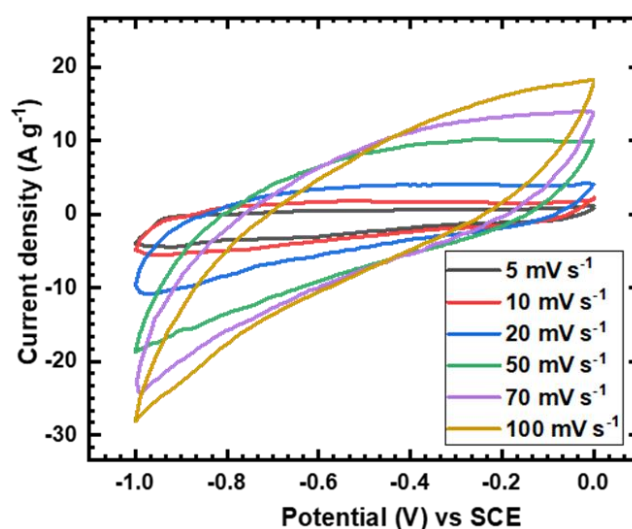
Fig. 5.3 The CV curves of rGO electrode at various scan rates from 5-100 mV s^{-1} in 1 M KOH electrolyte.

5.2.A.4.3 Galvanostatic charge-discharge (GCD) studies

The GCD study of rGO electrode carried out in the potential window of 0 to -1 V/SCE is shown in Fig. 5.4 (a). The nearly linear charge-discharge curves are obtained for rGO electrode, which shows its double layer capacitive nature. The specific capacitance of rGO electrode calculated by GCD analysis and is plotted in Fig. 5.4 (b) as a function of current density. The specific capacitance of 200 F g^{-1} is obtained for rGO electrode at 2 A g^{-1} current density and it decreases to 171 F g^{-1} at the current density of 2.6 A g^{-1}.
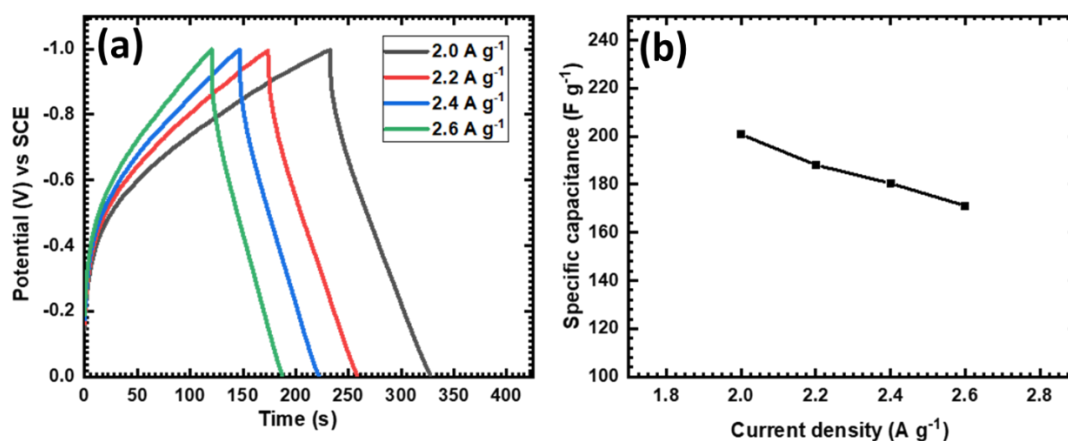
Fig. 5.4 (a) The GCD curves of rGO electrode at various current densities from 2.0-2.6 A g^{-1} and (b) the plot of specific capacitance of rGO electrode at various current densities.

5.2.A.4.4 Stability studies

The electrochemical stability (in terms of capacitive retention) of rGO electrode tested by GCD analysis for 3000 cycles at 8 A g^{-1} current density is shown in Fig. 5.5. The rGO electrode shows 73 % capacitive retention after 3000 cycles. A decrement in charge-discharge time in initial and final GCD cycles is observed and shown as inset Fig. 5.5. Moreover, observed decrement in capacitance may be due to depletion of minute active material during cycling.
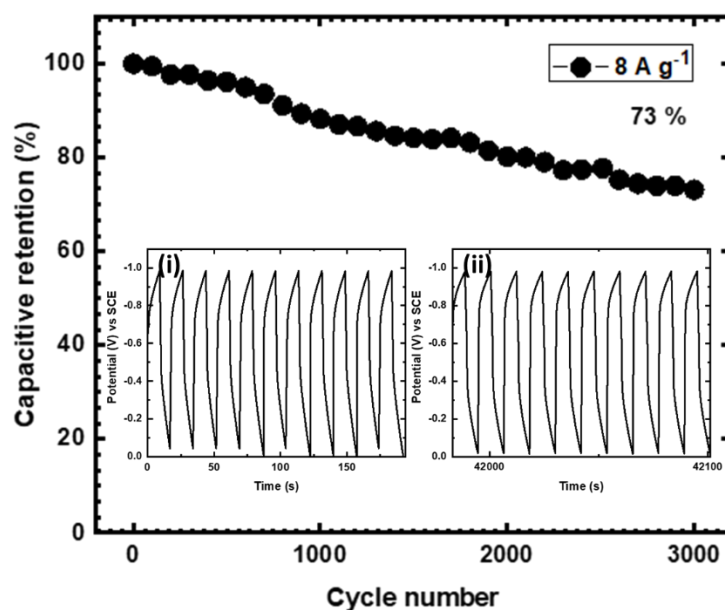
Fig. 5.5 Capacitive retention of rGO electrode at 8 A g^{-1} current density for 3000

cycles (inset: (i) initial and (ii) last 10 GCD cycles).

5.2.A.4.5 EIS study

The Nyquist plot of rGO electrode is presented in Fig. 5.6. The fitted circuit is

shown as inset of Fig. 5.6.
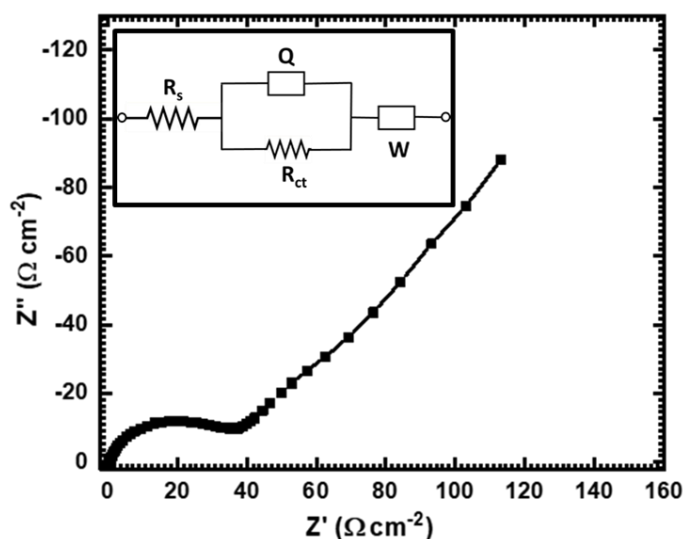
Fig. 5.6 Nyquist plot of rGO electrode (inset: equivalent circuit of the fitted data).

In fitted circuit, R_s is the solution resistance (0.45 Ω), R_{ct} is charge transfer resistance

(40 Ω), W is Warburg impedance (0.033 Ω) and Q is general imperfect capacitor (0.903

mF) with 0.75 correction factor (n). Imperfect capacitor is obtained due to semi-infinite

diffusion of charges [19]. The higher electrochemical performance of rGO electrode attributed to smaller values of R_s and R_{ct}.

5.2.A.5 Conclusions

In summary, modified Hummer's method followed by hydrothermal treatment is used to produce rGO nanosheets. The reduction of GO to rGO is confirmed by XRD and Raman analyses. The rGO electrode shows good supercapacitive performance with highest specific capacitance of 200 F g^{-1} at 2 A g^{-1} current density. Also, it exhibits ~73 % capacitive retention after 3000 GCD cycles. The results suggest that, rGO electrode is a promising candidate (anode) for supercapacitor application.

SECTION-B

FABRICATION AND ELECTROCHEMICAL PERFORMANCE EVALUATION OF ASYMMETRIC AQUEOUS SUPERCAPACITOR (AAS) DEVICES

5.2.B.1 Introduction

The present section deals with the electrochemical performance evaluation of asymmetric aqueous devices based on nickel cobalt phosphate as the cathode and rGO as the anode. The electrochemical performance of prepared asymmetric aqueous devices is measured using CV, GCD, cyclic stability and EIS techniques. The aqueous electrolyte is used, since it is inexpensive and easy to handle, and does not require any specific arrangements. Also, aqueous electrolyte has high ionic conductivity than solid electrolyte which also simplifies the fabrication and assembly process.

5.2.B.2 Electrodes preparation

As concluded from chapters III and IV, the best performing nickel cobalt phosphate electrodes are selected for device fabrication. The nickel cobalt phosphate (positive) electrodes are prepared by chemical bath deposition ($Ni_{1.38}Co_{1.62}(PO_4)_2$) and

electrodeposition ($Ni_{1.44}Co_{1.56}(PO_4)_2$) methods on large area of flexible stainless steel substrate (5 X 5 cm^2) using preparative parameters described in chapters III and IV, respectively. Also, the rGO (negative) electrode is prepared as discussed in section A of this chapter.

5.2.B.3 Electrochemical supercapacitive performance evaluation of chemical bath deposited $Ni_{1.38}Co_{1.62}(PO_4)_2$//rGO asymmetric aqueous supercapacitor (AAS) device

The important requirement for asymmetric device is that, both electrodes (positive and negative) should have different operating potential windows. Asymmetric device was fabricated using chemical bath deposited nickel cobalt phosphate as positive and rGO as negative electrodes with 1 M KOH as electrolyte. The important task in preparation of AAS device for high electrochemical performance is the balance of charge between both electrodes through mass variation, and it is determined by following equation,

$$\frac{m_+}{m_-} = \frac{C_- \times \Delta V_-}{C_+ \times \Delta V_+}$$

(5.1)

where, $m_{(+\,or-)}$, $\Delta V_{(+or-)}$, and $C_{(+or-)}$ is the mass of active material (g), potential window (V), and specific capacitance (F g^{-1}) of positive and negative electrodes, respectively [20]. In this case, the operative potential window (0 to 0.5 and -1 to 0 V/SCE) and capacitances (1116 and 200 F g^{-1}) of positive and negative electrodes are different. The calculated optimal mass ratio of positive and negative electrode is found to be 0.35:1. Accordingly, the obtained optimum mass is used to fabricate asymmetric device.

The electrochemical performance of $Ni_{1.38}Co_{1.62}(PO_4)_2$//rGO AAS device is tested by two electrode cell configuration. The potential window of

$Ni_{1.38}Co_{1.62}(PO_4)_2$//rGO AAS device optimized in range of 0 to 1.2-1.7 V and displayed in Fig. 5.7 (a). The quasi-rectangular shaped CV curves are obtained up to potential window of 0 to 1.6 V and sudden increase in current is observed due to oxygen evolution reaction process at 1.7 V, which may be responsible for irreversible reaction. From this study, the 0 to 1.6 V potential window is chosen for the electrochemical study of $Ni_{1.38}Co_{1.62}(PO_4)_2$//rGO AAS device. The CV curves of $Ni_{1.38}Co_{1.62}(PO_4)_2$//rGO AAS device at various scan rates from 5-100 mV s^{-1} within the potential window of 0 to 1.6 V are shown in Fig. 5.7 (b). Reversible and similar shape of CV curves is observed even at higher scan rate suggests good rate capability of device.
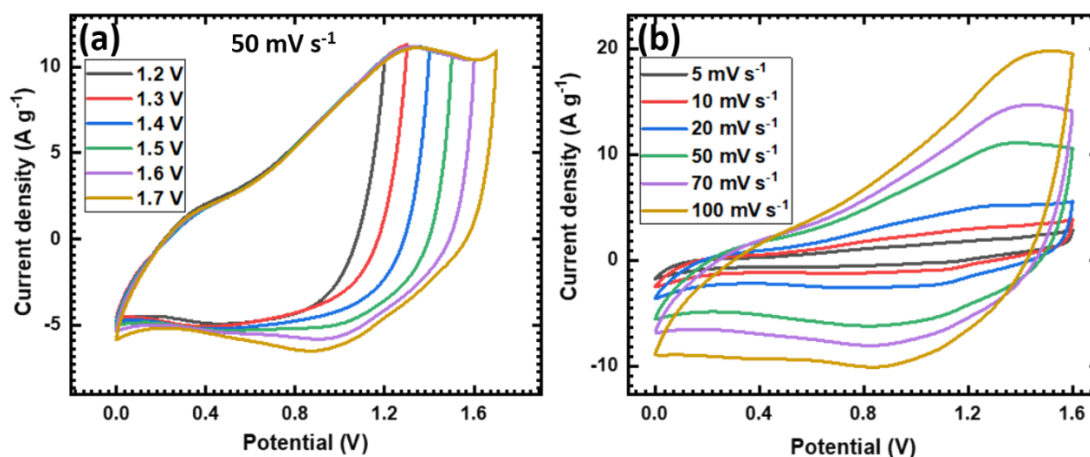
Fig. 5.7 The CV curves of $Ni_{1.38}Co_{1.62}(PO_4)_2$//rGO AAS device (a) in different potential windows and (b) at different scan rates from 5-100 mV s^{-1}.

The GCD curves of $Ni_{1.38}Co_{1.62}(PO_4)_2$//rGO AAS device in different potential windows at a constant current density of 2.1 A g^{-1} are shown in Fig. 5.8 (a). The GCD curves show better performance in potential window of 0 to 1.6 V by displaying symmetric nature. So, from CV and GCD analyses the operational potential window of 0 to 1.6 V was chosen for AAS device and used for further study. The GCD graphs of $Ni_{1.38}Co_{1.62}(PO_4)_2$//rGO AAS device at different current densities from 1.3-2.1 A g^{-1} are displayed in Fig. 5.8 (b). The non-linear GCD curves are observed for

$Ni_{1.38}Co_{1.62}(PO_4)_2$//rGO AAS device. The specific capacitance of AAS device calculated from GCD curves is illustrated in Fig. 5.8 (c). The AAS device achieves highest specific capacitance of 120 F g^{-1} at 1.3 A g^{-1} current density and it decreases up to 103 F g^{-1} at current density of 2.1 A g^{-1}. The specific capacitance of device decreases with an increase in current density due to less time available for electrode-electrolyte interaction [21, 22].
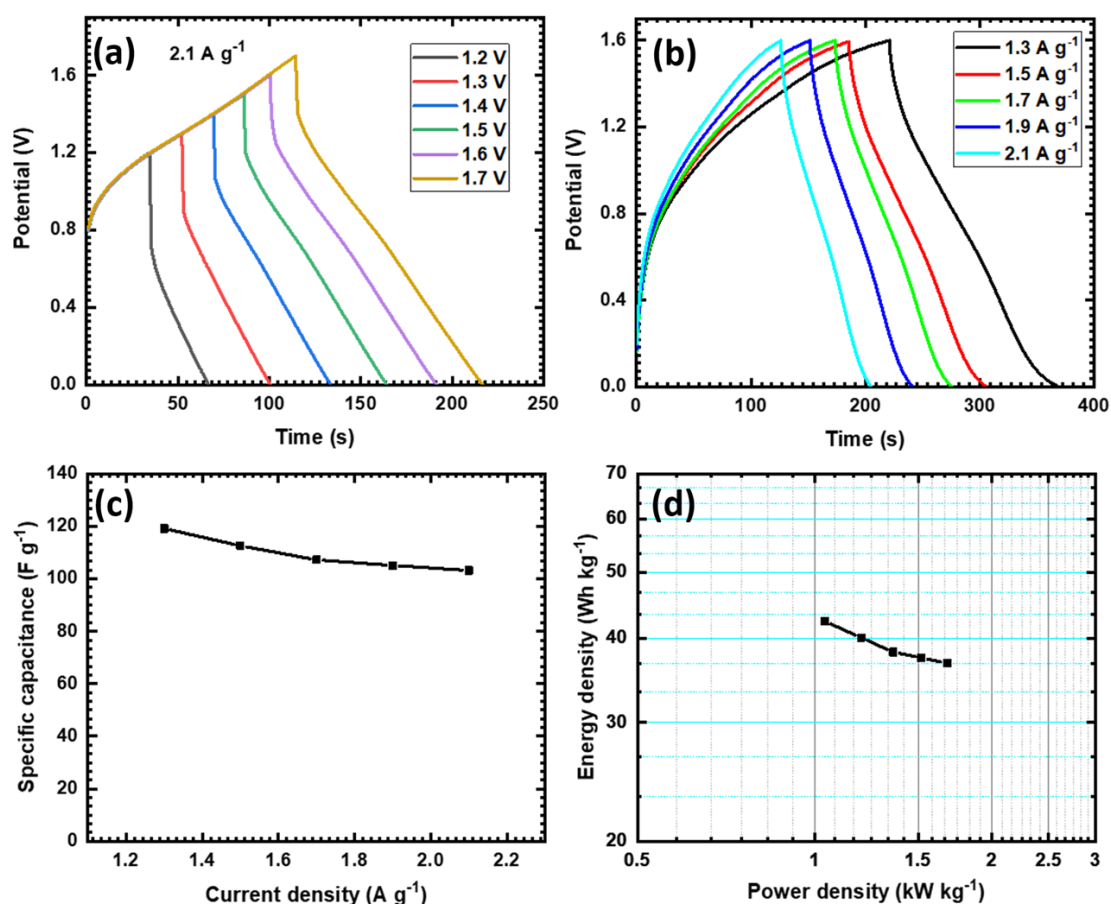

Fig. 5.8 The GCD curves of $Ni_{1.38}Co_{1.62}(PO_4)_2$//rGO AAS device (a) in different potential windows and (b) at different current densities. Plot of specific capacitance as a function of current density (c) and the Ragone plot (d) of $Ni_{1.38}Co_{1.62}(PO_4)_2$//rGO AAS device.

The AAS device maintained 89 % specific capacitance at higher current densities, which suggests that it is efficient at high current densities. The energy and power

densities are two crucial factors in the supercapacitor performance evaluation. The

energy and power densities of AAS device are calculated and illustrated in Fig. 5.8 (d).

The AAS device achieves highest energy density of 42.3 Wh kg^{-1} at 1 kW kg^{-1} power

density and it decreases up to 36.7 Wh kg^{-1} at power density of 1.7 kW kg^{-1}.

The stability (in terms of capacitive retention) of AAS device is tested by

continuous 4000 GCD cycles at the current density of 12 A g^{-1}. The cyclic stability of

AAS device with cycle number is shown in Fig. 5.9.
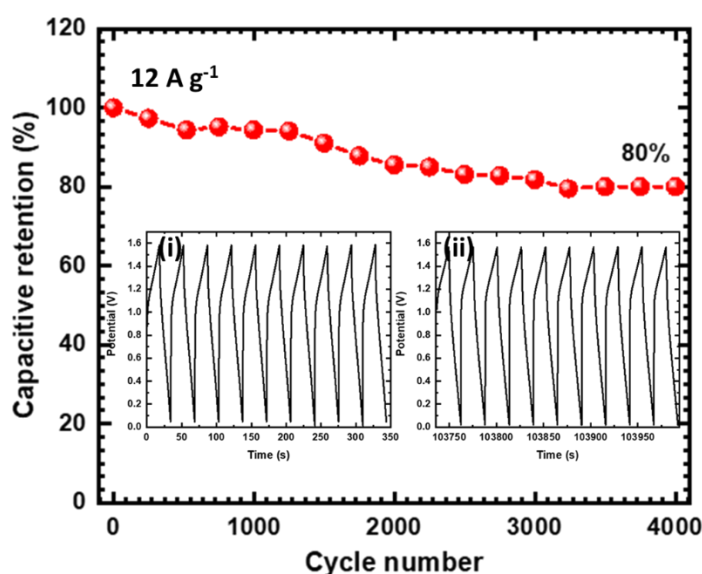
Fig. 5.9 The plot of capacitive retention at the current density of 12 A g^{-1} with respect
to cycle numbers (4000) of $Ni_{1.38}Co_{1.62}(PO_4)_2$//rGO AAS device (inset: (i) initial and
(ii) last 10 GCD cycles).

After 4000 continuous cycles, the AAS device shows ~80 % of initial capacitance

retention. Initial and final 10 GCD cycles are shown as inset of Fig. 5.9. The decrement

in capacitance observed due to minute depletion of active material after several number

of charge-discharge cycles. The good cyclic stability promotes usage of nickel cobalt

phosphate and rGO electrodes in the energy storage device application.

Furthermore, the properties of ion transfer in AAS device are investigated by EIS

analysis. The Nyquist plot of AAS device is presented in Fig. 5.10. The equivalent

circuit of impedance spectroscopy is shown as inset of Fig. 5.10. Low R_s (1.89 Ω) and

R_{ct} (70 Ω) values are observed due to high electrochemical conductivity of electrodes.

Also, in fitted circuit W (0.026 Ω) and Q (0.2 mF) are Warburg impedance and general

imperfect capacitor (correction factor n=0.84), respectively. The complementary nature

of both electrodes is responsible for good electrochemical performance of AAS device

with improved operating potential window, specific capacitance and energy density.
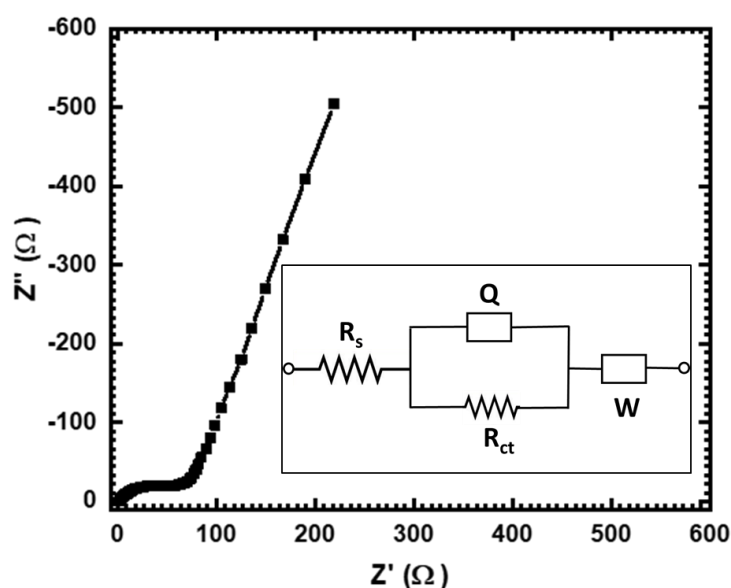
Fig. 5.10 Nyquist plot of $Ni_{1.38}Co_{1.62}(PO_4)_2$//rGO AAS device (inset: equivalent

circuit of the fitted data).

5.2.B.4 Electrochemical supercapacitive performance evaluation of electrodeposited $Ni_{1.44}Co_{1.56}(PO_4)_2$//rGO asymmetric aqueous supercapacitor (AAS) device

In this case, the operative potential window (0 to 0.5 and -1 to 0 V/SCE) and

capacitances (2286 and 200 F g^{-1}) of positive ($Ni_{1.44}Co_{1.56}(PO_4)_2$) and negative (rGO)

electrodes are different. To achieve highest electrochemical performance of AAS

device, the charge balance was maintained by varying mass of electrodes and calculated

optimal mass ratio of positive and negative electrode is 0.17:1. Furthermore, the

obtained optimum mass is used to fabricate asymmetric device. The operational

potential window of $Ni_{1.44}Co_{1.56}(PO_4)_2$//rGO AAS device is found by measuring CV in range of 0 to 1.2-1.7 V. The CV curves of $Ni_{1.44}Co_{1.56}(PO_4)_2$//rGO AAS device in different potential windows at fixed 50 mV s^{-1} scan rate are shown in Fig. 5.11 (a). The CV curves in potential range of 0 to 1.6 V shows good quasi-rectangular shape and it shows sharp increment in current which demonstrates irreversible reaction. So, the optimum potential window for the AAS device from the CV analysis is found to be 0 to 1.6 V. The CV curves of AAS device at different scan rates from 5-100 mV s^{-1} are shown in Fig. 5.11 (b).
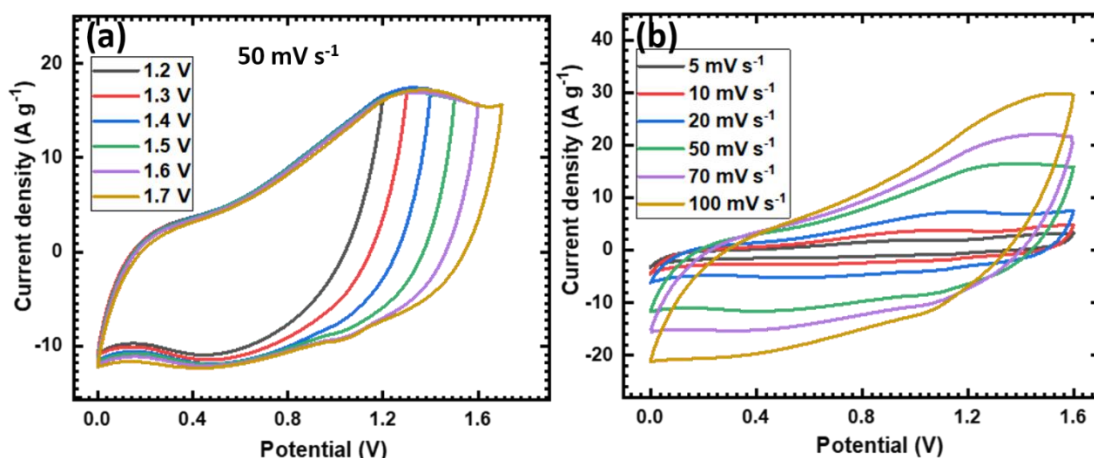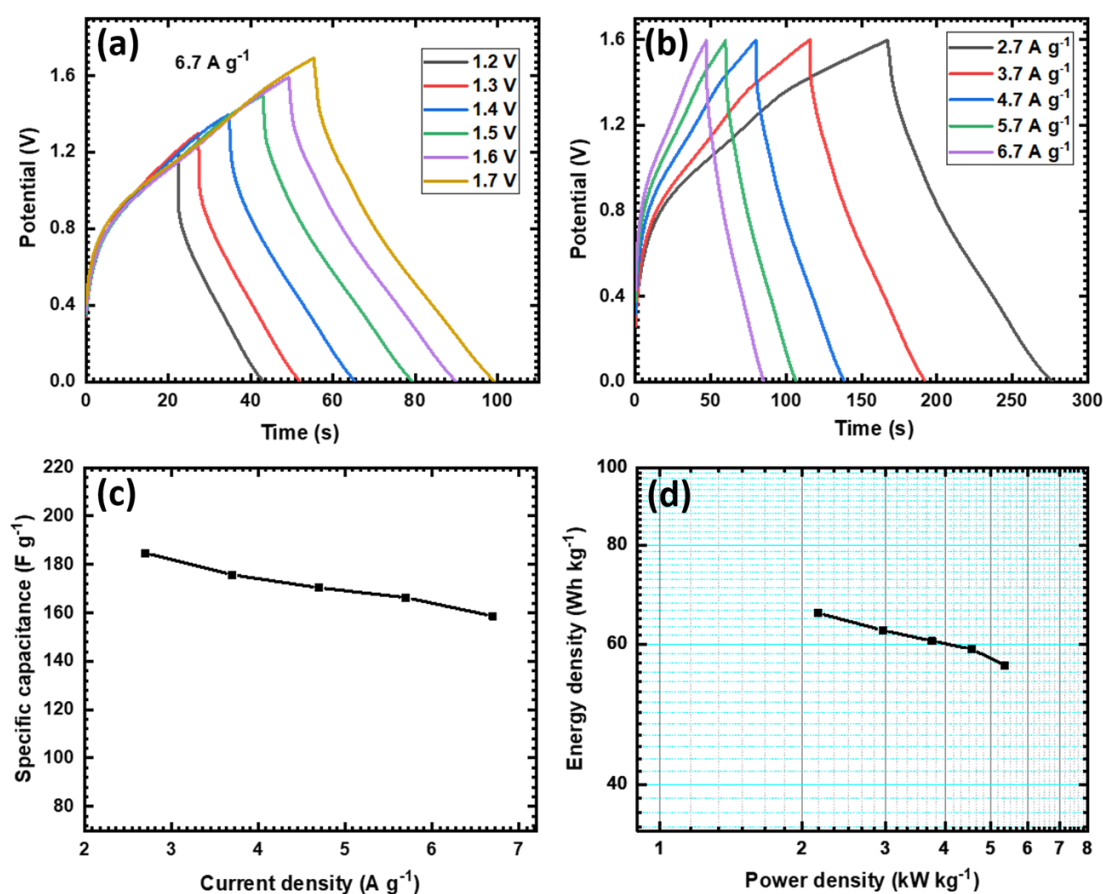

Fig. 5.11 The CV curves of $Ni_{1.44}Co_{1.56}(PO_4)_2$//rGO AAS device (a) in different potential windows and (b) at different scan rates from 5-100 mV s^{-1}.

The CV curves show approximately equal current response in cathodic and anodic regions. Also, the CV curves remain unaltered at higher scan rate indicating the good rate capability of AAS device.

The GCD curves are measured at different potential windows for finding operational potential window of $Ni_{1.44}Co_{1.56}(PO_4)_2$//rGO AAS device. The GCD curves at constant current density of 6.7 A g^{-1} in various potential windows are displayed in Fig. 5.12 (a). The symmetric GCD curves are observed from 0 to 1.6 V potential window. So, from CV and GCD analyses the optimal potential window for AAS device

was found to be 0 to 1.6 V. The GCD analysis carried out in the potential window of 0

to 1.6 V at different current densities from 2.7-6.7 A g^{-1} and corresponding graphs are

shown in Fig. 5.12 (b). As increase in current density discharging time decreases, may

be due to insufficient usage of active material at higher current density. The specific

capacitance of AAS device is calculated and plotted with respect to the current density

in Fig. 5.12 (c). The specific capacitance of device increases with decreasing current

density due to more availability of time for active material and electrolyte interaction.

Fig. 5.12 The GCD curves of Ni$_{1.44}$Co$_{1.56}$(PO$_4$)$_2$//rGO AAS device (a) in different

potential windows and (b) at different current densities. Plot of specific capacitance as

a function of current density (c) and Ragone plot (d) of Ni$_{1.44}$Co$_{1.56}$(PO$_4$)$_2$//rGO AAS

device.

The highest specific capacitance achieved by Ni$_{1.44}$Co$_{1.56}$(PO$_4$)$_2$//rGO AAS

device is 185 F g^{-1} at current density of 2.7 A g^{-1} and it decreases up to 159 F g^{-1} at

current density of 6.7 A g^{-1}. The AAS device maintains almost 86 % of specific capacitance at higher current density which suggests that device can be useful at high current density. Moreover, the energy density and power density of AAS device calculated from GCD curves are plotted in the Ragone plot as Fig. 5.12 (d). The AAS device achieves highest energy density of 65.7 Wh kg^{-1} at power density of 2.2 kW kg^{-1} and energy density decreases up to 56.4 Wh kg^{-1} at power density of 5.4 kW kg^{-1}. The asymmetric aqueous device Ni$_{1.44}$Co$_{1.56}$(PO$_4$)$_2$//rGO shows higher energy and power density as compared to available supercapacitor devices based on nickel cobalt phosphate [23-31]. But, Ni$_{1.44}$Co$_{1.56}$(PO$_4$)$_2$//rGO device shows less energy density than reported energy density by Liang et. al. [29] for KCo$_{0.33}$Ni$_{0.67}$PO$_4$//AC supercapacitor device. The main reason to obtain higher performance by Liang et. al. is due to use of nickel foam as a current collector, which added self-contribution to the total capacitance of the device. However, in present work SS substrate is used as a current collector for both positive and negative electrodes, and it doesn't interfere with the capacitive performance of device. The high energy density is achieved by Ni$_{1.44}$Co$_{1.56}$(PO$_4$)$_2$//rGO AAS device at lower current density due to slow discharge of device and at higher current density energy of supercapacitor discharge rapidly reveals a high power. The Ni$_{1.44}$Co$_{1.56}$(PO$_4$)$_2$//rGO AAS device exhibits high energy and power values. So, the device can be used at higher or lower current densities as per requirement of high power or energy values.

The GCD analysis is used to study electrochemical stability of Ni$_{1.44}$Co$_{1.56}$(PO$_4$)$_2$//rGO AAS device. The stability (in terms of capacitive retention) of AAS device is measured at 15 A g^{-1} current density for 4000 GCD cycles. The capacitance retention with respective cycles is plotted in Fig. 5.13 and the GCD curves of initial and last 10 cycles are displayed as inset of figure.
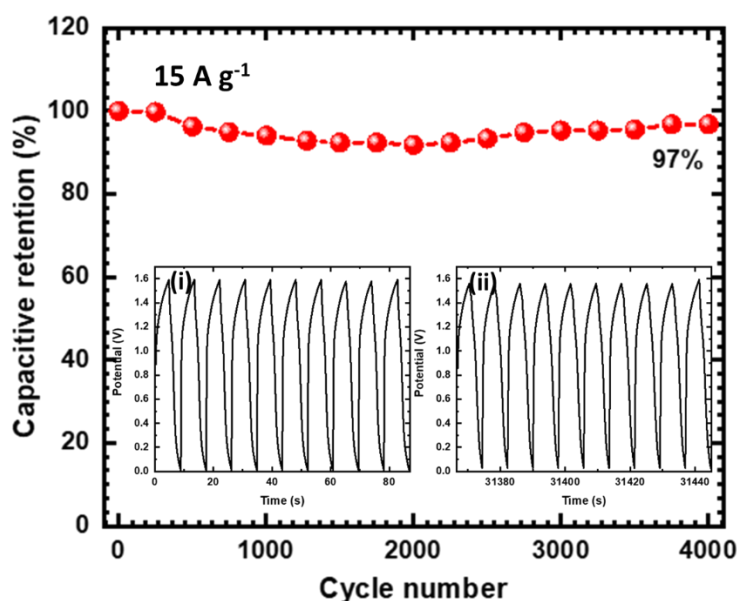
Fig. 5.13 The plot of capacitive retention at the current density of 15 A g^{-1} with

respect to cycle numbers (4000) of $Ni_{1.44}Co_{1.56}(PO_4)_2$//rGO AAS device (inset: initial

(i) and last (ii) 10 GCD cycles).

The AAS device shows 97 % capacitive retention after 4000 GCD cycles. The AAS

device shows decrement in the specific capacitance at initial cycles then increase in

specific capacitance due to expansion of electrochemical active volume of material after

several GCD cycles. The stable nature with good capacitance of AAS device

encourages further usage of electrodeposited nickel cobalt phosphate thin films and

rGO electrodes in the energy storage device application.

Nyquist plot of AAS device with an equivalent fitted circuit is shown in Fig. 5.14.

The lower values of R_s (2 Ω) and R_{ct} (72 Ω) of AAS device suggest easy interaction

between electrode and electrolyte and good contact of active material with current

collector. Also, in circuit W (0.02 Ω) and Q (0.56 mF) are Warburg impedance and

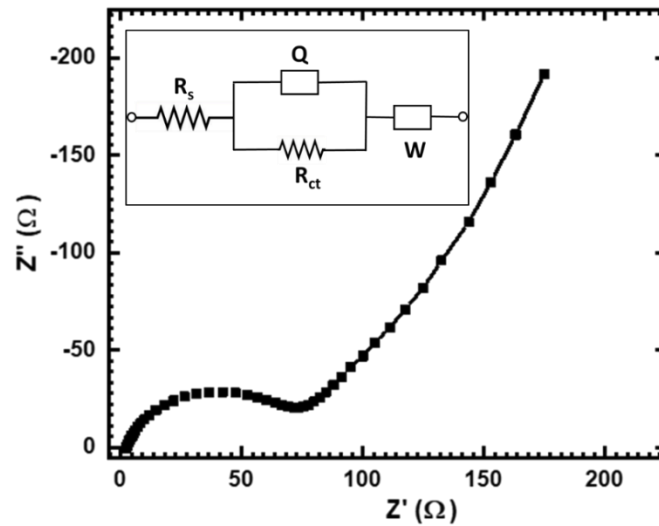general imperfect capacitor (correction factor n=0.9), respectively.

Fig. 5.14 Nyquist plot of $Ni_{1.44}Co_{1.56}(PO_4)_2$//rGO AAS device (inset: equivalent

circuit of the fitted data).

5.2.B.5 Conclusions

The aqueous asymmetric supercapacitor devices are successfully fabricated by combining nickel cobalt phosphate (prepared by CBD and electrodeposition methods) and rGO electrodes. The chemical bath deposited $Ni_{1.38}Co_{1.62}(PO_4)_2$//rGO AAS device exhibited maximum specific capacitance of 120 F g^{-1} with energy density of 42.3 Wh kg^{-1} at power density of 1 kW kg^{-1}. The electrodeposited $Ni_{1.44}Co_{1.56}(PO_4)_2$//rGO AAS device achieves higher specific capacitance than chemical bath deposited $Ni_{1.38}Co_{1.62}(PO_4)_2$//rGO AAS device. The electrodeposited $Ni_{1.44}Co_{1.56}(PO_4)_2$//rGO AAS device exhibited highest specific capacitance of 185 F g^{-1} and energy density of 65.7 Wh kg^{-1} at power density of 2.2 kW kg^{-1}. Also, the $Ni_{1.44}Co_{1.56}(PO_4)_2$//rGO AAS device retains 97 % initial capacitance after 4000 cycles. The results suggest that, AAS device fabricated using electrodeposited nickel cobalt phosphate electrode offers excellent supercapacitive performance.

SECTION-C

FABRICATION AND ELECTROCHEMICAL PERFORMANCE

EVALUATION OF ASYMMETRIC FLEXIBLE SOLID STATE

SUPERCAPACITOR (AFSSS) DEVICES

5.2.C.1 Introduction

The performance of supercapacitor device is not only depended upon the electrode material but also on the choice of electrolyte. The terms like boiling point, viscosity and freezing point of electrolytes can mostly affects the stability of device. The device with aqueous electrolyte is easy for fabrication and handling in the laboratory but practical usage is restricted due to operating temperature range [8]. In comparison with aqueous electrolyte, the solid/gel electrolyte gains great attention due to its solid nature which erases the problems arises from the aqueous electrolyte. The flexible solid state energy storage device becomes an attractive topic in the research field due to their application in flexible portable devices. Flexible energy storage device offers many advantages such as easiness in handling due to light weight, wide operational potential range and good stability [32]. Also, possible to produce in various shape and size as preferred for the application, since these devices are leakage free [6].

This section gives the information about electrochemical performance of asymmetric flexible solid state supercapacitor devices based on nickel cobalt phosphate and rGO electrodes. The electrochemical performance of prepared asymmetric flexible solid state supercapacitor devices is measured using CV, GCD, cyclic stability and EIS techniques. The chemical bath deposited nickel cobalt phosphate and electrodeposited nickel cobalt phosphate are used as positive (cathode) electrode and rGO as negative (anode) electrode to fabricate the AFSSS devices.

5.2.C.2 Experimental details

5.2.C.2.1 Preparation of PVA-KOH gel electrolyte

To prepare the AFSSS device, the water soluble PVA polymer with KOH used for the preparation of gel electrolyte. The optimized amount of PVA (3 g) was separately dissolved in 30 ml of double distilled water at 363 K under vigorous stirring. Until dissolution of polymer in water and formation of clear solution, the solution was continuously stirred. Then, 10 ml of 1 M KOH solution added in PVA solution and stirred continuously up to clear, viscous and homogeneous appearance of solution [33]. This viscous and transparent solution was used as a gel electrolyte and separator in the fabrication of AFSSS devices.

5.2.C.2.2 Fabrication of asymmetric flexible solid state supercapacitor devices

5.2.C.2.2.1 Chemical bath deposited $Ni_{1.38}Co_{1.62}(PO_4)_2$//rGO AFSSS device

The AFSSS device fabricated by comprising chemical bath deposited $Ni_{1.38}Co_{1.62}(PO_4)_2$ thin film as cathode and rGO electrode as anode with PVA-KOH as gel electrolyte as well as separator. The AFSSS device fabrication steps are illustrated in Fig. 5.15 (a-d). In first step, the large area electrodes (5 X 5 cm^2) are prepared as shown in Fig. 5.15 (a) and used as electrodes for the fabrication of AFSSS device. Then, the gel electrolyte painted on each electrode material and dried at room temperature (shown in Fig. 5.15 (b)). After drying, the edges of electrodes are sealed with plastic tape as illustrated in Fig. 5.15 (c) to avoid short circuit and again one more time the gel electrolyte painted on the surface of active material for proper contact between electrode and electrolyte. Then, the electrodes are packed together using transparent plastic strips. Later, the prepared device is pressed under hydraulic pressure of 0.5 ton for 12h. Photographs of prepared AFSSS device with it's flexibility are shown in Fig.

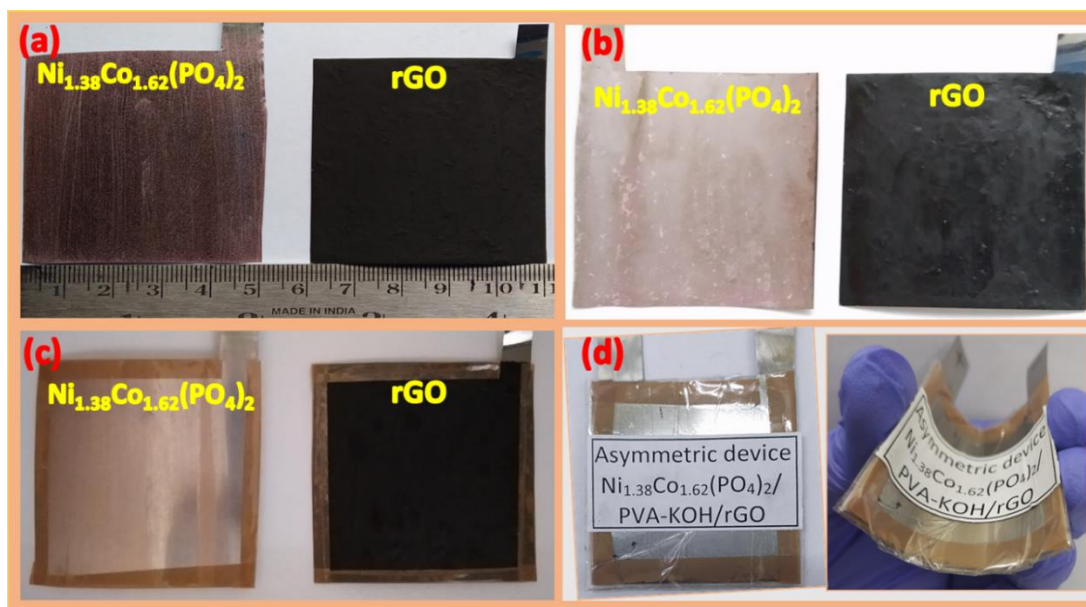5.15 (d). The electrochemical performance of AFSSS device was tested using ZIVE MP1 electrochemical workstation.

Fig. 5.15 The digital photographs of (a) $Ni_{1.38}Co_{1.62}(PO_4)_2$ (chemical bath deposited) and rGO thin film electrodes on flexible stainless steel substrate, (b) electrodes painted by PVA-KOH gel electrolyte, (c) sealed edges with tape and (d) fabricated flexible device.

5.2.C.2.2.2 Electrodeposited $Ni_{1.44}Co_{1.56}(PO_4)_2$//rGO AFSSS device

As discussed above, similar fabrication process was used for the electrodeposited $Ni_{1.44}Co_{1.56}(PO_4)_2$//rGO AFSSS device and steps are illustrated in Fig. 5.16 (a-d).
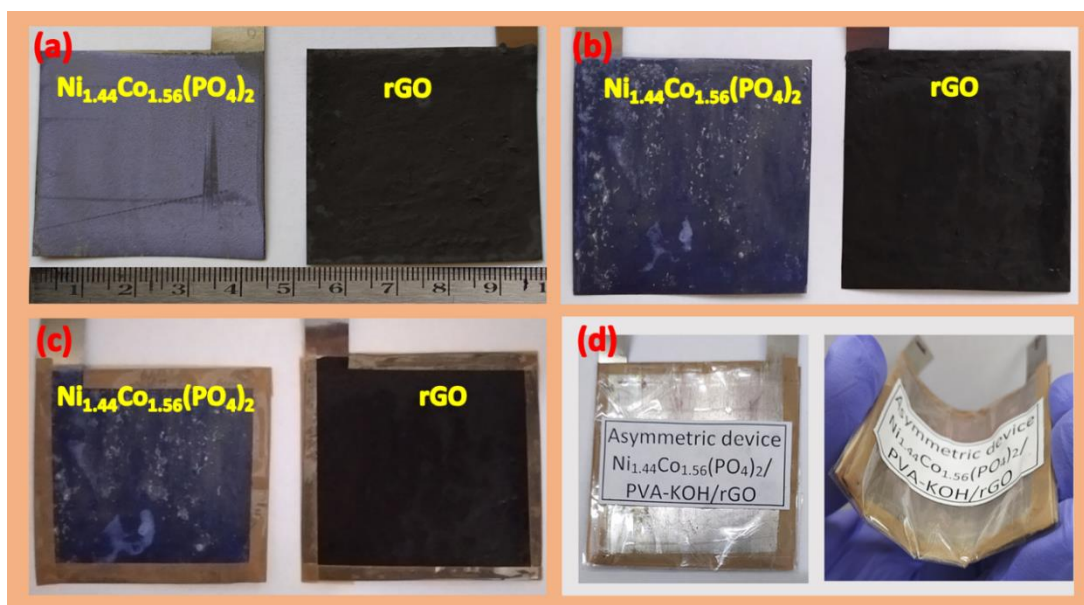
Fig. 5.16 The digital photographs of (a) $Ni_{1.44}Co_{1.56}(PO_4)_2$ (electrodeposited) and rGO

thin film electrodes on flexible stainless steel substrate, (b) electrodes painted by

PVA-KOH gel electrolyte, (c) sealed edges with tape and (d) fabricated flexible

device.

5.2.C.3 Electrochemical supercapacitive performance evaluation of chemical bath

deposited $Ni_{1.38}Co_{1.62}(PO_4)_2$//rGO asymmetric flexible solid state supercapacitor

device

The working potential window of individual $Ni_{1.38}Co_{1.62}(PO_4)_2$ and rGO

electrodes is 0 to 0.5 V/SCE and -1 to 0 V/SCE, respectively. The CV curves of AFSSS

device in different potential ranges of 1.2 to 1.7 V were measured at constant scan rate

of 50 mV s^{-1} and demonstrated in Fig. 5.17 (a). Area under CV curve increases in anodic

and cathodic regions up to the potential window of 0 to 1.6 V. After that potential

window, the current suddenly increases in cathodic region which demonstrates

irreversible electrochemical reaction due to oxygen evolution reaction. It is found that,

the potential window of 0 to 1.6 V is suitable for further electrochemical investigation

of AFSSS device. Fig. 5.17 (b) shows the CV curves of AFSSS device at different scan

rates ranging from 5-100 mV s^{-1}. The shape of CV curves is not rectangular that confirms the combined pseudocapacitive and EDLC behavior of AFSSS device.
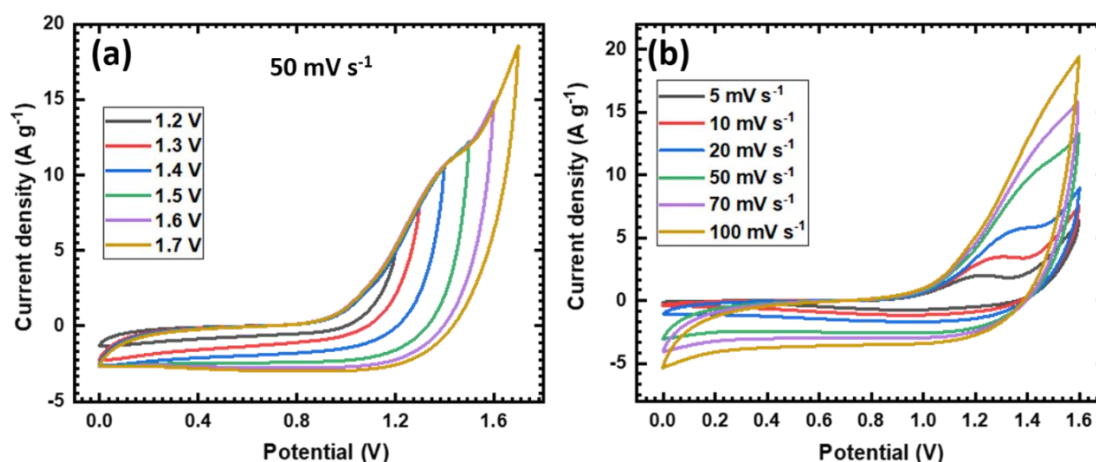

Fig. 5.17 The CV curves of Ni$_{1.38}$Co$_{1.62}$(PO$_4$)$_2$//rGO AFSSS device (a) in different potential windows and (b) at different scan rates from 5-100 mV s^{-1}.

The GCD curves of AFSSS device measured in different potentials range of 1.2 to 1.7 V at 1.75 A g^{-1} current density are displayed in Fig. 5.18 (a). In potential window of 0 to 1.6 V, the AFSSS device shows symmetric nature for charging and discharging profile and asymmetric nature up to 1.7 V. It concludes that, the GCD curves of AFSSS device shows better performance in potential window of 0 to 1.6 V. So, the 0 to 1.6 V potential window is chosen for the further electrochemical study of AFSSS device. The GCD curves of AFSSS device at various current densities are measured and shown in Fig. 5.18 (b). The non-linear GCD curves confirm the combined charge storage mechanism of EDLC and pseudocapacitive electrodes. The AFSSS device shows a maximum specific capacitance of 79 F g^{-1} at 0.75 A g^{-1} current density (Fig. 5.18 (c)). The AFSSS device maintains approximately 90 % of capacitance at a higher current density. Energy and power density of AFSSS device calculated from GCD curves and plotted in Fig. 5.18 (d). The AFSSS device exhibited highest energy density of 28 Wh

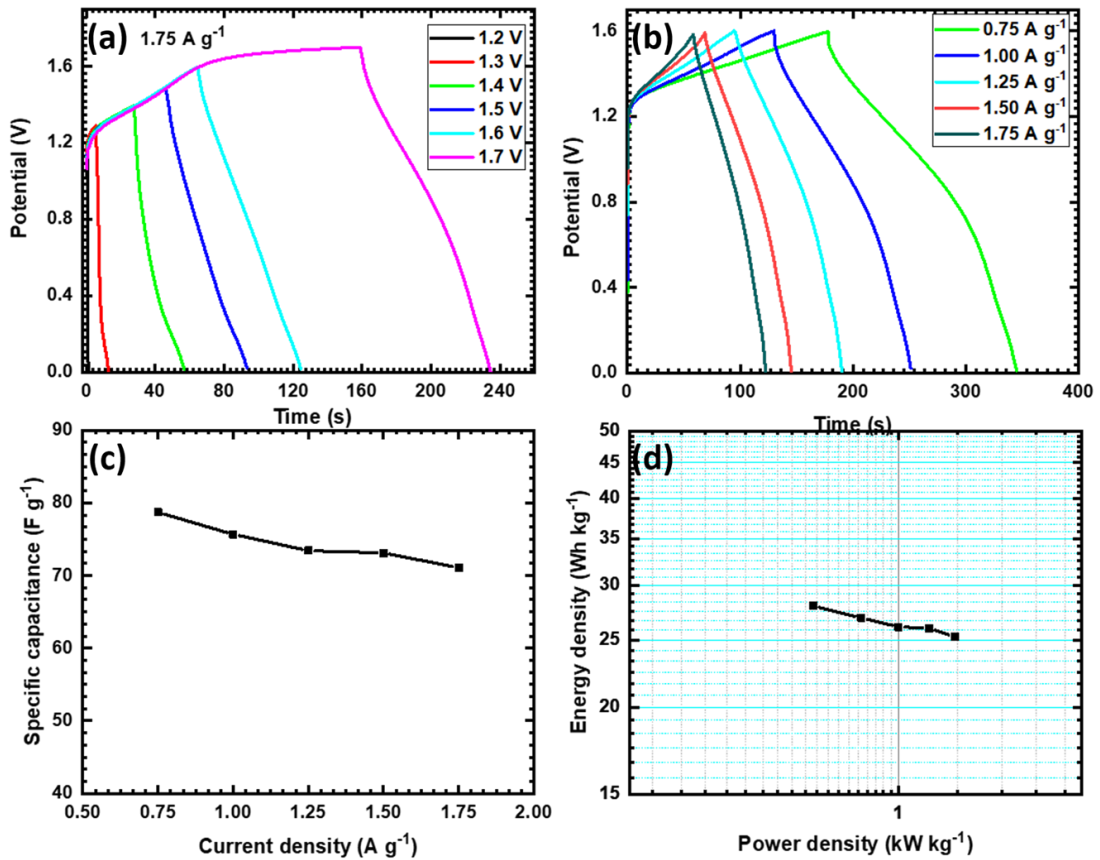kg^{-1} at power density of 0.6 kW kg^{-1} and it decreases up to 25.2 Wh kg^{-1} at power density of 1.4 kW kg^{-1}.

Fig. 5.18 The GCD curves of $Ni_{1.38}Co_{1.62}(PO_4)_2$//rGO AFSSS device (a) in different potential windows and (b) at different current densities. Plot of specific capacitance as a function of current density (c) and the Ragone plot (d) of $Ni_{1.38}Co_{1.62}(PO_4)_2$//rGO AFSSS device.

The mechanical flexibility of supercapacitor device is important for usage in portable electronic devices. The CV curves of AFSSS device are recorded at various bending angles (0, 45, 90, 135 and 170º) for the examination of mechanical stability of device. The CV curves (at 100 mV s^{-1}) at different bending angles are displayed in Fig. 5.19 (a). The shape of CV curves is not much altered with varying bending angles and that indicates good mechanical flexibility of the AFSSS device. The AFSSS device maintains ~ 90 % of initial capacitance at different bending angles (even at 170º) as

shown in Fig. 5.19 (b). This study proves good adhesion of active material with the

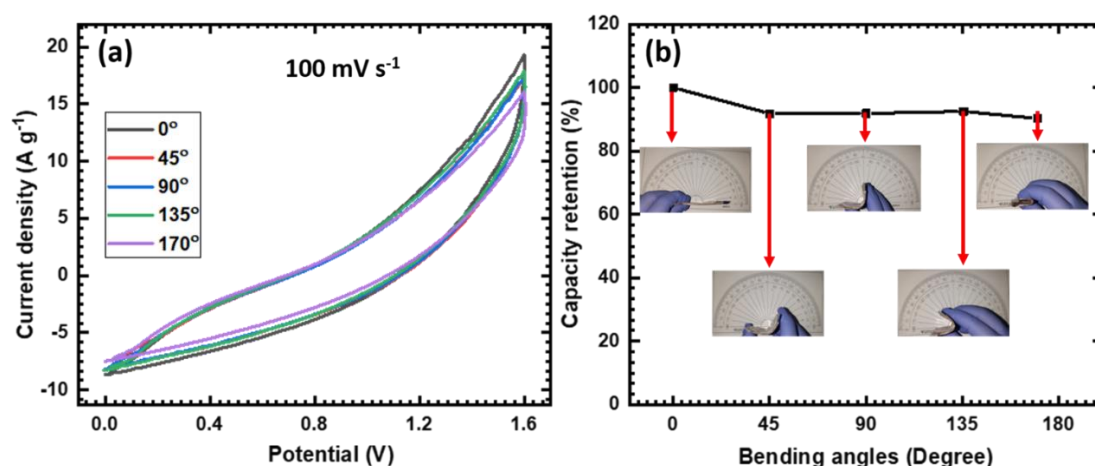flexible stainless steel substrate.

Fig. 5.19 (a) The CV curves at different bending angles and (b) plot of capacitive

retention with bending angle of $Ni_{1.38}Co_{1.62}(PO_4)_2$//rGO AFSSS device.

The electrochemical cyclic stability (in terms of capacitive retention) of

$Ni_{1.38}Co_{1.62}(PO_4)_2$//rGO AFSSS device is studied by GCD analysis (4000 cycles) at

constant current density of 5 A g^{-1}. The capacitive retention plot of AFSSS device is
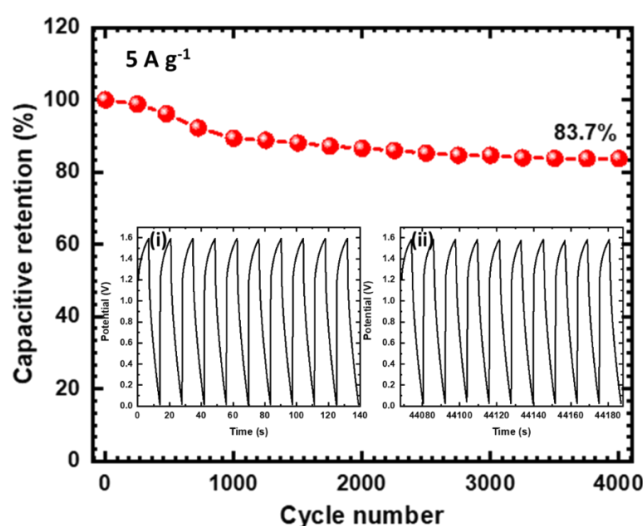
shown in Fig. 5.20.

Fig. 5.20 The plot of capacitive retention at the current density of 5 A g^{-1} with respect

to cycle numbers (4000) of $Ni_{1.38}Co_{1.62}(PO_4)_2$//rGO AFSSS device (inset: initial (i)

and last (ii) 10 GCD cycles).

The fabricated AFSSS device shows 83.7 % capacitive retention after 4000 GCD

cycles. The initial and last 10 GCD cycles are shown as inset of Fig. 5.20. The good

cyclic stability of device is observed and attributed to usage of gel electrolyte.

The Nyquist plot of $Ni_{1.38}Co_{1.62}(PO_4)_2$//rGO AFSSS device along with equivalent

circuit is shown in Fig. 5.21. The low values of R_s (0.19 Ω) and R_{ct} (14.2 Ω) of AFSSS

device suggest the easy interaction between electrode and electrolyte due to good

contact of active material. Also, in equivalent circuit, W (0.067 Ω) and Q (1.79 mF) are

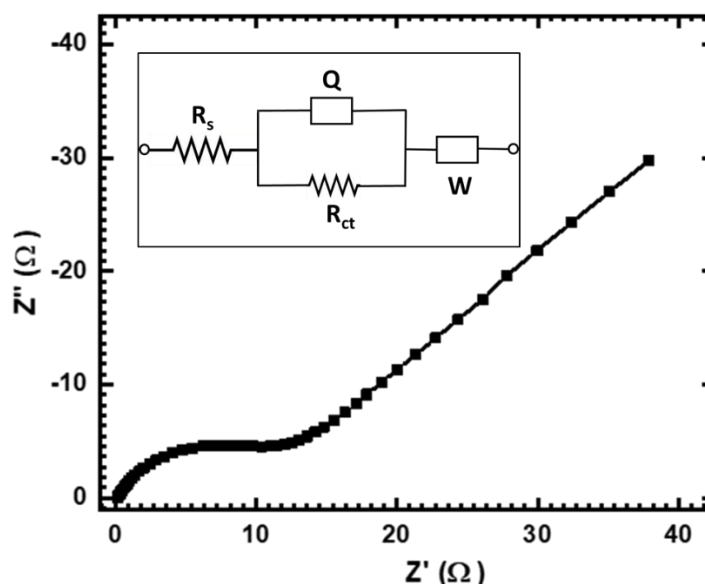Warburg impedance and general imperfect capacitor when n=0.84, respectively.

Fig. 5.21 Nyquist plot of $Ni_{1.38}Co_{1.62}(PO_4)_2$//rGO AFSSS device (inset: equivalent

circuit of the fitted data).

The practical applicability of AFSSS device is tested by charging two serially

connected devices for 30 s by applying constant potential of +3.2 V and discharged

through 201 red light emitting diodes (LEDs) arranged in text of "DYPU CDL

GROUP". The text contains "DYPU" stands for D. Y. Patil University, "CDL" stands

for Prof. C. D. Lokhande and "GROUP" stands for group. The 201 LED panel lights

up for 130 s by charging only for 30 s. The digital photographs of glowed LED panel

at different time periods are shown in Fig. 5.22. The demonstration of AFSSS device

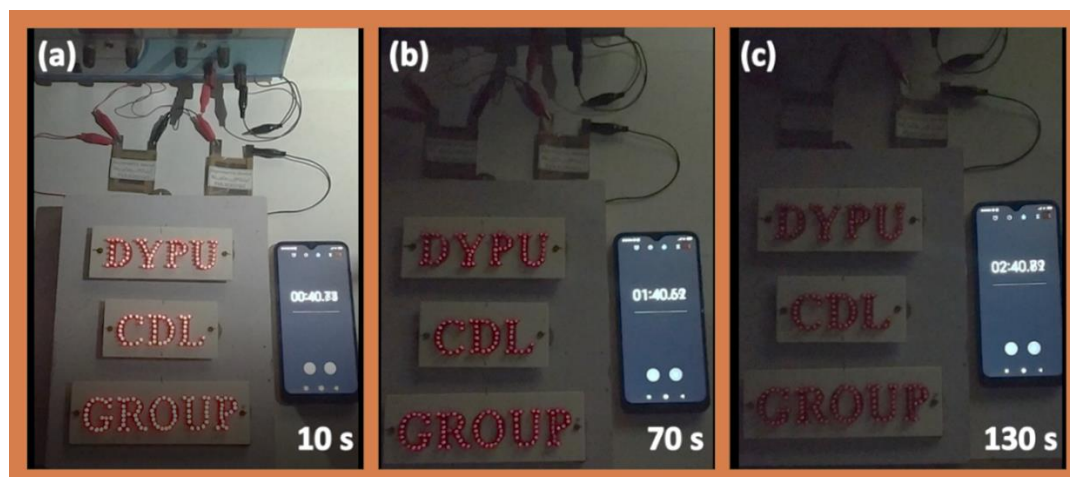suggest that, it is a promising flexible energy storage device and can be used in various applications.

Fig. 5.22 Digital photographs of serially connected two AFSSS devices glowing 201 LEDs panel at different time periods.

5.2.C.4 Electrochemical supercapacitive performance evaluation of electrodeposited $Ni_{1.44}Co_{1.56}(PO_4)_2$//rGO asymmetric flexible solid state supercapacitor device

The potential window of positive (electrodeposited $Ni_{1.44}Co_{1.56}(PO_4)_2$) and negative (rGO) electrode is 0 to 0.5 V/SCE and -1 to 0 V/SCE, respectively. To find the operational potential window, the CV curves of AFSSS device are measured at different potentials in range of 1.2 to 1.7 V at constant scan rate of 50 mV s^{-1}. The CV curves of AFSSS device are measured in various potential windows and plotted in Fig. 5.23 (a). The current response enhances with increasing potential window of the AFSSS device. The AFSSS device shows excellent performance in potential window of 0 to 1.6 V and it used for further study. The CV curves of AFSSS device recorded at various scan rates from 5-100 mV s^{-1} are displayed in Fig. 5.23 (b). Maintained CV shapes at various scan rates suggest good rate capability of device.

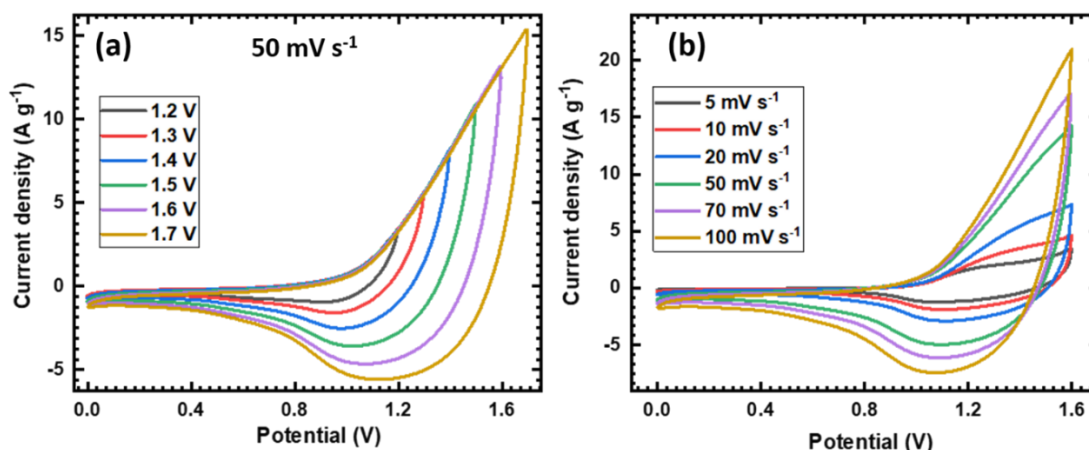Fig. 5.23 The CV curves of $Ni_{1.44}Co_{1.56}(PO_4)_2$//rGO AFSSS device (a) in different potential windows at scan rate of 50 mV s^{-1} and (b) at different scan rates from 5-100 mV s^{-1}.

The charge-discharge curves of AFSSS device in different potential windows at constant current density of 2 A g^{-1} were measured and plotted in Fig. 5.24 (a). The AFSSS device shows good performance in potential window of 0 to 1.6 V. The non-linear GCD curves observed for AFSSS device at various current densities in potential window of 0 to 1.6 V are displayed in Fig. 5.24 (b). The AFSSS device achieves high potential window with large discharging time can enhances capacitance and energy density of device. The specific capacitance of AFSSS device calculated from GCD curves at different current densities are shown in Fig. 5.24 (c). The AFSSS device exhibited highest specific capacitance of 90 F g^{-1} at 0.4 A g^{-1} current density and decreases up to 65 F g^{-1} at 2 A g^{-1} current density. The AFSSS device maintains 72 % initial capacitance at high current density. Fig. 5.24 (d) shows the Ragone plot of AFSSS device, the device achieved maximum energy density of 32 Wh kg^{-1} at power density of 0.32 kW kg^{-1} and retains 23.1 Wh kg^{-1} energy density at power density of 1.6 kW kg^{-1}, which suggest good rate capability of AFSSS device.
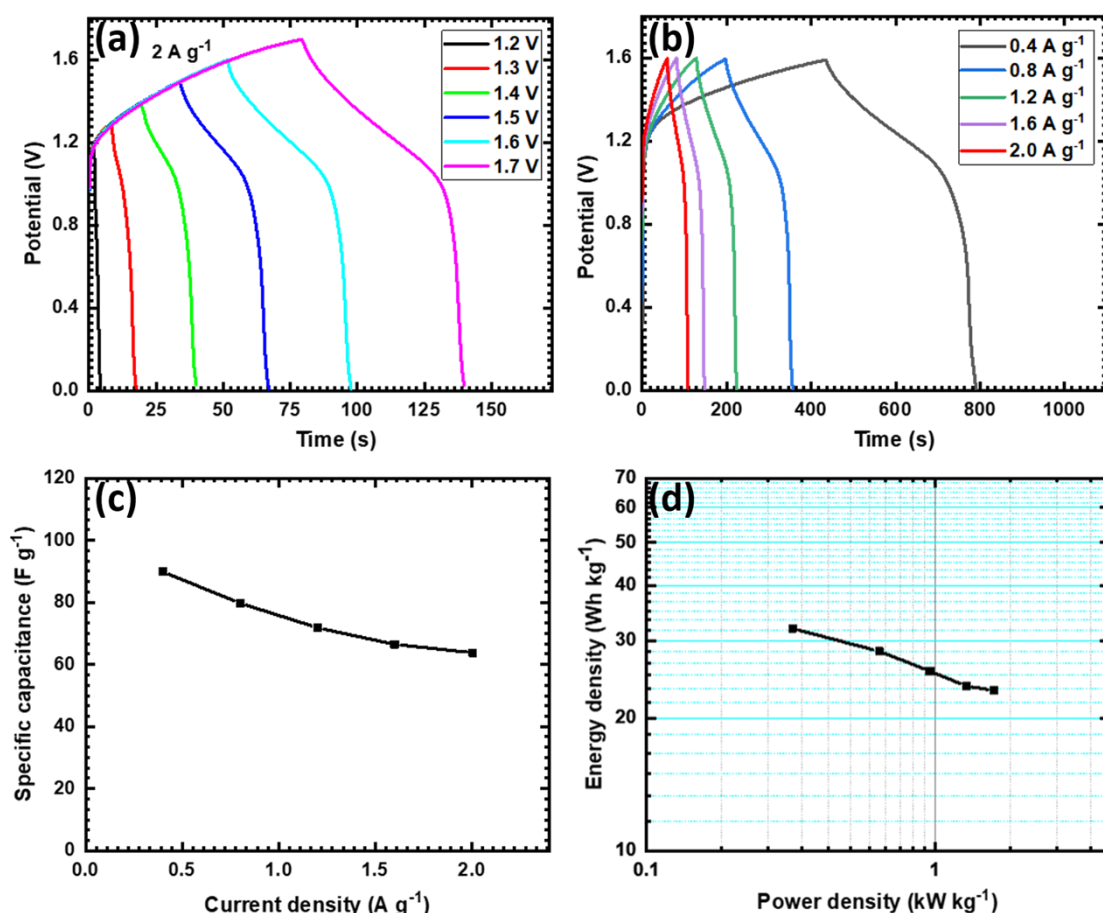
Fig. 5.24 The GCD curves of $Ni_{1.44}Co_{1.56}(PO_4)_2$//rGO AFSSS device (a) in different potential windows and (b) at different current densities. Plot of specific capacitance as a function of current density (c) and the Ragone plot (d) of $Ni_{1.44}Co_{1.56}(PO_4)_2$//rGO AFSSS device.

By measuring CV curves at different bending angles (0-170⁰), the mechanical flexibility of AFSSS device is tested. The CV curves (at 100 mV s⁻¹) of AFSSS device at different bending angles are shown in Fig. 5.25 (a). Nearly similar shape of CV curves demonstrates good mechanical stability of the device. Furthermore, the capacitive retention with respect to bending angles is plotted in Fig. 5.25 (b) and the device shows 88 % capacitive retention.
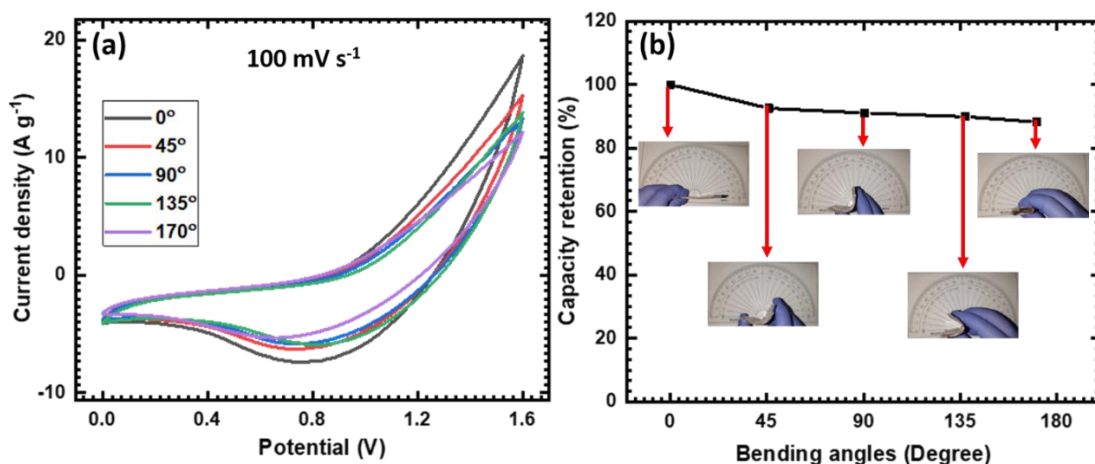
Fig. 5.25 (a) The CV curves at different bending angles and (b) plot of capacitance retention with bending angles of $Ni_{1.44}Co_{1.56}(PO_4)_2$//rGO AFSSS device.

Electrochemical stability (in terms of capacitive retention) of $Ni_{1.44}Co_{1.56}(PO_4)_2$//rGO AFSSS device is tested for 4000 GCD cycles at 5 A g^{-1} current density. The device retains 89 % of initial capacitance after 4000 cycles, the capacitive retention graph with respective cycle number is shown in Fig. 5.26. The initial and last 10 GCD cycles are shown as inset Fig. 5.26.
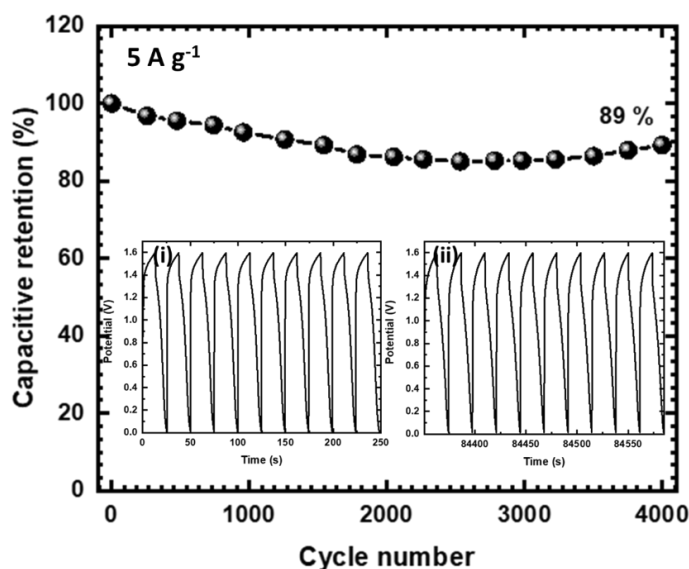

Fig. 5.26 The plot of capacitive retention at the current density of 5 A g^{-1} with respect to cycle numbers (4000) of $Ni_{1.44}Co_{1.56}(PO_4)_2$//rGO AFSSS device (inset: initial (i) and last (ii) 10 GCD cycles).

The device shows good cyclic performance for large number of cycles at very high current density, which suggests the AFSSS device efficiently works at very high rate and can be used in various portable devices.

The Nyquist plot of $Ni_{1.44}Co_{1.56}(PO_4)_2$//rGO AFSSS device is shown in Fig. 5.27 with equivalent circuit. The low values of R_s (0.25 Ω) and R_{ct} (15.13 Ω) arise due to the good ionic conductivity of gel electrolyte and its compatibility with active material. Warburg impedance (W) and general imperfect capacitor (Q) are found to be 0.037 Ω and 1.87 mF (correction factor n=0.74), respectively in equivalent circuit.
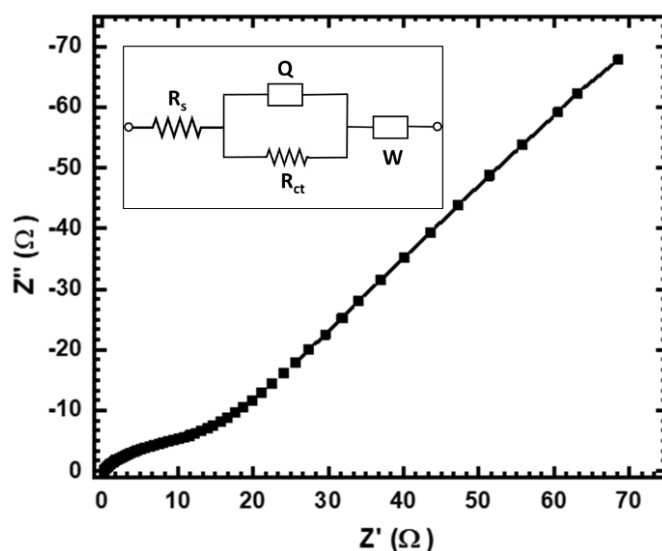

Fig. 5.27 Nyquist plot of $Ni_{1.44}Co_{1.56}(PO_4)_2$//rGO AFSSS device (inset: equivalent circuit of the fitted data).

The AFSSS device practical applicability is tested by charging two serially connected AFSSS devices for 30 s by applying constant potential of +3.2 V. The serially connected AFSSS devices discharged through parallelly connected 201 red light emitting diodes (LEDs).
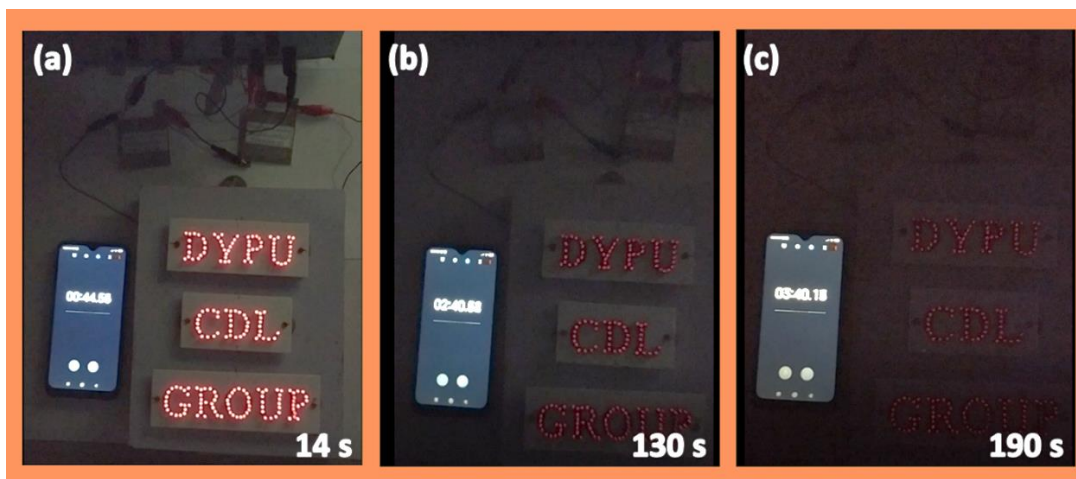
Fig. 5.28 Digital photographs of serially connected two AFSSS devices glowing 201

LEDs panel at different time periods.

201 red LEDs are lighted from two serially connected AFSSS devices for 190 s by

charging only for 30 s and digital photographs taken at different discharge time intervals

are shown in Fig. 5.28. The demonstration of practical usage of AFSSS device suggests

that, it can be used in various electronic appliances.

5.2.C.5 Conclusions

Asymmetric flexible solid state devices are successfully fabricated using nickel

cobalt phosphate (CBD or electrodeposition methods) as a positive electrode and rGO

as a negative electrode. The chemical bath deposited nickel cobalt phosphate based

solid state device exhibited maximum specific capacitance of 79 F g^{-1} with energy

density of 28 Wh kg^{-1} at power density of 0.6 kW kg^{-1}. The electrodeposited nickel

cobalt phosphate based solid state device showed good performance than the chemical

bath deposited nickel cobalt phosphate based solid state device and it achieves highest

specific capacitance of 90 F g^{-1} at 0.4 A g^{-1} current density with 32 Wh kg^{-1} energy

density at power density of 0.32 kW kg^{-1}. Additionally, the electrodeposited nickel

cobalt phosphate based flexible solid state device shows 89 % capacitive retention over

4000 cycles and 88 % retention over various bending angles. The electrodeposited

nickel cobalt phosphate based flexible solid state supercapacitor device exhibits excellent mechanical stability, good rate capability with superior cyclic stability and these features suggest significant potential of AFSSS device ($Ni_{1.44}Co_{1.56}(PO_4)_2$//rGO) for application in various portable and flexible electronic devices.

5.3 References

1. D. Dubal, N. Chodankar, S. Qiao, Small, 15 (2019) 1804104 (1-9).

2. A. Patil, A. Lokhande, P. Shinde, C. Lokhande, ACS Appl. Mater. Interfaces, 10 (2018) 16636-16649.

3. D. Mohapatra, S. Parida, S. Badrayyana, B. Singh, Appl. Mater. Today, 7 (2017) 212-221.

4. A. Patil, V. Lokhande, U. Patil, P. Shinde, C. Lokhande, ACS Sustain. Chem. Eng., 6 (2018) 787-802.

5. X. Wang, A. Mehandzhiyski, B. Arstad, K. Aken, T. Mathis, A. Gallegos, Z. Tian, D. Ren, E. Sheridan, B. Grimes, D. Jiang, J. Wu, Y. Gogotsi, D. Chen, J. Am. Chem. Soc., 139 (2017) 18681-18687.

6. C. Zhong, Y. Deng, W. Hu, J. Qiao, L. Zhang, J. Zhang, Chem. Soc. Rev., 44 (2015) 7484-7539.

7. N. Chodankar, H. Pham, A. Nanjundan, J. Fernando, K. Jayaramulu, D. Golberg, Y. Han, D. Dubal, Small, 16 (2020) 2002806 (1-35).

8. F. Luan, G. Wang, Y. Ling, X. Lu, H. Wang, Y. Tong, X. X. Liu, Y. Li, Nanoscale, 5 (2013) 7984-7990.

9. H. Gao, F. Xiao, C. Ching, H. Duan, ACS Appl. Mater. Interfaces, 4 (2012) 7020-7026.

10. A. Sumboja, C. Foo, X. Wang, P. Lee, Adv. Mater., 25 (2013) 2809-2815.

11. B. Choi, S. Chang, H. Kang, C. Park, H. Kim, W. Hong, S. Lee, Y. Huh, Nanoscale, 4 (2012) 4983-4988.

12. L. Liu, Z. Niu, J. Chen, Chem. Soc. Rev., 45 (2016) 4340-4363.

13. Q. Wang, J. Yan, Z. Fan, Energy Environ. Sci., 9 (2016) 729-762.

14. J. Chen, B. Yao, C. Li, G. Shi, Carbon, 64 (2013) 225-229.

15. D. Marcano, D. Kosynkin, J. Berlin, A. Sinitskii, Z. Sun, A. Slesarev, L. Alemany, W. Lu, J. Tour, ACS Nano, 4 (2010) 4806-4814.

16. S. Gurunathan, J. Han, A. Dayem, V. Eppakayala, J. Kim, Int. J. Nanomedicine, 7 (2012) 5901-5914.

17. C. Fu, G. Zhao, H. Zhang, S. Li, Int. J. Electrochem. Sci., 8 (2013) 6269-6280

18. S. Some, Y. Kim, Y. Yoon, H. Yoo, S. Lee, Y. Park, H. Lee, Sci. Rep., 3 (2013) 1929 (1-5).

19. P. Deshmukh, S. Pusawale, V. Jamadade, U. Patil, C. Lokhande, J. Alloys Compd., 509 (2011) 5064-5069.

20. K. Sankar, R. Selvan, D. Meyrick, RSC Adv., 5 (2015) 99959-99967.

21. S. Kandalkar, H. Lee, S. Seo, K. Lee, C. Kim, J. Mater. Sci., 46 (2011) 2977-2981.

22. F. Omar, A. Numan, S. Bashir, N. Duraisamy, R. Vikneswaran, Y. Loo, K. Ramesh, S. Ramesh, Electrochim. Acta, 273 (2018) 216-228.

23. C. Chen, N. Zhang, Y. He, B. Liang, R. Ma, X. Liu, ACS Appl. Mater. Interfaces, 8 (2016) 23114-23121.

24. B. Li, P. Gu, Y. Feng, G. Zhang, K. Huang, H. Xue, H. Pang, Adv. Funct. Mater., 27 (2017) 1605784 (1-11).

25. M. Liu, J. Li, Y. Hu, Q. Yang, L. Kang, Electrochim. Acta, 201 (2016) 142-150.

26. Y. Tang, Z. Liu, W. Guo, T. Chen, Y. Qiao, S. Mu, Y. Zhao, F. Gao, Electrochim. Acta, 190 (2016) 118-125.

27. Y. Zhao, Z. Chen, D. Xiong, Y. Qiao, Y. Tang, F. Gao, Sci. Rep., 6 (2016) 17613 (1-10).

28. M. Liu, N. Shang, X. Zhang, S. Gao, C. Wang, Z. Wang, J. Alloys Compd., 791 (2019) 929-935.

29. B. Liang, Y. Chen, J. He, C. Chen, W. Liu, Y. He, X. Liu, N. Zhang, V. Roy, ACS Appl. Mater. Interfaces, 10 (2018) 3506-3514.

30. J. Hu, P. Yang, S. Wang, J. Shi, ChemElectroChem, 6 (2019) 928-936.

31. H. Chen, S. Jiang, B. Xu, C. Huang, Y. Hu, Y. Qin, M. He, H. Cao, J. Mater. Chem. A, 7 (2019) 6241-6249.

32. Z. Tang, C. Jia, Z. Wan, Q. Zhou, X. Ye, Y. Zhu, RSC Adv., 6 (2016) 112307-112316.

33.   P. Katkar, S. Marje, S. Pujari, S. Khalate, A. Lokhande, U. Patil, ACS
       Sustain. Chem. Eng., 7 (2019) 11205-11218.

CHAPTER – VI

SUMMARY AND CONCLUSIONS

Summary and conclusions

Technology in the field of portable electronic devices is developing with increasing demand in a sustainable economy. To fulfill the all necessities in this sector efficient energy storage devices are needed. Therefore, energy storage technology is now a worldwide trending in research field. Among the various energy storage devices, supercapacitors fascinate in the field of portable electronics due to its storage performance stands between the batteries and conventional capacitors. The attention of researchers in the field of science and industry is now focused on supercapacitors, which makes it a rising star in the energy storage field. Supercapacitor offers higher power density, larger cyclic life and most importantly it is safe and almost maintenance free compared with battery.

The bulky and restricted nature of present supercapacitors is main problem in its usage for electronic devices. In the field of micro, portable and flexible electronic devices, flexible and gel based electrochemical energy storage devices are needed. With this concern, the recent research work is diverted towards the development of a flexible supercapacitor devices. The flexible nature of supercapacitor eliminates the problem that arises from the bulky nature of supercapacitors. Also, it offers high power, long cyclic stability with environmental friendly nature and safety. Moreover, along with these features, the flexible devices are light weight and small in size with high mechanical stability in bending, twisting and folding. The limited energy density values of flexible supercapacitor devices are the main restriction in the practical application. So, the important task in the flexible supercapacitor is improvement in energy density without changing its other electrochemical features. The most important requirement for high electrochemical performing supercapacitor is development of efficient electrode material with high surface area and conductivity, which enhances cyclic

stability and ion transfer rate due to easy electrochemical reaction. Along with electrode properties, the electrolyte is most effective parameter in the electrochemical capacitive performance. The combination of best performing active material with suitable electrolytes commendably enhances the energy and power of device. So, the final performance of the flexible device depends on the synthesis of high performing active material with use of proper electrolytes. The gel/solid state electrolyte offers high ionic conducting media and also works as a separator in the device. The simplest packaging process, high operating temperature range, and leakage free nature are some other advantages of gel/solid state electrolytes.

The aim of the present research was a synthesis of nickel cobalt phosphate thin films using simple chemical methods and fabricate asymmetric supercapacitor devices. So, the nickel cobalt phosphate thin films were synthesized on conducting (stainless steel) substrate via chemical bath deposition and electrodeposition methods. The composition of nickel and cobalt ratio varied to achieve better results by using synergy between them. Binder-free and good quality thin films of nickel cobalt phosphate were characterized by different physico-chemical methods. The best performing thin film electrodes were used for the fabrication of aqueous asymmetric device with 1 M KOH electrolyte and solid state device with PVA-KOH electrolyte. The present thesis work is described in six chapters.

Chapter I starts with the general introduction which talks about the necessity of supercapacitor in the recent world, current developments and working principle of supercapacitors, also the classification of supercapacitors based on charge storage mechanism is discussed. The high electrochemical performance of supercapacitor can be achieved by manipulating required active material with desired properties. So, the required properties of electrode material are discussed in detail with the type of

available active materials for supercapacitors. Furthermore, chapter consists of a literature survey of nickel phosphate, cobalt phosphate and nickel cobalt phosphate materials for supercapacitor application. Also, the Na, K rich nickel phosphate, cobalt phosphate and nickel cobalt phosphate materials with their composite for supercapacitor application are discussed. In the last part, the purpose and orientation of dissertation are described.

Chapter II contains introduction of thin film with different types of deposition techniques. Theoretical background of chemical bath deposition and electrodeposition methods with various preparative parameters and advantages are briefly explained. The working principles of characterization techniques used for thin film analysis such as X-ray diffraction (XRD) for structural analysis, X-ray photoelectron spectroscopy (XPS) for elemental analysis, field emission scanning electron microscopy (FE-SEM) for surface morphological study and energy dispersive X-ray spectroscopy (EDS) for elemental mapping are given in this chapter. Also, the electrochemical techniques used for the electrochemical performance evaluation of electrode material such as cyclic voltammetry (CV), galvanostatic charge-discharge (GCD) and electrochemical impedance spectroscopy (EIS) with their features are discussed in detail.

Chapter III deals with synthesis, characterization and electrochemical performance evaluation of chemical bath deposited nickel cobalt phosphate thin films. This chapter is divided into two sections 'A' and 'B'. Section 'A' consists synthesis of nickel cobalt phosphate thin films by simple and cost effective CBD method. The conducting and highly stable (in acid/base) stainless steel (SS) substrate is chosen for the deposition and nickel cobalt phosphate is directly grown on SS substrate by CBD method. The effect of nickel and cobalt molar ratio variation on structure and surface morphology of nickel cobalt phosphate thin film is studied. The deposited nickel cobalt

phosphate thin films are characterized by different characterization techniques. The XRD analysis confirms successful synthesis of nickel cobalt phosphate material in thin film form. The nickel, cobalt, oxygen and phosphorous elements are detected and confirmed by XPS study. The nickel and cobalt molar content influences the morphology of prepared thin film as it converts from microflower to microsheets like structure and EDS analysis confirms achievement of expected molar ratio (nickel and cobalt) in the samples.

Section 'B' consists of the supercapacitive performance evaluation of chemical bath deposited nickel cobalt phosphate thin films. The influence of molar ratio of nickel and cobalt on electrochemical performance is studied. Three electrode system is used for the supercapacitive performance evaluation. The highest specific capacitance of 1116 F g^{-1} is achieved by microflowers containing rectangular microsheets like structure of nickel cobalt phosphate (Ni$_{1.38}$Co$_{1.62}$(PO$_4$)$_2$) thin film at 0.5 A g^{-1} current density with 75 % capacitive retention over 3000 cycles. The good electrochemical results concluded that, microflowers containing rectangular microsheets like structure of nickel cobalt phosphate (Ni$_{1.38}$Co$_{1.62}$(PO$_4$)$_2$) thin film offers a large number of channels for easy ion penetration and charge transportation.

Chapter IV contains synthesis, characterization and electrochemical performance evaluation of electrodeposited nickel cobalt phosphate thin film electrodes. As like chapter III, chapter IV is divided into two sections 'A' and 'B'. Section 'A' deals with synthesis of nickel cobalt phosphate thin films by electrodeposition method. The electrodeposited nickel cobalt phosphate thin films are used as working electrode for supercapacitive study. The impact on structure and surface morphology with the variation in molar ratio of nickel and cobalt is studied. The XRD, XPS, FE-SEM and EDS analysis are used for confirmation of prepared

material. Amorphous to crystalline phase conversion from nickel phosphate to cobalt phosphate is observed in XRD analysis with composition variation (nickel and cobalt). The nickel, cobalt, oxygen and phosphorous elements with expected composition are detected in XPS and EDS study. The morphological evolution from microsphere to nanosheets is observed with increasing cobalt content in nickel cobalt phosphate thin films. Section 'B' describes the supercapacitive performance of electrodeposited nickel cobalt phosphate thin film electrodes and change in response is observed at different compositions of nickel and cobalt. The high specific capacitance exhibited by microspheres with nanocracks like morphology of nickel cobalt phosphate ($Ni_{1.44}Co_{1.56}(PO_4)_2$) thin film electrode of 2286 F g^{-1} at 1.5 A g^{-1} current density and 81.3 % capacitance maintained at high current density. Also, the electrode shows 81 % capacitive retention over 3000 cycles. The good performance of electrodeposited nickel cobalt phosphate ($Ni_{1.44}Co_{1.56}(PO_4)_2$) material is observed due to good contact between deposited material and stainless steel substrate (binder-free synthesis) and microspheres consisting nanocracks like morphology.

Chapter V deals with the preparation of anode and, fabrication and performance evaluation of asymmetric devices. This chapter divided into three sections as 'A', 'B' and 'C'. Section 'A' describes the synthesis, characterization and supercapacitive performance evaluation of rGO electrode. The famous modified Hummer's method is used for GO synthesis and then it reduced hydrothermally. The XRD and Raman study confirms successful conversion of GO to rGO. For electrochemical study, the anode is prepared by coating rGO material on stainless steel substrate by casting method. The electrochemical study of rGO electrode carried out in 1 M KOH electrolyte in three electrode system. The rGO electrode exhibits maximum specific capacitance of 200 F

g^{-1} at 2 A g^{-1} current density. So, the rGO electrode is used as negative (anode) electrode for device fabrication.

Section 'B' deals with the preparation and performance evaluation of asymmetric aqueous supercapacitor (AAS) devices. The best performed nickel cobalt phosphate thin film (C-NCP5 and E-NCP4) and rGO electrodes are selected as cathode and anode, respectively for the preparation of aqueous devices. This section subdivided into two parts. The first part related to fabrication and performance evaluation of chemical bath deposited nickel cobalt phosphate//rGO aqueous asymmetric supercapacitor (AAS) device. The chemical bath deposited $Ni_{1.38}Co_{1.62}(PO_4)_2$ and rGO used as positive and negative electrodes, respectively in two electrode system with 1 M KOH electrolyte. The charges are balanced between positive and negative electrodes to achieve good electrochemical capacitive performance of device. The $Ni_{1.38}Co_{1.62}(PO_4)_2$//rGO device achieved 0 to 1.6 V potential window and specific capacitance of 120 F g^{-1} at 1.3 A g^{-1} current density. Also, the AAS device achieved highest energy density of 42.3 Wh kg^{-1} at 1 kW kg^{-1} power density and shows 80 % capacitive retention after 4000 cycles. The second part contains fabrication and performance evaluation of electrodeposited nickel cobalt phosphate//rGO aqueous asymmetric supercapacitor (AAS) device. The electrodeposited $Ni_{1.44}Co_{1.56}(PO_4)_2$ and rGO are used as positive and negative electrodes, respectively for device fabrication, and supercapacitive performance of device is studied in 1 M KOH electrolyte. The $Ni_{1.44}Co_{1.56}(PO_4)_2$//rGO AAS device achieved maximum potential window of 0 to 1.6 V. The device exhibits maximum specific capacitance of 185 F g^{-1} at current density of 2.7 A g^{-1} and energy density of 65.7 Wh kg^{-1} at power density of 2.2 kW kg^{-1}. Also, the AAS device shows 97 % capacitive retention after 4000 cycles. The electrochemical capacitive performance of asymmetric aqueous supercapacitor devices is summarized in table 6.1.

Table 6.1 Electrochemical performance of asymmetric aqueous supercapacitor devices

Deposition method	AAS Device	Specific capacitance (F g^{-1}) at current density (A g^{-1})	Energy density (Wh kg^{-1})	Power density (kW kg^{-1})	Stability (%) at 4000 cycles
CBD	Ni$_{1.38}$Co$_{1.62}$(PO$_4$)$_2$// rGO	120 at 1.3	42.3	1	80 %
Electrodeposition	Ni$_{1.44}$Co$_{1.56}$(PO$_4$)$_2$// rGO	185 at 2.7	65.7	2.2	97 %

Section 'C' encloses fabrication and supercapacitive performance evaluation of asymmetric flexible solid state supercapacitor (AFSSS) devices. As like section 'B', it is also subdivided into three parts. In first part, preparation of electrodes and PVA-KOH gel electrolyte is discussed. Also, it describes stepwise fabrication process of solid state devices. Chemical bath deposition and electrodeposition methods are used for direct growth of nickel cobalt phosphate material on conducting and flexible stainless steel substrate (area = 5 X 5 cm^2). The prepared gel electrolyte PVA-KOH sandwiched between the flexible nickel cobalt phosphate and rGO electrodes and sealed with transparent tape. The second part describes performance of chemical bath deposited nickel cobalt phosphate (C-NCP5) and rGO electrodes based asymmetric flexible solid state supercapacitor device. The AFSSS (Ni$_{1.38}$Co$_{1.62}$(PO$_4$)$_2$//rGO) device achieves potential window of 0 to 1.6 V and maximum specific capacitance of 79 F g^{-1} at 0.75 A g^{-1} current density. Also, the device shows good flexibility and capacitive retention (90 %) at various bending angles. Also, the AFSSS device exhibits energy density of 28 Wh kg^{-1} with power density of 0.6 kW kg^{-1} and 83.7 % capacitive retention after 4000 cycles. The practical applicability of device is tested by connecting two flexible devices in series, charged for 30 s and discharged through 201 red LEDs panel as shown in Fig. 6.1.
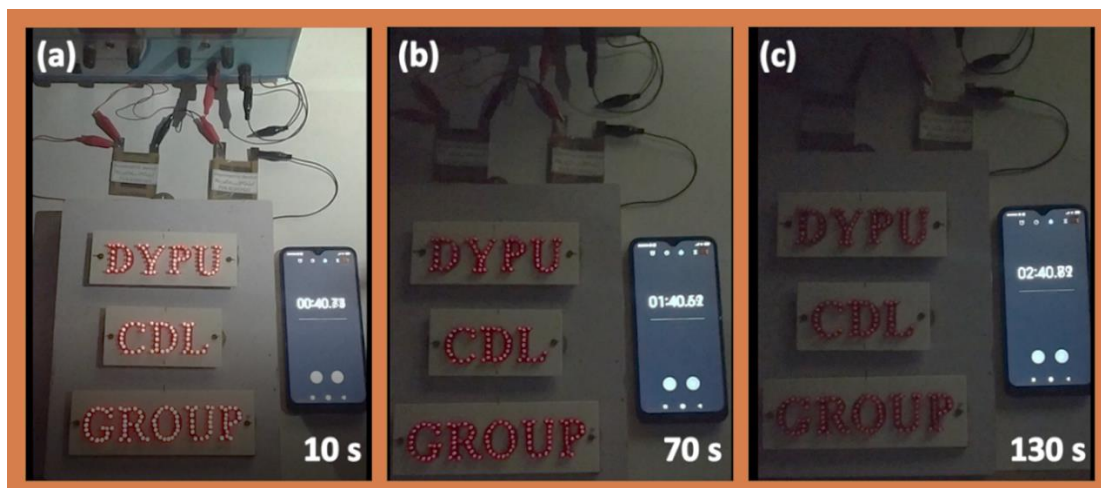
Fig. 6.1 Digital photographs of serially connected two $Ni_{1.38}Co_{1.62}(PO_4)_2$//rGO AFSSS

devices glowing 201 LEDs panel at different time periods.

The third part contains supercapacitive performance evaluation of electrodeposited nickel cobalt phosphate (E-NCP4) and rGO electrodes based asymmetric flexible solid state supercapacitor device. The solid state device ($Ni_{1.44}Co_{1.56}(PO_4)_2$//rGO) achieved operational potential window of 0 to 1.6 V. The AFSSS device shows maximum specific capacitance of 90 F g^{-1} at 0.4 A g^{-1} current density and energy density of 32 Wh kg^{-1} achieved at power density of 0.32 kW kg^{-1}. Also, $Ni_{1.44}Co_{1.56}(PO_4)_2$//rGO AFSSS device retains 89 % of capacitance after 4000 cycles. The good cyclic stability and high capacitive retention at high current density suggests that, the device can be used in flexible, portable and bendable electronic devices where high energy is required. Also, the practical usefulness of flexible device is tested by charging two series connected devices for 30 s and then discharged through 201 red LEDs panel. Interestingly, the panel lights up for 190 s after charging only for 30 s as displayed in Fig. 6.2.
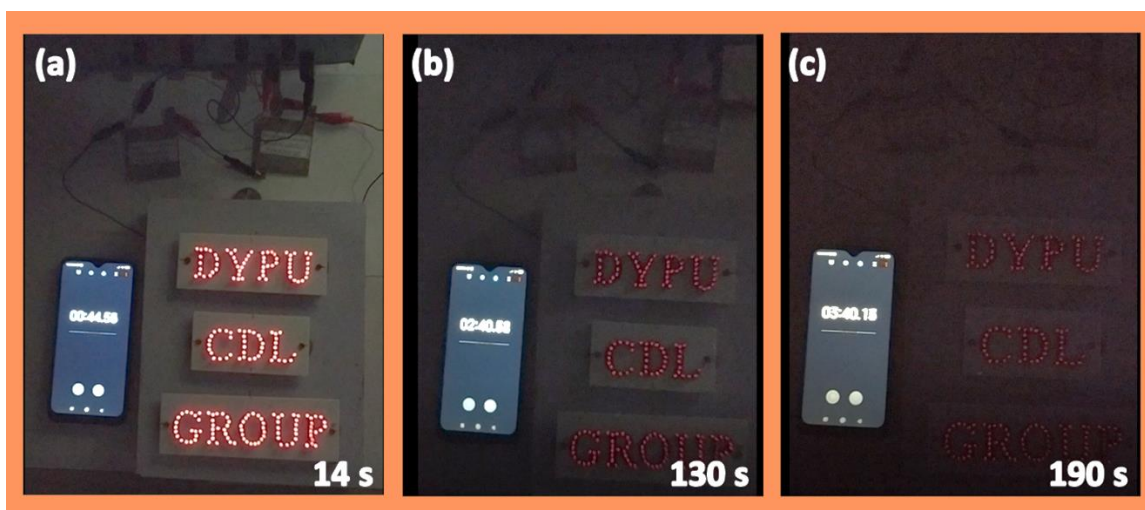
Fig. 6.2 Digital photographs of serially connected two $Ni_{1.44}Co_{1.56}(PO_4)_2$//rGO AFSSS

devices glowing 201 LEDs panel at different time periods.

The obtained results suggest commercial usefulness of prepared $Ni_{1.44}Co_{1.56}(PO_4)_2$//rGO AFSSS device. The supercapacitive performance of flexible devices is summarized in table 6.2.

Table 6.2 Electrochemical performance of asymmetric flexible solid state

supercapacitor devices

Deposition method	AFSSS Device	Specific capacitance ($F g^{-1}$) at current density ($A g^{-1}$)	Energy density ($Wh\ kg^{-1}$)	Power density ($kW\ kg^{-1}$)	Stability (%) at 4000 cycles
CBD	$Ni_{1.38}Co_{1.62}(PO_4)_2$//rGO	79 at 0.75	28	0.6	83.7 %
Electrodeposition	$Ni_{1.44}Co_{1.56}(PO_4)_2$//rGO	90 at 0.4	32	0.32	89 %

Chapter VI provides the extracts of all chapters i.e. summary and conclusions. In this work, nickel cobalt phosphate thin films are successfully prepared by chemical bath deposition and electrodeposition methods. The characterization techniques are used for analyses and confirmation of prepared nickel cobalt phosphate thin films. Their supercapacitive performance studied in terms of specific capacitance and cyclic stability. The result obtained from chapter III and IV proposes that, the ~1:1 ratio of nickel and cobalt content in nickel cobalt phosphate thin film exhibits high

electrochemical performance than other compositions. The microstructures of best performing electrodes prepared by both method (CBD and electrodeposition) are shown in Fig. 6.3 with their supercapacitive performance. The chemical bath deposited microflowers of nickel cobalt phosphate ($Ni_{1.38}Co_{1.62}(PO_4)_2$) electrode shows less performance than the electrodeposited microspheres with nanocracks like morphology of nickel cobalt phosphate ($Ni_{1.44}Co_{1.56}(PO_4)_2$) electrode. The microspheres containing nanocracks may offer high electroactive surface area than microflower for the electrochemical reaction and delivered enhanced electrochemical performance. Also, capacitive retention suggests efficient long durability of electrode during electrochemical reaction.
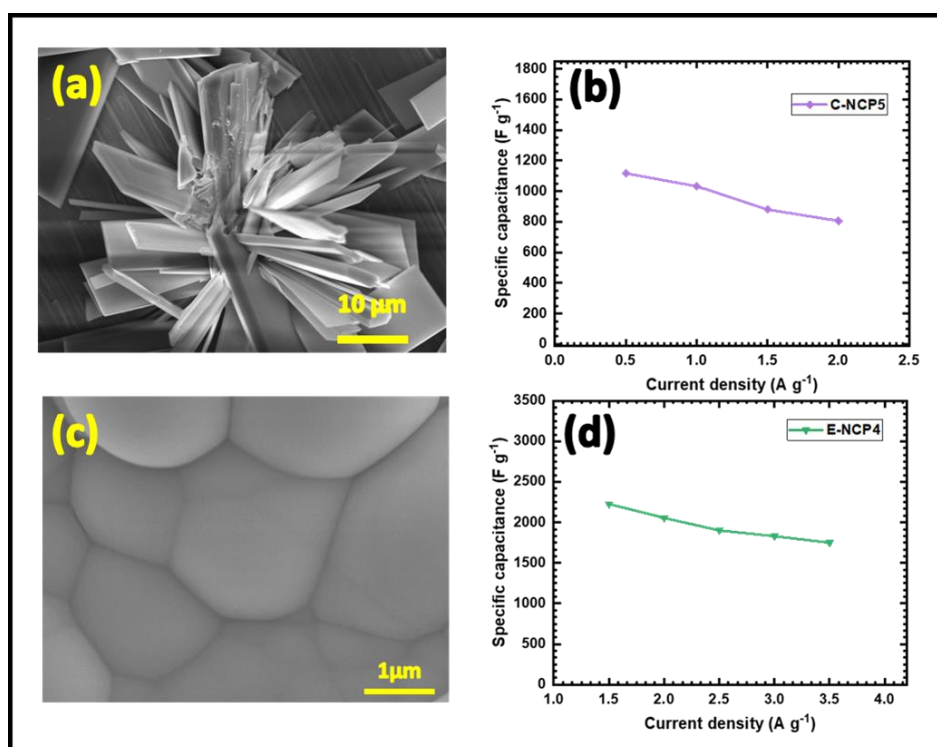

Fig. 6.3 The FE-SEM images of (a) $Ni_{1.38}Co_{1.62}(PO_4)_2$ (X2000) and (c) $Ni_{1.44}Co_{1.56}(PO_4)_2$ (X20000) thin films. The plots of specific capacitance versus current densities for (b) $Ni_{1.38}Co_{1.62}(PO_4)_2$ and (d) $Ni_{1.44}Co_{1.56}(PO_4)_2$ thin film electrodes.

The best performed chemical bath deposited (C-NCP5) and electrodeposited (E-NCP4) nickel cobalt phosphate flexible electrodes are used for the device fabrication and studied their supercapacitive performance. The aqueous and gel/solid state electrolyte are used for the supercapacitor device fabrication. The comparative energy density and power density (Ragon plot) of prepared asymmetric devices are plotted in Fig. 6.4. The available supercapacitors are unable to achieve high energy density than batteries and higher power density than capacitors. But, the asymmetric devices based on nickel cobalt phosphate electrode achieves higher values than the available supercapacitor devices, they exhibits energy density nearly equal to batteries and little less power density than capacitor.
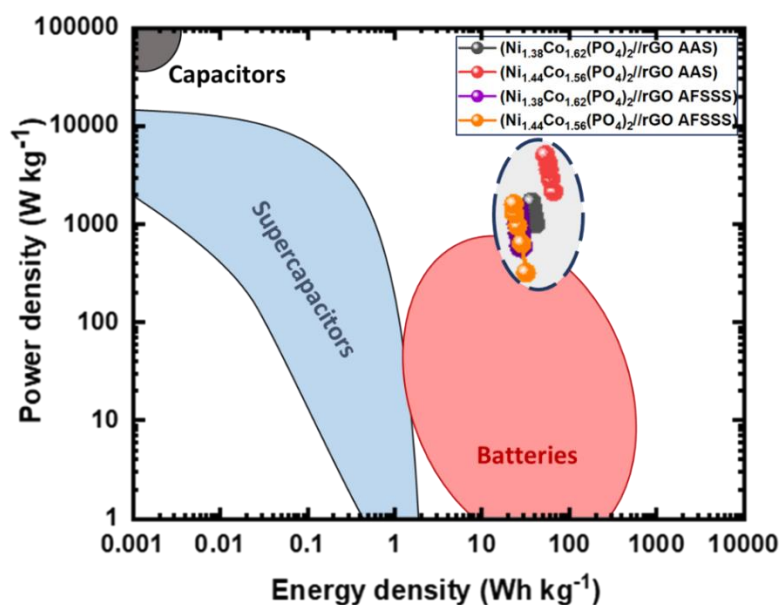

Fig. 6.4 The comparative Ragone plots of prepared asymmetric devices based on

nickel cobalt phosphate as positive and rGO as negative electrodes.

The electrodeposited nickel cobalt phosphate ($Ni_{1.44}Co_{1.56}(PO_4)_2$) based aqueous asymmetric device shows higher energy and power density than the other prepared aqueous and flexible solid state devices. The aqueous devices have limitations in their commercial application and that can be diminished by fabricating solid state devices. So, the electrodeposited nickel cobalt phosphate ($Ni_{1.44}Co_{1.56}(PO_4)_2$) thin film electrode

based flexible solid state supercapacitor device with comparable energy (32 Wh kg^{-1})

and power density (0.32 kW kg^{-1}) can be applicable at commercial level in flexible

portable electronic devices.